UNIVERSITY OF SOUTHAMPTON

FACULTY OF ENGINEERING, SCIENCE AND MATHEMATICS

School of Ocean and Earth Sciences

Meltwater Injections and their Impact on Atlantic Meridional Overturning Circulation and Climate during the time period of Heinrich Event 1 and the Last Deglaciation

By

Jennifer D. Stanford

Thesis for the degree of Doctor of Philosophy

November 2008

UNIVERSITY OF SOUTHAMPTON

UNIVERSITY OF SOUTHAMPTON

ABSTRACT

FACULTY OF ENGINEERING, SCIENCE AND MATHEMATICS
SCHOOL OF OCEAN AND EARTH SCIENCES

Doctor of Philosophy

MELTWATER INJECTIONS AND THEIR IMPACT ON ATLANTIC MERIDIONAL OVERTURNING CIRCULATION AND CLIMATE DURING THE TIME PERIOD OF HEINRICH EVENT 1 AND THE LAST DEGLACIATION

By JENNIFER D. STANFORD

The temporal relationship between meltwater pulse 1a (mwp-1a) and the climate history of the last deglaciation remains a subject of debate. By combining the GRIP $\delta^{18}O$ ice core record on the new Greenland Ice Core Chronology 2005 (GICC05) timescale with the U/Th-dated Barbados coral record, it is conclusively derived that mwp-1a did not coincide with the sharp Bølling warming, but with the abrupt cooling of the Older Dryas. To evaluate whether there is a relationship between meltwater injections, North Atlantic Deep Water (NADW) formation and climate change (i.e., the long term change in the average weather), a high-resolution magnetic (κ_{ARM}/κ) proxy record of NADW flow intensity from Eirik Drift, south of Greenland, is presented. A record of mean sortable silt grain sizes (an established proxy for near bottom current flow speed), obtained from the same samples on which the κ_{ARM}/κ was measured, shows remarkable similarity to the magnetic record and validates κ_{ARM}/κ as a proxy for NADW flow intensity. The record of κ_{ARM}/κ indicates only a relatively minor 200-yr weakening of NADW flow, coincident with mwp-1a. This compilation of records also indicates that during Heinrich event 1 (H1) and the Younger Dryas there were no discernible sea-level rises, and yet these periods were characterised by intense NADW slowdowns. Records of planktonic foraminiferal $\delta^{18}O$, as well as lithic and foraminiferal counts from Eirik Drift are combined with previous studies from the Nordic seas and the 'Ice Rafted Debris (IRD) belt', and portray a sequence of events through the interval of H1. These events progressed from an onset of meltwater release around 19 ka BP, through the 'conventional' H1 phase from ~17.5 ka BP, to a final phase between 16.5 and 14.6 ka BP, characterised by a pooling of fresh waters in the Nordic Seas, which were injected hyperpycnally. This build up of fresh waters was purged from the Nordic Seas, preconditioning the Nordic Seas for convective deep-water formation. This allowed the abrupt re-start of NADW formation in the Nordic Seas at the Bølling warming. In contrast to previous estimates for the duration of H1 (i.e., 1000 years to only a century or two), the total, combined composite signal of H1 presented here had a duration of nearly 4000 yrs (~19–14.6 ka BP), now spanning the established period of NADW shutdown. Clearly, deep-water formation and climate are not simply controlled by the magnitude or rate of meltwater addition. Instead, the results presented here emphasise that the location of meltwater pulses may be more important, with NADW formation being particularly sensitive to surface freshening in the Arctic/Nordic Seas

CONTENTS

LIST OF FIGURES AND TABLES

It should be noted that supplementary information, units and citations which are given in the figure and table captions themselves are not replicated in this listing.

Figures

Tables

DECLARATION OF AUTHORSHIP

I, JENNIFER DAWN STANFORD, declare that the thesis entitled "Meltwater injections and their impact on Atlantic meridional overturning circulation and climate during the time period of Heinrich event 1 and the last deglaciation" and the work presented in the thesis are both my own, and have been generated by me as the result of my own original research. I confirm that:

- this work was done entirely or mainly whilst in candidature for a research degree at this University;
- where any part of the thesis has previously been submitted for a degree or any other qualification at this University or any other institution, this has been clearly stated;
- where I have consulted the published work of others, the source is always given. With the exception of such quotations, this thesis is entirely my own work;
- I have acknowledged all main sources of help;
- where the thesis is based on the work done by myself jointly with others, I have made clear exactly what was done by the others and what I have contributed myself;
- parts of this work have been published as:

Stanford, J. D., E. J. Rohling, S. E. Hunter, A. P. Roberts, S. O. Rasmussen, E. Bard, J. McManus, and R. G. Fairbanks (2006), Timing of mwp-1a and climate responses to meltwater injections, *Paleoceanography*, *21*, PA4103, doi:10.1029/2006PA001340, 2006.

Hunter, S. E., D. Wilkinson, **J. D. Stanford**, D. A. V. Stow, S. Bacon, E. J. Rohling, A. M. Akhetmetzhanov, and N. H. Kenyon (2007a), *The Eirik Drift: a long-term barometer of North Atlantic deepwater flux south of Cape Farewell, Greenland*. In: Viana, A. R., and M. Rebesco (Eds) *Economic and Palaeoceanographic Significance of Contourite Deposits*, Geological Society Special Publications, *276*, 245-263.

Signed:

Date:

ACKNOWLEDGEMENTS

The author would like to acknowledge and thank the following:

The crew and scientists onboard *RV Professor Logachev* during the cruise TTR-13 and the *RRS Discovery* during cruise D298.

Professor Eelco J. Rohling for his insightful comments and for his help in formulating ideas. The author would also like to thank Dr. Sheldon Bacon and Professor Dorrik A. V. Stow, who have co-supervised this thesis, Professor Alan Kemp who was her panel chair, and Dr. Samantha Gibbs and Mr. Adrian Lester who proof read chapters.

Sincere thanks are extended to Mr. Mike Bolshaw, Mr. Ross Williams, Dr. Richard Pearce, Dr. Guy Rothwell, Mr. Robert Jones and Mr. John Ford for their advice and help with analytical procedures and data acquisition. The author would also like to acknowledge Professor Andrew P. Roberts and Dr. Christopher Rowan for their analytical advice and help with the interpretation of the magnetic data, Professor Pieter M. Grootes and *Leibniz Labor*, *Kiel*, for the AMS^{14}C datings, BOSCORF for use the ITRAX core-scanner and their facilities, and Dr. Ian R. Hall and Helen Medley at the *School of Planetary*, *Earth and Ocean Science* at *Cardiff University* for the use of the *Multisizer 3* coulter counter and for their help with the sortable silt grain size analyses.

Professor Eelco J. Rohling, Professor Andrew P. Roberts, Dr. Sally Hunter, Dr. Sune O. Rasmussen, Professor Edouard Bard and Professor Rick Fairbanks, who contributed helpful ideas and data for Stanford *et al*. (2006).

On a personal note, the author would like to thank her close friends and family for their support.

This study was funded as part of the NERC Rapid Climate Change Program under Grants NER/T/S/2002/00453 and NER/T/S/2002/00436.

FREQUENTLY USED ABBREVIATIONS

AABW	Antarctic Bottom Water
AAIW	Antarctic Intermediate Water
AMOC	Atlantic Meridional Overturning Circulation
AMS^{14}C	Accelerated Mass Spectrometric ^{14}C
ARM	Anhysteretic Remanent Magnetisation
CGFZ	Charlie Gibbs Fracture Zone
DSOW	Denmark Strait Overflow Water
DWBC	Deep Western Boundary Current
EGC	East Greenland Current
EGCC	East Greenland Coastal Current
FORC	First Order Reversal Curve
H1	Heinrich event 1
IRM	Isothermal Remanent Magnetisation
ISOW	Iceland-Scotland Overflow Water
LGM	Last Glacial Maximum
LSW	Labrador Sea Water
MOC	Meridional Overturning Circulation
NAD	North Atlantic Drift
NADW	North Atlantic Deep Water
NRM	Natural Remanent Magnetisation
SEM	Scanning Electron Microscope
SIRM	Saturated Remanent Magnetisation
SQUID	Superconducting Quantum Interference Device
THC	Thermohaline Circulation
XRD	X-ray Diffraction
XRF	X-Ray Fluorescence

CHAPTER 1

1. INTRODUCTION

1.1. Rationale

It has been widely speculated that fresh water additions in the North Atlantic would result in decreased rates of North Atlantic Deep Water (NADW) formation, reducing the poleward oceanic heat transport (e.g., Stommel, 1961; Rooth, 1982; Broecker, 1991). Palaeoceanographic inferences drawn from studies of deep-sea cores, as well as ocean-atmosphere models, give support to this hypothesis (e.g., Boyle and Keigwin, 1987; Broecker, 1994; Sarthein et al., 1994; Keigwin & Lehman, 1994; Rahmstorf, 1994; 1995; Schiller *et al*., 1997; Bianchi & McCave, 1999; Curry *et al*., 1999; van Kreveld *et al*., 2000; Ganopolski and Rohmstorf, 2001; McManus *et al*., 2004; Rahmstorf *et al*., 2005; Robinson *et al*., 2005; Marchitto *et al*., 2007; Peck *et al*., 2007a, b; Keigwin and Boyle, 2008). Observations of present–day surface freshening around the Arctic and the Nordic Seas (e.g., Lindsay & Zhang, 2005; Rignot and Kanagaratnam, 2006), and recent inferences of reduced NADW formation (e.g., Bryden *et al*., 2005), underline the need to better understand the ocean/climate relationship in both the past and the present day context.

Given this requirement to further our knowledge on how the ocean-climate system responds to North Atlantic freshwater injections, this thesis aims to provide new insight into past oceanic responses to meltwater injections, focussing on the time period of Heinrich Event 1 (dated at around 17.5-16 ka BP) (ka BP refers to thousands of years before 1950 AD) (e.g., Bard *et al.*, 2000; Hemming, 2004) and the last deglaciation, during which time period northern hemisphere climate (e.g., Grootes and Stuiver, 1997; Stuiver and Grootes, 2000; Johnsen *et al.*, 2001; Rasmussen *et al.*, 2006) and ice sheet volumes (e.g., Fairbanks, 1989; 1990; Bard *et al.*, 1990a, b; 1996; Peltier and Fairbanks, 2006) fluctuated rapidly.

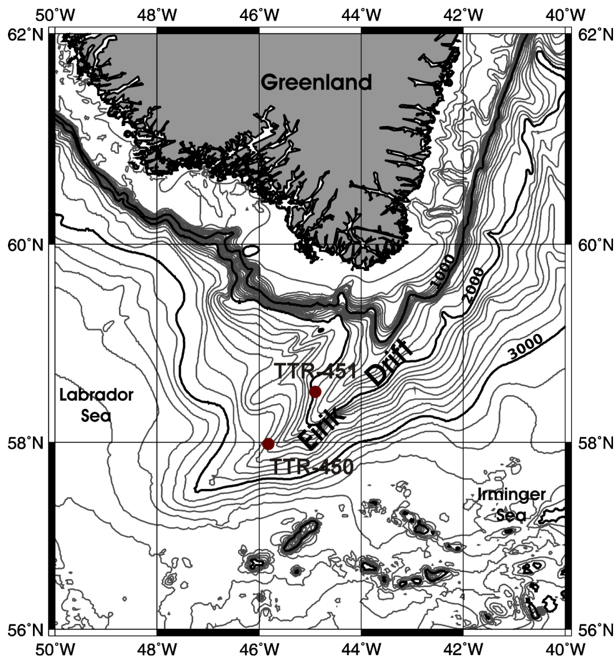

Figure 1.1 Location map of marine sediment cores TTR-450 and TTR-451 (bathymetry is from the GEBCO Digital Atlas published by the British Oceanographic Data Centre on behalf of the Intergovernmental Oceanographic Commission of UNESCO (IOC) and the International Hydrographic Organisation (IHO) (2003)). The 1000, 2000 and 3000 (heavy, black) contours are denoted.

This report presents new insights from the study of marine sediment cores TTR13-AT450G and TTR13-AT451G (hereafter TTR-450 and TTR-451) recovered from Eirik Drift, south of Greenland (Figure 1.1). This site is sensitive to changes in both deep and surface water hydrography in relation to the outflow from the 'critical' regions of NADW formation, the Arctic and Nordic Seas (e.g., Dickson and Brown, 1994; Bacon, 1998; 2002). Proxy records generated from core TTR-451 are compared with previously published datasets from around the North Atlantic, and allow the synthesis of ocean-wide reconstructions. This has provided an impact assessment for the oceanographic changes associated with ice sheet volume reductions (meltwater injections) that occurred during the time period of H1 and the last deglaciation. Insight has also been gained into the how linearly the Atlantic Meridional Overturning Circulation (AMOC) and climate responded to very different magnitudes and rates of North Atlantic meltwater injections (i.e., whether the amount of decrease in AMOC intensity was directly proportional to the amount of freshwater forcing). Better constraints on the timing and impact of deglacial meltwater injections are needed in order to provide a more robust test bed for coupled ocean-climate models.

1.2. Thesis layout

The next chapter outlines the context of the study presented in this thesis, by presenting an overview of existing literature on (1) the global thermohaline circulation and its role in climate modulation, (2) the climate history of the last glacial cycle and the last deglaciation, (3) the mechanisms for the climate transitions during the last glacial cycle (based upon evidence from palaeo-records and ocean-climate models) and (4) the deep and surface water hydrographies around Eirik Drift/Cape Farewell, south of Greenland. The overview of the deep water hydrographies has been largely published by Hunter *et al*. (2007a) as a *Geological Society, London, Special Publications*, for which the author of this thesis was a co-author and contributed by aiding the interpretation of the geophysical data used.

Chapter 3 describes the location of cores TTR-450 and TTR-451, and the laboratory methods which were used in this study. An overview of the equipment used is provided in this chapter, along with a critical assessment of the sampling methods and laboratory techniques employed for the generation of the proxy records.

The fourth chapter presents the results from this study, which include sedimentary core descriptions, core scanning X-ray fluorescence (XRF) counts, environmental magnetics and palaeomagnetics, bulk and planktonic foraminiferal stable carbon and oxygen isotope ratios, lithic (ice-rafted debris – IRD) and total planktonic foraminiferal counts, mean sortable silt grain size analyses and Accelerated Mass Spectrometric (AMS)^{14}C datings. The development of the age-model for core TTR-451 is presented in sub-chapter 4.5. The magnetic susceptibility data was generated in part by Dr. Sally Hunter.

Chapter 5 provides discussion on three key areas of research. The first section entitled 'The timing of mwp-1a and climate responses to meltwater injections' was largely published in *Paleoceanography* (Stanford *et al*., 2006). For reference, a copy of the published paper is provided in the Appendix 4 to this thesis. This piece of work was done in collaboration with E. J. Rohling, S. E. Hunter, A. P. Roberts, S. O. Rasmussen, E. Bard, J. McManus, and R. G Fairbanks. The second section focuses upon the timing of mwp-1a in the Barbados and Sunda Shelf sea level records. Presented in this section is a careful re-evaluation of the Sunda Shelf record in order to reconcile these two sea level indicators. The final section presents a new concept for the sequence of events that were associated with Heinrich event 1 in the northern North Atlantic and the Nordic Seas. Here, proxy records from TTR-451 are compared with other well-dated surface ocean and climate records.

The appendices of this thesis include: calibration plots of the AMS^{14}C datings from the Sunda and Vietnamese Shelves (appendix 1), and a digital appendix which provides the data used within this thesis (appendix 2).

CHAPTER 2

2. BACKGROUND

2.1. Global Thermohaline Circulation and climate modulation

The Thermohaline Circulation (THC) globally redistributes heat, and it is also critical for distribution of carbon and nutrients (e.g., Broecker, 1991; Dickson and Brown, 1994; Ganachaud and Wunsch, 2000). The THC is driven by a combination of wind stress, convection, and (tidal) mixing/turbulence, resulting in a process of high-latitude sinking of relatively saline surface waters to form intermediate and deep water masses and upwelling at low latitudes and in the Pacific (e.g., Broecker, 1991; Wunsch, 2002). Nearly all but the top 100 m of the oceans is stratified and stable, hence returning the deep water masses to the surface requires turbulent mixing and Ekman divergence via wind stress and tidal stirring (Wunsch, 2002). In general, upwelling of the deep-water masses occurs in the Indian and Pacific Oceans, which returns as relatively warm surface currents. Often used incorrectly as a synonym for the THC, the Meridional Overturning Circulation (MOC) is a closely related concept, which refers to the north-south flow as a function of depth and latitude, including the wind-driven processes, and Ekman and meridional overturning cells (Rahmstorf, 2003).

The THC is primarily driven by high-latitude cooling and sinking of surface water masses (e.g., Broecker, 1991; Dickson and Brown, 1994). In the North Atlantic, relatively warm and saline surface waters are transported northeast across the North Atlantic, from the tropics to the Nordic Seas and Arctic, via the wind driven Gulf Stream and the density/thermohaline driven North Atlantic Drift (NAD) (e.g., Schmitz and McCartney, 1993) (Figure 2.1). Transporting up to 10^{15} W of heat (Ganachaud and Wunsch, 2000), the Gulf Stream/NAD is thought to maintain temperatures in Northwest Europe at around 5-8 °C warmer than if it were 'switched off' (Broecker, 1991; Seager *et al*., 2002). At high latitudes within the northern North Atlantic, wind driven evaporative cooling releases the heat carried within the Gulf Stream/NAD to the atmosphere, causing surface water masses to become not only colder, but also more saline. These surface waters therefore become denser than the surrounding water masses, and resultant convective instability causes them to sink to form intermediate and deep water (e.g., Broecker, 1991; Wunsch, 2002).

Primarily a process that occurs within the Nordic Seas, the evaporative cooling of the Gulf Stream/NAD results in the formation of North Atlantic Deep Water (NADW) (e.g., McCartney, 1992; Dickson and Brown, 1994; Rudels *et al*., 2002; Bacon, 2002). Other localised key sites of deepwater formation as a result of convective processes include: the Labrador Sea, forming Labrador Sea Water (LSW); the Mediterranean Sea, forming the Mediterranean Outflow current; and the Weddell Sea and Ross Sea, forming Antarctic Bottom Water (AABW) (e.g., Wust, 1935; Worthington, 1976; Schmitz and McCartney, 1993; Dickson and Brown, 1994; Schmitz, 1996; Pickart *et al*., 2003). These deep waters spread out at depth. Generated from partial freezing, AABW is the coldest and densest of the deep-water masses (Wust, 1935; Dickson and Brown, 1994). A further important water mass is Antarctic Intermediate Water (AAIW), however, its method of formation is still debated (e.g., Wust, 1935; Santosa and England, 2004 and references therein). The intermediate and deep water masses in the vicinity of Eirik Drift spread out at depth, and Coriolis force causes westward intensification of the currents, forming the so-called Deep Western Boundary Current (DWBC) (review in Hunter *et al*., 2007a, b).

The Nordic Seas are bounded to the south by the Denmark Strait (~640 m deep sill) and the Iceland-Scotland Ridge (~450 m deep sill and ~850 m deep in the Faroe Bank Channel), and NADW overflows these ridges as Denmark Strait Overflow Water (DSOW) and Iceland-Scotland Ridge Overflow water (ISOW) respectively, before mixing with other water masses to form the DWBC (e.g., Bacon, 1998; Bacon, 2002; Hunter *et al*., 2007b). However, the mechanisms that govern NADW overflow over the topographic high of Denmark Strait remains poorly understood (review in Bacon, 2002), with suggestions of intermediate waters forming from; (a) deep winter mixing (Swift, 1986), (b) the mixing within the East Greenland Current and the western Greenland Sea gyre (Strass *et al*., 1993), (c) the mixing of deep Arctic waters with re-circulated Atlantic waters carried in the lower portion of the EGC (Rudels *et al*., 1998; 2002), and (d) the transformation of Atlantic waters that are circulated around the Arctic, giving the water mass the properties of DSOW, and separate to the EGC (Mauritzen, 1996). It seems unlikely however, that DSOW overflows the Denmark Strait with the properties (density) of fully formed NADW (Bacon, 2002). The combined southward outflow of NADW from the Nordic Seas is compensated in terms of mass balance by the northward inflow of the Gulf Stream/NAD (e.g., Schmitz and McCartney, 1993).

In essence, the global THC is driven by the thermal, and hence density gradients between equator (warm and less dense) and pole (cold and more dense). Zones of higher surface water salinity occur in evaporative regions i.e. the tropics and subtropics, and impart an influence upon the equator-pole density gradient. The effect of salinity therefore makes the THC into a non-linear and bistable system (e.g., Rahmstorf, 2000) (Figure 2.2). Using a simple box model, Stommel (1961) was the first to demonstrate that increasing salinity at high-latitudes (deep-water formation regions) would invigorate the THC and increase the flow of saline waters to high-latitude regions, thereby forming a positive feedback loop. Based upon this observation, it is suggested that increased wind stresses within the subpolar gyre would locally increase surface water salinity, which would have stabilising effect on the THC (Schiller *et al*., 1997; Timmermann and Goose, 2004).

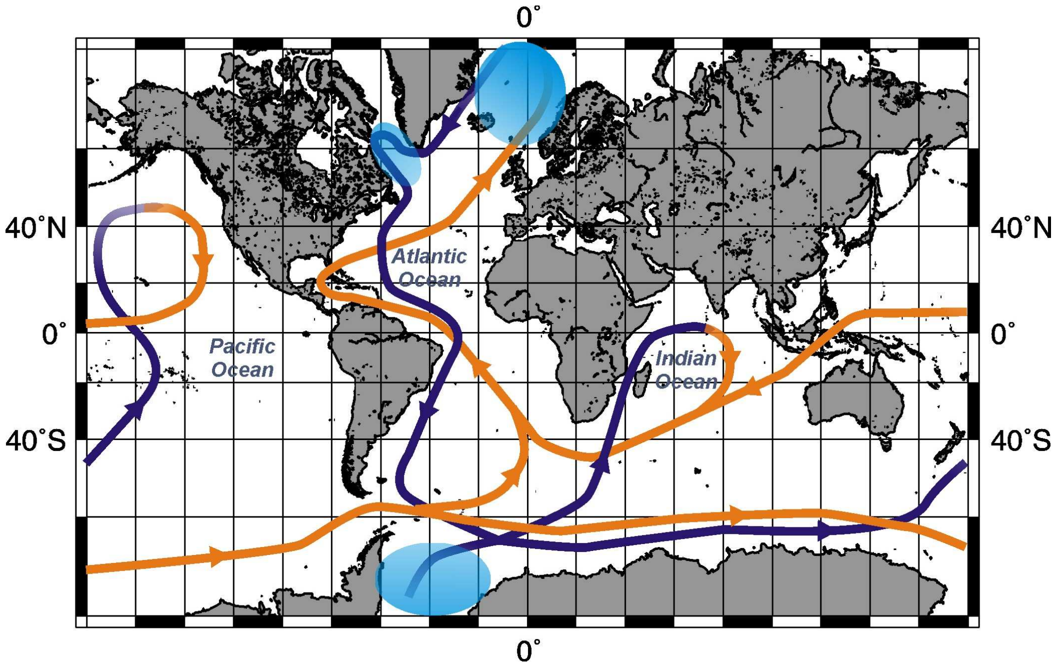

Figure 2.1. Schematic diagram of the global thermohaline circulation (modified after Broecker, 1991). Warm surface currents are represented in orange, and deep/bottom water currents in blue. Shaded blue zones indicate the key areas of deep-water formation.

2.1.1. The THC/MOC stability and climate modulation

The stability of the MOC in ocean circulation models has been described in terms of the strength of the MOC versus freshwater forcing/reduced salinity in the northern Atlantic (e.g., Rahmstorf, 1995; 2002; Manabe and Stouffer, 2000; Rahmstorf and Ganopolski, 1999; Rahmstorf *et al*., 2005). Results from ocean-circulation models show that with reduced northern Atlantic salinity, the MOC intensity is eventually reduced to a complete shutdown, and that it recovers with increasing salinity along a different pathway, forming a hysteresis loop (e.g., Rahmstorf, 1995; Rahmstorf *et al*., 2005) (Figure 2.2.). This hysteresis behaviour of the THC to freshwater forcing has also been observed in laboratory experiments (Mullarney *et al*., 2007).

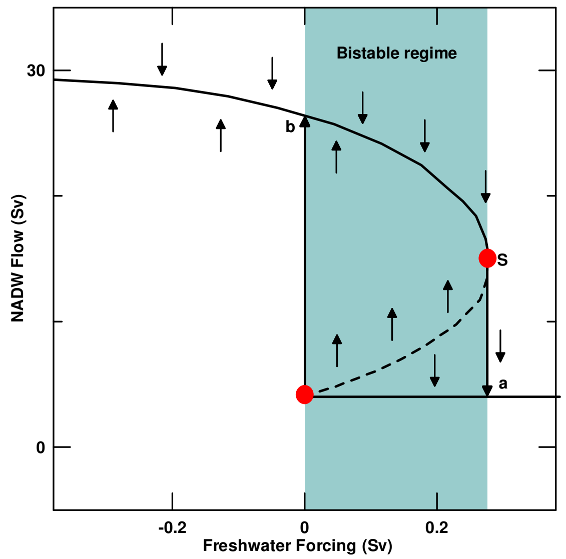

Figure 2.2. Schematic representation of the Atlantic THC stability with freshwater forcing (modified from Rahmstorf, 2002). Stable equilibrium states are indicated by solid lines, whereas the dashed line represents unstable states. Arrows show the transitions between states. 'S' indicates the '*Stommel bifurcation*' point after which NADW formation is shut down. Arrow (a) represents advective spindown (i.e., when the overturning remains collapsed due to reduced salt transport) and (b) the resumption of the THC, with (a) and (b) forming the complete hysteresis loop.

Comparison of temperatures at equivalent latitudes between the North Pacific and the North Atlantic would suggest that the Gulf Stream/NAD heat supply to the northern North Atlantic equates to around 5-8 °C of warming (Broecker, 1991; Rahmstorf, 2002). Coupled climate models indicate that if the THC was 'switched off', the cooling around the northern North Atlantic would be of a similar value, with maximum temperature decreases in the Nordic Seas where sea-ice margin expansion and positive feedbacks exacerbate the cooling (Schiller *et al.*, 1997; Rahmstorf, 2000; 2003). A weakening or shutdown of the THC/MOC due to freshwater forcing, cutting off the northern North Atlantic heat supply, has been widely speculated as the cause of past cold events observed in the palaeo-records (e.g., Broecker and Denton, 1989; Broecker, 1991; Stocker *et al.*, 1992; Rahmstorf, 1995; 2000; 2002; Schiller *et al.*, 1997; Manabe and

Stouffer, 1997; 2000; Ganopolski and Rahmstorf, 2001; Vellinga and Wood, 2002; Schmittner *et al*., 2003; Rahmstorf *et al*., 2005).

2.2. Overview of the climate history of the last glacial cycle

Studies of ice cores recovered from Greenland (e.g., GRIP, NGRIP, GISP2 and DYE-3) and Antarctica (e.g., Vostok, Byrd, Taylor Dome, and most recently EPICA, Dronning Maud Land) provide high-resolution proxies for past changes in temperature, aridity and atmospheric circulation, as well as direct measurements of atmospheric methane and CO_2 concentrations trapped in air bubbles within the ice (e.g., Dansgaard *et al*., 1993; Grootes *et al*., 1993; Jouzel *et al*., 1993; Taylor *et al*., 1993; Mayewski *et al*., 1994; 1997; Grootes and Stuiver, 1997; Bender *et al*., 1999; Petit *et al*., 1999; Severinghaus and Brook, 1999; Blunier and Brook, 2001; Johnsen *et al*., 2001; Brook *et al*., 2005; Rasmussen *et al*., 2006; EPICA community members, 2006), and are often considered as the 'master records' for climate event stratigraphy (Rohling *et al*., 2003). For the Greenland $\delta^{18}O$ ice core record (a proxy for air temperature above Greenland), data correlation have been made as far afield as the North Pacific Ocean (e.g., Hendy and Kennett, 1999; 2003) and East Asia (e.g., Wang *et al*., 2001; Yuan *et al*., 2004).

The Greenland and Antarctic ice core $\delta^{18}O$ and δD records show that the last glaciation started at around 115,000 ka BP and took around 80,000 yrs to reach peak glacial conditions (the Last Glacial Maximum – LGM) (Dansgaard *et al*., 1993; Grootes *et al*., 1993; Jouzel *et al*., 1993; Petit *et al*., 1999; Johnsen *et al*., 2001; EPICA community members, 2006; Figure 2.3a, e). Using the relationship that 0.33 ‰ increase in $\delta^{18}O$ corresponds to a 1°C temperature increase, Cuffey and Clow (1997) estimated that LGM temperatures above Greenland were around 15 °C colder than today. Comparison of these high-latitude values with low-latitude estimates, which were around 3°C colder than the present day (Pierrehumbert, 1999), a much larger equator-pole temperature gradient was developed during Northern Hemisphere glaciation. The global temperature decrease allowed for mountain snowlines to descend (e.g., Denton *et al*., 1999), and the formation of continental ice sheets across the Northern Hemisphere (e.g., Bowen *et al*., 2002; Dyke *et al*., 2002). As a result, sea-level was around 120 m lower at the LGM than the present-day (e.g., Fairbanks, 1989; Lambeck *et al*., 2002; Siddall *et al*., 2003; Peltier and Fairbanks, 2006). Reduced global temperatures also allowed for the southward expansion of polar sea-ice (e.g., Gildor and Tziperman, 2003; Pflaumann *et al*., 2003; Nørgaard-Pederson *et al*., 2003; Weinelt *et al*., 2003; de Vernal *et al*., 2005). Model simulations of the LGM show that such vast expanses of ice expansion over the Northern Hemisphere would have caused significantly reduced atmospheric temperatures and change in geostrophic wind pathways and patterns (e.g., Ganopolski *et al*., 1998; Kageyama *et al*., 2001).

The globally lowered land and ocean temperatures at the LGM (e.g., Alm, 1993; Atkinson *et al*., 1987; Grootes *et al*., 1993; Jouzel *et al*., 1993; Johnsen *et al*., 2001; Mix *et al*., 2001; Petit *et al*., 1999; Weinelt *et al*., 2003; Pflaumann *et al*., 2003; de Vernal *et al*., 2005; 2006; EPICA community members, 2006; Weldeab *et al*., 2007) led to a weaker global hydrological cycle (e.g., Wang *et al*., 2001; Gasse, 2000; Weldeab *et al*., 2007). Direct measurements from trapped air bubbles contained within the ice cores from Antarctica show that global atmospheric methane and CO_2 concentrations were markedly lower during the LGM (190 ppm) in comparison to interglacials (280 ppm) (Figure 2.3b, c) (Chappellaz *et al*., 1993; Petit *et al*., 1999). During the last glacial cycle, the Greenland ice cores also record increased concentrations of continentally sourced [K^+, Ca^{2+} and Mg^{2+}] ions (Mayewski *et al*., 1994; 1997; Rohling *et al*., 2003) (Figure 2.3f, g) and high levels of electrical conductivity (which reflect concentrations of $CaCO_3$ bearing dust) (Taylor *et al*., 1993). These suggest that generally windier/dustier conditions were coincident with the globally reduced temperatures during the last glacial cycle and the LGM, most likely resulting from the coupled effect of increased aridity along with a significant re-arrangement of the atmospheric circulation patterns, forced by the expansion of the polar ice caps (Mayewski *et al*., 1997). Evidence for a more vigorous atmospheric circulation has also been found in Chinese Loess deposits (e.g., Kukla, 1988; 1990), as well as the Antarctic ice core record (Figure 2.3d), with

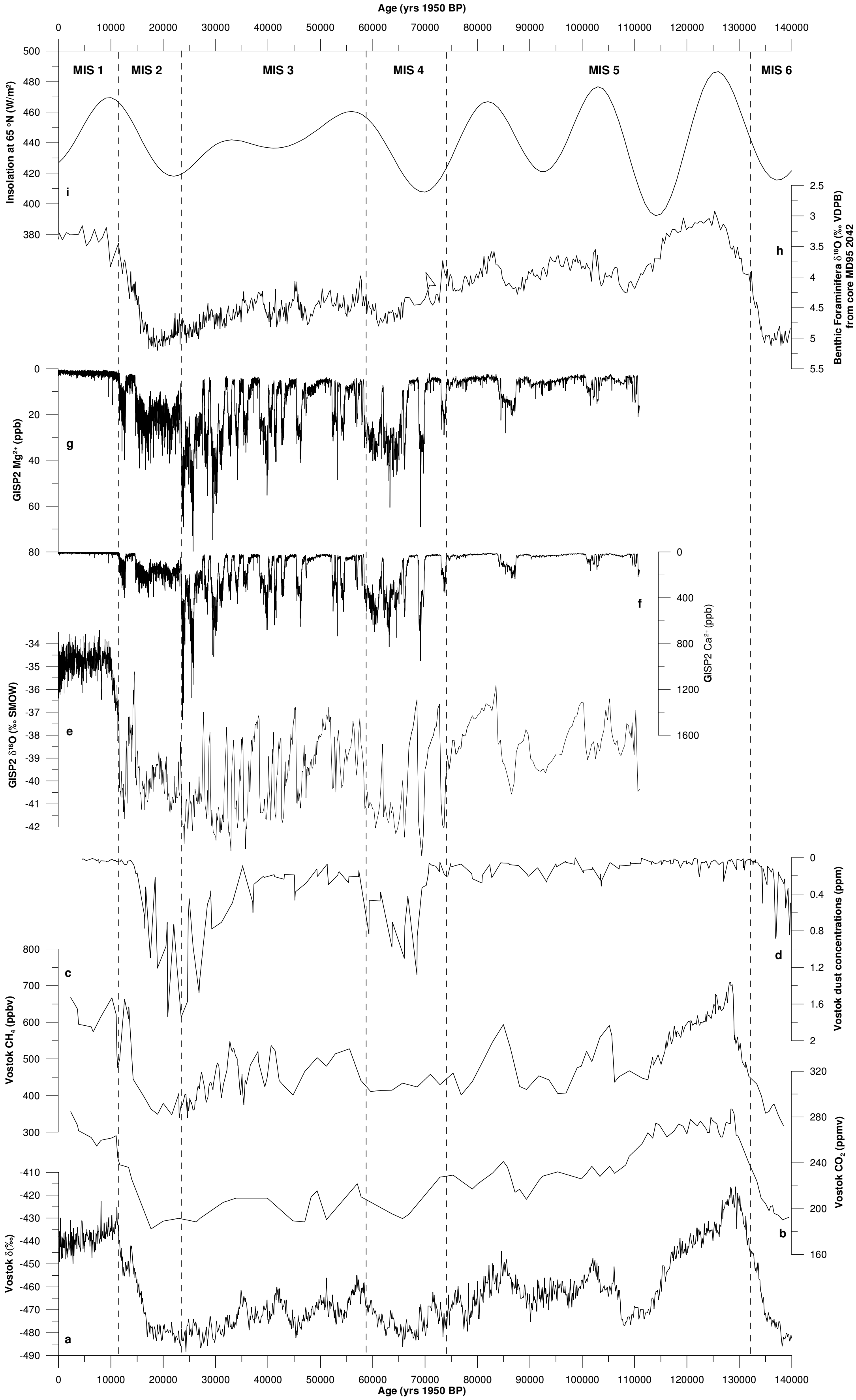

Age (yrs 1950 BP)
MIS 1
MIS 2
MIS 3
MIS 4
MIS 5
MIS 6
Insolation at 65 °N (W/m²)
Benthic Foraminifera δ18O (‰ VDPB) from core MD95 2042
GISP2 Mg2+ (ppb)
GISP2 Ca2+ (ppb)
GISP2 δ18O (‰ SMOW)
Vostok dust concentrations (ppm)
Vostok CH4 (ppbv)
Vostok CO2 (ppmv)
Vostok δ(‰)
i
h
g
f
e
d
c
b
a

Figure 2.3. (a). The Vostok δD ice core record (Petit *et al.*, 1999). Higher values indicate warmer air temperatures. Records of atmospheric carbon dioxide (b), methane (c) and dust (d) concentrations measured from air bubbles in the Vostok ice core (Petit *et al.*, 1999). (e) The GISP2 $\delta^{18}O$ ice core record (Grootes *et al.*, 1993) and the Ca^{2+} (f) and Mg^{2+} (g) ion series (Mayewski *et al.*, 1994). (h) The benthic $\delta^{18}O$ record measured on the species *Cibicidoides wuellerstorfi* from marine core MD95-2042 and synchronised on the GISP2 timescale (Shackleton *et al.*, 2000). More enriched values represent greater ice-sheet volumes, and hence, lower sea-level. MIS stands for Marine Isotope Stage. (i) the July insolation curve at 65 °N (Berger, 1991; 1999).

marked increases in dust concentration towards full glaciation (Jouzel *et al.*, 1993; Petit *et al.*, 1999; EPICA community members, 2006).

It has been suggested that glacial-interglacial cycles may have been forced by insolation changes (Milankovitch, 1949), but it is likely that secondary feedback mechanisms due to the extension of the North Hemisphere ice margins (e.g., albedo, deflection of atmospheric planetary waves, freshening of the North Atlantic and weakening/rearrangement of the THC, and reductions in greenhouse gases) may have been important in achieving full glacial conditions (e.g., Broecker, 1991; Chappellaz *et al.*, 1993; 1997; Rahmstorf, 1995; Brook *et al.*, 1996; reviews in Broecker, 2000a and Maslin *et al.*, 2001; Raymo *et al.*, 2004; Lynch-Stieglitz *et al.*, 2007). Further discussion of this topic is outside of the scope of this thesis.

2.3. Dansgaard-Oeschger Cycles and Heinrich Events

Dansgaard-Oeschger (D-O) cycles were identified in the Greenland ice core $\delta^{18}O$ records as a series of asymmetrical 'warm' events and cold 'stadials' that punctuated Northern Hemisphere climate of the last glacial cycle with millennial-scale (~1500 yr) timings (e.g., Dansgaard *et al*., 1993; Grootes *et al*., 1993) (Figure 2.4a). The D-O warmings are numbered GIS 1 to GIS 24 (Figure 2.4a) and are characterised by sharp temperature increases in the order of around 10 °C (Dansgaard *et al*., 1993; Severinghaus and Brook, 1999). Synchronous with the cold portions of the D-O cycles were abrupt increases in the glaciochemical series (Figure 2.4b-d) (Mayewski *et al*., 1994; 1997; Rohling *et al*., 2003) and ECM values (Taylor *et al*., 1993) recorded in the Greenland ice cores. This suggests that dustiness, and hence, aridity and the vigour of the atmospheric circulation, in the Northern Hemisphere increased rapidly to maximum values within a few decades (e.g., Taylor *et al*., 1993). Atmospheric concentrations of CH_4 also increased from glacial values by around 15 % during D-O interstadials (Chappellaz *et al*., 1993; Petit *et al*., 1999), synchronous with drying pulses north of 10 °S in Africa (Gasse, 2000). Speleothem $\delta^{18}O$ records from China suggest reductions in East Asian monsoon intensity were synchronous with D-O stadials (Wang *et al*., 2001; Zhou *et al*., 2008).

Records of lithic counts from marine cores in the North Atlantic show increased Ice Rafted Debris (IRD) concentrations that were contemporaneous with the D-O stadials in Greenland indicating melt water was being injected into the North Atlantic during these cold intervals (e.g., Bond *et al*., 1992; 1993; 1997; 1999; Bond and Lotti, 1995; Grousset *et al*., 2000; Sarnthein *et al*., 2000; van Kreveld *et al*., 2000). Note, however, that these IRD rich layers are not exclusive to the last glacial cycle, but occurred pervasively during the last interglacial (Oppo *et al*., 1998) and throughout the Holocene until the Laurentide and Fennoscandian ice sheets had disappeared (e.g., Bond *et al*., 1997; 1999), but with much smaller magnitude than during glacials.

Proxy palaeo-temperature records obtained from marine sediment cores have sparked debate about the global synchroneity of D-O climate events (e.g., Vidal *et al*., 1999; Hendy and Kennett, 2003; Kiefer *et al*., 2001). However, in the marine realm, this debate suffers from large dating uncertainties between core sites, which often are greater than inferred phase offsets. For the Greenland and Antarctic ice core records, methane synchronisation has allowed for sensible

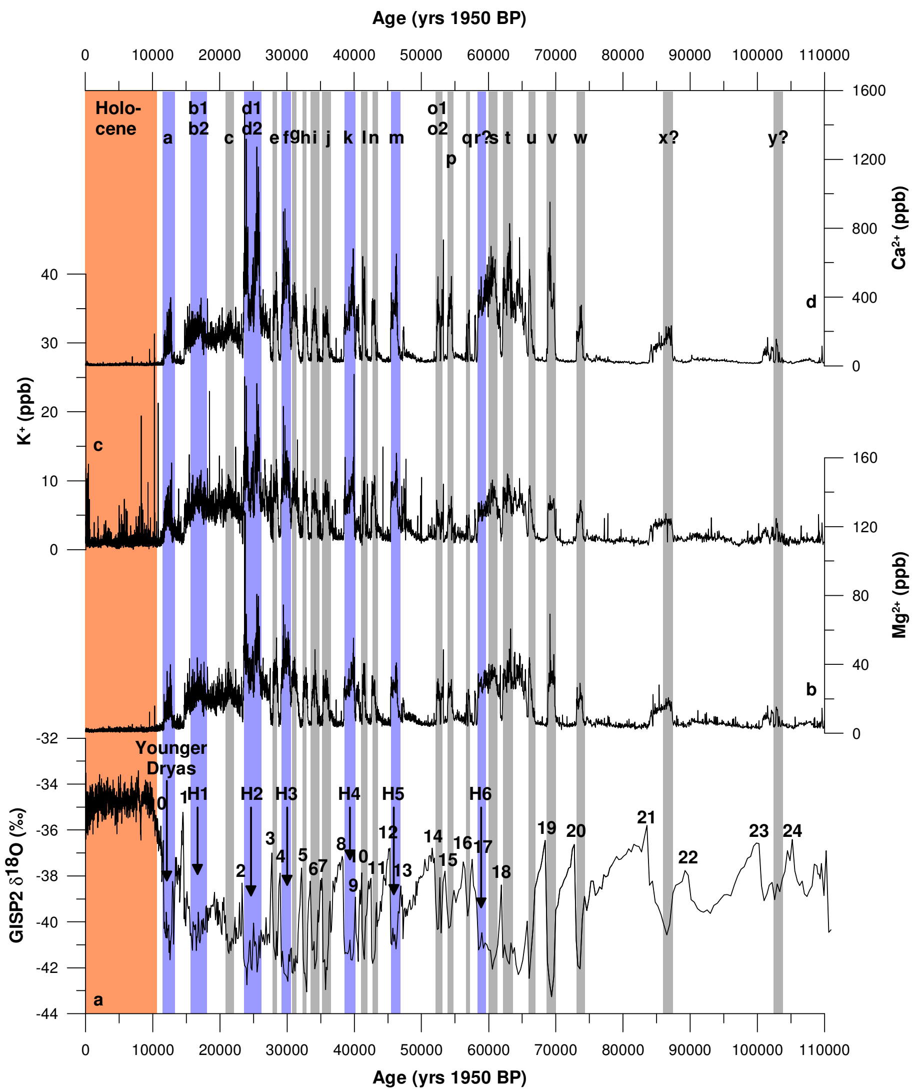

Figure 2.4. a. The GISP2 δ^{18}O ice core record (Grootes *et al.*, 1993), with the D-O stadials numbered 0 to 24 (Dansgaard *et al.*, 1993). H1 to H6 denotes the Heinrich events, and their timings are indicated by blue shaded bars (Bond *et al.*, 1993). The orange shaded bar represents the Holocene. b-d are the Mg^{2+}, K^{+} and Ca^{2+} continentally sourced ion series measured in the GISP2 ice core (Mayewski *et al.*, 1994; 1997). The grey shaded bars show the D-O millennial scale variability in the GISP2 ion series and are denoted after Rohling *et al.* (2003).

phase lag comparisons of millennial scale temperature oscillations (Bender *et al.*, 1994; Blunier *et al.*, 1997; 1998; Blunier and Brook, 2001; EPICA community members, 2006). This shows an out of phase relationship, and also that the temperature transitions were much sharper and asymmetrical in Greenland than in Antarctica (e.g., Stocker *et al.*, 2002; Stocker and Johnsen, 2003; Figure 2.5). Furthermore, the EPICA EDML ice core temperature record shows Antarctic counterparts to all the D-O events are recorded in the Greenland ice cores (EPICA community members, 2006).

Heinrich (1988) described cm–scale horizons in North Atlantic marine cores that were rich in IRD, containing nearly 100 % lithic fragments, and which have since been termed 'Heinrich layers' (Broecker, 1994). Further studies have shown that these Heinrich layers occurred quasi-periodically at intervals of around 7000 yrs (7200 +/- 2400 in Sarnthein *et al.*, 2000), with the highest concentrations of IRD found within the central North Atlantic – the so called 'IRD (Ruddiman) Belt' (Ruddiman, 1977), and coincide with highs in magnetic susceptibility, reduced numbers of planktonic foraminifera and planktonic foraminiferal $\delta^{18}O$ light excursions (e.g., Heinrich, 1988; Bond *et al.*, 1992; 1993; 1997; 1999; Broecker *et al.*, 1992; Grousset *et al.*, 1993; 2000; 2001; Andrews *et al.*, 1994; 2003; Robinson *et al.*, 1995; Rasmussen *et al.*, 1996a, b; Cortijo *et al.*, 1997; Elliot *et al.*, 1998; 2002; Stoner *et al.*, 1996; 2000; Vidal *et al.*, 1999; Bard *et al.*, 2000; Broecker, 2000a; Scourse *et al.*, 2000; van Kreveld *et al.*, 2000; Hemming *et al.*, 2002; Hemming and Hajdas, 2003; review in Hemming, 2004; Knutz *et al.*, 2001; 2002; 2007; Peck *et al.*, 2006; 2007a, b; 2008; Figure 2.4).

The excellent preservation of bioturbation in sediments that immediately precede Heinrich layers is thought to indicate that these ice-rafting events were near instantaneous, with 'iceberg armadas' filling the North Atlantic (e.g., McCave *et al.*, 1995a; Hemming, 2004). Bond *et al.* (1993) correlated the associated inferred cooling that is recorded in North Atlantic sediment cores with the most extreme of the D-O stadials recorded in the Greenland $\delta^{18}O$ stratigraphy; the so-called 'Heinrich stadials' (Figure 2.5). Alkenone thermometry suggests that sea surface temperatures (SSTs) were reduced by up to 8 °C in the eastern North Atlantic during Heinrich events (Bard *et al.*, 2000) and $\delta^{18}O$ records from the northern North Atlantic and the Nordic Seas have been used to infer that extreme temperature reductions allowed for the southward migration of the sea ice margin (e.g., Dokken and Jansen, 1999; Hilliare-Marcel and de Vernal, 2008). Generally harsher conditions are also recorded in terrestrial climate archives synchronous with Heinrich events (e.g., Allen *et al.*, 1999; Genty *et al.*, 2003; Clemens, 2005)

Concomitant with the temperature deteriorations observed in the Greenland ice core $\delta^{18}O$ records, increased concentrations of continentally source ions in the GISP2 glaciochemical series (Mayewski *et al.*, 1994; 1997; Rohling *et al.*, 2003) (Figure 2.4), suggest more arid condition prevailed during H events than the preceding and succeeding D-O stadials, and spectral analysis of the glaciochemical series suggests a periodicity of ~6100 yrs (Mayewski *et al.*, 1997). During these time periods, a southward migration of the inter-tropical convergence zone has been inferred (e.g., Gasse, 2000), and when compared to background glacial conditions, generally drier conditions have been found in archives from the Mediterranean (e.g., Cacho *et al.*, 1999; Bartov *et al.*, 2003), the tropical Indian Ocean (e.g., Burns *et al.*, 2003), and in the Caribbean (Schmidt *et al.*, 2004). Conversely, it is suggested that the western North Atlantic may have experienced a wetter climate during H events (e.g., Grimm *et al.*, 1993). It has also been suggested that increased storminess across the North Atlantic was associated with Heinrich events (Rashid and Boyle, 2007). Further palaeo-environmental studies from both the marine and terrestrial realm have shown that H events had a near global impact with climate deteriorations as far afield as South America (Lowell *et al.*, 1995; Denton *et al.*, 1999), the South China Sea (Wang *et al.*, 1999; Kiefer *et al.*, 2001), the Pacific Ocean (Hendy and Kennett; 1999; 2003), and East Asia (Wang *et al.*, 2001; Zhou *et al.*, 2008).

Relatively light benthic foraminiferal $\delta^{13}C$ values and Cd/Ca ratios for cores from the North Atlantic suggest that North Atlantic deep waters were poorly ventilated during H events and D-O stadials due to decreased AMOC vigour (e.g., Boyle and Keigwin, 1987; Boyle *et al.*, 1992; Sarnthein *et al.*, 1994; Curry *et al.*, 1999; 2000 van Kreveld *et al.*, 2000; Shackleton *et al.*, 2000; Knutz *et* al.,

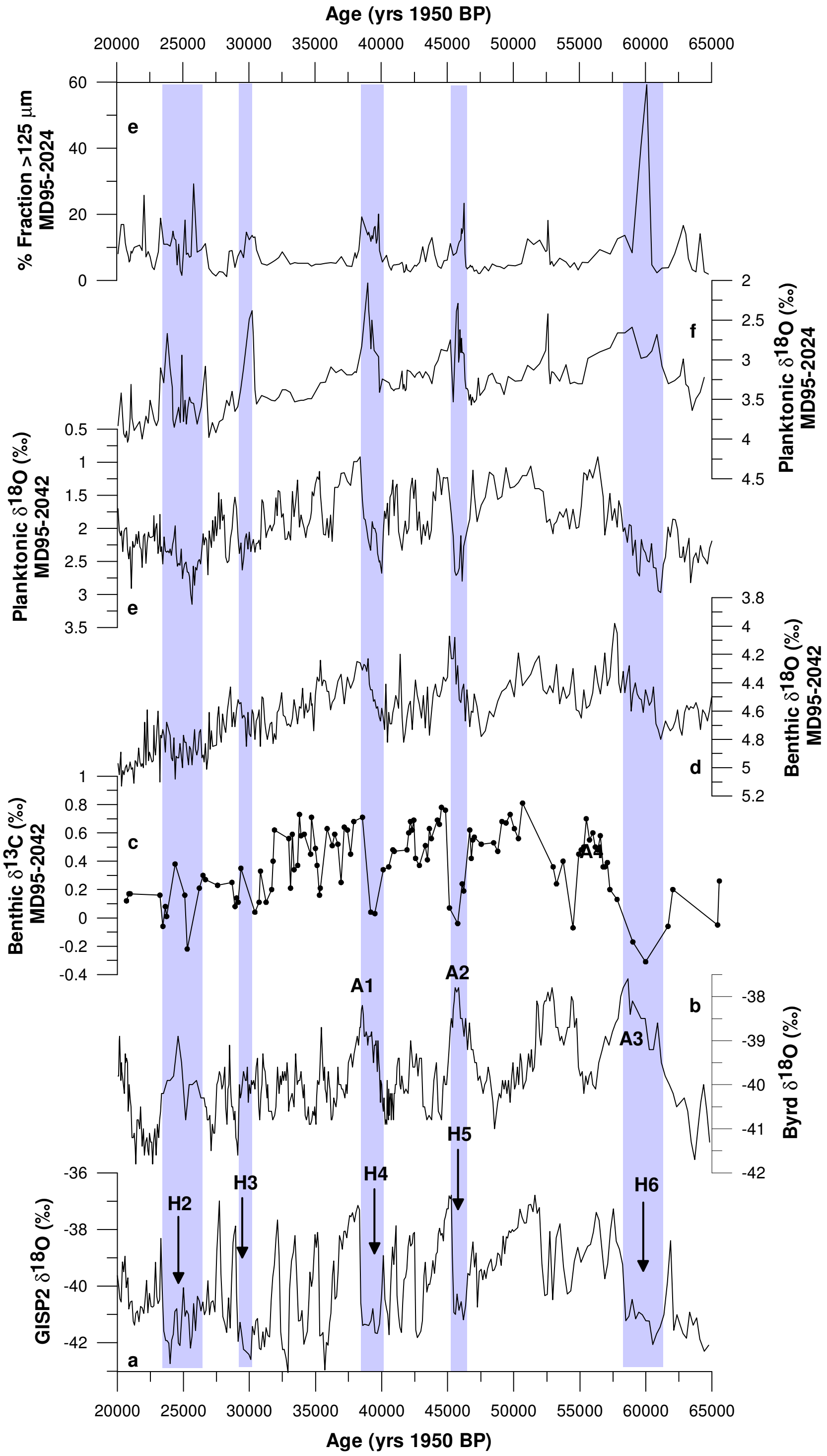

Figure 2.5. a. The GISP2 ice core $\delta^{18}O$ record (Grootes *et al.*, 1993) and the Byrd ice core $\delta^{18}O$ ice core (b), synchronised using methane concentrations (Blunier *et al.*, 1998). c & d. The benthic $\delta^{13}C$ and $\delta^{18}O$ record from the species *Cibicidoides wuellerstorfi* from Iberian margin marine sediment core MD95-2042 (Shackleton *et al.*, 2000). e. Planktonic $\delta^{18}O$ record for the

species *Globigerina bulloides* in MD95-2042 synchronised on the GISP2 timescale (Shackleton *et al.*, 2000). f. Planktonic $\delta^{18}O$ record for the species *Neogloboquadrina pachyderma* (left-coiling), and g. Percentage dry weight of the sediment fraction >125 µm for core MD95-2024, Labrador Sea (Stoner *et al.*, 2000).

2001; Moreno *et al.*, 2002; Peck *et al.*, 2007a; Figure 2.5), and similar inferences have be drawn from environmental magnetic studies of reduced ISOW/NADW intensities during the D-O stadials of MIS 3 (Kissel *et al.*, 1997; 1999a, b; Moros *et al.*, 1997; Laj *et al.*, 2002; Snowball and Moros, 2003). A study of planktonic foraminiferal abundances from the Nordic Seas indicates that relatively warm (4-7ºC) surface waters were only evident during D-O interstadials, and not during D-O stadials Heinrich events, and therefore, provides further indication of compromised AMOC vigour during D-O stadials and Heinrich events (Rasmussen and Thomsen, 2008).

Recent attention has been given to studies of intermediate and deep water circulation in the North Atlantic spanning the time period of Heinrich Event 1 (17.5 -16 ka BP). Records of $^{231}Pa/^{230}Th$ from the North Atlantic show evidence that the AMOC was near completely shutdown during H events (McManus *et al.*, 2004; Gheraudi *et al.*, 2005; Hall *et al.*, 2006), similar to inferences drawn from records of benthic foraminiferal $\delta^{13}C$ (e.g., Sarnthein *et al.*, 1994; Peck *et al.*, 2007b). It is additionally suggested that past reductions in AMOC intensity would have likely reduced the surface to deep water exchange, increasing ^{14}C reservoir ages, or ΔR, of the oceans (e.g. Hughen *et al.*, 2000; 2004; Muscheler *et al.*, 2000; 2008; Waelbroeck *et al.*, 2001; Laj *et al.*, 2002; Robinson *et al.*, 2005; Cao *et al.*, 2007). Studies of past changes in ^{14}C reservoir ages suggest that poorly ventilated waters filled the North Atlantic and Pacific basins to intermediate depths during the time period of H1 (Robinson *et al.*, 2005; Marchitto *et al.*, 2007; Keigwin and Boyle, 2008). However, this entire period of NADW slowdown is not supported by neodymium isotope ratios in a southeastern Atlantic core (Piotrowksi *et al.*, 2004).

2.3.1. Mechanisms for Heinrich Events

Due to high percentages of anomalous detrital carbonate comprising the IRD fraction in cores recovered from the IRD Belt, the cause of H events has been attributed to the periodic collapse of the Laurentide ice sheet (Bond *et al.*, 1992; 1993; 1997; 1999; Bond and Lotti, 1995; Broecker, 1992; 1994; MacAyeal, 1993; Grousset *et al.*, 2000; 2001). Lithological studies of the IRD admixtures, along with geochemical provenance studies, and dating of the typical lithic fragments confirms that the majority of IRD was sourced from the Laurentide ice-sheet, with lesser involvement of the British and Fennoscandian Ice sheets (Bond *et al.*, 1992; 1997; 1999; Bond and Lotti, 1995; Grousset *et al.*, 2000; 2001; Scourse *et al.*, 2000; Hemming *et al.*, 2002; Hemming and Hajdas, 2003; review in Hemming, 2004; Knutz *et al.*, 2001; 2007; Peck *et al.*, 2006; 2008). Based upon the large volume of IRD that was deposited in the North Atlantic (100-350 km^3 – Hemming, 2004), and the widespread planktonic foraminiferal calcite $\delta^{18}O$ anomalies that coincided with these IRD increases, relatively large volumes of freshwater were being injected into the North Atlantic during Heinrich events. This has led to the suggestion that in response to these North Atlantic fresh water perturbations, the AMOC would have either slowed or shut down (e.g., Bond *et al.*, 1993; Schiller *et al.*, 1997; Ganopolski and Rahmstorf, 2001; Vellinga and Wood, 2002; Schmittner *et al.*, 2003; Rahmstorf *et al.*, 2005).

The Heinrich (IRD) events occurred on sub-orbital timescales. Therefore, they are thought to have resulted from internal harmonics in the ocean-climate system and ice-sheet instabilities, as opposed to an external solar forcing. A number of hypotheses have been suggested for the cause of Heinrich events, and debate still remains whether they display periodic or stochastic behaviour (Bond *et al.*, 1997; Mayewski *et al.*, 1997; Alley *et al.*, 2001a, b). Here, a brief overview of the triggers for Heinrich events is provided.

Because of the apparent global synchronicity between glacier growth during H-events, the ‘Global Climate Model’ was used to explain the periodic decay of ice sheets as a process of global cooling and resultant ice-sheet growth and destabilisation (Broecker, 1994; Lowell *et al*., 1995). It has also been suggested that global cooling may have resulted in icesheet growth and jökulhaup type outburst flooding events (Hulbe, 1997; Hulbe *et al*., 2004; Alley *et al*., 2006). The 'binge-purge' mechanism was suggested by MacAyeal (1993) to explain why the ice sheets destabilised near instantaneously and with such regular pacing. MacAyeal (1993) suggested that global cooling and ice sheet growth would have caused increased geothermal heat and friction at the base of the ice sheet, which would have resulted in destabilisation of the ice-streams. Alternatively, internal oscillations in the ice sheet–climate system have been invoked to explain the periodic ice sheet surges (Calov *et al*., 2002). Additionally, an ocean-climate model has been used to suggest that AMOC slowdowns may have caused enough increased global ocean heat uptake and steric sea level rise to have floated off the grounded ice-shelves (Shaffer *et al*., 2004; Flückiger *et al*., 2006). It has also been suggested that increased tidal ranges may have destabilised the Laurentide ice shelf around the Hudson Strait (Arbic *et al*., 2004; 2008).

However, several lithological studies of IRD admixtures, along with geochemical provenance studies, as well as evidence of freshwater injections have suggested that precursor IRD events, which were sourced from the British, Icelandic and Fennoscandian ice sheets, preceded the Laurentide ice-sheet surges (Bond *et al*., 1992; 1997; 1999; Bond and Lotti, 1995; Elliot *et al*., 1998; Darby and Bischof, 1999; Grousset *et al*., 2000; 2001; Scourse *et al*., 2000; Hemming *et al*., 2002; Hemming and Hajdas, 2003; review in Hemming, 2004; Lekens *et al*., 2005; 2006; Knutz *et al*., 2001; 2007; Menot *et al*., 2006; Peck *et al*., 2006; 2007a). This has lead to the suggestion that the early surging from European and Fennoscandian ice sheets acted as a stimulus for the reaction of the Laurentide ice sheet (e.g., Grousset *et al*., 2000), which was the 'key-player' in Heinrich events (e.g., Marshall and Koutnik, 2006). Note also, that an early timing for IRD pulses from around the Arctic Canadian Archipelago has also been inferred from IRD in Arctic cores (e.g., Darby *et al*., 1997; 2002; Stokes *et al*., 2005). Scourse *et al*. (2000) hypothesised that the comparatively smaller European and Fennoscandian ice sheets, which have a higher frequency (1-3 kyr) pacing for surging, would have had a shorter response time than the larger Laurentide ice sheet, to an external forcing. Alternatively, sea level rise due to precursor IRD events has been invoked as a mechanism for destabilising the Laurentide ice-shelves (MacAyeal *et al*., 1993; van Kreveld *et al*., 2000).

However, it has been suggested that warming may have triggered these early precursor IRD events from the more sensitive, smaller, British and Fennoscandian ice sheets, which then may have triggered the Laurentide IRD event (e.g., Stocker and Wright, 1991; McCabe and Clark, 1998; Knutz *et al*., 2001; Hulbe *et al*., 2004; Lekens *et al*., 2005; 2006; McCabe *et al*., 2007), and it has been suggested that Southern Ocean warming, and surface advection of relatively warm saline waters to northern high latitudes may have been the cause (e.g., Knorr and Lohmann, 2007). Inferred warming trends prior to the onset and during Heinrich event 1 have been recorded in marine archives from the Caribbean (Rühlemann *et al*., 1999), the northeast Atlantic (Weinelt *et al*., 2003; Peck *et al*., 2008), within the southern sector of Nordic Seas (Rasmussen and Thomsen, 2008), and the Indian Ocean (Peeters *et al*., 2004). Rasmussen and Thomsen (2008) interpret the inferred warming of the Nordic Seas prior to Heinrich events to represent increased inflowing relatively warm (4-7ºC) Atlantic surface waters. With a duration of 1600 to 2000 yrs, Rasmussen and Thomsen (2008) suggest that these long-lived increases in surface water temperatures corresponded to one or two ‘normal’ D-O events.

Based upon the out of phase nature of the climate shifts between Antarctica and Greenland (e.g., Blunier *et al*., 1998; Blunier and Brook, 2001) – the so called ‘bipolar seesaw’ has been proposed as a concept to explain these timing offsets, and provides a concept to explain the pattern of D-O cycles (Broecker, 1998; Stocker, 1998; Seivdov and Maslin, 2001; Seivdov *et al*., 2005). The concept of the bipolar seesaw originates from the observation that the THC in its present-day ‘on’ mode draws heat from the Southern Ocean (Stocker *et al.*, 1992), and an ocean-circulation model has shown that in the ‘off’ mode, the SST difference changes from positive to negative when moving across the equator (i.e. cooling in the north and warming in the south) (Stocker *et al.*, 1992; Stocker and

Johnsen, 2003). Ocean-climate models have been used to show that the opposite is true when switching the THC back to an 'on' state (Weaver *et al.*, 2003). Stocker and Johnsen (2003) formulated an energy balance (the 'thermal bipolar seesaw') based upon the assumption that the heat storage in the southern hemisphere was proportional to the temperature difference between the reservoir and the southern end of the seesaw. Therefore according to the box model, the southern temperatures reflect a 'faded memory' of the past northern hemisphere temperatures (Stocker and Johnsen, 2003; Figure 2.6). The bipolar seesaw is a simple concept which can be considered limited due to SST transmission to the ice-sheet interiors and terrestrial ice-sheets causing thermal damping (Stocker and Johnsen, 2003). However, Stocker and Johnsen (2003) also show that when the GRIP $\delta^{18}O$ ice core record is convolved using the Laplace transform, and with τ = 1120 yrs (the timescale of the heat reservoir), the modelled curve bears remarkable resemblance to the Antarctic Byrd ice core $\delta^{18}O$ record. Knutti *et al.* (2004) have also used an extended bipolar seesaw model to show a strong hemispheric coupling during Marine Isotope Stage (MIS) 3, which reconciles model and palaeo-proxy archives.

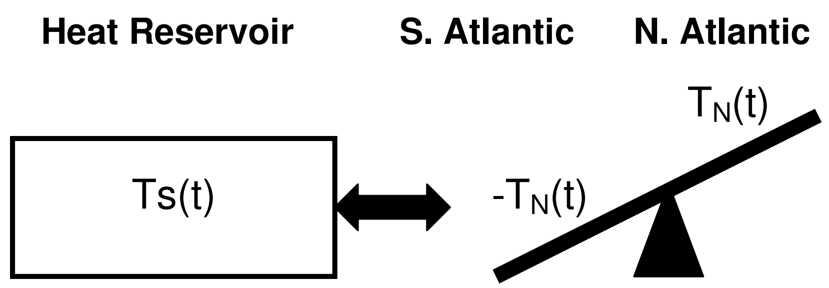

Figure 2.6. Schematic representation of the bipolar seesaw where Ts is the thermal anomaly of the heat reservoir and T_N is the time-dependent temperature anomaly on the northern side of the seesaw whereas $-T_N$ represents the southern end. The double arrow represents the diffusively parameterised heat exchange in the reservoir within the box model (Stocker and Johnsen, 2003).

Although it is likely that freshwater additions (as evident from the large quantities of IRD) impinged upon the MOC during H events, inconsistencies remain between the coupled ocean circulation models and the palaeo-data, with respect to the nature of the slowdowns/shutdowns of the MOC and the amount of surface freshening required to cause the slowdown/shutdown (Lohmann and Schultz, 2000; Seager and Battisti, 2006). For example, records of sea level from the Red Sea (Siddall *et al.*, 2003) and ice-volume from benthic foraminiferal $\delta^{18}O$ (Shackleton *et al.*, 2000; Waelbroeck *et al.*, 2002) show that periods of sea level rise coincided with increased air temperatures over Antarctica, and not coeval with the timings of warming in the Greenland ice core $\delta^{18}O$ records. Furthermore, IRD pulses have been recorded in Southern Ocean cores, which coincided with the increased rates of sea level rise, predating those in the North Atlantic (Kanfoush *et al.*, 2000).

Calculations from North Atlantic IRD fluxes (MacAyeal, 1993) would suggest that around 3.5 m sea-level rise (or 0.16 to 0.08 Sv of freshwater over 250-500 yrs) was associated with H events. A model study of the magnitude of planktonic $\delta^{18}O$ change recorded in North Atlantic marine sediment cores for Heinrich event 4 reveals only 2 +/-1 m of sea-level rise (Roche *et al.*, 2004a). Coupled ocean circulation models, however, require much larger threshold values of freshwater forcing to invoke a shutdown of the AMOC, for example, 0.625 Sv in Schiller *et al.*, (1997) and a range between 0.15 and 0.5 Sv in Rahmstorf *et al.* (2005).

Reconciliation between the ocean circulation models and observational palaeo-proxy data may be gained from sea-level records of coral horizons from Barbados (e.g., Fairbanks, 1989; Peltier and Fairbanks, 2006), the Huon Peninsula (Yokoyama *et al.*, 2000) and Papua New Guinea (Chappell, 2002; Cutler *et al.*, 2003), which have been interpreted to show a 10 to 15 m sea-level rise just prior to Heinrich event 1 (H1), at around 19 ka BP. Due to relatively minor increases in IRD concentration in North Atlantic marine cores during this interval of sea-level rise at around 19 ka BP, in comparison with the IRD associated with the main phase of H1 (e.g., Grousset *et al.*, 2000; 2001), it remains questionable where this freshwater could have been sourced. As previously discussed, North Atlantic cores indicate precursory IRD pulses and sea-surface freshening episodes, sourced from the Greenland and British Ice sheets prior to the main Laurentide phase of H1 (e.g., Bond and Lotti, 1995; 1999; Grousset *et al*., 2000; 2001; Hemming, 2004; Knutz *et al*., 2007; Peck *et al*., 2006; 2008), but it is questionable whether these relatively minor ice sheet surges could account for the magnitude of sea level rise observed. It is possible that a component of the sea level rise during Heinrich events and Antarctic warming transitions may have been sourced from the Southern Hemisphere (Rohling *et al*., 2004), or alternatively, from the southern Laurentide ice sheet (Hill *et al*., 2006).

Increased IRD concentrations and significant reductions in sea surface salinity have been recorded in Arctic and Nordic Seas cores, with timings just prior to or contemporaneous with the start of H events (Darby *et al*., 2002; 2003; Lekens *et al*., 2006). This has invoked the suggestion that the higher-latitude ice-sheets may have been of greater importance than originally thought for triggering AMOC slow downs, with relatively fresh water injected into the critical regions of NADW formation (Lekens *et al*., 2006). Similar suggestions of an 'out of the Arctic' melt water forcing have been made for the Younger Dryas cold event that occurred at the end of the last glacial period/deglaciation (Moore, 2005; Tarasov and Peltier, 2005). Further reconciliation between the observed climate signals, AMOC responses and coupled ocean-circulation models maybe achieved, when considering additional feedback mechanisms on northern North Atlantic climate and the MOC that may have amplified and propagated the climate signals, such as increased storminess, dustiness and albedo (e.g., Broecker, 2001; Wunsch, 2006), or seasonality changes (e.g., Denton *et al*., 2005; Seager and Battisti, 2006).

2.4. Climate Event Stratigraphy of the Last Deglaciation

The Greenland ice core $\delta^{18}O$ records show that the first sharp temperature rise of the last deglaciation occurred in the Northern Hemisphere at around 14.6 ka BP

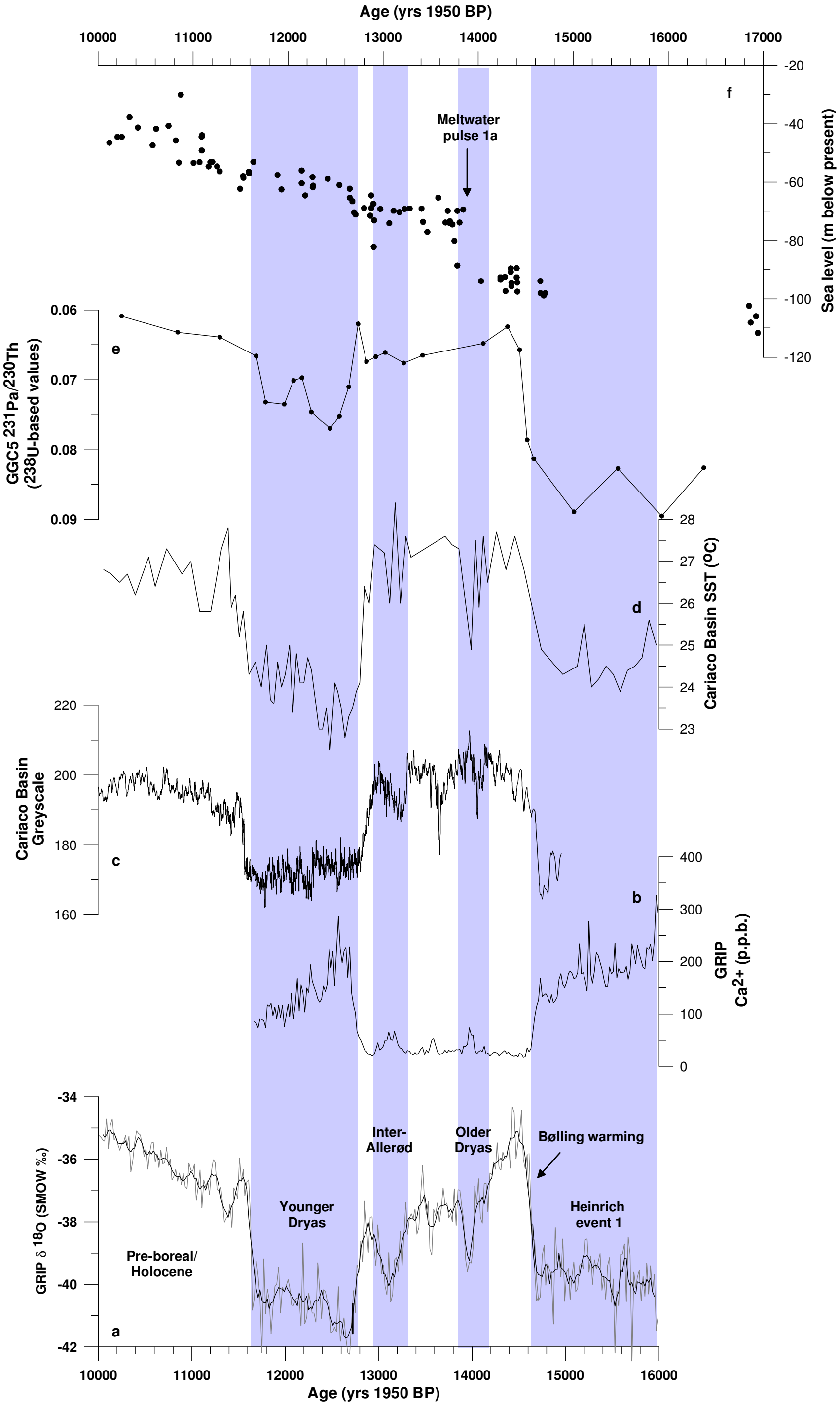

Figure 2.7. a The GRIP ice core $\delta^{18}O$ record (a) and the Ca^{2+} ion series (b) on the latest GICC05 chronology (Fuhrer *et al.*, 1993; Rasmussen *et al.*, 2006; Andersen *et al.*, 2006). c. Greyscale record from the Cariaco Basin measured on core PL07-39PC (Hughen *et al.*, 2000). Lower values represent drier/windier conditions. d. Cariaco Basin SST values calculated from Mg/Ca for the planktonic foraminifera *G. ruber* from core PL07-39PC (Lea

***et al.*, 2004). e. 230Pa/^{231}Th record from core GGC5 recovered from the Bermuda Rise (McManus *et al.*, 2004), plotted on an inverted axis. Lower values represent a more vigorous AMOC. f. Sea level change recorded in fossil coral data (Fairbanks, 1989; Bard *et al.*, 1990b; Edwards *et al.*, 1993; Cutler *et al.*, 2003; Chappell, 2002).**

(e.g., Dansgaard *et al.*, 1993; Grootes *et al.*, 1993; Jouzel *et al.*, 1993; Grootes and Stuiver, 1997; Johnsen *et al.*, 2001; Rasmussen *et al.*, 2006). This was characterised by a series of rapid climate ameliorations and deteriorations termed the 'late glacial oscillation' (Björk *et al.*, 1998; Figure 2.7a).

The last deglaciation encompasses one of the most marked climate transitions, the Bølling warming (~14.6 ka BP), when Greenland temperatures rapidly increased in the order 10 ºC in just a couple of centuries (Dansgaard *et al.*, 1993; Severinghaus and Brook, 1999), and a similarly abrupt amelioration occurred in Europe (Atkinson *et al.*, 1987). At around 14 ka BP, the Bølling warm period abruptly ended with the Older Dryas; a relatively minor cold 'snap' (Björck *et al.*, 1998; Rasmussen *et al.*, 2006). The Allerød warm period followed the Older Dryas, which was briefly interrupted by the Inter-Allerød cooling, at around 13.1 ka BP (Rasmussen *et al.*, 2006). The Younger Dryas extreme cold event is dated between ~12.8 and ~11.6 ka BP (Rasmussen *et al.*, 2006) and was the last of the rapid climate events of the 'late glacial oscillation', and it terminated the Allerød warm period (Figure 2.7a). The Younger Dryas was then followed by the Holocene. The climate transitions into the Bølling-Allerød warm period and the Younger Dryas are sometimes considered to represent the last of the D-O cycles of the last glacial period (e.g., Broecker, 2000a; Rahmstorf, 2002). The Greenland temperature history of the last deglaciation is mirrored in numerous high-resolution marine (e.g., Hughen *et al.*, 1996; Waelbroeck *et al.*, 2001; Lea *et al.*, 2003) and terrestrial (von Grafenstein *et al.*, 1999; Wang *et al.*, 2001) records.

Proxies for the dust concentrations in the Greenland ice cores show rapid responses to the climate changes (Taylor *et al*., 1993; Mayewski *et al*., 1994; 1997), where coolings are associated with sharp dust increases (Figure 2.7b and 1.9d), indicative of rapid re-arrangement of the atmospheric circulation. Dry/wet phases in Europe (von Grafenstein *et al*., 1999), Africa (Gasse, 2000) and Cariaco Basin (Hughen *et al*., 2000 – Figure 2.7), indicate that the Inter Tropical Convergence Zone (ITCZ) shifted southwards during the cold intervals.

Records from sediment cores show that the MOC in both the Atlantic (McManus *et al*., 2004) and the Pacific (Marchitto *et* al., 2007) basins underwent a sharp increase in intensity at the Bølling warming, up to intensities similar to those of the present day (Figure 2.8e). Similar inferences have been drawn from $\Delta^{14}C$ ages of the oceans (e.g., Hughen *et al*., 1998; 2000; 2004; Robinson *et al*., 2005; Keigwin and Boyle, 2008) and from studies of benthic foraminiferal $\delta^{13}C$ (e.g., Sarnthein *et al*., 1994). During the Bølling-Allerød warm interval, the Northern Hemisphere ice-sheets and glaciers rapidly retreated from their LGM/H1 positions (e.g., McCabe and Clark, 1998; Dyke *et al*., 2002; Bowen *et al*., 2002; Ivy-Ochs *et al*., 2004; Licciardi *et al*., 2004) and atmospheric methane concentrations increased (e.g., EPICA community members, 2006 – Figure 2.8b), possibly as a result of associated vegetation changes (e.g., Allen *et al*., 1999; Alley and Clark, 1999). The time-transgressive/gradual retreat of polar waters across the North Atlantic during the warm Bølling-Allerød period was most likely also a reflection of the shrinking Northern Hemipshere ice-sheets (Ruddiman and McIntyre, 1973).

The largest recorded meltwater pulse (mwp-1a) (around 20 m sea-level rise in ~500 years) occurred during the last deglaciation (e.g., Bard *et al*., 1996; Hanebuth *et al*., 2000; Fairbanks, 1990; Fairbanks *et al*., 2005) (Figure 2.7f). U/Th dated fossil coral sea-level records indicate timing for mwp-1a coincident with the Older Dryas cooling event at around 14.2 ka BP (Fairbanks *et al*., 2005; Peltier and Fairbanks, 2006). However, a radiocarbon dated sea-level record from the Sunda Shelf has been suggested to date mwp-1a some 300 years earlier, placing the event coincident with the Bølling warming, at around 14.6 ka BP

(Hanebuth *et al*., 2000). Based upon this earlier timing for mwp-1a, subsequent papers have used an isostatic rebound model to suggest an Antarctic meltwater origin (Clark *et al*., 2002), and an ocean circulation model to infer that an Antarctic meltwater origin could have caused the sharp increase in AMOC intensity that occurred at, and likely caused the Bølling warming (Weaver *et al*., 2003).

At around 12.8 ka BP (Rasmussen *et al*., 2006), the ice sheets and glaciers that were in retreat during the Allerød began to quickly re-advance (e.g., Denton *et al*., 1999; Dyke *et al*., 2002; Ivy-Ochs *et al*., 2004), polar waters once again migrated southwards across the North Atlantic (Ruddiman and McIntyre, 1973), and sea-ice margins extended southward (deVernal and Hilliare-Marcel, 2000), associated with the Northern Hemisphere cooling of the Younger Dryas back to glacial temperatures.

During the Younger Dryas, the atmosphere shifted back to a glacial (D-O stadial) configuration (Figure 1.8b and c) (e.g., Taylor *et al*., 1993; Mayewski *et al*., 1994; 1997; Gasse and van Campo, 1994; von Grafenstein *et al*., 1999; Gasse, 2000; Hughen *et al*., 2000; Haug *et al*., 2001; Wang *et al*., 2001), and concentrations of atmospheric CH_4 dropped by around 30% (Chappellaz *et al*., 1993; EPICA community members, 2006; Figure 2.8b). Marine sediment core records of $\delta^{13}C$ and $\Delta^{14}C$ indicate that during the Younger Dryas ocean ventilation was reduced (Keigwin and Lehman, 1994; Sarnthein *et al*., 1994; Hughen *et al*., 1998; 2000; 2004; Austin and Kroon, 2001; Robinson *et al*., 2005; Bondevik *et al*., 2006; Marchitto *et al*., 2007), and the record of $^{231}Pa/^{230}Th$ from Bermuda Rise suggests that the AMOC was in nearly completely shutdown (McManus *et al*., 2004; Figure 2.7e). Consequently, the mechanism for the Younger Dryas has been widely attributed to North Atlantic freshening (Broecker, 2000a), possibly sourced from Lake Agassiz (e.g, Teller *et al*., 2002; Broecker, 2006). However, records of IRD and planktonic foraminiferal $\delta^{18}O$, as well as ocean circulation models suggest relatively early meltwater injections from out of the Arctic (Darby *et al*., 1997; Moore, 2005; Tarasov and Peltier, 2005), and off east Greenland (Jennings *et al*., 2006).

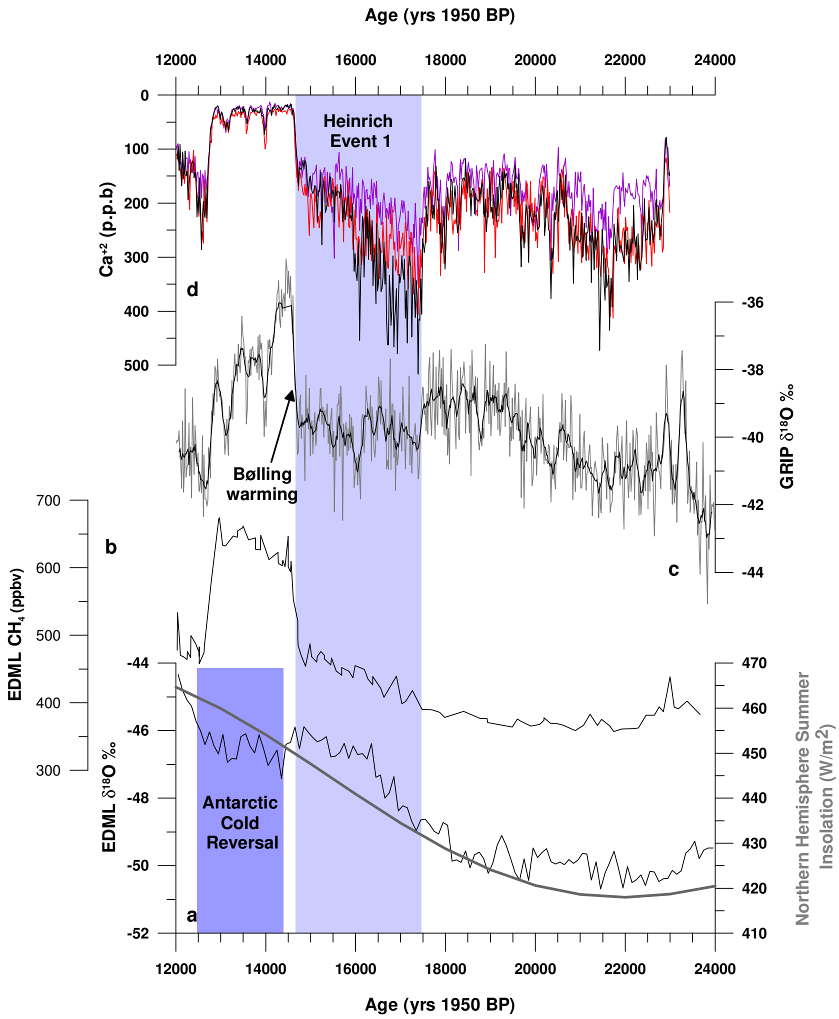

Figure 2.8 a. In black, the EDML $\delta^{18}O$ ice core record on the GICC05 timescale (EPICA community members, 2006) and in grey, the July insolation curve at 65 °N (Berger, 1991; 1999). b. Atmospheric methane concentrations measured in the EDML ice core (EPICA community members, 2006). c. GRIP $\delta^{18}O$ ice core record on the GICC05 timescale (Andersen *et al.*, 2006; Rasmussen *et al.*, 2006; 2007; Svensson *et al.*, 2006; Vinther *et al.*, 2006). d. The GRIP (black), GISP2 (dark grey) and NGRIP (light grey) Ca^{2+} ion series plotted on the GICC05 timescale (Fuhrer *et al.*, 1993; Mayewski *et al.*, 1994; Bigler *et al.*, 2004; Andersen *et al.*, 2006; Rasmussen *et al.*, 2006; 2007; Svensson *et al.*, 2006; Vinther *et al.*, 2006).

On the southern hemisphere, the chronology of the last deglaciation seems different. Antarctic ice core $\delta^{18}O$ and δD records, show the deglacial temperature rise started some 5000 yrs earlier than in Greenland at around 18 ka BP (Figure 2.8) (Bender *et al.*, 1994; Jouzel *et al.*, 1993; Blunier *et al.*, 1998; EPICA community members, 2006), near synchronous with the global increase in atmospheric CO_2 (Marchitto *et al.*, 2007). However, some glaciers on the Southern Hemisphere (e.g., Denton *et al.*, 1999; Lamy *et al.*, 2004) appear to have responded synchronously with those in the Northern Hemisphere (Denton *et al.*, 1999). At around 14.5 ka BP, air temperatures above Antarctica decreased, initiating a period known as the 'Antarctic Cold Reversal' (Blunier *et al.*, 1997), which lasted until around 12.5 ka BP.

The apparent asynchrony between the northern and southern hemisphere's deglacial climate history has led to a modified bipolar seesaw model, in which the 'south dials north' (i.e., the climate transitions were led from the Southern Hemisphere) (Stocker, 2003). Stocker (2003) suggests that the shutdown of the THC during Heinrich event 1 would have led to warming in the south, turning the THC back 'on' due to advection of saline waters and southern sourced meltwater injections, causing the Bølling warming. Alternatively, the Indian Ocean may have also provided a source of relatively warm and saline waters to the North Atlantic via the Agulhas Current, and may have triggered the abrupt AMOC resumption at the Bølling warming (Peeters *et al.*, 2004). The warming in the north is suggested to have cooled the south (the Antarctic Cold Reversal), and the resultant meltwater release into the North Atlantic would have switched the 'conveyor' 'off' again, causing cooling in the north (the Younger Dryas). The resultant southern warming is thought to have 'kick-started' the THC in the Northern Hemisphere, and finally the Southern and Northern Hemisphere climates warmed, marking the start of the Holocene.

2.5. Eirik Drift, south of Greenland: the study setting

It is widely accepted that North Atlantic Deep Water (NADW) is exported from the Nordic Seas as a product of the cooling and sinking of northward flowing, relatively warm and saline, surface waters (the Gulf Stream/NAD), and that it forms the Deep Western Boundary Current (DWBC) after the entrainment of intermediate water masses (e.g., Dickson and Brown, 1994; Bacon, 1998; Hunter *et al*., 2007a). South of the Denmark Strait, the DWBC is responsible for the construction of Eirik Drift: an elongate, mounded contourite drift, located on the slope and rise off the southern tip of Greenland, south of Cape Farewell (Chough and Hesse, 1985; Arthur *et al*., 1989; Hunter *et al*., 2007a). Eirik Drift contains a semi-continuous sediment record from the Early Eocene, through to the Holocene/present day (Hunter *et al*., 2007a). Sediments on Eirik Drift represent the first deposition of particles carried in NADW as it flows over the Denmark Strait and rounds the southern tip of Greenland. Therefore, sediments from Eirik Drift provide an excellent opportunity to study past changes in NADW flow intensity associated with past rapid climate changes.

2.5.1. Modern oceanographic setting of Eirik Drift

2.5.1.1. Surface Waters

The East Greenland Current (EGC) and East Greenland Coastal Current (EGCC) are southward flowing western boundary currents that today transport relatively fresh and cold waters out of the Arctic (Aagaard and Carmack, 1989; Bacon *et al*., 2002), and which dominate surface waters above Eirik Drift (Figure 2.9). The EGC/EGCC freshwater flux today comprises continental runoff, icebergs, sea-ice, precipitation, as well as a component of admixture from the subpolar gyre/Nordic Seas surface waters (e.g., Rudels *et al*., 2002; Sutherland and Pickart, 2008). Sutherland and Pickart (2008) have estimated the EGC/EGCC total transport to be around 2 Sv (during the summer of 2004), of which the total freshwater flux was calculated as between 59 to 96 mSv (referenced to a salinity of 34.8), increasing along their southward paths. Located directly beneath the EGC and EGCC, sediments from Eirik Drift preserve a record of past changes in freshwater discharge from the East Greenland margin, the Arctic and the Nordic Seas (one of the key regions of present-day NADW formation (e.g., Bacon, 1998; 2002)).

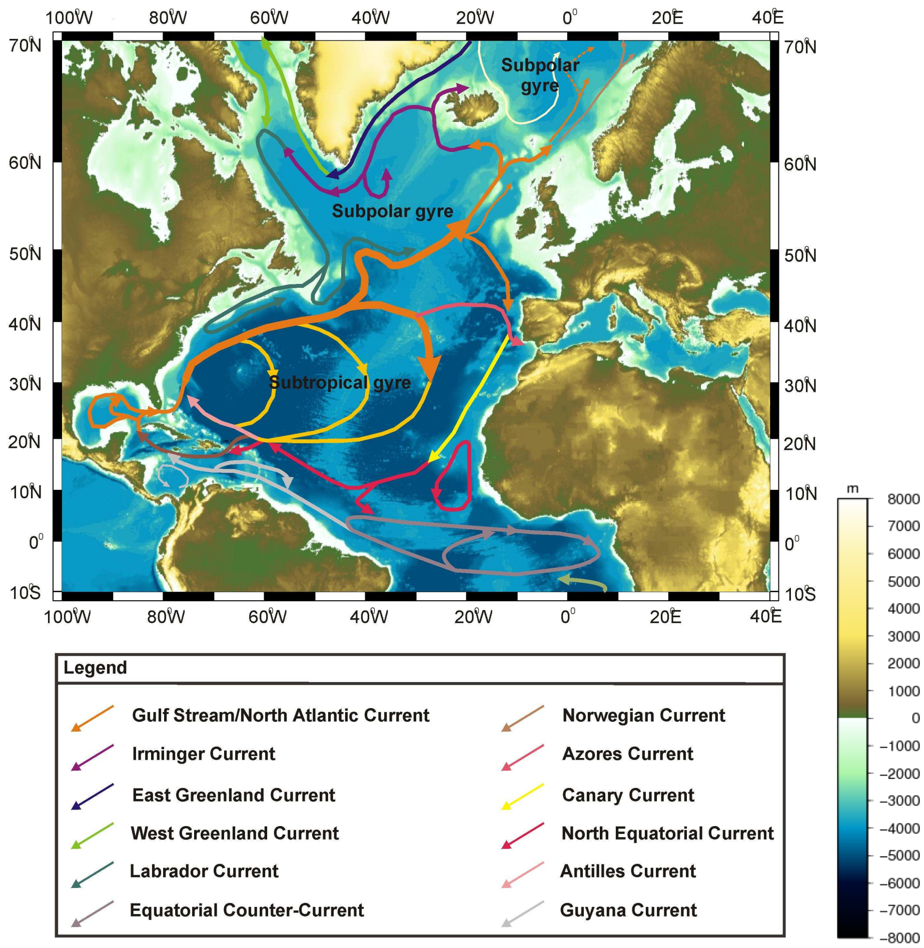

Figure 2.9. Map of the North Atlantic region showing the location of surface water currents and surface water circulation (modified from Schmitz and McCartney, 1993).

2.5.1.2. Deep and Intermediate Waters – Hunter et al. (2007a)

The modern DWBC in the region of Cape Farewell is concentrated between the 1900 and 3000 m isobaths towards the bottom of the continental slope (Clarke, 1984). The DWBC transport is commonly accepted to be around 13-14 Sv (1 Sv = 1 x 10^6 m^3s^{-1}); for example, Dickson and Brown (1994) quoted 13.3 Sv for the flow below the 27.80 isopycnal. Although this value is often referred to it is largely based on a single dataset collected in 1978 by the *R.V. Hudson* (Clarke, 1984). Bacon (1998) calculated a much lower value of 6 Sv from data collected in 1991 by the *RRS Charles Darwin*, and argued that a comparison of data collected between 1958 and 1997 illustrates decadal variability in the DWBC, which he attributed to changes in the output from the Nordic Seas.

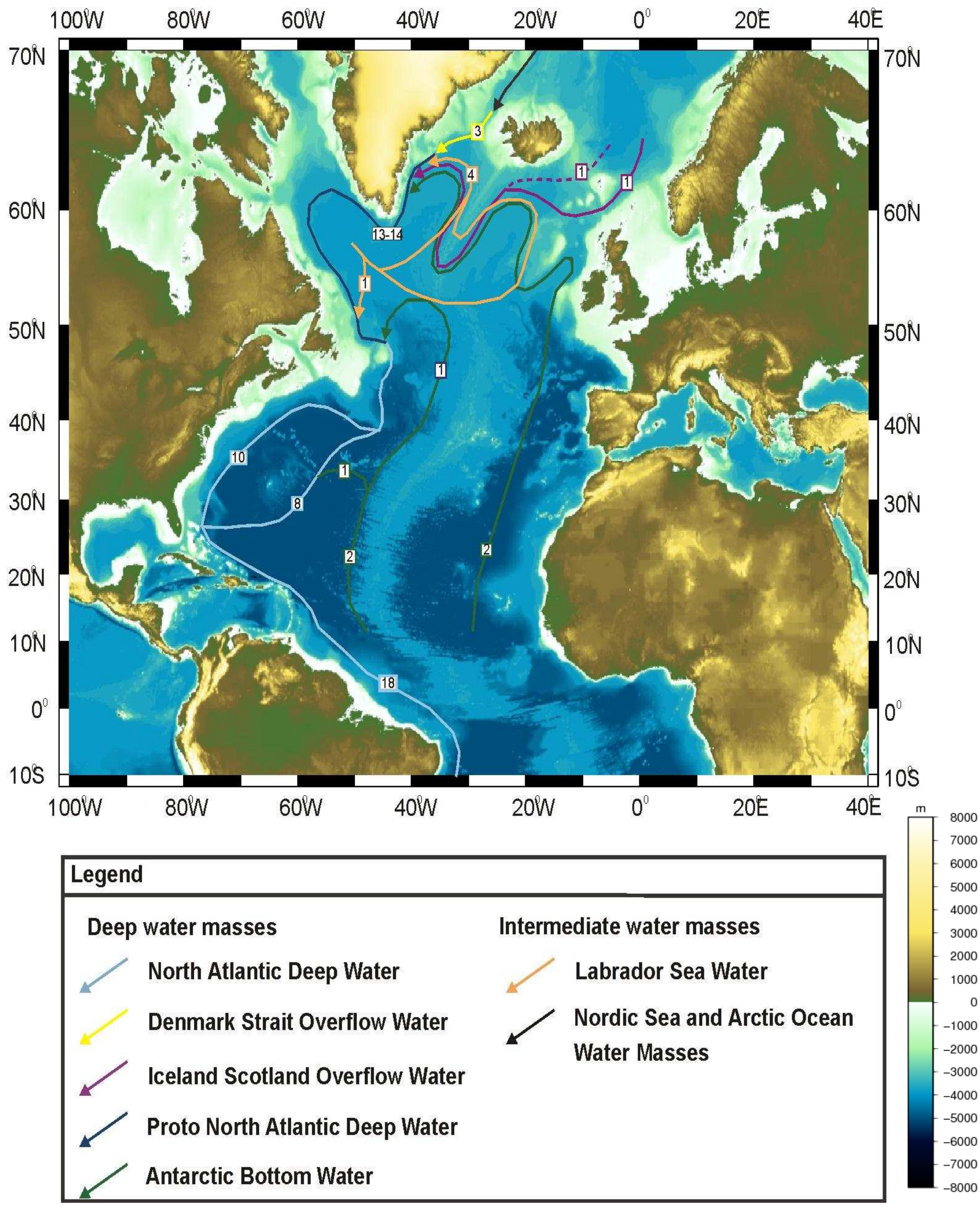

Figure 2.10. Map of the North Atlantic region showing the water masses contributing to the formation of North Atlantic Deep Water (modified from Schmitz, 1996; Pickart *et al.*, 2003, and after Hunter *et al.*, 2007a). Boxed numbers indicate the volume flux in Sverdrups of the water masses (see text for description).

The DWBC in the vicinity of Cape Farewell is composed of four main water masses (e.g., Dickson and Brown, 1994): the Denmark Strait Overflow Water (DSOW), Iceland Scotland Overflow Water (ISOW), Labrador Sea Water (LSW) and modified Antarctic Bottom Water (AABW) (Figure 2.10).

DSOW is composed of Nordic Seas intermediate waters that cross the Denmark Strait sill (maximum depth of 550 m). After crossing the sill the overflow waters descend rapidly, entraining ambient waters, primarily LSW. The resultant modified DSOW is identifiable as the lower layer of the DWBC off Cape Farewell. The transport of DSOW across the Denmark Strait and into the DWBC is estimated to be around 2.9 Sv (Dickson and Brown, 1994; Figure 2.10), increasing to around 10 Sv via entrainment of ambient waters *en route* to Cape Farewell.

Similarly, ISOW comprises Nordic Seas intermediate waters that cross the Iceland-Scotland Ridge to the east of Iceland. Dickson and Brown (1994) estimated the total eastern overflows to be around 2.7 Sv, of which 1.7 Sv flows through the Faeroe Bank Channel (maximum depth of around 850 m). The remainder overflows via a series of five smaller channels between Iceland and the Faeroes. The density of ISOW is reduced by entrainment of ambient waters as it travels around the Reykjanes Ridge and into the Irminger Basin via the Charlie Gibbs Fracture Zone (CGFZ), such that it forms the upper layer of the DWBC at a depth of around 2000 m. The contribution of this modified ISOW to the DWBC off Cape Farewell is estimated at between 2 and 3 Sv (Dickson and Brown, 1994; Schmitz, 1996).

LSW is formed by wintertime deep convection in the Labrador and Irminger Seas. Originally, as the name suggests, it was thought to be formed solely in the Labrador Sea, but more recent work (Bacon *et al.*, 2003; Pickart *et al.*, 2003) has concluded that a second formation site exists in the Irminger Sea. LSW spreads across the North Atlantic and populates the low-velocity layer between about 700 m and 1500 m off the east coast of Greenland. LSW contributes a significant proportion of the DWBC at around 4 Sv off Cape Farewell.

However, inverse modelling has produced a value as high as 8 Sv (Alvarez *et al.*, 2004).

AABW spreads north from its point of formation in the Antarctic and after modification joins the southward-flowing DWBC at various points in the North Atlantic. Estimates of the component joining off Greenland are in the region of 1-2 Sv (Schmitz and McCartney, 1993; Schmitz, 1996). A further 2 Sv is thought to be entrained, equally split between sites off Newfoundland and Florida.

In summary, the DWBC off Cape Farewell provides the major input to North Atlantic Deep Water (NADW). NADW is usually considered to have formed by the time the DWBC reaches the Grand Banks of Newfoundland after further addition of LSW, AABW and ISOW in the Labrador Basin, although further modification does occur along its southward path. Therefore, the deep water transported in the vicinity of Cape Farewell is referred to as Proto North Atlantic Deep Water in Figure 2.10. The transport of DWBC is typically considered to be between 16 and 18 Sv as it flows across the equator and into the South Atlantic (Schmitz and McCartney, 1993). Although we still lack detailed knowledge about the drivers and variability of the DWBC, we can assume that, as NADW is essentially the lower limb of the AMOC, the strength of the DWBC off Cape Farewell has a major influence upon the AMOC, and hence, most likely North Atlantic climate also.

CHAPTER 3

3. METHODS

The aim of the investigation has been to reconstruct past surface and deep-water hydrographies around Eirik Drift, south of Greenland during the time period of Heinrich event 1 and the last deglaciation. This has been achieved through multi-proxy study of 14.7 cm diameter gravity cores TTR13-AT450G (2326 m water depth; 57°59.998'N and 45°49.002'W) and TTR13-AT451G (1927 m water depth; 58°30.886'N; 44°54.333'W) (hereafter TTR-450 and TTR-451, respectively), which were obtained during the Training-Through-Research (TTR-13) cruise in 2003, with *RV Professor Logachev* (Figure 3.1.).

Analyses from cores TTR-450 and TTR-451 include ITRAX core scanning X-Ray Fluorescence (XRF) counts, environmental rock magnetics and palaeomagnetics, bulk and foraminiferal stable carbon and oxygen isotope ratios, lithic (ice-rafted debris – IRD) and total planktonic foraminiferal counts, mean sortable silt grain size analysis and Accelerated Mass Spectrometric (AMS)^{14}C datings. Petrological studies were also performed using X-ray diffraction and scanning electron microscopy (SEM). Analyses were carried out on the whole core, as well as u-channel, discrete and toothpick samples. Except for where specified analyses were conducted in laboratories within the *National Oceanography Centre, Southampton*. This chapter provides a description on the sampling techniques, a background to each analysis, as well as details on the methods that were used.

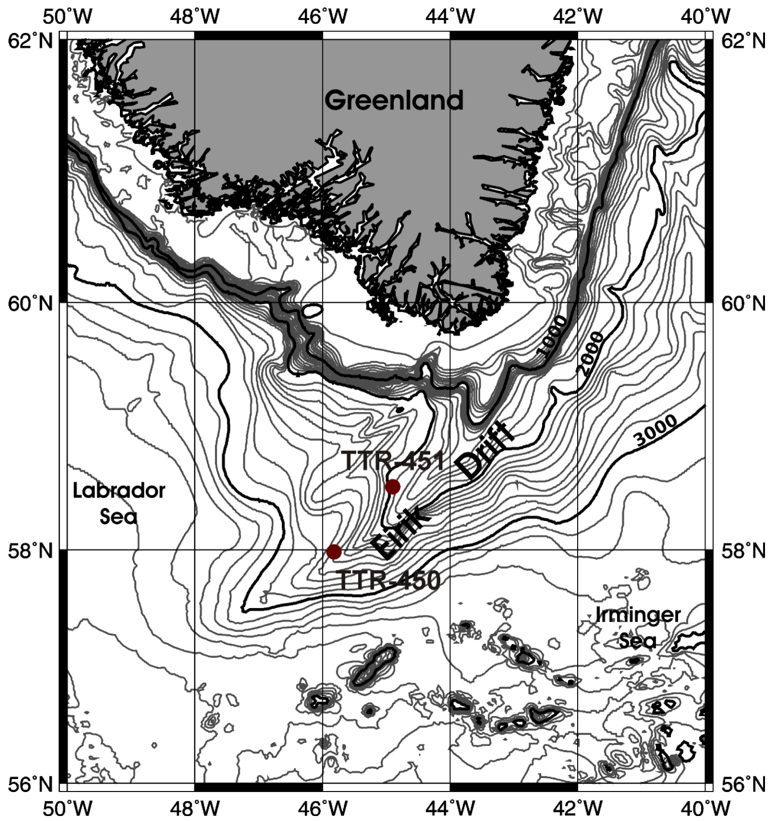

Figure 3.1. Regional bathymetric map of Eirik Drift, south of Greenland showing the locations of cores TTR-450 and TTR-451. The bathymetry is from the GEBCO Digital Atlas published by the British Oceanographic Data Centre on behalf of the Intergovernmental Oceanographic Commission of UNESCO (IOC) and the International Hydrographic Organisation (IHO) (2003)). The 1000, 2000 and 3000 (heavy, black) contours are denoted.

Prior to sampling, cores TTR-450 and TTR-451 were photographed and the sediment was visually logged, taking note of sedimentary and grain size changes. The split sediment cores were also scanned with the NOCS BOSCORF ITRAX-XRF core scanner. Figure 3.2 summarises the analyses that were performed and the sampling technique used for sediments from cores TTR-450 and TTR-451. For an overview of the sampling procedure see Figure 3.3.

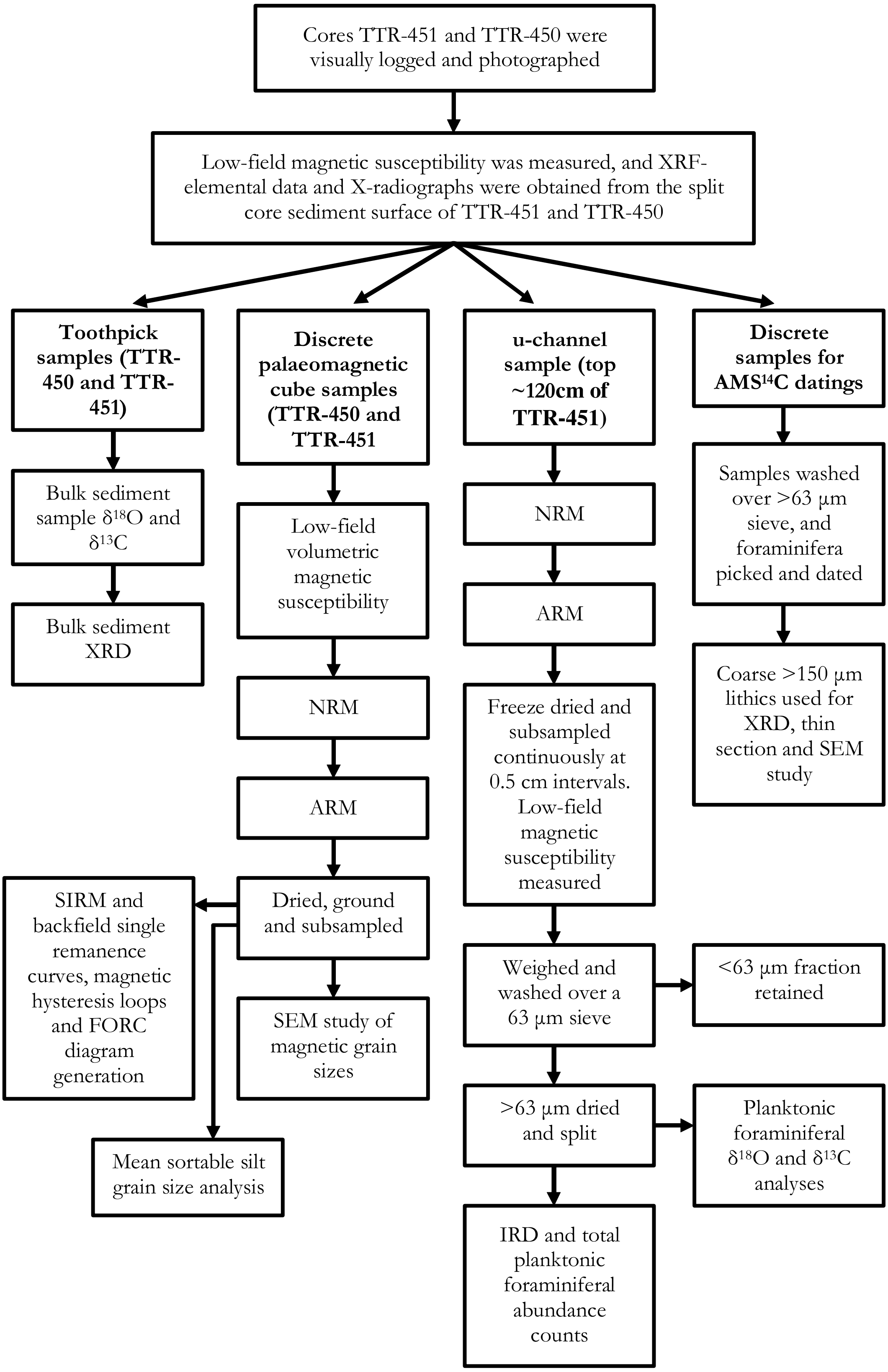

Figure 3.2. Summary flow diagram of the analyses performed, and the sampling techniques used, on sediments from cores TTR-450 and TTR-451.

3.1. ITRAX-XRF Core Scanning

The NOCS BOSCORF ITRAX-XRF core scanner provides a non-destructive means of acquiring a suite of high-resolution elemental profiles. Measurements were made on cores TTR-450 and TTR-451 as a first line approach to identify intervals of sediment that were of interest for further study. The intensity of elements such as iron and titanium were of particular interest to compare with magnetic measurements. Details of the NOCS BOSCORF ITRAX-XRF core scanner are given in Croudace *et al*. (2006) and a technical account of the ITRAX-XRF method and comparison with discrete sample data is given in Jansen *et al*. (1998).

Data are acquired by irradiating the sediment via an intense micro-X-ray beam. The incident X-rays emit an electron from an inner atomic shell and an electron from the outer shell replaces the resultant vacancy (Jansen *et al*., 1998). Electromagnetic radiation, in the form of X-rays, is produced as the electron gives up its surplus energy, equal to the energy difference between the two electron shells. The emitted radiation is characteristic for each couple of atomic shells. Different elements are therefore identified based upon the energy and wavelength spectra of X-ray emitted. The incident X-ray beam only interacts with small sediment volumes, and hence the ITRAX-XRF core scanner only provides data from a thin, less than a few hundred micron thick, surface layer of the sediment. For light elements (e.g., Al and Si), the response depth is only a few µm, whereas for the heavier elements (e.g., Ca and Fe) this depth increases to tens and hundreds of µm, respectively (Jenkins and De Vries, 1970; Jansen *et al*., 1998). The acquired data is expressed in terms of the intensity of the emitted X-rays in counts per second (cps) or kilo counts per second (kcps).

The ITRAX-XRF core scanner is an automated system as data is collected incrementally by moving the split core section through the X-ray-beam using a stepped motor-drive (Croudace *et al*., 2006). The ITRAX-XRF core scanner has advantages over the traditional XRF method that uses discrete sediment samples, which is both destructive as well as time consuming. However, a disadvantage of the ITRAX-XRF core scanner technique is that heterogeneities in the core surface such as roughness, water content, porosity and grain size can result in biased data. For discussions see Jansen *et al*. (1998), Kido *et al*. (2006) and Böning *et al*. (2007).

It is common for ITRAX-XRF results to be calibrated against data acquired using discrete samples and traditional XRF methods to give normalised results of percentage by mass of the oxide (weight %) (e.g., Jansen *et al*., 1998; Kido *et al*., 2006; Böning *et al*., 2007; Spofforth *et al*., 2008). As this study focuses upon relative changes in the concentration of elements and not absolute values, calibration was not deemed as essential.

Using the NOCS BOSCORF ITRAX-XRF core scanner, XRF data were acquired along a central 2 cm wide strip of the split core sediment surface of cores TTR-451 and TTR-450. The top two sections of core TTR-451, which together span a total core length of around 120 cm, were subsampled using a 0.5 cm thick u-channel lid. This u-channel lid was used to make the XRF measurements and X-radiograph images (not shown). In order to remove contamination of the split core and u-channel sediments, the surface was scraped using a glass slide. Due to the lengthy time required for the XRF spectra acquisition, the sediment surface was covered with *Mylar* film in order to prevent desiccation.

The XRF measurements were made at increments of 500 μm. A 50 second count time was used for the XRF measurements. Mean square error (MSE) values of <40 cps were achieved by fine-tuning the settings using the *Core Scanning Navigator* user interface graphical software. The 3 kW molybdenum target tube was operated at 30 kV and 30 mA. These settings are considered suitable for most elements (Croudace *et al*., 2006).

The XRF intensities were calculated from the raw XRF spectra, and were processed using the *Q-spec* spectral analysis programme. Over time the 3 kW molybdenum target tube decays, resulting in reduced total intensities of the emitted X-ray beam. As measurements were made over a number of weeks, the 'line camera signal' (i.e., the total intensities), which is recorded for each individual core section by the *Q-spec* spectral analysis programme, was used to correct for shifts to reduced intensities, over time.

3.2. Sampling of cores TTR-450 and TTR-451

Discrete samples from cores TTR-450 and TTR-451 have provided sediment for environmental and magnetic studies, and subsamples of them have been used for further analyses. Sampling was done at 2.35 cm intervals in a continuous strip and using palaeomagnetic cubes. Toothpick samples were taken at 5 cm intervals from both TTR-450 and TTR-451 for bulk sediment stable oxygen and carbon isotope ratio analyses. Discrete sediment samples were additionally taken for AMS^{14}C datings.

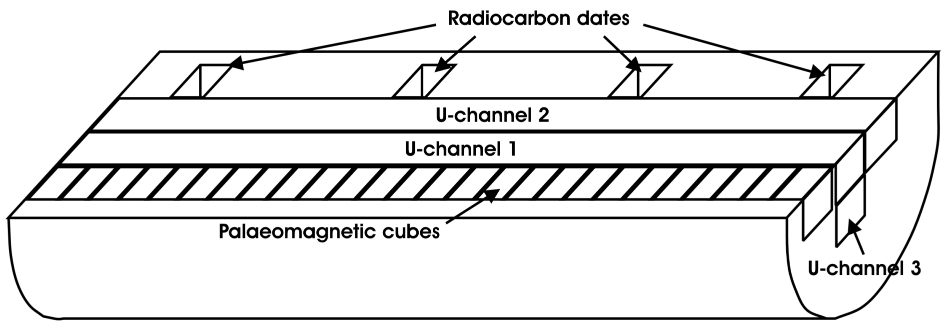

Figure 3.3. Schematic diagram illustrating the sampling of the top two sections of core TTR-451. U-channel 3 was a 0.5 cm thick filled u-channel lid.

Two u-channels were sampled in parallel from the top two ~60 cm sections of core TTR-451 and have been used for further magnetic investigation, as well as planktonic foraminiferal stable oxygen and carbon stable isotope studies, and counts of IRD and total foraminiferal abundances. A u-channel is a 2 x 2 cm square-cross-section, transparent plastic liner in which continuous samples are taken from the centre of the split core section (Tauxe, 1993; Weeks *et al*., 1993). The relatively short ~60 cm long individual core sections were spliced into one length of u-channel. An additional sample set was removed from these upper two sections of TTR-451 using a 0.5 cm thick u-channel lid that provided XRF data. As core edges can be affected by sediment flow, no samples were removed less than 1 cm from the core liner. Sedimentary boundaries were noted upon removal of these u-channels, providing further information to allow depths to be accurately inter-calibrated between sample sets. Figure 3.3 illustrates schematically the sampling techniques for these upper two core sections of TTR-451.

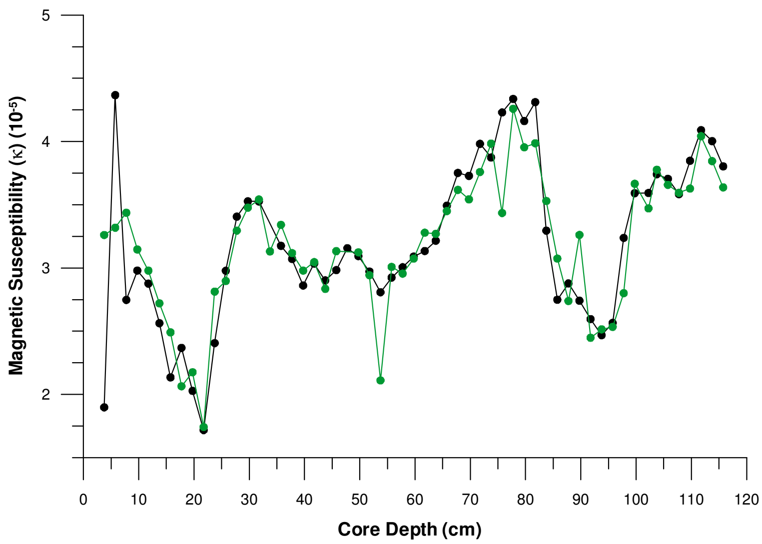

Figure 3.4. Volumetric low-field magnetic susceptibility obtained from 2 cm^3 subsamples from u-channels 1 (black) and 2 (green). With no relative vertical movement of the u-channels to each other, the peak R^2 value of 0.72 was obtained where n=55. For details of the magnetic susceptibility see 3.3.

Magnetic measurements of the u-channel sediment samples prior to and after sub-sampling have also given stratigraphic control between sample sets. Both visual and cross correlations of the different magnetic parameters, as well as stepped/lagged correlations (carried out both manually and by using the *X-corr* function in *Matlab*), to find the peak R^2 value, allowed for the sample set intercalibration of depths within half the sample resolution of the dataset. An example is shown in Figure 3.4.

3.3. Palaeomagnetic and Environmental Magnetic Measurements

The palaeomagnetic and environmental magnetic measurements made on sample sets from cores TTR-450 and TTR-451 included magnetic susceptibility (κ), Natural Remanent Magnetisation (NRM) and Anhysteretic Remanent Magnetisation (ARM). Saturated Isothermal Remanent Magnetisation (SIRM) and backfield single remanence curves, magnetic hysteresis loops as well as First Order Reversal Curve (FORC) diagrams were generated. This section provides an introduction to the magnetic parameter and a rationale for why it was measured, and an overview of the techniques and laboratory instruments. Also discussed in this chapter is a critique of the methods, as well as error identification, quantification and reduction.

3.3.1. Magnetic Susceptibility

Magnetic susceptibility (κ) is defined as the 'ratio of induced (temporary) magnetisation acquired by a sample in the presence of a weak magnetic field, to the applied field itself' (Verosub and Roberts, 1995). Variation in magnetic susceptibility is primarily controlled by the quantity and grain size (domain configuration) of ferromagnetic (iron, nickel and copper) and ferrimagnetic (e.g., magnetite) material present within the sample (e.g., Verosub and Roberts, 1995; Stoner *et al*., 1996). Large ferrimagnetic (>10 μm) and superparamagnetic (>0.03 μm) grains result in enhanced magnetic values whereas, for sediments with low ferromagnetic concentrations, variations in magnetic susceptibility are more likely influenced by paramagnetic (e.g., Fe, Mg silicates), antiferrimagnetic (e.g., haematite) and diamagnetic (e.g., calcium carbonate and silica) grains (Stoner *et al*., 1996). Low-field magnetic susceptibility measurements are relatively rapid to make and provide a first line approach to characterising sediment components. Therefore, it is commonly one of the first measurements to be made on sediment cores after recovery.

Previous study of cores in vicinity of Eirik Drift have shown that sediments have a relatively strong magnetic character, which likely results from transport of (titano)magnetite out of the Nordic basaltic province by North Atlantic Deep Water (NADW) (e.g., Kissel *et al.*, 1997; 1999a, b; Moros *et al.*, 1997; Laj *et al.*, 2002; Snowball and Moros, 2003). Eirik Drift represents a key region for deposition of suspended matter transported out of the Nordic Seas, especially for transportation via deep-water overflow through Denmark Strait (between Iceland and Greenland).

Unlike cores recovered from the 'IRD belt' (for definition see Hemming, 2004) that show a strong magnetic signature during North Atlantic ice-rafting events (e.g., Grousset *et al.*, 1993; Robinson *et al.*, 1995), relatively high abundances of coarse grained quartz and detrital carbonate (IRD), combined with reduced (titano)magnetite input result in distinct lows in magnetic susceptibility in high latitude marine sediment cores during these same IRD events (e.g., Stoner *et al.*, 1996; Kissel *et al.*, 1997; 1999a; Moros *et al.*, 1997; Dokken and Jansen, 1999; Laj *et al.*, 2002). Magnetic susceptibility was therefore measured on sediments from cores TTR-450 and TTR-451 in order to give stratigraphic control, as well as a key environmental proxy.

Low-field volumetric susceptibility (κ) was acquired from discrete sample cubes, which were continuously sampled at 2.35 cm intervals down cores TTR-450 and TTR-451, and measured using a Kappabridge KLY-4 with the *Sufam* user interface software. A higher resolution low-field magnetic susceptibility dataset was also obtained from core TTR-451 using a Geotek MSCL 6.1 magnetic susceptibility logger, with a Bartington Instruments MS2E1 point sensor, and was measured at 0.5 cm intervals using a stepper motor and placing the probe in contact with the split 'whole core' sediment surface. The 'whole core' magnetic susceptibility data was obtained not only to provide a more detailed record, but also to cross- validate the discrete sample dataset. However, as the MS2E1 point sensor is only sensitive to the uppermost few millimetres of sediment, slight variation in the near surface sediment composition may cause discrepancy between the two sets of measurements.

Low-field magnetic susceptibility was additionally acquired from 0.5 cm thick sub-samples of the 2 x 2 cm u-channels. Measurements were made using a Kappabridge KLY-4 with *Sufam* user interface software. These additional magnetic susceptibility measurements were not used for interpretation, but have allowed for inter-calibration of datasets and better stratigraphic control (see section 3.2).

3.3.2. Anhysteretic Remanent Magnetisation

Anhysteretic Remanent Magnetisation (ARM) is defined as the magnetisation acquired when a sample is subjected to a direct current (DC) bias field, which is of the order of the Earth's magnetic field, in a decreasing alternating magnetic field that is steadily reduced from a preset value to zero (Verosub and Roberts, 1995; Evans and Heller, 2003). Magnetic particles with remnant coercivities less than or equal to the maximum field will become magnetised along the direction of the biasing DC field. It is customary to express ARM in terms of its anhysteretic susceptibility (κ_{ARM}), whereby the ARM intensities are normalised by the bias field applied.

Variations in ARM intensity are interpreted to reflect changes in ferrimagnetic material concentration within the sediment samples. Unlike magnetic susceptibility, ARM tends to be sensitive to variations in the small (<10 μm), single domain and pseudo-single domain grain sizes (Verosub and Roberts, 1995; Stoner *et al*., 1996). Previous study of marine sediment cores recovered from the northern North Atlantic show a high degree of covariance between records of magnetic susceptibility and ARM, and supports the assumption that the magnetic signal results from the transport of (titano)magnetites out of the Nordic Basaltic Province. Reduced ARM intensities along the NADW flow path would suggest that the magnetic mineral content of sediments in that region originates from this single common source (e.g., Kissel *et al.*, 1999a; Laj *et al.*, 2002).

The ratio of susceptibility of anhysteretic remanent magnetisation (κ_{ARM}) to low-field magnetic susceptibility (κ) is a measure of average magnetic grain size where the magnetic mineralogy is dominated by (titano)magnetite (Banerjee *et al.*, 1981; Verosub and Roberts, 1995). The ratio of κ_{ARM}/κ is particularly sensitive to grain size variations within the 1 to 10 μm size range, and is inversely correlated with magnetic grain sizes; i.e., with the coarser grain sizes represented by lower values (Banerjee *et al.*, 1981). Significant proportions of superparamagnetic (SP) grains within a sediment sample, which exclusively contributes to κ and not κ_{ARM}, means that variations in κ_{ARM}/κ need interpreting with caution (King *et al.*, 1982; Verosub and Roberts, 1995).

Based upon these assumptions from previous work (e.g., Kissel *et al.*, 1997; Laj *et al.*, 2002), it was therefore likely that a κ_{ARM}/κ record from core Eirik Drift would reflect variations in the size of the coarsest magnetic grains that can be carried by NADW out of the Nordic Seas and that settle out on Eirik Drift as NADW rounds the southern tip of Greenland. The ratio of the magnetic parameters κ_{ARM}/κ would therefore likely provide a proxy for NADW flow intensity.

ARM data were acquired at 2.35 cm intervals along a continuous strip of cores TTR-450 and TTR-451, using discrete sediment sample cubes. ARM was imparted using a 50 μT DC bias field and a 100 mT peak alternating field (AF), with measurements made using a long-core *2G Enterprises* cryogenic magnetometer. A technical report on the NOCS *2G Enterprises* cryogenic magnetometer is given in Roberts (2006).

The ARM was imparted using an in-line solenoid that is located within the axial demagnetisation coil (z axis coil). The decay rate of the imparted field (including AF demagentisation) affects the successfulness of the treatment, which for long core magnetometers, is equal to the speed at which the sample is passed through the field (Roberts, 2006). This is given the term translation speed for which, at higher velocities, samples experience fewer AF half cycles. For long-core magnetometers, as the sample is passed through the coil at a constant speed, an AF field decays in space rather than time (Roberts, 2006). Although this has greater implications for u-channel measurements, it is noted here that the NOCS *2G* cryogenic magnetometer has a translation speed of 1 cm/s (Roberts, 2006), which is recommended by Brachfield *et al*. (2004).

Superconducting quantum interference device (SQUID) sensors, which are immersed in liquid helium, detect weak magnetisations of the sediment samples by inducing a small persistent DC supercurrent into the SQUID pick-up coil array, and give rise to the generic name 'cryogenic' magnetometer (Roberts, 2006). Samples are loaded onto a sample holder and passed through the centre of the SQUID sensors through an access space at room temperature. A stepper motor with computer controlled micro-switches at either end of a pulley system controls the position of the sample through the SQUID sensors with precise positional control of within a few tenths of microns. Such positional control is essential for accurate remanence stability critical assessment through stepwise AF demagnetisation treatments.

AF demagnetisation treatment (the application of a linearly decaying alternating field) using the NOCS *2G Enterprises* cryogenic magnetometer is done 'in-line' using three mutually orthogonal demagnetisation coils positioned along the x, y and z axis of the sample. The field is ramped up in the demagnetisation coil to the desired field and the sample is passed through the coil whilst the field is 'tracked' at a constant peak value. This AF field is ramped down to zero and the process is repeated for each coil individually, prior to the samples being passed back through the SQUID sensors and the magnetisation measured. The narrow access *2G Enterprises* cryogenic magnetometer within NOCS is fitted with high-resolution SQUID sensors. The response curve of these pick-up coils within the SQUID sensors has a relatively sharp peak (Weeks *et al*., 1993; Roberts, 2006), and the ratio of the half width versus the maximum height of the curve (half power width) is around 5 cm for the NOCS *2G Enterprises* cryogenic magnetometer (Roberts, 2006). With such a narrow response curve, on which samples need to be centred, positional precision is therefore essential for accurate measurement of ~2 cm wide discrete samples.

A further complication of measurements made with long-core magnetometers are 'flux jumps' where strongly magnetic material, with intensities ≥1 A/m, cause non-reversible jumps in magnetisation, because the SQUID electronics are unable to count the large magnetic flux at a fast enough rate (Roberts, 2006). Identification of flux jumps can be done by assessing the linearity of decay of the magnetisation measured after each AF demagnetisation treatment, and may be resolved by re-measurement of the sample. For further operational details of SQUID magnetometers see in Goree and Fuller (1976), Weeks *et al.* (1993), Clarke (1994), and Roberts (2006)

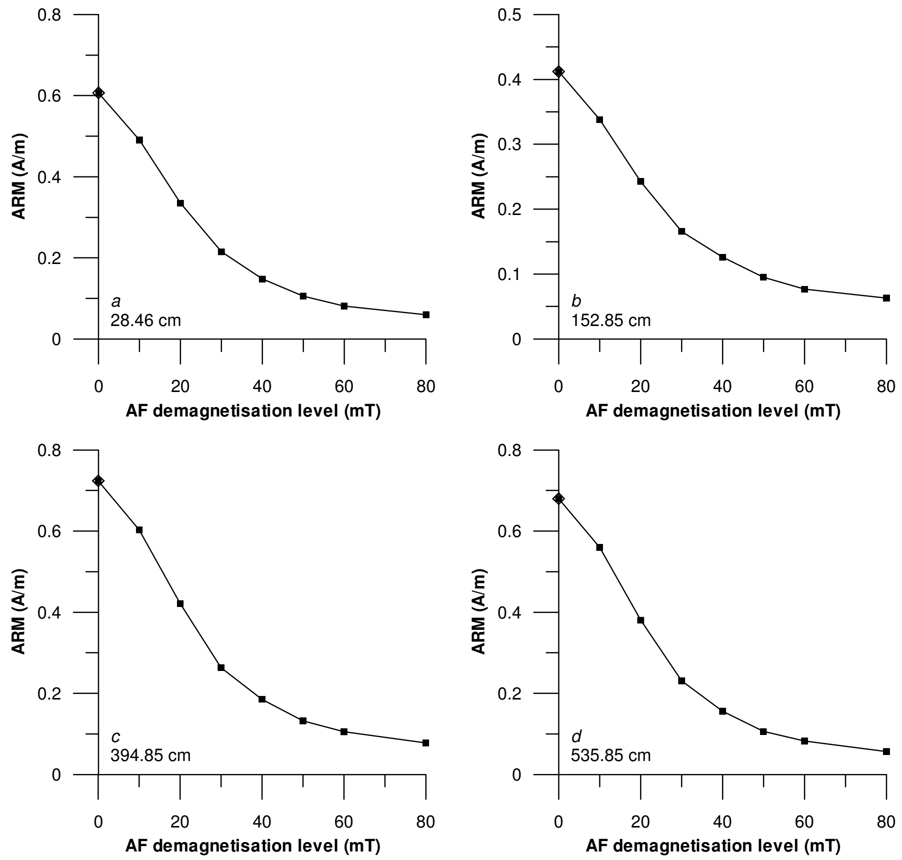

Figure 3.5. Representative ARM AF demagnetisation curves for core TTR-450.

Initially, ARM data were obtained from every tenth discrete sample down-core, and measured after AF demagnetisation at peak fields of 10, 20, 30, 40, 50, 60 and 80 mT. Such a high, and somewhat unconventional number of AF demagnetisation treatments were used for assessment of remanent stability. Representative AF demagnetisation curves for a selection of samples are shown in Figure 3.5 and 3.6. The smooth nature of the curves indicates a good stability of remanence. Subsequently, therefore, the remaining samples were measured after AF demagnetisation at peak fields of 20, 25 and 30 mT. The ARM intensities were automatically corrected for the sample volumes with the *Longcore* user interface software, and the data were therefore output in the GCS unit emu/cm^3 (10^{-3} emu/cm^3 = 1 A/m; SI unit).

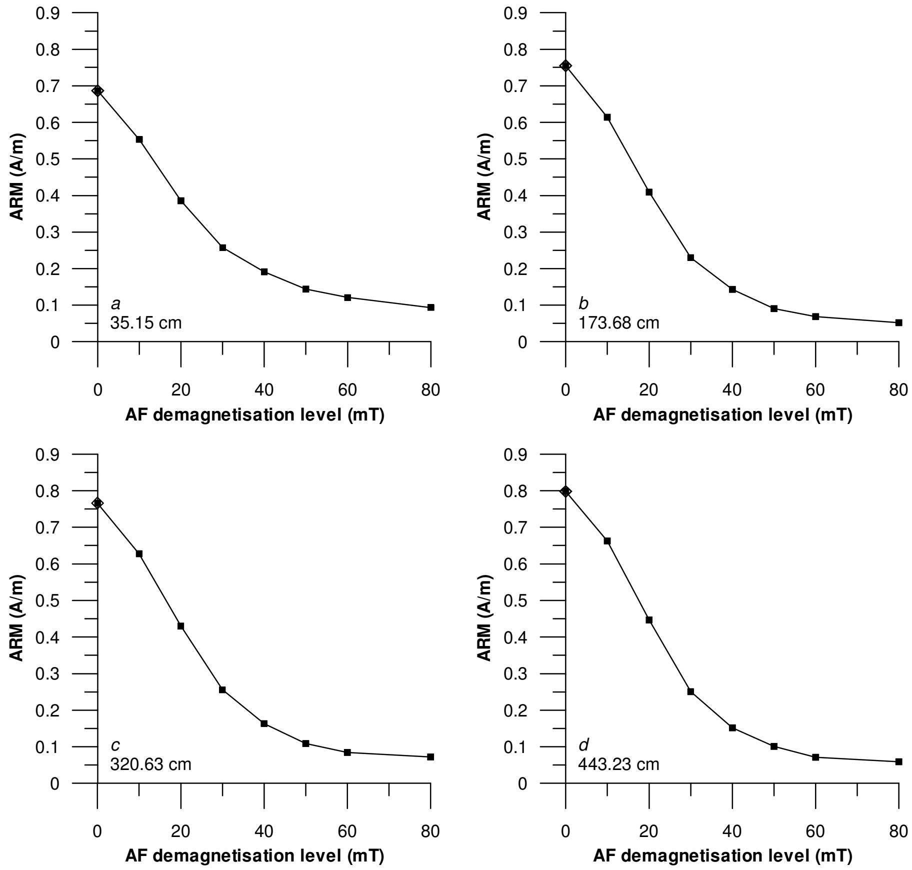

Figure 3.6. Representative ARM AF demagnetisation curves for core TTR-451.

In order to cross-validate ARM measurements from the discrete sample set, and to provide additional evidence for stratigraphic control, ARM was measured at 1 cm intervals along a continuous u-channel sample of sediments from the upper two sections of TTR-451, which spans a total core length of ~120 cm of the core. ARM was imparted along the axis of the u-channel using a 100 mT alternating field and a 50 μT DC bias field and using the previously described NOCS *2G Enterprises* cryogenic magnetometer. Measurements were made after stepwise AF demagnetisations of 0, 10, 20, 25, 30, 50 and 60 mT peak fields, and comparison of the ARM measurements after each treatment reveals no evidence of flux jumps (Figure 3.7).

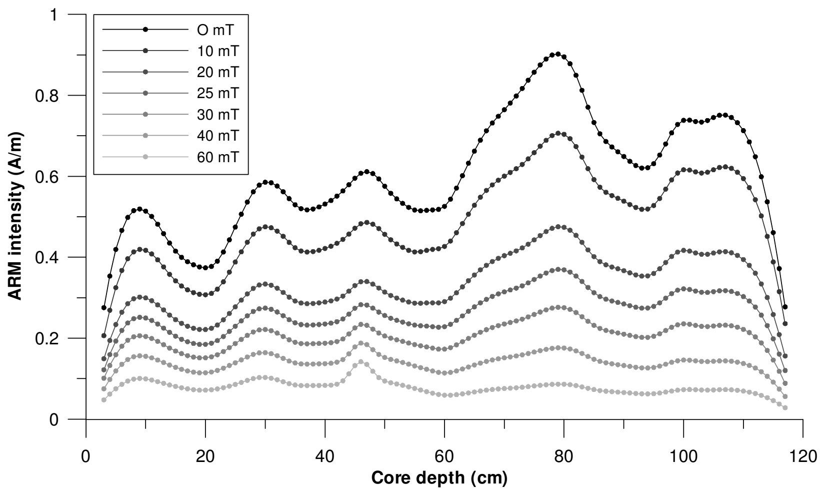

Figure 3.7. Continuous u-channel ARM measurements from core TTR-451.

Owing to the aforementioned response function of the SQUID pick-up coils, the data acquired from the u-channel sample were effectively ‘smoothed’ over a 5 cm sliding window. Figure 3.8 plots the continuous u-channel and discrete sample ARM measurements and the good agreement gives cross-validation of the discrete sample data. Slight discrepancy between the datasets occurs at around 45 cm depth and possibly results from the smoothing of the u-channel measurements.

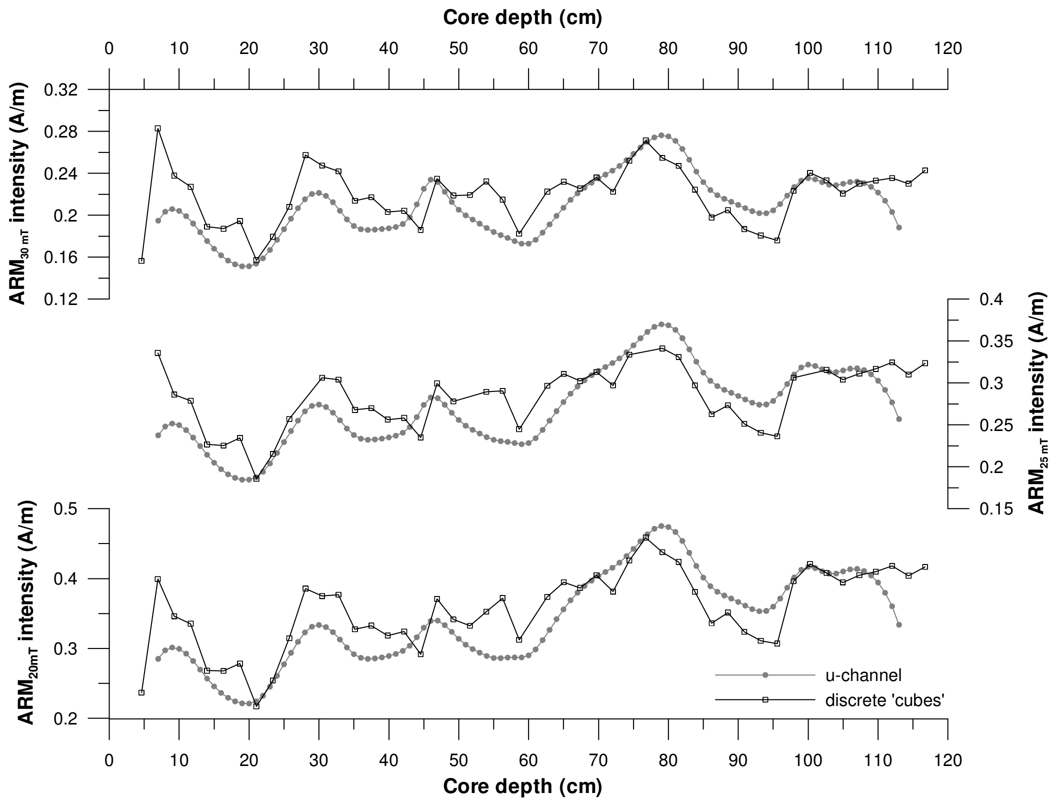

Figure 3.8. Comparison of the continuous u-channel and discrete sample ARM data, measured after stepwise AF demagnetisation treatment at 20, 25 and 30 mT.

3.3.3. Natural Remanent Magnetisation

Natural remanent magnetisation (NRM) is the remanent magnetisation present in a sample prior to laboratory treatment. The NRM intensity is determined by the intensity of the geomagnetic field at the time of, or just subsequent to, sedimentary deposition, as well as the concentration, mineralogy and grain size of the magnetic remanence carriers (e.g., McElhinney and McFadden, 1999; Stoner *et al.*, 2000). ARM and magnetic susceptibility both respond to variations in magnetic mineral concentration, and therefore these magnetic parameters can be used to normalise NRM intensities. The resulting NRM/ARM and NRM/κ ratios therefore provide records of the relative changes in the intensity of the Earth's geomagnetic field (relative palaeointensity), with the effect of variation in the magnetic mineral concentration removed (e.g., Opdyke *et al.*, 1973; Levi and Banerjee, 1976; Tucker, 1981; King *et al*., 1982; Weeks *et al*., 1993; 1995; Stoner *et al*., 2000; Laj *et al*., 2000; 2002).

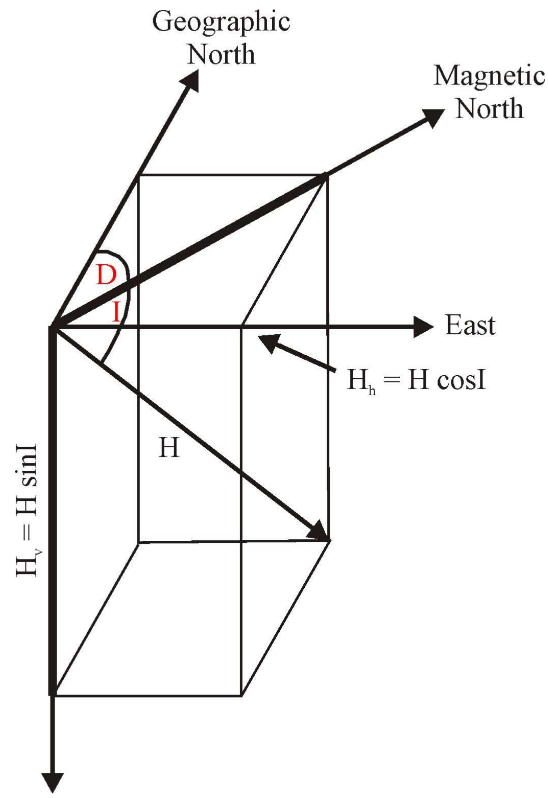

Figure 3.9. Directional vector components of the geomagnetic field after McElhinney (1973) and Butler (1992). The total surface geomagnetic field (*H*) can be described by two components; the vertical (*H_v*) and the horizontal (*H_h*). In the geographic north direction, the component of the magnetic field is described as *H* cos *I* cos *D*, and *H* cos *I* sin *D* describes the east component.

Stacked records of relative palaeointenisty from marine sediment cores recovered from the North Atlantic, synchronised to the GISP2 ice-core chronology using evidence from cosmogenic nuclide records (NAPIS-75 - Laj *et al*., 2000 and the revised GLOPIS-75 – Laj *et al*., 2004), provides an excellent basin-wide, marine sediment core correlative and dating tool. Two key palaeointensity excursions have been correlated between North Atlantic marine cores and well-dated lake sediments. These include the Laschamp event dated at around 41 ka BP (Laj *et al*., 2000; 2004; Guillou *et al*., 2004), and the contentious Mono Lake event (Kent *et al*., 2002; Benson *et al*., 2003; Zimmerman *et al*., 2006), dated in the GLOPIS palaeointensity stack at around 67 ka BP (Laj *et al*., 2004). The Laschamp event is also associated with a directional anomaly with a sharp and distinct negative excursion to lower inclination values (Laj *et al*., 2000; 2004). NB: see below for definition of the '*inclination*' directional component.

The use of palaeointensity as a dating tool has advantages over AMS^{14}C datings, as the latter can have large error not only due to the measurement techniques, but also variable reservoir ages and uncertainties in calibration (e.g., Hughen *et al*., 2000; 2004; Muscheler *et al*., 2000; 2008; Reimer and Hughen, 2008). A disadvantage, however, of using palaeointensity for sediment dating is that NRM intensities have a 'lock-in' depth, which means that magnetic grains are still be affected by the geomagnetic field just after deposition (e.g., Laj *et al*., 2000). Therefore, sedimentation rates need taking into account when assessing palaeointensity records.

Over time, it is not just the intensity of the Earth's geomagnetic field which changes, but also the direction of the geomagnetic field. Changes in the direction of the Earth's geomagnetic field over time periods of less than 10^5 years are termed as geomagnetic secular variation. The direction of the geomagnetic field and, hence, geomagnetic secular variation can be completely described by two vector components: the angle of inclination and the angle of declination, and are represented schematically in Figure 3.9.

The angle of inclination (I) of the total surface geomagnetic field (H) from the horizontal is defined as positive downward and ranges between –90° and +90° (i.e., the vertical angle between H and the horizontal). Whereas, the angle of declination (D) is the azimuthal angle between geomagnetic north to the horizontal component of H, ranging from 0° to 360°, positive clockwise (e.g., Butler, 1992). The so-called "dipole equation" (Equation 3.1) forms the basis of our understanding of many of the palaeomagnetic methods. The dipole equation describes how the angle of inclination relates to latitude (McElhinney, 1973). The angle of inclination increases from –90 ° at the geographic South Pole to +90 ° at the geographic North Pole.

$$\tan I = (H_v/H_h) = (2 \sin\lambda/\cos\lambda) = 2 \tan\lambda \qquad \text{(Equation 3.1; McElhinney, 1973)}$$

where H_v is the vertical component of the surface geomagnetic field, H_h is the horizontal component and λ is the geographic latitude.

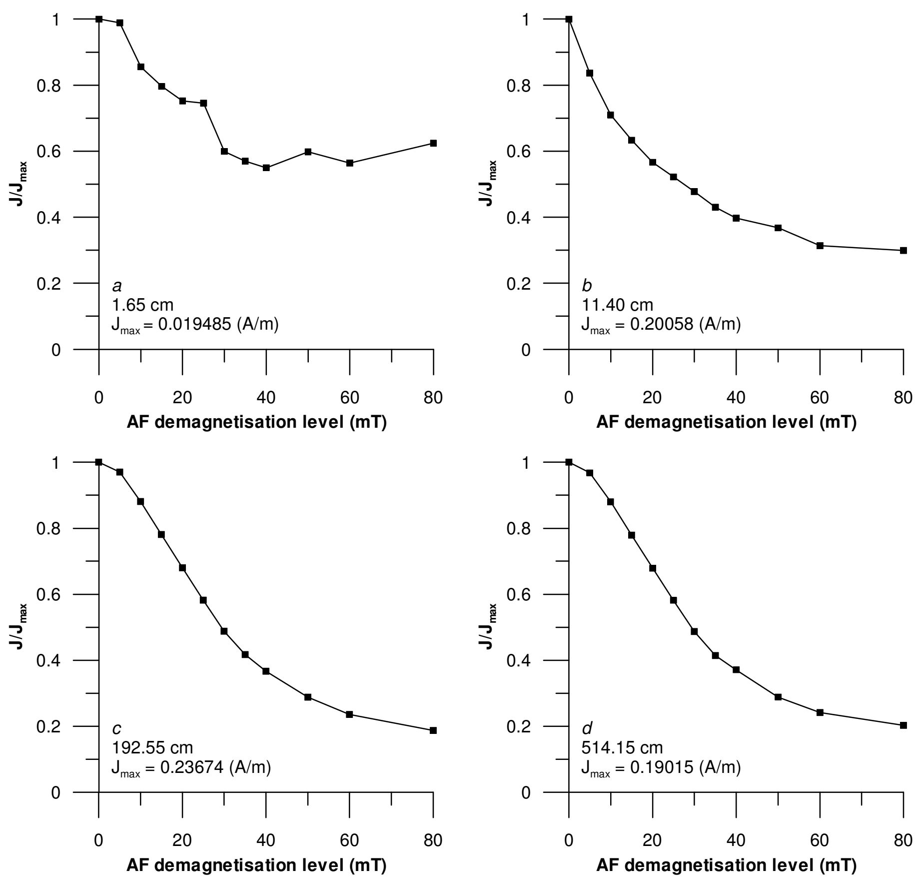

Figure 3.10. Representation NRM AF demagnetisation intensity decay curves for core TTR-450. *J/J_{max}* is the ratio of the NRM intensity over the 0 mT NRM intensity.

NRM was acquired from the same discrete sediment samples as the magnetic susceptibility and ARM were measured, and collected at 2.35 cm intervals along a continuous strip of cores TTR-450 and TTR-451. Measurements were made prior to the ARM treatment and using the previously described *2G Enterprises* cryogenic magnetometer. NRM was measured after stepwise AF demagnetisation treatments of 0, 5, 10, 15, 20, 25, 30, 35, 40, 50, 60, and 80 mT. Intensities were automatically corrected for the sample volumes with the *Longcore* user interface software, and the data were therefore output in the GCS unit, emu/cm^3 (10^{-3} emu/cm^3 = 1 A/m; SI unit)

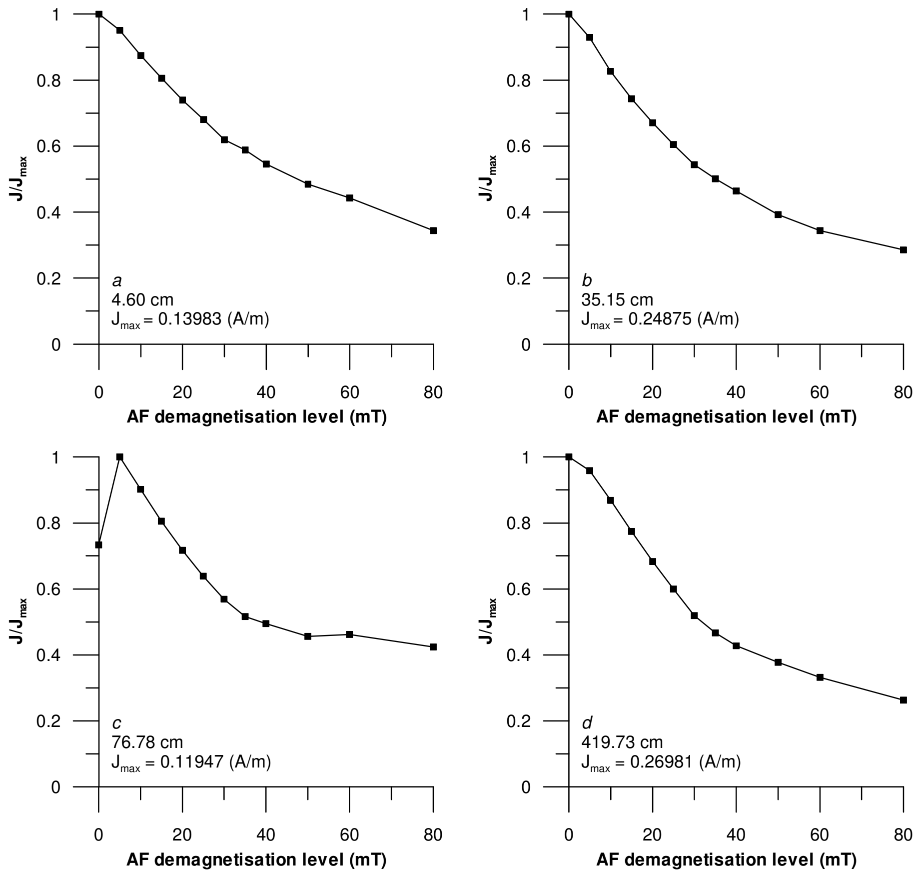

Figure 3.11. Representation NRM AF demagnetisation intensity decay curves for core TTR-451. *J/J$_{max}$* is the ratio of the NRM intensity over the 0 mT NRM intensity.

a.

TTR-450 1.65 cm

J_{max} = 0.0195 (A/m) MAD(3) = 3.9°

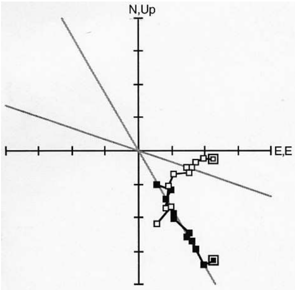

b.

TTR-450 11.40 cm

J_{max} = 0.2006 (A/m) MAD(3) = 3.1°

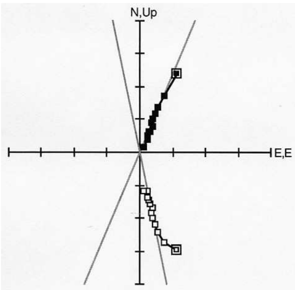

c.

TTR-450 192.55 cm

J_{max} = 0.2367 (A/m) MAD(3) = 1.9°

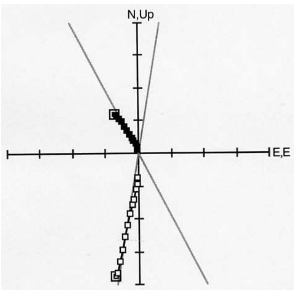

d.

TTR-450 514.15 cm

J_{max} = 0.1902 (A/m) MAD(3) = 3.0°

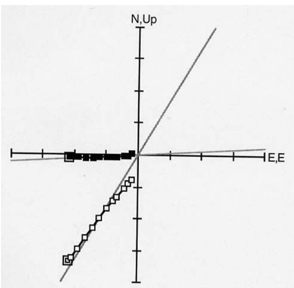

e.

TTR-451 4.60 cm

J_{max} = 0.1398 (A/m) MAD(3) = 1.8°

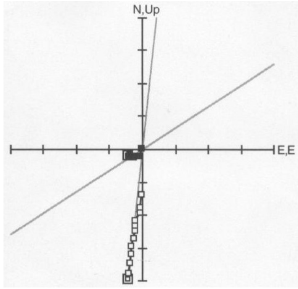

f.

TTR-451 35.15 cm

J_{max} = 0.2488 (A/m) MAD(3) = 0.9°

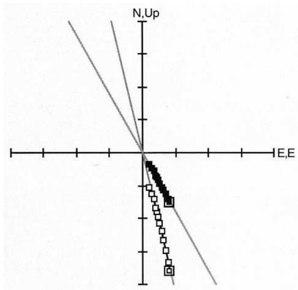

g.

TTR-451 76.78 cm

J_{max} = 0.1195 (A/m) MAD(3) = 3.7°

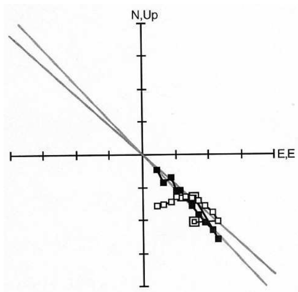

h.

TTR-451 419.73 cm

J_{max} = 0.2698 (A/m) MAD(3) = 1.3°

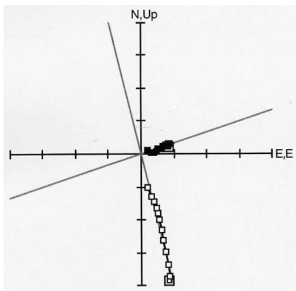

Figure 3.12. Representative Zijderveld diagrams of discrete sediment samples from cores TTR-450 and TTR-451. Filled and open circles correspond to projections on the horizontal and vertical planes, respectively. Where direction components show a non-linear decay toward the origin (e.g., a and g), primary stability was not attained.

Representative AF demagnetisation intensity decay curves for sediment samples from core TTR-450 and TTR-451 are shown in Figures 3.10 and 3.11, respectively. Typically, the sediments show smooth decay profiles, indicating that a good stability of remanence was attained. Figure 3.10a shows the demagnetisation curve for the uppermost sample of core TTR-450, which is centred at 1.65 cm core depth, and is representative for the top ~11 cm of the core. For this sample a stable single component was not attained, and the peak NRM intensity (J_{max}; obtained after an AF demagnetisation of 0 mT) for this sample was considerably weaker than NRM intensities acquired from sediment samples collected from lower depths in core TTR-450. This poor remanence stability most likely results from the high proportion of sandy admixture within this upper sedimentary unit and the relatively low concentration of magnetic grains. The data from this portion of core is therefore interpreted with caution. Figure 3.11b shows the demagnetisation curve for a sample centred around 76.8 cm depth of core TTR-451 and shows a rare example of where a stable single component was not attained for this core. Even the relatively sand-rich sediments from the top of core TTR-451 yielded stable remanence curves (Figure 3.10a).

Component declination and inclination directions were calculated from the NRM data using the *Z-plot* programme. Zijderveld plots, which were generated with the *Z-plot* programme, define stable primary NRM in the presence of noise and hence, give further evidence for the stability of remanence and the suitability of the acquired NRM data for calculation of palaeomagnetic component directional data. Zijderveld diagrams are plots of vector magnetisation during AF treatment and are projected on two orthogonal planes (e.g., Dunlop, 1979). Zijderveld diagrams, which show linear component decay toward the origin during progressive AF demagnetisation, represent samples with stable primary magnetisation directions (e.g., Dunlop, 1979; Weeks *et al.*, 1993; Laj *et al.*, 2000).

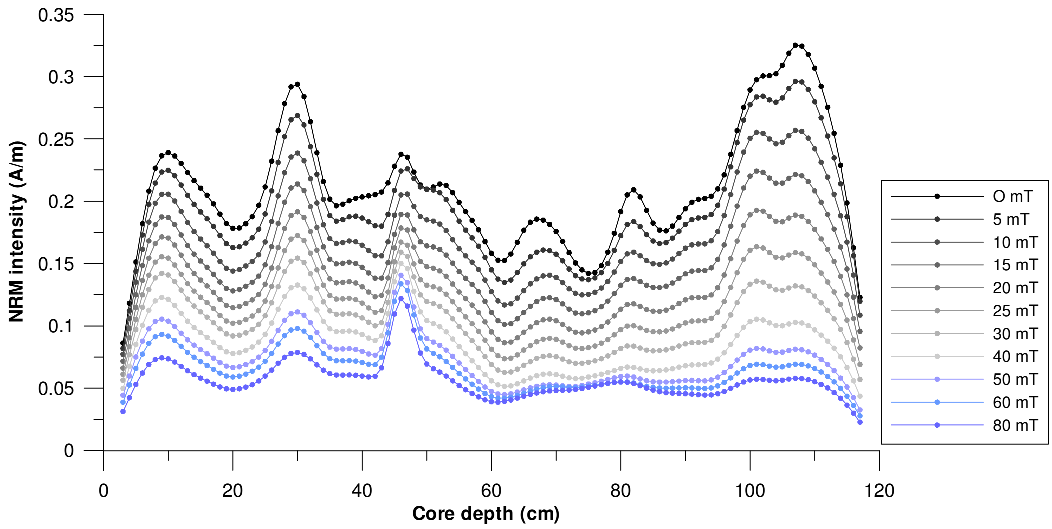

Figure 3.13. Continuous u-channel NRM measurements from core TTR-451.

The *Z-plot* programme allows for the removal of AF demagnetisation treatment steps from the component directional data calculation where stable primary magnetisation directions did not occur, i.e., if the decay toward the origin is not linear. Critical assessment of the linearity of the decay was provided by maximum angular deviation (MAD)(3) values, which were calculated concurrently within the *Z-plot* software. MAD(3) values less than 3° was considered acceptable. Subsequent to data processing, an average MAD(3) value of 2.3° was achieved for core TTR-450 and 1.5° for core TTR-451. Figure 3.12 shows representative Zijderveld diagrams for cores TTR-450 and TTR-451, and their AF demagnetisation decay intensity curves are presented in Figures 3.9 and 3.10. Combined with their MAD(3) values, these pieces of evidence indicate that the samples had stable and well-defined primary directional components. Figures 3.11a and g show examples when NRM stable primary directions were not attained and likely resulted from relatively high abundances of coarse material within the samples.

NRM intensities were additionally measured at 1 cm intervals along a continuous u-channel sample of the top ~120 cm of core TTR-451, and using the previously described NOCS *2G Enterprises* cryogenic magnetometer. Note that the NRM measurements were performed prior to ARM treatment. Measurements were made in order to cross-validate NRM measurements from the discrete sample set, and to provide additional evidence for stratigraphic control between the sample sets. NRM intensities were measured after stepwise AF demagnetisation in peak fields of 0, 5, 10, 15, 20, 25, 30, 40, 50, 60 and 80 mT. Figure 3.13 shows the NRM data collected after each AF demagnetisation treatment and reveals no evidence of flux jumps.

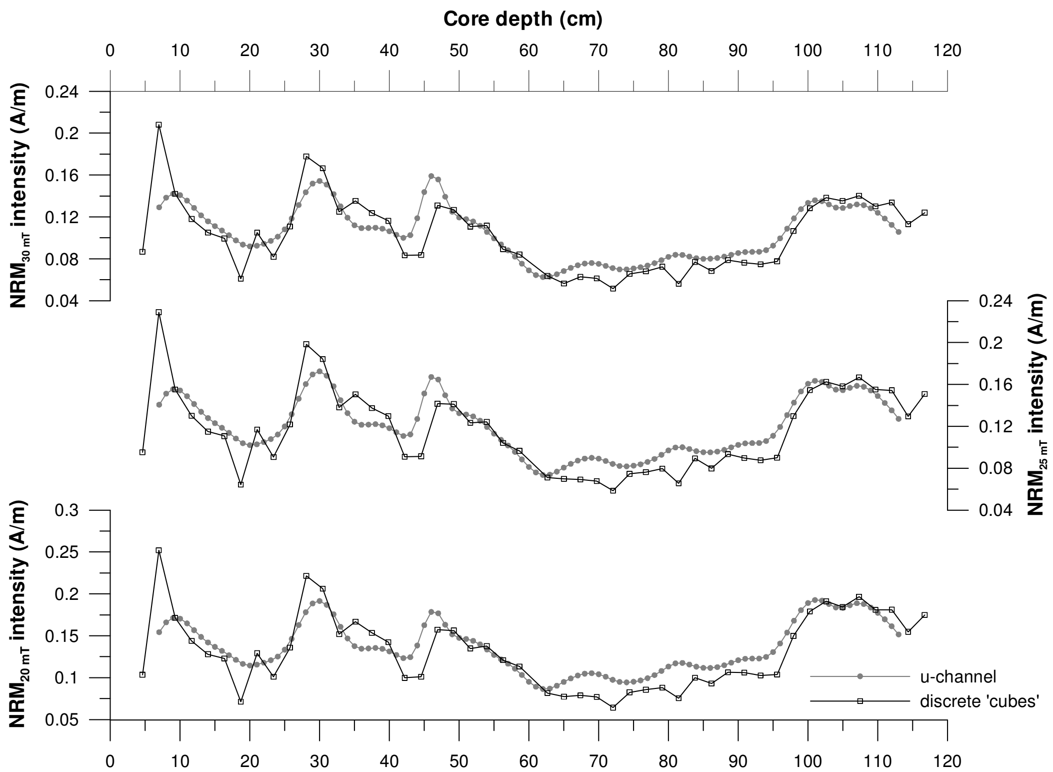

Figure 3.14. Comparison of the continuous u-channel and discrete sample NRM data, measured after stepwise AF demagnetisation treatment at 20, 25 and 30 mT.

Figure 3.14 plots the continuous u-channel and discrete sample NRM measurements and the good agreement gives cross-validation of the discrete sample data. Note that as with the ARM measurements, the NRM u-channel data was smoothed over a 5 cm sliding window, as a result of the pick up function of the coils. Slight discrepancy between the datasets occurs at around 45 cm depth and possibly results from the smoothing of the u-channel measurements. However, it cannot be ruled out that this discrepancy may also result from lateral variation across the core.

3.3.4. SIRM and backfield single remanence curves, magnetic hysteresis loops and FORC diagrams.

When a sample is as magnetised as its mineralogical composition and the laws of thermodynamics permit, then the sample is said to be fully magnetically saturated. If this magnetisation is measured whilst the sediment is still within the strong DC applied field then this is know as the saturation magnetisation (M_s) (Verosub and Roberts, 1995). Once the applied field is removed or reduced to zero, the magnetic particles within the sample start to lose their alignment, and the magnetisation is therefore reduced. This measured magnetisation is termed the saturation remanence (M_r), and is equivalent to the SIRM.

If a DC field is applied in the opposite direction, so the sample is exposed to what is termed a 'backfield', then IRM is overcome and the magnetisation of the sample is reduced to zero (e.g., Verosub and Roberts, 1995;. McElhinney and McFadden, 1999). The field in which this occurs is known as the coercivity or coercive force (B_c). If a backfield is applied and then removed, and the remanence of the sample is reduced to zero, then this field is called the coercivity of remanence (B_{cr}). Note that it is sometimes more appropriate to denote the coercive forces (B_c and B_{cr}) in terms of their equivalent fields; H_c and H_{cr}, respectively. If the applied field is repeatedly cycled, and saturation is reached, then the magnetisation of the sample will follow a hysteresis loop. Minor hysteresis loops can also be measured when the maximum applied field does not cause the sample to become magnetically saturated. For further discussions see

Day *et al*. (1977), Verosub and Roberts (1995), and McElhinny and McFadden (1999).

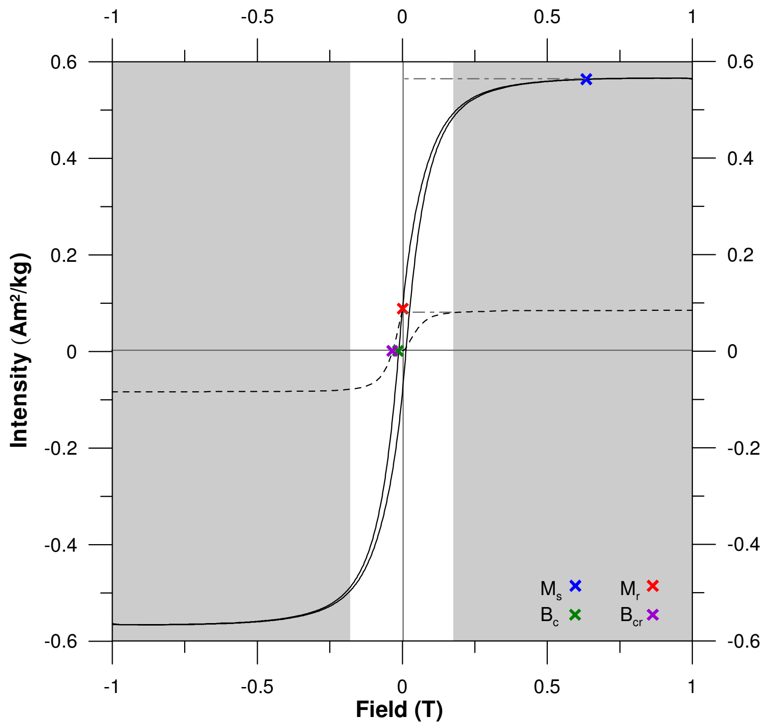

Figure 3.15. An example major magnetic hysteresis loop (solid black line), and SIRM and backfield single remanence curves (dashed black line) from sample TTR-451 2-7, which defines the magnetic parameters M_s, M_r, B_c and B_{cr}. The grey boxes shows the intensity of the DC field in which the sample is magnetically saturated, or when removed results in a measured SIRM. The grey dashed line shows the intensity of the magnetic moment when saturation magnetisation or SIRM is attained.

Figure 3.15 shows an example major hysteresis loop (solid line) and SIRM and backfield remanence curves (dashed curve). When the gradient of the curves are close to zero, the sample is magnetically saturated, and is represented by the grey area of Figure 3.15. Ferrimagnetic material (e.g., magnetite) becomes fully magnetically saturated in applied magnetic fields of around 300 mT, whereas canted anitferrimagnetic minerals (e.g., hematite) saturate in fields in excess of 2.5 T (e.g., Verosub and Roberts, 1995). Hysteresis loops with constricted narrow waists, are typical of sediments dominated by grains with PSD/MD domain states; whereas larger wasted loops indicate finer average magnetic grain sizes (e.g., Dunlop, 1986; Dunlop *et al*., 1990; Stoner *et al*., 1996). Therefore, analysis of the slope of the IRM acquisition curve and the shape of the major hysteresis loop, give indication of the predominant magnetic mineral content, as well as the average grain size of the sample.

Where the magnetic content of a sediment sample is known to be magnetite, magnetic hysteresis loop parameters and their ratios can be used to determine the domain state and grain size of the magnetic material (Day *et al*., 1977; Dunlop, 2002a, b). For samples containing coarse multi-domain (MD) grains, M_r/M_s <0.05 and B_{cr}/B_c >4, whilst samples dominated by fine grain single domain (SD) grains, M_r/M_s >0.5 and B_{cr}/B_c <1.5 (Day *et al*., 1977). Pseudo single domain grains (PSD) are represented by values that lie in between these two extremes. For magnetite, the SD/MD grain size transition is estimated primarily based upon theoretical calculations, at around 70 ηm. For PSD grains, which show high remanence (SD), but low coercivity (MD) characteristics, the grain size range is estimated between 0.1 and 20 μm (Fabian *et al*., 1996). Previous studies of marine core sediment samples from the North Atlantic indicate a constant magnetic mineralogy of (titano)magnetite with predominantly PSD grain sizes (e.g., Stoner *et al*., 1996; Kissel *et al*., 1997; 1999a; Laj *et al*., 2000).

Interpretation of domain state and grain size from hysteresis parameters can be ambiguous due to magnetostatic interactions (e.g., Dunlop, 2002a, b), and where samples contain different admixtures of magnetic particles with variable domain states they do not provide for detailed understanding of the individual components (Roberts *et al*., 2000).

FORC diagrams provide a better way of characterising individual magnetic components i.e. magnetic grain type and domain state. FORC diagram analyses were first introduced into geomagnetic studies by Roberts *et al*. (2000) and have since been used to investigate a wide range of magnetic particle systems with both synthetic and natural samples (Pike *et al*., 1999; 2001; Roberts *et al*., 2000; Muxworthy and Dunlop, 2002; Carvallo *et al*., 2003; 2005; 2006).

FORC diagrams are calculated from a large number of partial hysteresis loops or first order reversal curves (FORCs). A FORC is the magnetisation curve measured when the applied reverse field (H_r) is increased until saturation is reached. The FORCs used in the generation of a FORC diagram have different initial values of H_r so that the interior of the major hysteresis loop is filled. The magnetisation in the applied field (H) with the reversal point of the FORC (H_r), is denoted by $M(H_r, H)$. Roberts *et al*. (2000) define the FORC distribution as the second mixed derivative:

$$\rho(H_r, H) \equiv \partial^2 M(H_r, H) / \partial H_r \partial H \qquad \text{(Equation 3.2)}$$

where $\rho(H_r, H)$ is well defined for $H > H_r$. $\rho(H_r, H)$ is the FORC distribution, which at a given point (P) is calculated with a polynomial surface which is fitted onto a local square grid with P at the centre (Pike *et al*., 1999; Roberts *et al*., 2000; Carvallo *et al*., 2006). A FORC diagram is a contour plot of the FORC distributions rotated to a 45º angle, where the coercive field $\{H_c = (H - H_r)/2\}$ is plotted on the horizontal axis and the local interaction field $\{H_b = (H + H_r)/2\}$ is plotted on the vertical axis. For further details and discussions on the generation and interpretation of FORC diagrams the reader is referred to Roberts *et al*. (2000) and Carvallo *et al*. (2003; 2006).

Experimental and theoretical studies have shown that magnetic particles with different domain states and interactions plot in different areas of the FORC diagram (e.g., Roberts *et al*., 2000). SD grains are represented by minimal spread along the (H_b) vertical axis and have closed contours, PSD grains have closed contours, but with a horizontal peak at lower H_c values, and MD grains typically show an open and divergent contour distribution that is spread along the vertical (H_b) axis (Pike *et al*., 1999; 2001; Roberts *et al*., 2000; Muxworthy and Dunlop, 2002; Carvallo *et al*., 2003; 2005; 2006).

In order to better characterise magnetic mineral composition and grain size/domain state of sediments from core TTR-451, SIRM and backfield remanence curves, major magnetic hysteresis loops and FORC diagrams were generated. Eight of the discrete palaeomagnetic samples, on which magnetic susceptibility, ARM and NRM were measured, were used for this study and samples were selected on the basis of their very different κ_{ARM}/κ (inferred magnetic grain size) values.

The eight discrete palaeomagnetic cube samples (samples TTR-451 1-5, 1-8, 1-14, 1-19, 1-24, 2-3, 2-7 and 2-14) were dried and lightly ground, therefore ensuring that the sediments were not only homogenised, but also demagnetised. Subsamples with volumes of ~0.8 cm^3, were placed into plastic capsules and were tightly packed with cotton wool in order to prevent particles moving whilst measurements were being made. Measurements were made using a *Princeton Measurements Coporation*, *Micromag*, *Vibrating Sample Magnetometer* (VSM), and all analyses were performed at normal room temperature. The principle of how a VSM works is based upon Faraday's Law, whereby a time-varying magnetic flux induces an electromagnetic field in a conductor. The VSM vibrates the sample sinusoidally in the homogenous area of an electromagnet. The resulting magnetic moment of the sample induces a signal in voltage that is proportional to it in the adjacent pick-up coil (Evans and Heller, 2003).

The SIRM and backfield single remanence curves, magnetic hysteresis loops, and FORCs were generated with maximum applied DC fields of +1/-1 Tesla. After each measurement, the samples were treated with a 100 mT AF in order to remove the remanence of the previously imparted strong DC field.

FORC measurements were made with a smoothing time of 150-200 ms. The boundaries for the coercive field (H_c) were set between 0 to 120 mT and the local interaction field (H_b) between –80 and +80 mT. The FORC diagrams were generated using the '*FORC*' analysis programme and is run using *Matlab* software. A user-defined smoothing factor (SF) determines the size of the local grid on which the polynomial fit of the magnetisation is done, where the area of the grid is given by $(2SF + 1)^2$ over which ρ is smoothed (Pike *et al.*, 1999). In this study a smoothing factor of 4 was used. A more complete explanation of how FORC diagrams are constructed is given by Muxworthy and Roberts (2006).

3.4. Scanning Electron Microscope (SEM) study of magnetic mineral grain sizes

Scanning Electron Microscopy (SEM) image analysis of polished thins sections were used to validate the assumption that (titano)magnetite dominate the magnetic mineral composition of northern North Atlantic sediments beneath the NADW flow path (e.g., Kissel *et al*., 1997; Laj *et al*., 2000). Furthermore, the SEM image analysis study was performed in order to 'ground-truth' the magnetic mineral grain size estimates that were gained from the environmental magnetic measurements.

Subsamples, with volumes of around 0.5 cm^3 of lightly ground and, hence, homogenised sediments from eight discrete samples TTR-451 1-5, 1-8, 1-14, 1-19, 1-24, 2-3, 2-7 and 2-14, were made into polished thin sections. These samples were selected on the basis of their very different κ_{ARM}/κ values, and the sediment subsamples from which, VSM measurements were made. The polished thin sections were carbon coated and imaged using a *Carl Zeiss SMT Ltd.*, *Leo 1450VP* (*variable pressure*) *tungsten filament Scanning Electron Microscope* (*SEM*). Mosaics of 15 x 15 SEM images were collected for each sample at a magnification of x1000, and using a backscatter detector where the brightness of the individual grains is related to the relative atomic number and porosity. In total, 1800 separate images were collected, of which every twentieth were analysed.

SEM – Energy Dispersive Spectroscopy (EDS) allowed for identification of (titano)magnetites. These were recognised by an elemental composition of only iron, titanium, silica and aluminium oxides. The titanomagnetites were, by far, the brightest grains within the sediment samples. *PGT IMIX* image analysis software was used to process the acquired images. The software was calibrated for the brightness of the (titano)magnetite grains in order to automatically count and measure the cross-sectional diameter of titanomagnetite grains. The *PGT IMIX* image analysis software was additionally calibrated for magnification (1 pixel = 0.359241 μm), so that the data was output in microns.

Although not quantified, error in this analysis can be assumed. Firstly, pitted grains were counted by the image analysis software as multiple grains. During processing, however, this error was reduced by manipulation of the software. Secondly, areas of polished thin sections with no sediment coverage were included in the image analysis, and likely affected the percent area calculations.

3.5. Sortable silt material, preparation and analyses

The grain size distribution of terrigenous particles within the 10-63 μm size range, or sortable silt size range as defined by McCave *et al.* (1995a, b), is a sensitive index for near bottom current strength. Variations of the mean grain sizes within the sortable silt grain size window have been interpreted to reflect changes in intensity of near bottom strength (e.g., Bianchi and McCave, 1999), as more vigorous flow prevents deposition of the finer grains and therefore biases the mean grain size towards higher values (Ledbetter, 1984; McCave *et al.*, 1995a, b). Records of mean sortable silt grain sizes have shown agreement with geochemical proxies for nutrient concentration along deep and bottom current flow paths (e.g., Hall *et al.*, 2001). For an in-depth review on the background understanding, techniques and pitfalls of the sortable silt method see McCave *et al.* (2006) and McCave and Hall (2006).

Mean sortable silt grain sizes were measured on samples from core TTR-451 to test whether the magnetic proxy κ_{ARM} versus κ (also measured on samples from TTR-451) is a sensitive index for near bottom current strength. Mean sortable silt grain sizes were additionally measured on core top samples that were collected from cores D298-P1 (3452 m water depth; 57º30.227´N and 48º43.369´W) and D298-P3 (3430 m water depth; 58º13.025´N and 48º21.765´W). These cores were recovered from the western toe of Eirik Drift during the D298 cruise in 2005 with *RRS Discovery*. Mean sortable silt grain size data were also gained from core top samples of TTR-451 and TTR-450. These core top measurements were made in order to compare with mean scalar current velocities that were calculated from Lowered Acoustic Doppler Current Profiler (LADCP) data that was additionally collected during D298. Figure 3.16

shows the location of the cores relative to the D298 CTD stations that were used in this study.

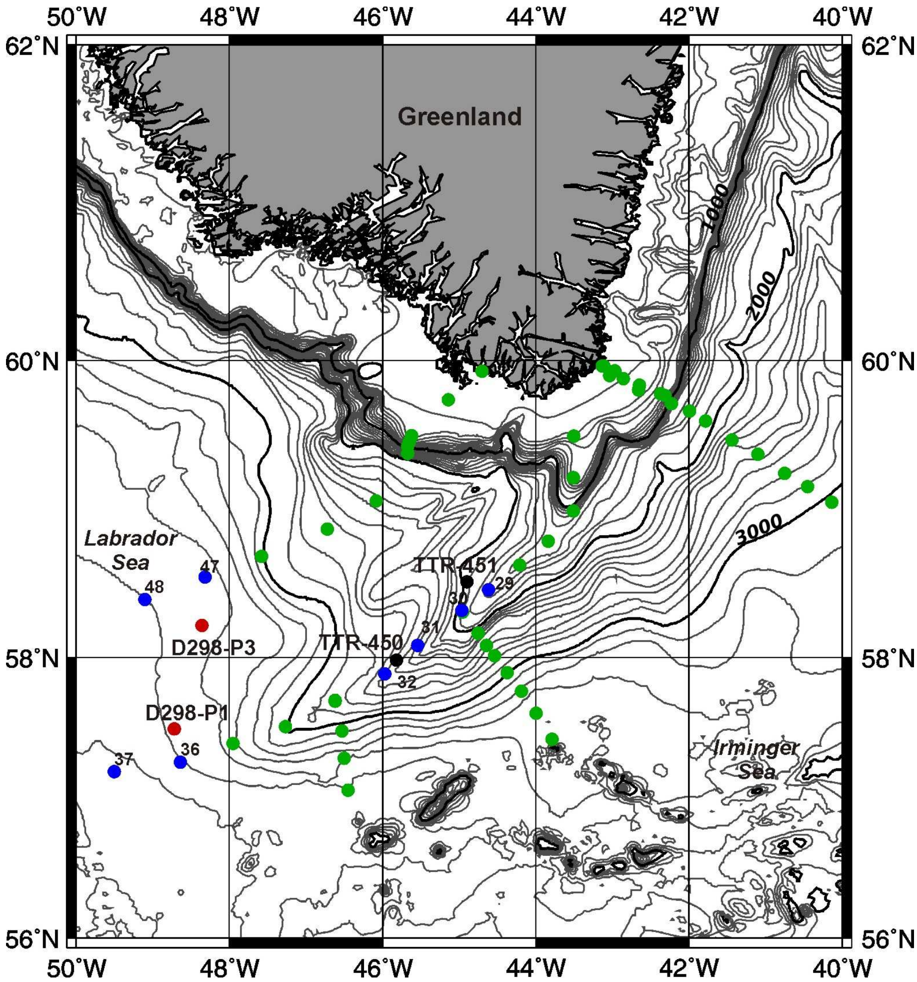

Figure 3.16. Location map of the study region. The black and red dots represent the cores collected during the TTR-13 and D298 cruises, respectively. The D298 CTD stations that are not used in this study are shown in green and those that are used are shown in blue, with their station numbers denoted, and the 1000, 2000 and 3000 (heavy, black) contours are shown.

The preparation techniques for the mean sortable silt grain size analyses were after McCave *et al*. (1995b) and are summarised in Figure 3.17. Analyses were conducted on approximately 3 g of dried, lightly ground (homogenised) subsamples from the upper 48 discrete samples from core TTR-451 (spanning ~120 cm of the core); the same samples from which the κ_{ARM} and κ measurements were made. For details on the magnetic methods see section 3.4.

Mean sortable silt analyses were also carried out on core top samples. Approximately, 1.5 g of terrigenous sediment within the sortable silt grain size range, was required for analysis. Therefore, up to 6 g of bulk sediment was sampled from the core tops of TTR-450 and TTR-451 as the core tops mostly comprised a winnowed foraminiferal sand.

Samples were dispersed overnight in a 0.1 % calgon (sodium hexametaphsophate) solution, under continuous agitation using a 'shaker bed' to help disaggregate the sediment. Initial pilot studies showed that the total organic carbon (% TOC) content for core TTR-451 was very low (less than 0.3 %). In accordance to the methods in McCave *et al*. (1995b), it was considered unnecessary to disperse the sediment in hydrogen peroxide (H_2O_2). Treatment of the sediment with hydrogen peroxide is used to digest organics, but the process is potentially damaging to pyrite and feldspars, and even quartz (e.g., Mikutta *et al*., 2005).

Samples were wet sieved at 63 µm using RO water, and the greater than 63 µm size fraction was retained and oven dried at 50 °C overnight. The retained coarse fraction was inspected under a binocular microscope to ensure all the silt and clay fraction had been successfully removed.

Samples were dispersed overnight in 500 ml of 1 M acetic acid solution (the reactant in excess to ensure a complete reaction) in order to remove biogenic carbonate. Unlike the conventional preparation method wherein samples are settled overnight between washes (e.g., McCave *et al*., 1995b); the samples were triple washed with RO water using a centrifuge after 24 hours. This deviation from the published method was for 2 key reasons. Firstly, flocculates were evident in suspension after 24 hours of dispersion. SEM imaging, showed that these flocculates contained grains within the sortable silt grain size range (10 –

63 μm), and therefore could not be wasted. Secondly, testing of the acetic acid solution with litmus paper indicated a pH of 2 and a pH of 3-4 after the first wash. Therefore, it was considered prudent to remove all of the reactant immediately to prevent removal of detrital carbonate as well as the biogenic carbonate. Smear slide examination under a petrological microscope of a toothpick sample after the removal of the reactant showed complete extraction of the biogenic carbonate, with some detrital carbonate remaining. After triple washing, the remaining solution was tested with litmus paper to ensure that the sediment was dispersed in a dilutant with a neutral ≠ 5-6 pH.

The sediments were then dispersed in 500 ml of 2 M sodium carbonate ($NaCO_3$) solution (with the reactant in excess) for 5 hours in a heated water bath at 85 ° C in order to extract the biogenic silica. Using a centrifuge, the sediments were triple washed with RO water in order to remove both the reactant and the silica in solution. The dilutant was tested with litmus paper to ensure that the remaining solution had a neutral pH. With the neutralisation process of washing, the pH of the solution changed from strongly alkaline (pH close to 14) with the sodium carbonate, to slightly acidic (pH of 5-6) with only RO water, and hence ensured complete removal of the reactant. The samples were dispersed in a 0.2 % calgon solution and stored in the cold and dark in order to prevent algal growth.

The sediment samples were spun overnight to facilitate disaggregation, and then placed in an ultrasonic bath for 2 minutes immediately prior to analysis. The samples were vigorously shaken by hand and 300 μl of sediment solution was immediately pipetted into an *Isoton* electrolyte solution. The volume of sample was adjusted for the analysis of the D298 core top samples to 400 μl in order to maintain similar grain concentrations during analysis.

The time taken between the shaking of the samples to pippetting likely varied during each batch run as it is logical that the process became faster with repetition. This would imply that the first few samples would be biased towards finer grain sizes as the coarse grains settle out first. This was tested by reanalysis of the first few samples from the start of the batch to the end of the batch.

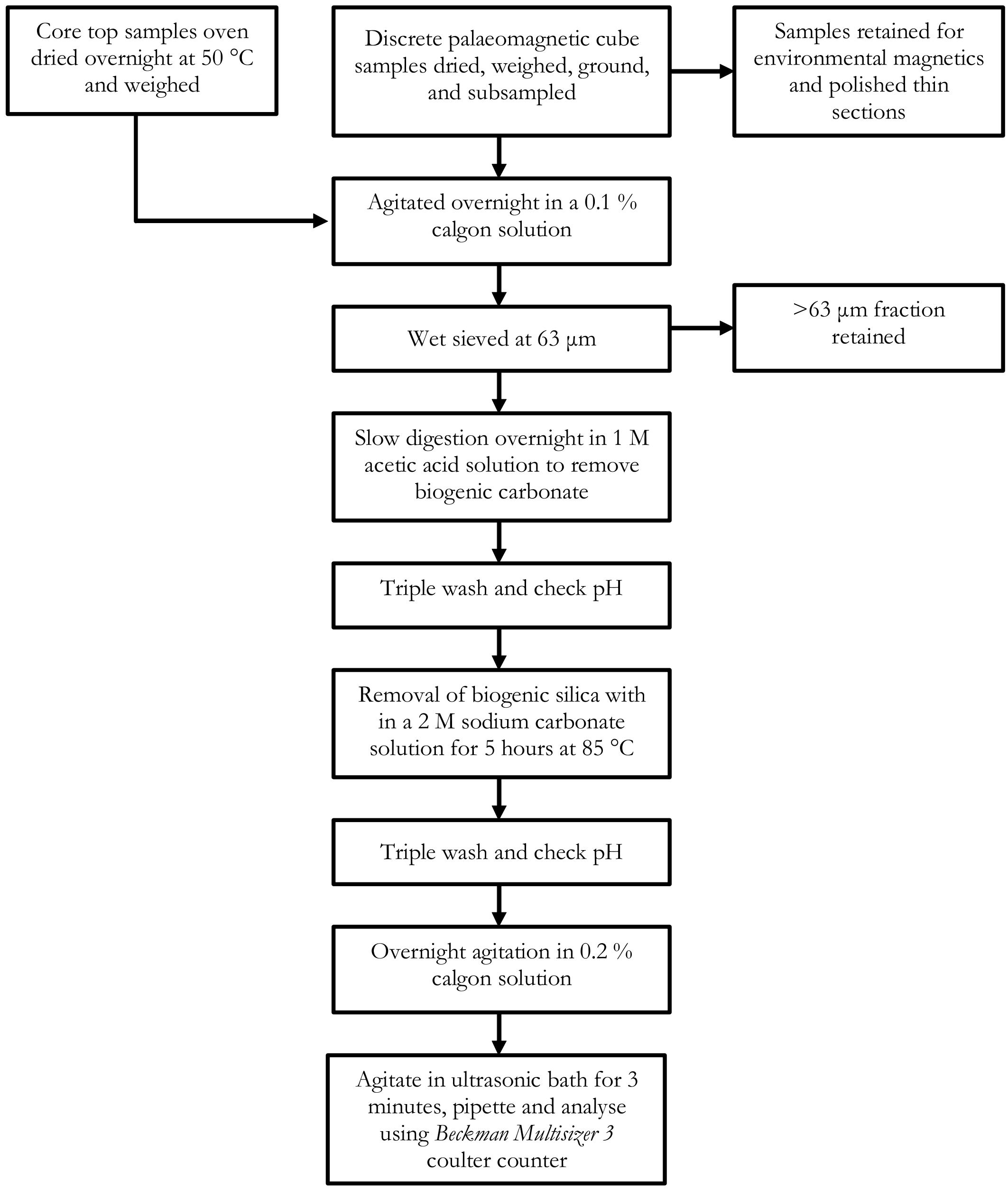

Figure 3.17. Summary flow diagram of the preparation techniques for sortable silt analyses. Methods are after McCave *et al.* (1995b)

The sortable silt grain size distributions were measured using a *Beckman Multisizer 3* coulter counter at *Cardiff University*, and the mean sortable silt grain sizes calculated using the *Beckman Coulter Multisizer 3* software. A standard solution with known grain sizes was measured prior to the sample batches in order to test the machine accuracy and calibration.

There are three key analytical devices that are used for grain size distribution measurements of deep sea fine-grained sediments; the coulter counter (used in this study), the sedigraph, and particle laser sizers, of which non measure the actual grain sizes. The coulter counter uses electrical conductivity to estimate volume-equivalent spherical diameters (Bianchi *et al.*, 1999; McCave and Hall, 2006). Particles are detected when they are sucked through an aperture and past a laser. The diameter of the aperture determines the grain size range of particles that can be detected. Due to this limited grain size window, coulter counters are only able to record mean sortable silt grain sizes, and not percent sortable silt. The sedigraph estimates particle grain sizes based upon their settling velocities, and hence provides a 'dynamical' grain size distribution that is directly related to the depositional setting (e.g., McCave *et al.*, 1995a, b; McCave and Hall, 2006).

Particle laser sizers estimate grain sizes based upon diffraction of coherent light as the particle passes a laser beam. This method is unsuitable for the measurement of platey minerals as their sizes are dominated by their relatively large surface area, and hence are recorded as larger grains. Note that according to Stoke's law of settling, it is the particle volume and density that dictates its settling velocity and dynamical behaviour within a current. McCave *et al.* (2006) compare results from sedigraph and laser sizer data, measured on the same sediment samples from the Gardar Drift. This paper shows large discrepancies between their grain size distributions that likely resulted from machine artefact in the laser sizer data. For further discussions see McCave and Syvitiski (1991), Bianchi *et al.* (1999), McCave *et al.* (2006), McCave and Hall (2006).

3.6. Studies of planktonic foraminifera carbon and oxygen stable isotope ratios, planktonic foraminifera (>150 µm counts) and coarse sediment fraction (>150 µm) counts and analyses

3.6.1. Sampling and preparation

The planktonic foraminiferal stable carbon and oxygen isotope measurements and the coarse fraction (>150 µm) analyses were carried out on sediment subsamples that were removed at continuous 0.5 cm intervals from a 2 x 2 cm square-cross-section u-channel sample. The u-channel sediment spanned the upper two core sections of core TTR-451. This provided an interval of study that was around 120 cm in length down-core.

The u-channel subsamples were freeze-dried, weighed and wet-sieved over a 63 μm sieved and using de-ionised, reverse osmosis (RO) water. The sediment fraction finer than 63 μm was retained. RO water was used as opposed to tap water to ensure that the foraminiferal tests were not contaminated with modern carbonate. Care was taken to minimise the exposure of the sediment samples to the RO water as it is inherently slightly acidic (pH of around 5-6). Exposure of foraminiferal specimens to acidic solutions can cause dissolution of the carbonate tests, resulting in erroneous stable oxygen and carbon isotope ratios.

The retained sediment coarser than 63 μm was inspected using a binocular microscope to ensure that the silt and clay fraction had been successfully removed and was oven dried overnight at 50ºC. The dried sediment samples were dry sieved through 125 and 150 μm meshes and weighed. Using a sediment splitter, the sediment coarser than 125 μm was divided into equal aliquots.

3.6.2. Ice rafted debris counts and planktonic foraminiferal abundances

Contained within marine sediment cores, lithic grains with diameters larger than 150 μm are too large to be carried by bottom currents. Instead, they are transported to core sites within ice-bergs and termed 'ice rafted debris' (IRD) (Bond *et al.*, 1992). Counts of IRD have been used in palaeoceanographic studies as an indicator of ice-berg discharge events and high abundances have been associated with Heinrich events (e.g., Heinrich, 1988; Bond *et al.*, 1992; 1993; 1997; 1999; Broecker *et al.*, 1992; Grousset *et al.*, 1993; 2001; Hilliare-Marcel *et al.*, 1994; Darby *et* al., 2002; Elliot *et al.*, 2002; Hemming and Hajdas, 2003; Hemming, 2004; Peck *et al.*, 2006; 2007 amongst others). For more detailed definition of Heinrich events see chapter 2.3.

Individual grain types have given indication of the source region of the ice-berg discharge. North Atlantic marine sediment core IRD provenance studies (e.g., Bond and Lotti, 1995; Bond *et al*., 1999; Elliot *et al*., 1998; Grousset *et al*., 2000; 2001) have attributed the origin of ice-bergs carrying hematite stained grains of quartz and feldspar to the Greenland and British ice sheets, detrital carbonate to the Laurentide and Fennoscandian ice-sheets, and shards of volcanic glass to the vicinity around Iceland, erupted onto the surface of sea-ice. A previous study by Knutz *et al*. (2001) suggested that for a marine core recovered from the Barra Fan, igneous and detrital carbonate grains were likely ice-rafted from the British ice-sheet. These previous studies have indicated a time-transgressive pulsing, or phasing, of the circum-North Atlantic ice-sheets over the duration of and just prior to the key IRD events of the last glacial cycle; Heinrich events.

Core TTR-451 is located beneath the pathway of the East Greenland Current, which today is a key carrier of both freshwater and icebergs out of the Arctic. Therefore, it was assumed that sediments from TTR-451 likely contained a past record of IRD deposited from ice-bergs carried out of the Arctic, Nordic Seas and off the East Greenland margin.

Often associated with sediment horizons rich in IRD are reduced abundances of planktonic foraminiferal tests (e.g., Grousset *et al*., 2001; Knutz *et al*., 2001; Hemming and Hajdas, 2003; Hemming, 2004). Such reduced numbers of planktonic foraminifera may have resulted from dilution by the increased IRD concentration, or from the significantly lowered sea surface temperatures, which occurred concurrently with these IRD events (e.g., Hemming, 2004; de Vernal and Hilliare-Marcel, 2000; Snowball and Moros, 2003; McManus *et al*., 2004; Peck *et al*., 2008). Therefore, numbers of planktonic foraminiferal tests that were larger than 150 μm were also counted from TTR-451 sediments, in order to provide a palaeoclimate indicator, with careful consideration of sedimentation rates. Planktonic foraminiferal species abundances (also a palaeoclimate indicator) were additionally counted from these same samples, but with sizes greater than 125 μm. Counts were performed using a binocular microscope and abundances of planktonic foraminiferal species were field counted.

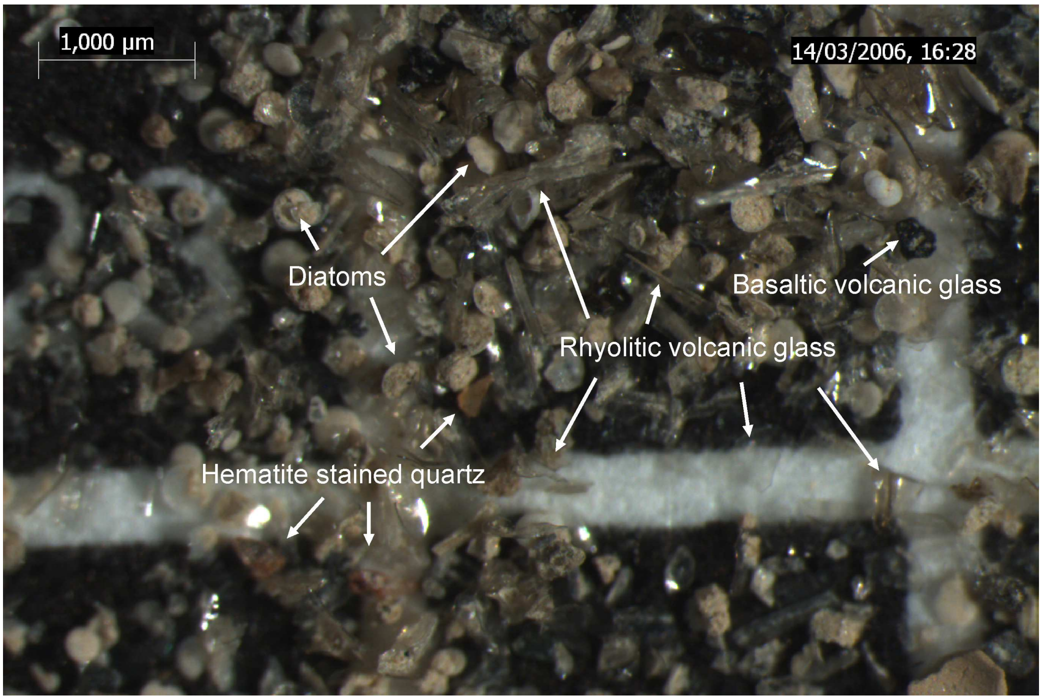

Figure 3.18. The >150 µm size fraction sample from core TTR-451, showing some of the key lithic grains. Shown here are hematite stained grains of quartz, rhyolitic glass and basaltic glass. For this portion of the core, the sediments were rich in diatoms, which are also highlighted.

The sediment fraction containing grains with diameters larger than 150 µm from the aliquot allocated for the IRD and foraminiferal abundance counts (see section 3.2 for further details) was transferred into a counting slide and weighed. Lithic and total planktonic foraminiferal abundance counts were carried out concurrently and in a systematic manor using a 64 square slide and a binocular microscope. On average, ~500 grains were counted per sample, and the grain types distinguished. Figure 3.18 shows the key lithic grains counted. The total mass of the aliquot of sediment counted was used to quantify the results in terms of numbers of grains or foraminifera tests per gram of dried sediment. A selection of samples was recounted in order to quantify the counting error, and counts of different aliquots of sediment from the same sample were used to test the reproducibility of the results. The results of the above showed a less than 4 % discrepancy between the counts. Both lithic and foraminiferal counts were converted into flux (numbers cm^{-2} yr^{-1}) using the age model and mass accumulation rate of the core.

The identification of grains was aided by analyses of thin sections, SEM-EDS of selected grains, which were placed onto an SEM stub, and mineralogical investigation using X-ray diffraction (XRD) techniques. These investigations were performed using toothpick samples that were collected for pilot study. NB: The latter technique was also applied to ~200 μg of dried and ground bulk toothpick samples that were also used for bulk sediment stable carbon and oxygen isotope studies. XRD measurements were made using a *Phillips ExPert Pro X-ray Diffractometer* running on a cobalt tube, and with an illuminated area of 17mm. Step sizes of 0.02 degrees were used, with 2 theta per step and 1 sec per step. Mineralogical identification was done using *Phillips* software and the JCPDS database.

3.6.3. Carbon and oxygen stable isotope ratios

The geochemistry of planktonic foraminiferal calcite tests is intrinsically linked to the carbonate equilibrium of ambient seawater in which it was formed. The analysis of stable oxygen ($\delta^{18}O$) and stable carbon ($\delta^{13}C$) isotopic ratios of foraminiferal tests has been widely used in palaeoceanographic reconstructions of ocean temperatures, salinity, primary productivity, carbonate ion concentration and carbon dioxide concentrations (e.g., Emiliani, 1955; Shackleton and Opdyke, 1973; Duplessy *et al.*, 1984; Imbrie *et al.*, 1984; Zachos *et al.*, 1994; 2001; 2008; Sarnthein *et al.*, 1995; Weinelt *et al.*, 1996; 2003; Shackleton *et al.*, 2000; de Vernal *et al.*, 2002; Raymo *et al.*, 2004; Hilliare-Marcel and de Vernal, 2008).

A more complete hydrographic reconstruction is achieved by combining stable isotope records from different depth dwelling foraminiferal species (e.g., Boyle and Keigwin, 1987; Duplessy *et al.*, 1988; Keigwin *et al.*, 1991; Dokken and Jansen, 1999; Shackleton *et al.*, 2000; Hilliare-Marcel and Bilodeau, 2000; Hagen and Hald, 2002; Peck *et al.*, 2008). Stable oxygen isotope records generated from foraminiferal tests are also used as a global stratigraphic tool, with Pleistocene fluctuations shown to occur on regular glacial-interglacial time-scales as a result of global ice-volume changes (e.g., Aharon, 1983; Labeyrie *et al*., 1987; Martinson *et al*., 1987; Shackleton 1987; Fairbanks, 1989; Raymo *et al*., 2004). Detailed reviews on foraminiferal calcite stable isotope geochemistry are given in Rohling and Cooke (1999) and Bijma *et al*. (2002).

The $\delta^{18}O$ and $\delta^{13}C$ notation stands for the ratio of ^{18}O to ^{16}O, and ^{13}C to ^{12}C, respectively, relative to an external standard with known composition (Equation 3.3, where R represents the ratio of $^{18}O/^{16}O$ or $^{13}C/^{12}C$).

$$\delta_{sample} = [(R_{sample} - R_{standard})/R_{standard}] \times 1000 \qquad \text{(Equation 3.3)}$$

For carbonates this reference standard is Pee Dee Belemite (PDB) which, by definition, has $\delta^{18}O = 0$ and $\delta^{13}C = 0$ (Epstein *et al*., 1953). Today, measurements are commonly made relative to the laboratory standards NBS-18 and NBS-19, provided by the National Institute of Technology (NIST) and the Vienna based International Atmomic Energy Agency (IAEA). The NBS-18 and NBS-19 laboratory standards are calibrated against Vienna Pee Dee Belemite (VDPB), and for the former, Vienna Standard Mean Ocean Water (VSMOW) (Coplen, 1988; 1994; NIST, 1992).

There are two key factors that determine the stable oxygen isotope geochemistry of planktonic foraminiferal carbonate, the temperature at which the carbonate was formed and the salinity of the ambient seawater. The reaction for the precipitation of carbonate is: $Ca^{2+} + 2HCO_3^- \Longleftrightarrow CaCO_3 + CO_2 + H_2O$, and occurs under equilibrium fractionation. Equilibrium fractionation occurs as a function of temperature and the net effect equates around a 0.2 to 0.25 ‰ $\delta^{18}O$ decrease for every 1 °C increase (e.g., O'Neil *et al*., 1969; Shackleton, 1974; Kim and O'Neil, 1997), allowing $\delta^{18}O$ ratios to be used as a useful 'palaeothermometer' (e.g., Urey, 1947; McCrea, 1950; Shackleton, 1974). However, since temperature decreases with depth, vertical migration of foraminifera at different ontogenic stages will influence the $\delta^{18}O$ ratio of the foraminiferal carbonate (e.g., Emiliani, 1955; Berger, 1971; Bemis *et al*., 1998). Some species also grow a secondary calcite layer at depth, which has increased $\delta^{18}O$ ratios (Simstich *et al*., 2003; Hamilton *et al*., 2008).

Salinity and the $\delta^{18}O$ of seawater are directly linked through the equilibrium fractionation processes with evaporation and precipitation (Craig and Gordon, 1965). During evaporation at the air-sea interface the lighter (^{16}O) isotope with a higher vapour pressure become preferentially enriched in the vapour phase. With precipitation, the process works in the opposite sense. Humidity and 'roughness' at the air-sea interface may influence the isotopic exchange during evaporation (review in Rohling and Cooke, 1999). The equilibrium fractionation process means that surface seawaters with high evaporation rates have increased salinity and enriched $\delta^{18}O$, whereas precipitation and riverine runoff that reduce surface water salinity have depleted $\delta^{18}O$ values (e.g., Craig and Gordon, 1965).

Due to the repetition of this distillation process, higher latitude regions receive precipitation/snow with much depleted $\delta^{18}O$ values and hence, the mean value of modern Arctic runoff is around -21 ‰ (Rohling and Bigg, 1998; Bauch *et al*., 1995; 2005). Meltwater runoff from the Greenland ice sheet has a composition of –20 ‰ or lighter (Reeh *et al*., 2002). The net effect of equilibrium fractionation is the preferential sequestration of the lighter (^{16}O) isotope in ice-sheets resulting in long-term storage. Comparison of foraminiferal calcite $\delta^{18}O$ records with sea-level records reveals a relationship between mean ocean $\delta^{18}O$ enrichment and sea level lowering (ice-sheet 'lock-up') of 0.012 +/-0.001 ‰ m^{-1} (Shackleton, 1987; Fairbanks, 1989). Duplessy *et al*. (2002) suggests an ice volume component of 1.05 ‰.

Sea-ice formation results in very characteristic seawater $\delta^{18}O$ signatures (e.g., Tan and Strain, 1980; Dokken and Jansen, 1999; Hilliare-Marcel and de Vernal, 2008). When low salinity waters freeze to produce sea-ice, isotopically light brines are formed that sink and mix with subsurface waters within the halocline. An additional $\delta^{18}O$ depletion of the residual brine results from an enrichment of sea ice of around 3 ‰ under equilibrium conditions (O'Neil *et al*., 1969). When sea-ice melts it results in the addition of isotopically heavy, but low salinity surface waters.

The endmember $\delta^{18}O$ composition of seawater results from advection and mixing of watermasses with their different $\delta^{18}O$ signatures that have resulted from the above described varying processes in the hydrological cycle. Rohling and Cooke (1999) define the $\delta^{18}O$ endmember as the volumetrically weighted average $\delta^{18}O$ composition of its components, and are described by equation 3.4.

$$\delta^{18}O_{endmember} = (A\delta^{18}O_A + B\delta^{18}O_B + C\delta^{18}O_c)/(A+B+C) \qquad \text{(Equation 3.4)}$$

where A, B and C are the volumes of the components and $A\delta^{18}O_A$, $B\delta^{18}O_B$ and $C\delta^{18}O_c$ are their respective isotopic compositions.

Carbon dioxide in seawater is primarily contained within bicarbonate ions (HCO_3^-), which weakly dissociates to form CO_3^{--}. The formation of foraminiferal tests are affected by the inorganic carbon pool within the oceans (e.g., Swart, 1983; Wolf-Gladrow *et al*., 1999; for review see Rohling and Cooke, 1999). The $\delta^{13}C$ composition of foraminiferal tests is primarily controlled by photosynthesis and export productivity. Photosynthesis occurs in the euphotic zone and strongly discriminates against ^{13}C. This, combined with the remineralisation of organic matter, cause ambient near surface waters to become enriched in $\delta^{13}C$. Remineralisation of organic matter at depth causes a transfer of ^{12}C to the deep ocean and, hence, increased export productivity results in increased $\delta^{13}C$ gradients between the surface and the deep ocean. Consequently, the $\delta^{13}C$ composition of foraminiferal tests in marine sediments have been used as a proxy for nutrient concentration and, hence, also deep water ventilation or 'age' (e.g., Broecker, 1982; Broecker and Peng, 1982; Boyle and Keigwin, 1987; Sarnthein *et al*., 1994; Keigwin and Boyle, 2008).

Weathering of sedimentary carbonates, organic carbon burial, and changes in atmospheric CO_2 concentration, as well as $\delta^{13}C$ composition, also affect the carbonate ion chemistry of the oceans and can be recorded in foraminiferal carbonate contained within marine sediment (e.g., Garlick, 1974; for review see Rohling and Cooke, 1999). However, these changes typically occur over geological time-scales that are outside the scope of this study.

Deviations from equilibrium in the formation of foraminiferal carbonate may result from the incorporation of respiratory CO_2 (e.g., Grossman, 1987; Wefer and Berger, 1991), which is shown to vary during the foraminiferal life cycle due to decreased metabolic rates with ontogenic stage (e.g., Kroon and Darling, 1995). Vertical migration during ontogeny and, hence, dwelling in water masses with different $\delta^{18}O$ and $\delta^{13}C$ compositions and temperature during the foraminiferal life cycle, will also result in deviations from equilibrium. Other 'vital' effects include; symbiotic photosynthesis (e.g., Spero and Lea, 1993), changes with growth and growth rate (e.g., Spero *et al.*, 1991; Billups and Spero, 1995), carbonate ion concentration (e.g., Spero *et al.*, 1997), and the production of gametogenic calcite (e.g., Duplessy *et al.*, 1981; Spero and Lea, 1993; Bemis *et al.*, 1998).

Ambient water pH has an effect on foraminiferal test formation, as well as differential dissolution post death (e.g., Broecker and Peng, 1982; Dittert *et al.*, 1999; Schiebel, 2002; Schiebel *et al.*, 2007). Ontogenic and vital effects on the stable carbon and oxygen isotopic geochemistry of the foraminiferal calcite may be minimised by study of specimens within a narrow size range and of one species. The effect of differential dissolution of planktonic foraminiferal tests may also be reduced by the above, but can also be assessed by planktonic foraminiferal test appearance, ratios of benthic versus planktonic specimens, and average test weights (e.g., Schiebel *et al.*, 2007). For a comprehensive review and further discussions of the stable isotope geochemistry of foraminiferal calcite tests see Rohling and Cooke (1999), Bijma *et al.* (2002) and Schiebel and Hemleben (2005).

Carbon and oxygen stable isotope measurements were performed on bulk sediment and planktonic foraminiferal carbonate samples, using a Europa Geo-2020 mass spectrometer. Calibration of laboratory standards shows that the reproducibility of the Geo-2020 mass spectrometer is +/-0.027 ‰ for $\delta^{13}C$ and

+/-0.053 for $\delta^{18}O$ (M. Bolshaw, *pers. comm.*). The Europa Geo-2020 mass spectrometer has a Carbonate Acid Preparation System (CAPS) individual acid dosing, or 'drip method' preparation system where samples were reacted with phosphoric acid at 70 °C to produce CO_2 gas. The CO_2 gas was analysed relative to a reference gas and results expressed in terms of mass ratios of 45/44 (δ45) or (46/44) δ46.

Samples were run in batches of 19, with 3 laboratory standards ('SC-1', which is calibrated to the international NBS-19 standard) placed at the front and 2 laboratory standards at the back of the run. Using the laboratory standard values, measurements were drift corrected and the sample values were linearly shifted to give per mille ($\delta^{18}O$ and $\delta^{13}C$) values relative to VPDB (Coplen, 1988; 1994) (Equation 3.3). Further corrections must be applied when converting the mass ratios of δ45 and δ46 onto the VDPB ‰ scale (Rohling and Cooke, 1999). Firstly, for the mass ratio of $^{17}O/^{18}O$ (Craig, 1957), and secondly, for the fractionation effect of the temperature at which the reaction of the carbonate with the phosphoric acid took place (Swart *et al.*, 1991).

The size of sample analysed dictates whether the sample CO_2 gas is frozen in the cold finger or expanded into the bellows (Figure 3.19). Changing between these methods during batch runs would likely produce a shift in values due to variable amounts of fractionation. In order to avoid the above scenario, similar sample sizes were maintained. Additionally, re-analyses samples allowed for the reproducibility of the measurements to be tested for individual sample batches.

The $\delta^{18}O$ and $\delta^{13}C$ ratios were measured from toothpick size, bulk sediment samples collected at 5 cm intervals from the split core sediment surface of cores TTR-450 and TTR-451. Analyses were done in order to provide an initial stratigraphy and to identify intervals of core for further study. Samples were oven dried overnight at 50°C and lightly ground so that particles sizes were close to fine sand. Approximately 500 μg of sample was analysed and the sample size was varied according to sediment colour, so that samples contained similar quantities of carbonate.

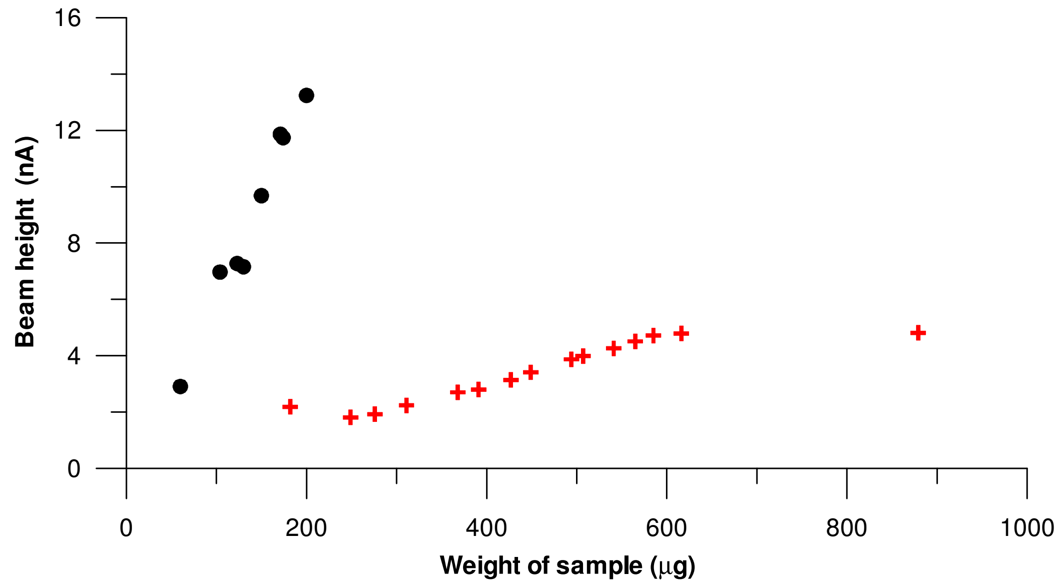

Figure 3.19. Plot of carbonate (SC-1 laboratory standard) sample weight versus the reference gas volume (beam height), measured in nAmps. Measurements were made using a Europa Geo-2020 mass spectrometer. Black dots indicate sample that were frozen in the cold finger and red crosses show samples that were expanded into the bellows. Data is courtesy of M. Bolshaw.

Records of planktonic foraminiferal $\delta^{18}O$ and $\delta^{13}C$ were acquired from the allocated aliquot of sediment subsample of the u-channel sediment collected from the upper ~120 cm of core TTR-451 (see section 3.6.1). Records were generated in order to give palaeoclimate reconstruction. Analyses were performed using monospecific samples of the planktonic foraminifera *Neogloboquadrina pachyderma* (left coiling); a sub-surface polar species that strongly dominated the sediment samples. Using RO water, approximately 30 individuals were picked from each sample, with sizes ranging between 225 and 275 μm. The sizes were estimated using a calibrated graticule under a binocular microscope. The $\delta^{18}O$ record was corrected for ice volume changes using the sea level relationship of Duplessy *et al*. (2002).

The second most abundant species was the planktonic foraminifera *Globigerina bulloides*. For samples that contained enough specimens for analysis, $\delta^{18}O$ and $\delta^{13}C$ data were additionally acquired from *G. bulloides* in order to compare with those obtained from *N. pachyderma* (left coiling). *G. bulloides* was picked within a size range of 250-300 µm, and due to variable abundances, the total number of specimens per sample ranged from 8 to 22. All monospecific samples were oven dried overnight at 50°C, prior to analysis.

3.7. Accelerated Mass Spectrometric (AMS) ^{14}C datings

In total, seven discrete sediment samples provided AMS^{14}C datings from core TTR-451 (Table 3.1). Samples were wet sieved through a 63 µm seive using RO water, and the coarse fraction retained and oven dried overnight at 50 °C. The most abundant planktonic foraminiferal polar species *N. pachyderma* (left coiling). were picked using RO water, giving carbonate weights in excess of 8 mg for analysis. The picked foraminiferal tests were oven dried overnight at 50 °C and were dated using accelerated mass spectrometry at the department of *Leibniz Labor für Altersbestimmung und Isotopenforschung, Kiel.*

KIA- sample number	Core	Depth (cm)	Number of specimens of *N. pachyderma* (lc).	Weight of carbonate sample (mg)
KIA-26998	TTR-451	12.00	1457	8.389
KIA-27856	TTR-451	40.00	2252	8.070
KIA-25853	TTR-451	57.50	1125	8.586
KIA-27857	TTR-451	76.00	1995	9.910
KIA-27858	TTR-451	83.50	1300	8.133
KIA-27859	TTR-451	94.25	1204	10.140
KIA-25854	TTR-451	102.25	1000	10.793

Table 3.1. AMS^{14}C samples from cores TTR-450 and TTR-451.

CHAPTER 4

4. RESULTS

This chapter presents the analytical results obtained from marine sediment cores TTR-450 and TTR-451. First, a brief description is given of the core sediments and the results obtained from ITRAX-X-Ray Fluorescence (XRF) core scanning, which are presented along with the bulk sediment $\delta^{13}C$ and $\delta^{18}O$. These analyses were conducted to provide an initial, low resolution stratigraphy in order to give better indication of where to focus further studies. The reproducibility of the ITRAX core scanning data is tested (sub-chapter 4.1). Next follows the palaeomagnetic and environmental magnetic data, and results are compared with the key elemental data from the ITRAX core scanning (subchapter 4.2).

This chapter then focuses upon the upper two core sections of TTR-451, which together span a core depth of ~120 cm. An environmental magnetic dataset (κ_{ARM}/κ), a record of magnetic grain sizes, is compared with a record of mean sortable silt grain sizes. The relationship between magnetic grain sizes and κ_{ARM}/κ values are investigated further with magnetic measurements and a scanning electron microscopy (SEM) image analysis study (sub-chapter 4.3). Next, results are presented for the high-resolution records of lithic counts, planktonic foraminiferal $\delta^{18}O$, and total planktonic foraminiferal abundance counts (sub-chapter 4.4).

In sub-chapter 4.5, Accelerated Mass Spectrometric (AMS)^{14}C datings are presented along with their calibrated ages, and the age model development for the key interval of study, which spans the upper ~120 cm of core TTR-451. Estimates of ΔR (^{14}C marine reservoir age) values for the Eirik Drift region, for time period of the Heinrich event 1 and the last deglaciation, are also presented.

4.1. Core descriptions, ITRAX-XRF results, and bulk sediment $\delta^{18}O$.

4.1.1. Description of core TTR-450

Core TTR-450 is a 14.7 cm diameter gravity core with a total length of 569 cm. The core was divided into ten sections, with each section around 60 cm in length and one short (~30 cm) bottom section. For location of TTR-450 see chapter 3 and Figure 3.1. The core was split and logged onboard *RV Professor Logachev*, and the core log is published in the post-cruise report (Kenyon *et al.*, 2004). The core log that was compiled onboard *RV Professor Logachev* likely gives the most accurate description of core TTR-450 prior to oxidation of the sediment surface, core top collapse, water loss and shrinkage.

In general, the top ~7 cm of core TTR-450 is a winnowed foraminifera-rich sand, that includes some <0.5 cm lithic fragments, small gastropods and bivalves. The base of the sand is irregular and is gradational over a few centimetres into a foraminifera rich, silty clay unit. The silty clay is continuous over ~155 cm of the core, and contains mm-size lithic fragments which are scattered throughout, and also form localised lithic-rich horizons. Some bioturbation, mainly *Planolites* burrows, is evident on the scraped and fresh sediment surface. Centimetre-size lithic clasts are abundant between 115 and 125 cm depth.

Throughout the entire silty clay interval (7 - 155 cm depth), the sediment colour varies between dark and light brownish grey, with marked sharp transitions at around 14 cm and 90 cm depth. As the grain sizes appear to remain constant between 7 cm and 155 cm, this entire portion of core TTR-450 is classified as one sedimentary interval, in agreement with Kenyon *et al*. (2004).

The sediments between 155 and 300 cm are characterised by slightly darker coloured grey silty clay, with higher clay content than the previous interval. Lithic fragments and foraminifera abundances are similar to those in the upper interval, but there are horizons with localised increased concentrations. Between 300 and 569 cm the sediments are classified as silty clay, but with marginally higher silt content. This interval has a gradational upper boundary, associated only with a change in grain size and no distinct sediment colour change. Lithic fragments (>1 cm) are observed throughout this portion of the core. The core logs published in Kenyon *et al*. (2004) describe greenish grey clay clasts between 190 and 360 cm, and 440 and 510 cm depth, as well as subparallel layering of greenish clay between 500 and 510 cm depth. Because of oxidation of the sediments since opening these cores, these details are no longer visible.

4.1.2. Bulk sediment C and O stable isotope ratios for TTR-450

Within this section the bulk $\delta^{18}O$ and $\delta^{13}C$ records for core TTR-450 are described. The methods for analyses are provided in chapter 3.6. Note that the terms ‘enriched’ and ‘depleted’, which are used here to describe trends, refer to the ^{13}C isotope with respect to the ^{12}C isotope and the ^{18}O isotope with respect to the ^{16}O isotope. More enriched values are more positive (and greater $^{13}C/^{12}C$ or $^{18}O/^{16}O$ isotopic signatures can be described as ‘heavier’), and vice-versa.

The bulk sediment stable oxygen isotope ratios ($\delta^{18}O$) for core TTR-450 ranges between –0.66 and 2.33 ‰ (Figure 4.1g; note the inverted axis), with a mean of 0.59 ‰. Notable $\delta^{18}O$ depletions occur between 29 and 61 cm depth, and 90 and 127 cm depth, with minimum values of –0.66 and -0.39 ‰ respectively. Both depletions develop gradually and terminate sharply, returning to more enriched values. It is noteworthy that the culmination of the $\delta^{18}O$ depletion at around 127 cm depth is coincident with the onset of the increased concentrations of lithic fragments between 115 and 125 cm depth (Figure 4.1). A broad anomaly of relatively enriched $\delta^{18}O$ occurs between 250 and 350 cm depth, with a maximum value of 2.33 ‰. Another, less pronounced enrichment occurs between 487 and 543 cm depth, with a maximum of 1.13 ‰.

The bulk sediment stable carbon isotope ratios ($\delta^{13}C$) are more variable than the $\delta^{18}O$ record (Figure 4.1f), with a range between -3.32 and 2.74 ‰, and a mean of 0.76 ‰. A notable depletion forms a broad anomaly between core depths of 325 and 385 cm, with a minimum of around –2.2 ‰. The start of this $\delta^{13}C$ anomaly has no counterpart in the $\delta^{18}O$ record, however, the $\delta^{13}C$ record returns to heavier values when $\delta^{18}O$ shift to lighter values. Between 482 and 520 cm depth, a shift to light $\delta^{13}C$ values occurs some 20 cm above transition in the $\delta^{13}C$ record.

Further significant $\delta^{13}C$ depletions occur between depths of 20 and 61 cm, and 90 and 115 cm, with minima of –3.32 and –2.56 ‰, respectively. The $\delta^{13}C$ depletion, at 61 cm depth, is coincident with depleted $\delta^{18}O$ values, but terminates later at around 22 cm depth, and develops gradually over ~25 cm of the core, and terminates sharply when the $\delta^{18}O$ returns to heavier values.

4.1.3. ITRAX-XRF core scanning results for core TTR-450

The NOCS ITRAX-XRF core scanner provides a non-destructive means of acquiring a suite of high-resolution elemental profiles. Data were acquired at 500 µm intervals by passing the split core sections through an X-ray beam, and moved incrementally using a stepper motor (Croudace *et al.*, 2006). Described in this section are the key elemental data: potassium, calcium, titanium and iron. For further details on methods see sub-chapter 3.1.

Figure 4.1a shows the potassium intensity record. The element potassium is contained within the terrigenous sedimentary fraction (e.g., Yaroshevsky, 2006). Variations in the intensity of potassium counts therefore likely reflect changing

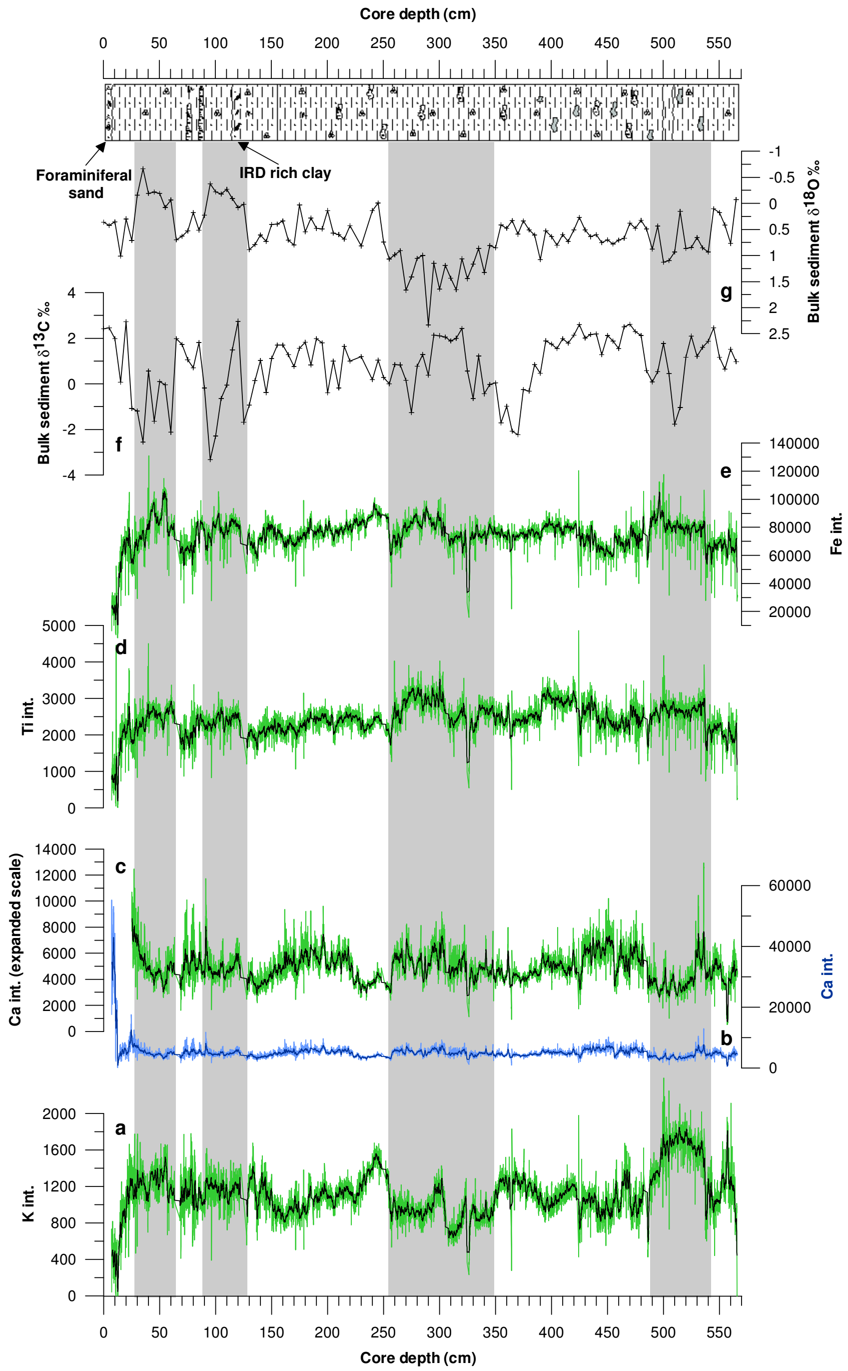

Figure 4.1. The key ITRAX-XRF core scanning results for the elements K, Ca, Ti and Fe (a-e), bulk sediment carbon ($\delta^{13}C$) and oxygen ($\delta^{18}O$) stable isotope ratios (f and g, respectively), and the core log (Kenyon *et al.*, 2004) for core TTR-450. In panels a to e the data is shown in green/light blue and a 17-point running average is shown in black/dark blue. In panel c, the top 12.5 cm of the Ca data are removed. Int. stands for intensity in counts per second (cps). NB: panel g is plotted on an inverted axis. Shaded zones demarcate intervals that have relatively depleted or enriched $\delta^{18}O$ values.

abundances of continental, acidic sediment sources (Yaroshevsky, 2006), which are predominantly contained within the silt and clay sediment fractions. Note, however, that an additional source of potassium is rhyoltitic volcanic glass, which has an acidic mineralogical composition. Because of the proximity of the core site to the Icelandic volcanic centre, results need to be carefully interpreted.

The counts of potassium for core TTR-450 are generally around 1000 cps, with high frequency variability between ~1400 and ~500 cps. A significant increase to nearly 2000 cps occurs between about 500 and 535 cm depth. This may reflect the increased greenish-clay content and sub-parallel layering that was described in the core logs (Kenyon *et al*., 2004). Between 250 and 350 cm depth, the counts of potassium are reduced to around 500 cps. The top ~20 cm of core TTR-450 shows relatively low concentrations of potassium; a reflection of the relatively higher foraminifera content of the sediment, and hence, low concentrations clay and silt.

The calcium intensity record is shown in Figure 4.1b and c, and variations likely represent changes in the abundance of biogenic and detrital carbonate. Calcium intensity values range between ~1000 and ~15000 cps. Lows in the calcium intensity record occur around depths of 30 and 72 cm, 94 and 153 cm, 222 and 260 cm, 303 and 421 cm, and 475 and 530 cm. The top ~12 cm of core TTR-450 shows exceptionally high counts of calcium (55217 cps), and likely reflects the predominantly foraminiferal composition.

In order to assess whether variations in calcium composition result from either relative changes in the clay and silt fraction, or alternatively are due to increased abundances of detrital carbonate, as opposed to a general increase in foraminiferal abundances, the calcium intensity is cross plotted versus the potassium intensity. The latter is an element that has an exclusively terrigenous source. Therefore, if relative changes in calcium do indeed result from variations in foraminiferal abundances and hence, sediment dilution, then the datasets should be expected to show a strong inverse correlation.

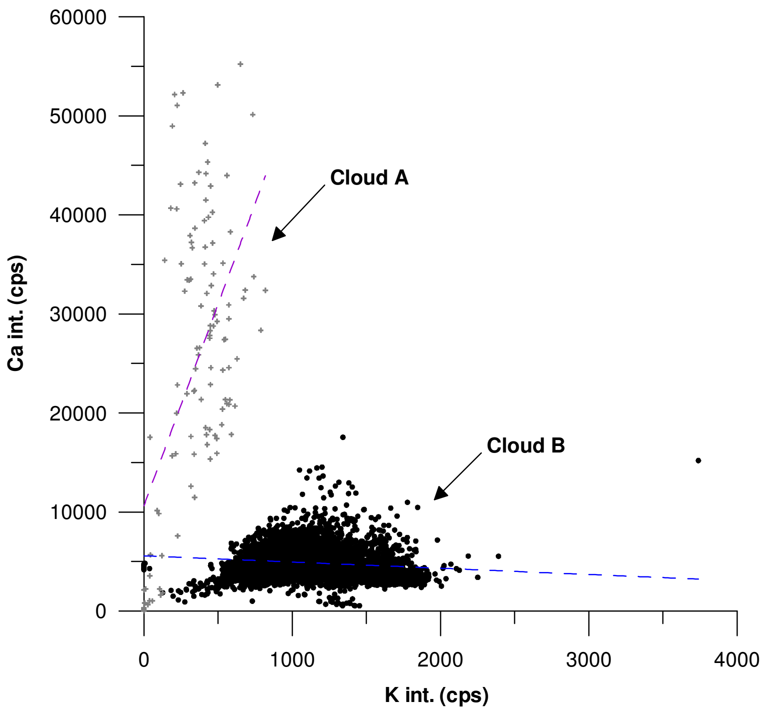

Figure 4.2. Cross-plot of the K and Ca intensities in counts per second (cps). The regression line for Cloud A (grey crosses) has an R^2 = 0.31 (Y = 40.65976324 * X + 10641.98922), n = 118, and for cloud B (black dots), an R^2 = 0.02 (Y = -0.6294532018 * X + 5584.319186), n = 10529.

In Figure 4.2, the potassium and calcium intensities are cross-plotted and this reveals two separate clouds of data. Cloud A represents the sandy top of the core; here high calcium counts correspond to low potassium counts. Cloud A shows potassium intensities change very little, despite a large range of calcium count values of between ~55000 and 500. There is a linear least squares regression line with a positive trend, but with an R^2 value that is very low (0.31), the statistical relationship is not significant (n = 118). The overall trend however, would suggest that as the numbers of foraminifera decrease there is no, or very little, relative increase in the clay and/or silt sediment fraction. Low porosities, large grain sizes and/or high surface roughness may have reduced the validity of the XRF data (Jansen *et al.*, 1998; Kido *et al.*, 2006; Tjallingii *et al.*, 2007).

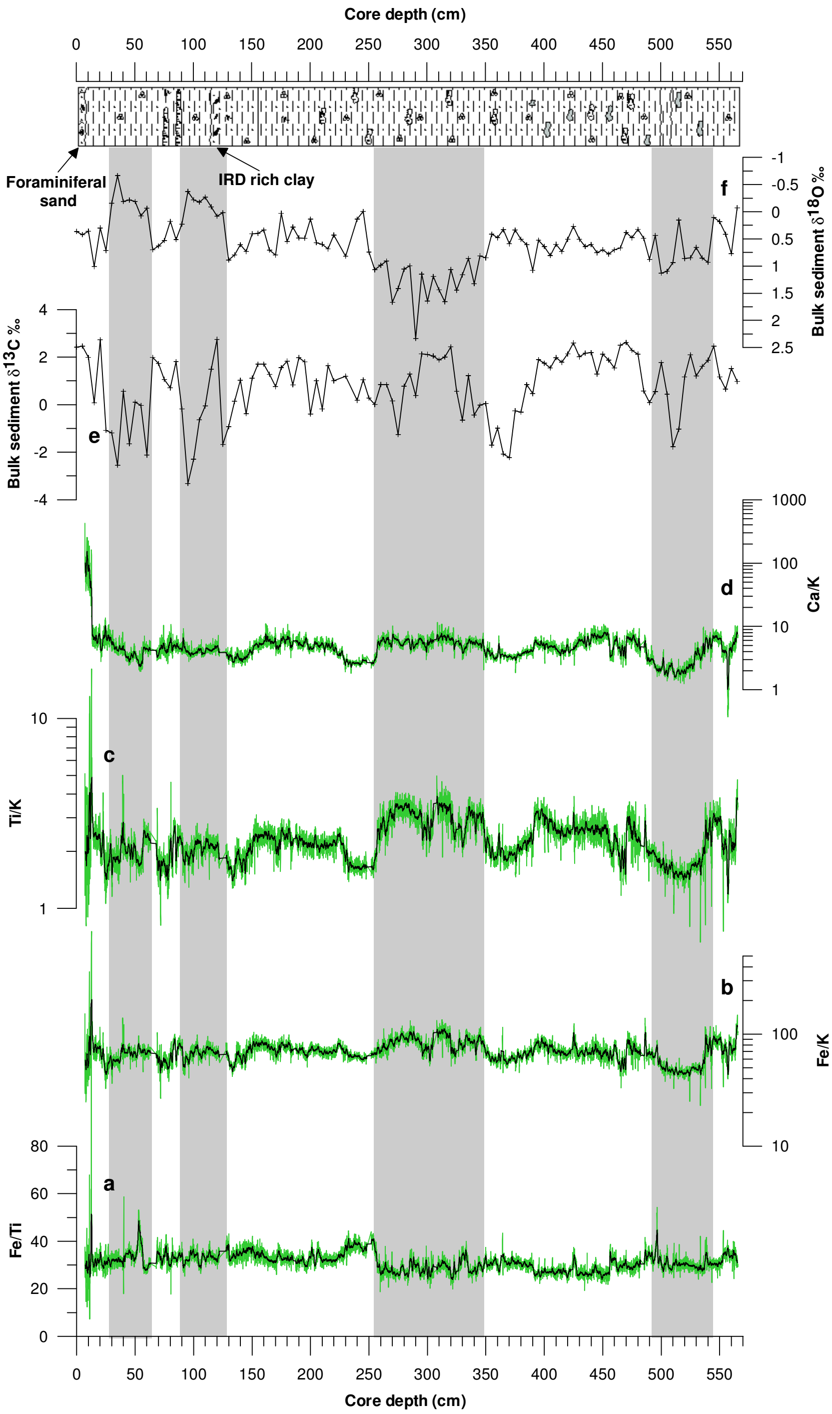

Figure 4.3. Ratios of Fe/Ti (a), Fe/K (b), Ti/K and Ca/K for core TTR-450. Shown in green are the data and the black line shows a 17-point running average through the data. Panels b-d are shown on a logarithmic scale. Panels e and f are the bulk sediment $\delta^{13}C$ and $\delta^{18}O$ records, respectively, for core TTR-450. In the top panel is the core log for TTR-450 (Kenyon *et al.*, 2004). Shaded boxes demarcate intervals that have relatively depleted or enriched $\delta^{18}O$ values.

Cloud B shows that, below counts of around 500 cps, low counts of calcium correspond to low counts of potassium. Above 500 cps, the overall trend indicates that lower calcium counts occur with higher potassium counts. However, the data is very scattered (r^2 of 0.02), and therefore no statistical relationship can be inferred.

Figure 4.3d shows the ITRAX-XRF calcium counts versus the potassium counts, in order to show trends independent of variations in the terrigenous component of the sediment. Here, the Ca/K ratio shows near identical fluctuations to the raw calcium counts (Figure 4.1b), with distinctive lows between 30 and 72 cm, 94 and 153 cm, 222 and 260 cm, 330 and 421 cm, and 475 and 530 cm depth. These reductions in the concentration of calcium relative to potassium coincide with depletions in the bulk sediment $\delta^{13}C$ record.

Figure 4.1d and e show the titanium and iron intensities for core TTR-450. In general, the records of iron and titanium intensities have similar patterns. Highs are observed in both records at around 40 to 55 cm and 85 to 120 cm depth. Peak values occur in the titanium record at around 270 to 305 cm core depth. Relatively smaller amplitude changes can be seen in the iron record for this portion of core. However, between 488 and 540 cm depth, a peak in iron counts is not reproduced in the titanium record. A prominent low is seen in the upper ~12 cm of core TTR-450 due to the predominantly foraminiferal sediment composition.

Variations in the titanium count intensity are interpreted here to reflect the abundance of (titano)magnetites contained within the terrigenous sediment fraction. At Eirik Drift, (titano)magnetites are likely sourced from the Nordic Basaltic Province (north of the Denmark Strait) (e.g., Kissel *et al.*, 1999a), which is located up-stream of the core TTR-450. A previous study has shown that sediments recovered from the northern North Atlantic have high abundances of the clay mineral smectite, which indicates a basaltic sediment origin (Kissel *et al.*, 1997).

If the iron and titanium datasets do reflect the same source and pathway, then a high degree of covariance between the datasets would be expected. Because (titano)magnetites are iron-rich, they are likely to be the primary source of the iron contained within the TTR-450 sediments. However, variable amounts of iron-monosulphides and pyrite may also be reflected in the iron count intensity record. In order to investigate whether iron and titanium have the same origin throughout the core records, the two datasets are cross-plotted (Figure 4.4). If they do indeed have the same source, a positive linear relationship and a high R^2 value would be expected.

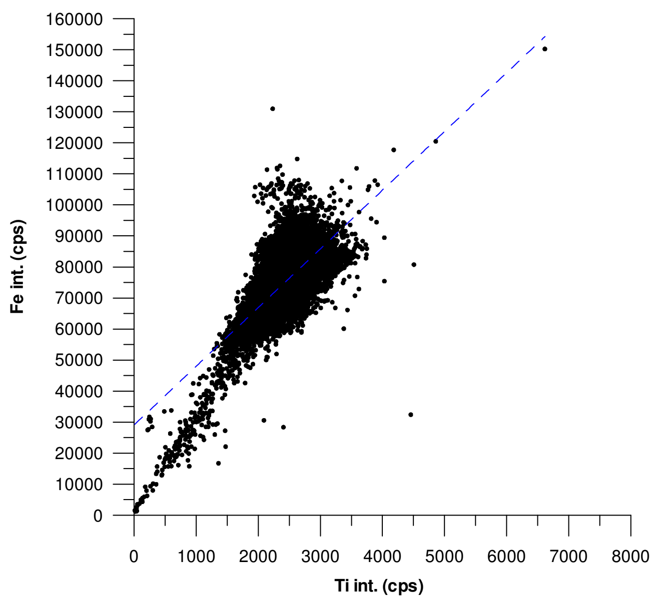

Figure 4.4. Cross-plot of the Ti and Fe intensities in counts per second (cps). A regression line is shown in blue and gives an R^2 value of 0.53 (Y = 18.9123627 * X + 29098.78647, n = 10646).

Figure 4.4 shows that the iron and titanium counts correlate with an R^2 value of 0.53 (n = 10646), however, toward the higher counts, the data is scattered, and it is clear that the regression line is effected by outliers. The scatter may in part be due to percentage error, or because of a variable iron source. Figure 4.3a, shows the ratio of the iron and titanium counts. A high Fe/Ti ratio is observed in the upper 12 cm of core TTR-450, most likely owing to iron-oxide coating on the foraminiferal tests. The remainder of the record shows very few large amplitude changes, suggesting a similar source for both titanium and iron. A shift to lower Fe/Ti values occurs at around 250 cm depth. Kido *et al*. (2006) and Tjallingii *et al*. (2007) demonstrate that interstitial water and the sediment surface water film can affect XRF core-scanning results by absorption of the emitted X-rays, with the lighter elements most affected. Therefore, the shift to lower Fe/Ti values maybe explained by a change in the water content or porosity of the sediment.

In order to assess whether iron and titanium ((titano)magnetites) share the same sediment pathway as potassium (continental, acidic source), the potassium, and the iron and titanium datasets were cross-plotted (Figure 4.5). Figure 4.5 reveals similar shaped clouds of scattered data for the potassium versus the iron and the potassium versus titanium plots, but with R^2 values of 0.28 and 0.13, respectively (n =10646). These low correlation coefficients indicate that grains rich in potassium were deposited at a different rate to the (titano)magnetite, suggesting different sediment pathways.

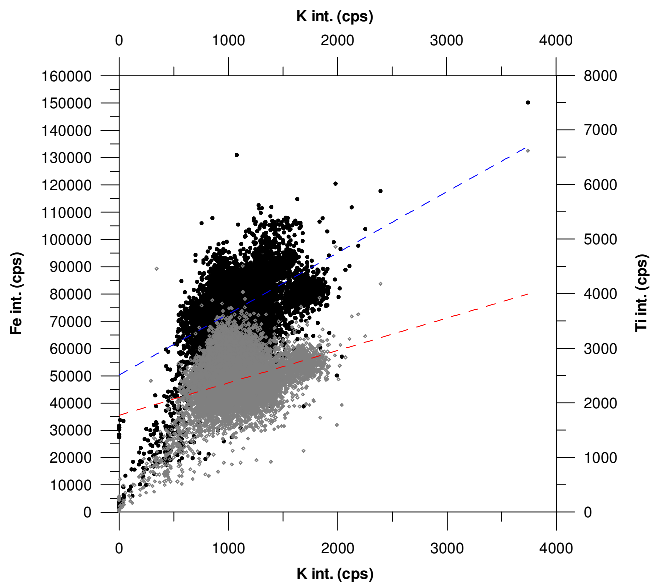

Figure 4.5. Cross-plots of the K intensity (cps) versus the Fe intensity (cps) (black dots), and the Ti intensity (cps) (grey open diamonds). Regression lines are shown in blue (K versus Fe) and red (K versus Ti) and reveal R^2 values of 0.28 (Y = 22.41926174 * X + 50301.3741) and 0.13 (Y = 0.5935070925 * X + 1774.420929) respectively (n = 10646).

The records of titanium and iron intensities are divided by the potassium intensity in order to show relative titanium and iron abundances with respect to the total clay fraction. The results are shown in figures 4.3b & c, respectively. The records show minor reductions that coincide approximately with reductions in the Ca/K record at around 120-153 cm, 230-260 cm and 480-540 cm depth. A low of shorter duration occurs between 350 and 370 cm. Minor reductions in the Ti/K and Fe/K records occur at around ~30 cm and ~80 cm core depths. A prominent high in both records is observed between 250 and 350 cm depth, coincident with the $\delta^{18}O$ enrichment event.

4.1.4. ITRAX - XRF core scanning reproducibility

The reproducibility of XRF measurements acquired using the NOCS ITRAX-XRF core scanner was tested using one section (section 4) of core TTR-450. The section was re-run using identical methods within 24 hours of the previous run. The relatively short time between runs meant that decay of the 3 kW molybdenum target tube would not have affected the data. A lengthy delay of weeks or months between data acquisition would likely result in lowered total counts for the later run.

Prior to the re-measurement of the core section, the *Mylar* film was left in place so that the surface sediment remained undisturbed, and the core section was placed back into the cold store (~6 °C) overnight in order to prevent desiccation. Unfortunately, this resulted in a need to reload and reposition the core section in the ITRAX core scanner. When acquiring data at such high resolution (500 µm) from split core section halves (as opposed to u-channel samples), good depth control and lateral core positioning is difficult to attain as the core top is selected manually, and the core section is positioned by hand. Therefore, prior to data analysis and run comparison, the core depths for the first dataset were linearly adjusted to match the second dataset using the key transitions in the calcium data, thereby ‘tuning’ the data from the two separate runs to a common depth scale.

Figure 4.6 shows the ITRAX-XRF core scanner data, which were acquired from

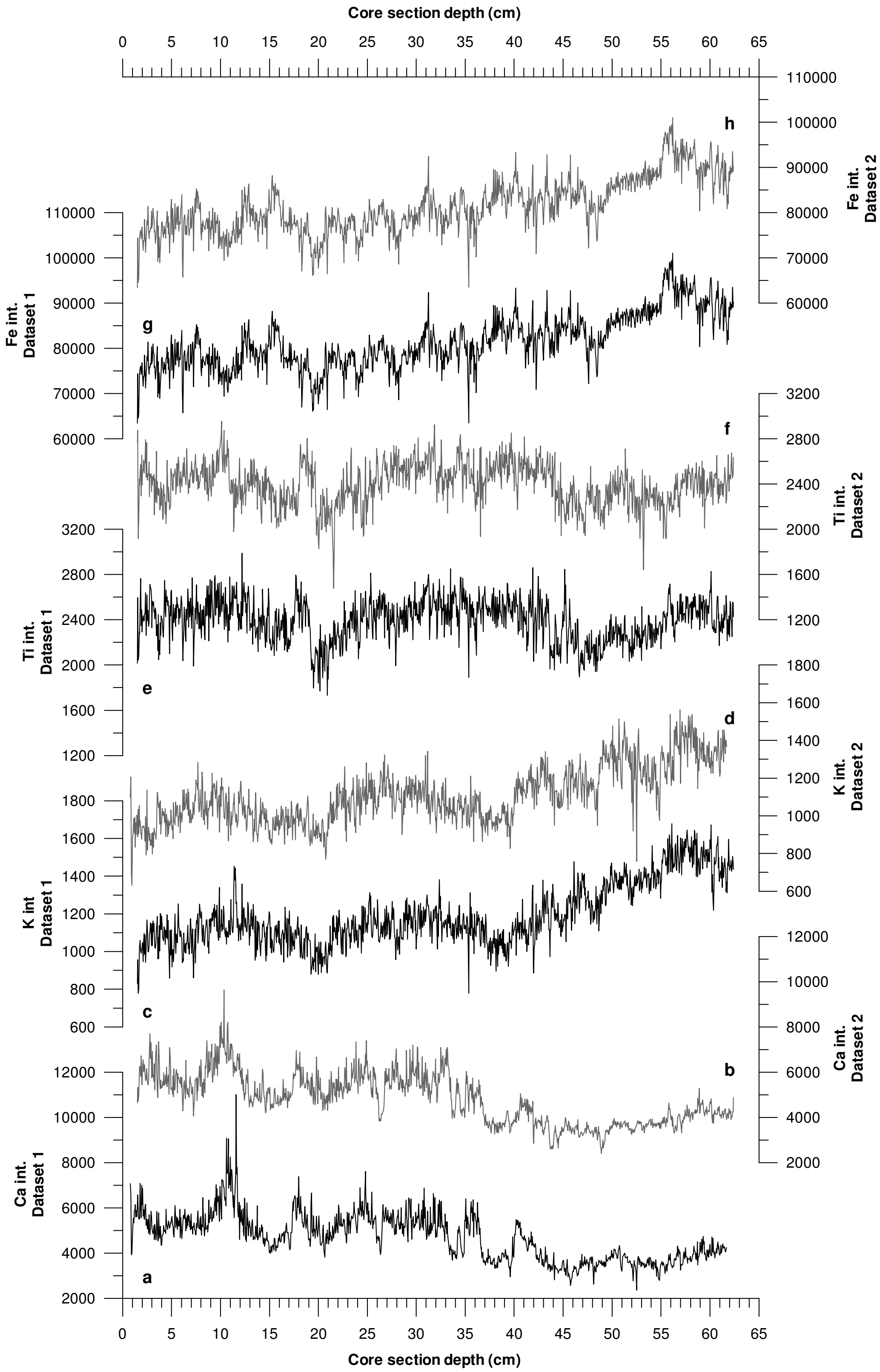

Figure 4.6. Comparison of Ca, K, Ti and Fe intensity data in counts per second (cps) from two datasets acquired in an identical manner from section 4 of core TTR-450. Shown in black is dataset 1 and in grey is dataset 2.

the two separate runs. In black are the data from the first run (dataset 1) and in grey are the data from the second run (dataset 2). Only the calcium, potassium, titanium and iron data are compared as these relatively heavy elements are considered to be the most reliably determined with this XRF method (e.g., Jansen *et al.*, 1998; Böning *et al.*, 2007). Overall, the two datasets for all four elements show good visual agreement.

The calcium count intensity data (in counts per second – cps) for the two datasets is shown in Figures 4.6a & b. Clearly, key transitions are present in both records, but, finer scale features are not. For example, compare section depths between ~25 and 35 cm. Within this portion of core there are two distinct and sharp lows, centred at around 26 and 34 cm section depth. These lows are virtually identical in both datasets in terms of the shape, duration and the abruptness of the anomalies. Between these two sharp reductions, two lows with approximately half the amplitude of change occurs in dataset 2, but these are not present in dataset 1. Conversely, a sharp peak in counts is observed at a section depth of around 12 cm in dataset 1, which is not present in dataset 2. The datasets for iron count intensity also show a similar degree of coherency (Figure 4.6g & h). This high general degree of structural similarity between the two records for the calcium and iron data is reflected in the relatively high R^2 values of 0.56 and 0.48, respectively (n = 1219) (Figures 4.7a & d).

In the upper 40 cm of the potassium dataset 1, two broad increases are closely reproduced in dataset 2. Despite visual differences between the potassium datasets in the lowermost ~25 cm of the core section, in particular the amplitude of the changes, these data also display a high R^2 value of 0.52 (n = 1219).

Histograms showing the frequency distribution of the two datasets for each element are plotted in figure 4.8, and a gaussian fit with similar mean and standard deviation as the data is shown in black to allow for comparison. The histograms show a bimodal distribution of the calcium data in both datasets (Figure 4.8a & b), and the calculated standard deviations are very similar with a value for dataset 1 of 1110.35, and for dataset 2, a value of 1017.08.

The two datasets for iron also show very similar distributions (Figures 4.8g & h), although these are, in contrast to the calcium datasets, distinctly uni-modal, with standard deviations of 6031.54 and 5932.34. The potassium frequency distribution for dataset 1 (Figures 4.8c) shows a more skewed distribution towards lower values than that for dataset 2 (Figure 4.8d). This skewness in the distribution of dataset 1 cannot be explained in terms of the visual differences in the lowermost ~25 cm of the core section, as the values obtained for this lower portion of core are relatively high. However, the standard deviation of the two datasets are again, very similar, with a value of 164.618 for dataset 1 and 150.027 for dataset 2.

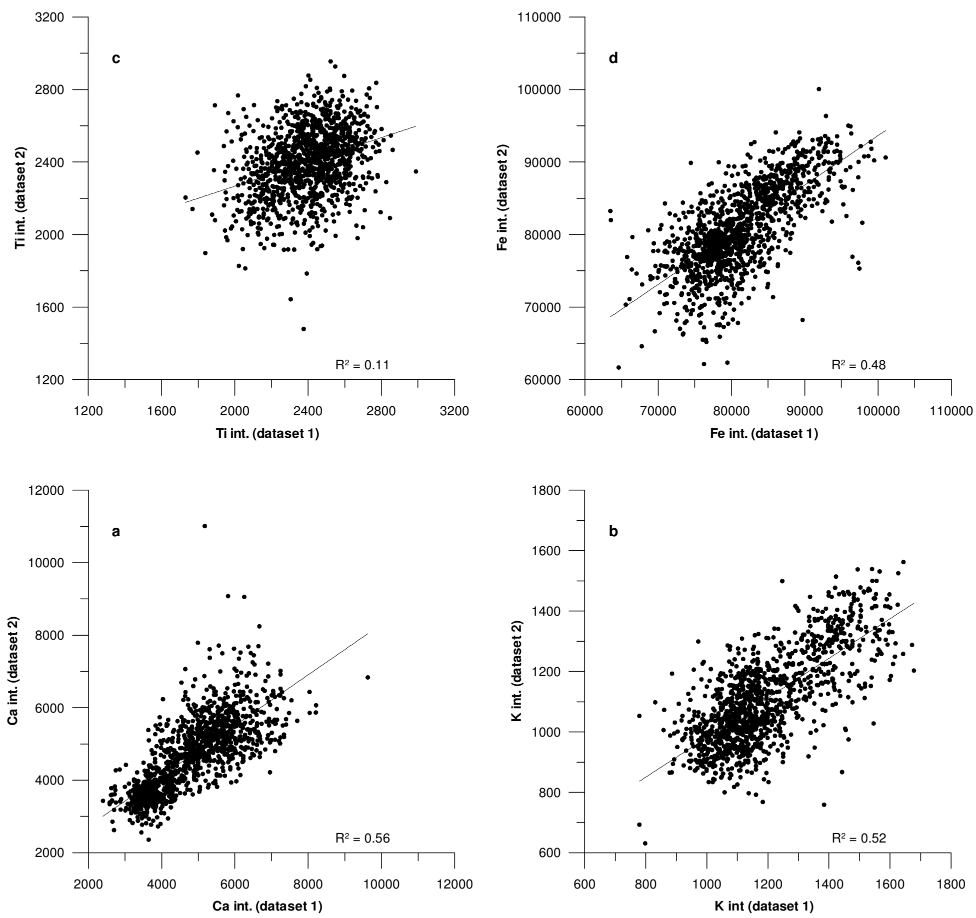

Figure 4.7. Cross-plots of the calcium (a), potassium (b), titanium (c) and iron (d) datasets 1 and 2 (re-run) for each element, which were acquired from section 4 of core TTR-450. The thin black line is the regression line for the datasets.

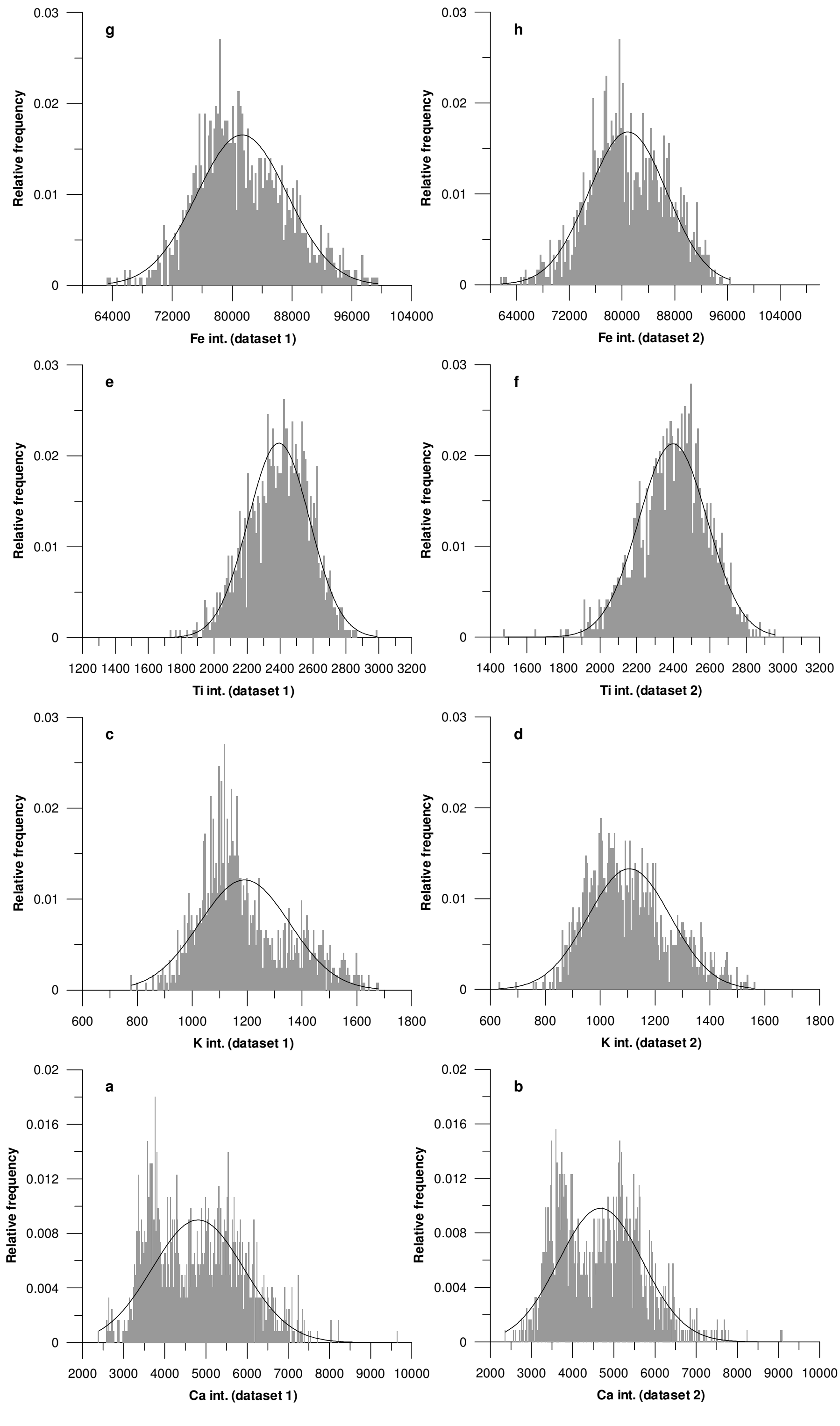

Figure 4.8. Frequency distribution histograms (grey bars) showing the Ca (a & b), K (c & d), Ti (e & f) and Fe (g & h) intensities in counts per second (cps) for datasets 1 and 2 acquired from section 4 of core TTR-450. The thin black line shows a gaussian fit with similar mean and standard deviation as the data to allow comparison.

The two datasets of titanium count intensity are presented in Figures 4.6e & f. Here, it is apparent that the correlation between dataset 1 and 2 is much poorer than is the case of the other elements, and when the data are cross-plotted (Figure 4.7c) a R^2 value of only 0.11 is apparent (n = 1219). The frequency distributions (Figures 4.8e & f) are however similar, with standard deviations of 186.464 and 187.485, separated by less than 1 %.

The population distribution of the datasets is further tested using variance (t- and f-test) analyses. The results are shown in Table 4.1. Comparatively high p-values are obtained for both the iron and titanium datasets, indicating some correlation between the separate runs, but are not statistically significant. No correlation is apparent for the calcium and potassium datasets.

	Calcium	Potassium	Titanium	Iron
Mean 1	4805.7	1190.7	2393.1	81348
Mean 2	4683.1	1106.4	2398.5	80885
Variance 1	1233900	27121	34797	36698000
Variance 2	1067300	22527	35180	35495000
F-test	1.156	1.204	1.011	1.0339
F-test p-value	0.011458	0.0012113	0.84886	0.56078
T-test	2.8222	13.216	-0.70778	1.9021
T-test p-value	0.0048083	$1.4589 * 10^{-38}$	0.47915	0.057282

Table 4.1. Variance analyses between datasets 1 and 2 for the calcium, potassium, titanium and iron elemental data (n = 1219).

Visual correlation of the two elemental datasets for section 4 of core TTR-450 (a homogeneous silty clay) indicates good agreement. However, based upon regression plots and R^2 values, as well as variance analyses, it is apparent that the reproducibility is better for some elements than for others. Deviations between datasets 1 and 2 are unlikely to have resulted from instrumental error, as this would be expected to increase as a percentage error for the elements with the higher counts, whereas this does not occur (for example, the calcium data with the highest R^2 value actually has the second highest count rate). Instead, the discrepancies between the two datasets most likely result from the re-positioning of the core section within the ITRAX core scanner between the two sets of measurements, and lateral variations across the core. This hypothesis is tested by cross plotting running averages of the elemental data, which is smoothed over 4.5 and 9 mm (Figure 4.9), effectively reducing the minor point-to-point variations between the datasets by smoothing out the noise. If the above were true then one would expect significantly higher correlation coefficients with the greatest smoothing applied.

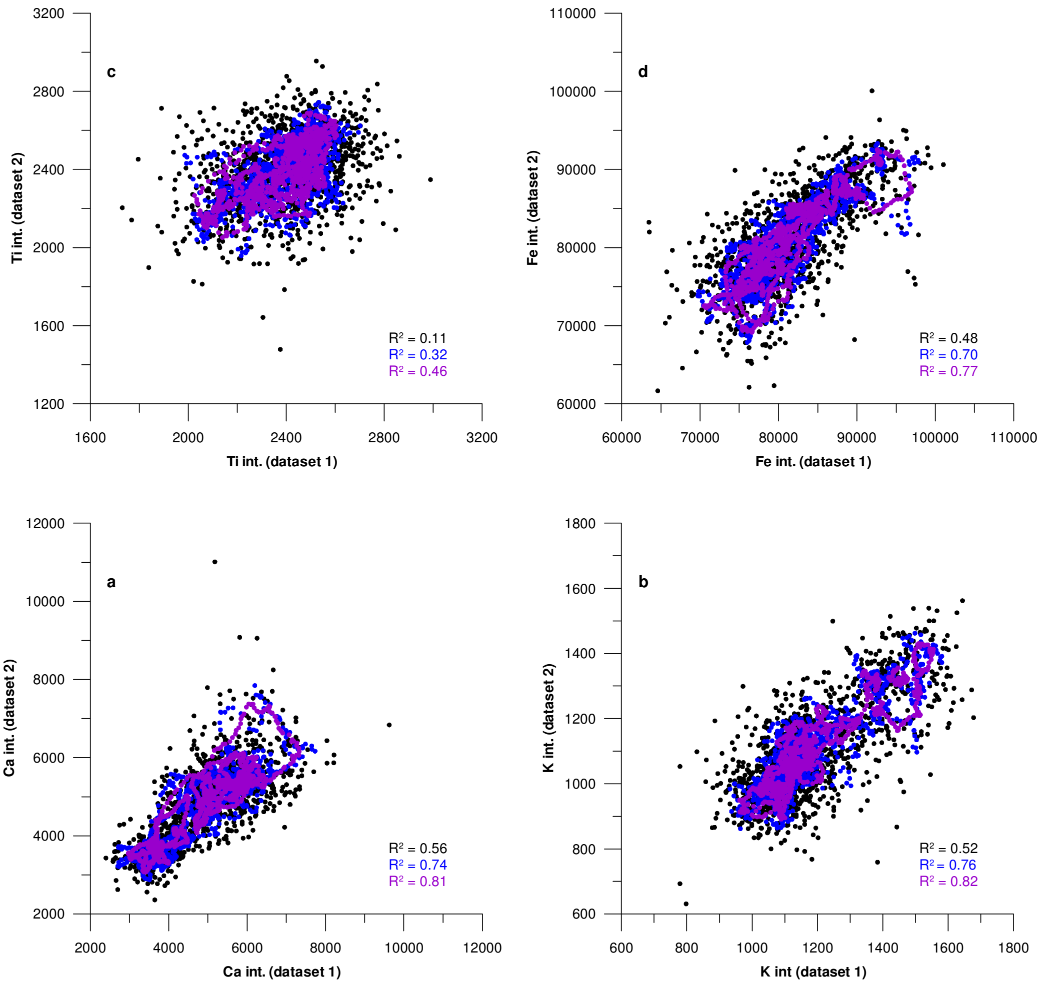

Figure 4.9. Cross-plots of the calcium (a), potassium (b), titanium (c) and iron (d) datasets 1 and 2 (re-run) for each element, which were acquired from section 4 of core TTR-450. The raw data is shown in black, the 9-point running average is shown in blue, and the 19-point running average is shown in purple.

The cross-plots of the smoothed datasets show much improved R^2 values (Figure 4.9), suggesting that the poorer R^2 values for the raw datasets indeed likely resulted from lateral variations across the split core sediment surface, which caused offsets between the very fine (500 µm) individual point measurements.

4.1.5. Description of core TTR-451, ITRAX-XRF core scanning results and bulk sediment C and O stable isotope ratios

Core TTR-451 is a 14.7 cm diameter gravity core, but with a total length of 465 cm. The core was divided into eight sections, with each section around 60 cm in length and one slightly shorter (~47 cm) bottom section. The core was split and logged on board *RV Professor Logachev*, and the core log is published in the post-cruise report (Kenyon *et al*., 2004). As previously suggested for core TTR-450, these core logs that were compiled onboard *RV Professor Logachev* most likely give the most accurate core description, as observations were made prior to oxidation of the sediment surface, core top collapse, water loss and shrinkage. However, sampling of the upper two section of core TTR-451 allowed for an opportunity for detailed logging of the fresh sediment surface. Therefore core log for TTR-451 reported here for the upper 120 cm of the core (i.e. the top two sections of the core) differs from Kenyon *et al*. (2004) in characterisation of the individual sedimentary units.

Similar to core TTR-450, the top ~3 cm of core TTR-451 is a winnowed unconsolidated foraminifera-rich sand, which also contains some <1 cm lithic fragments, small gastropods and bivalves, some of which were fully articulated and unfragmented. The base of the sand is irregular and is gradational over a few centimetres into a foraminiferal-rich, brownish-grey, silty clay.

The foraminifera-rich silty clay is observed between core depths of 3 to ~27 cm and contains mm sized lithic fragments (identified using a hand lens as basaltic volcanic glass), with localised higher abundances between 3 to 11 cm depth and 18 to 20 cm depth. At the top of this sequence, sand-filled *Planolites* burrows are evident on the scraped and fresh sediment surface. Irregular, millimetre thick, red-brown laminae are also evident down to around 12 cm core depth, but maybe an artefact of the core top oxidation, as opposed to textural or grain size changes. A blackish coloured horizon, rich in basaltic volcanic glass is observed between 23 and 26 cm core depths.

A distinct sedimentary unit is observed between 27 and 53.5 cm depth. This interval is light grey-brown silty clay, similar to the sedimentary sequence above, however with less sand sized lithic (ice-rafted debris – IRD) admixtures. Slightly darker brown silty clay, with marginally higher abundances of millimetric lithic fragments is observed between 34 and 41 cm.

At 53.5 cm depth is a sharp boundary. Below this boundary is a homogeneous, stiff, darker coloured brown-grey silt/silty clay with no visible sedimentary structures. This interval has a finer grained sandy admixture and contains fewer lithic fragments than the above intervals, however cm sized lithic clasts are sparsely scattered throughout. The base of this interval is defined by an irregular and bioturbated boundary at around 84 cm core depth, below which is lighter grey, homogeneous and structureless silty clay. This unit contains a higher abundance of mm size lithic fragments (most likely basaltic glass) and darker grey clay clasts. The base of this interval occurs at around 95.5 cm depth and is irregular and slightly bioturbated with *Chondrites* burrows.

The sediments below 95.5 cm depth are characterised by darker brown-grey, homogeneous and structureless silty clay. Sparsely distributed throughout are millimetric to centimetric sized lithic fragments, with localised higher abundances at 224 and 231 cm depth. The sediments below 95.5 cm depth also have much lower abundances of foraminifera and bioturbation is rare.

4.1.6. Bulk sediment C and O stable isotope ratios for core TTR-451

The bulk sediment stable oxygen isotope ratios ($\delta^{18}O$) measurements for core TTR-451 were mainly made by Dr. S. E. Hunter. The $\delta^{18}O$ data have a range of –9.07 ‰ to 2.46 ‰ (Figure 4.10f; note the inverted axis), with a mean value of

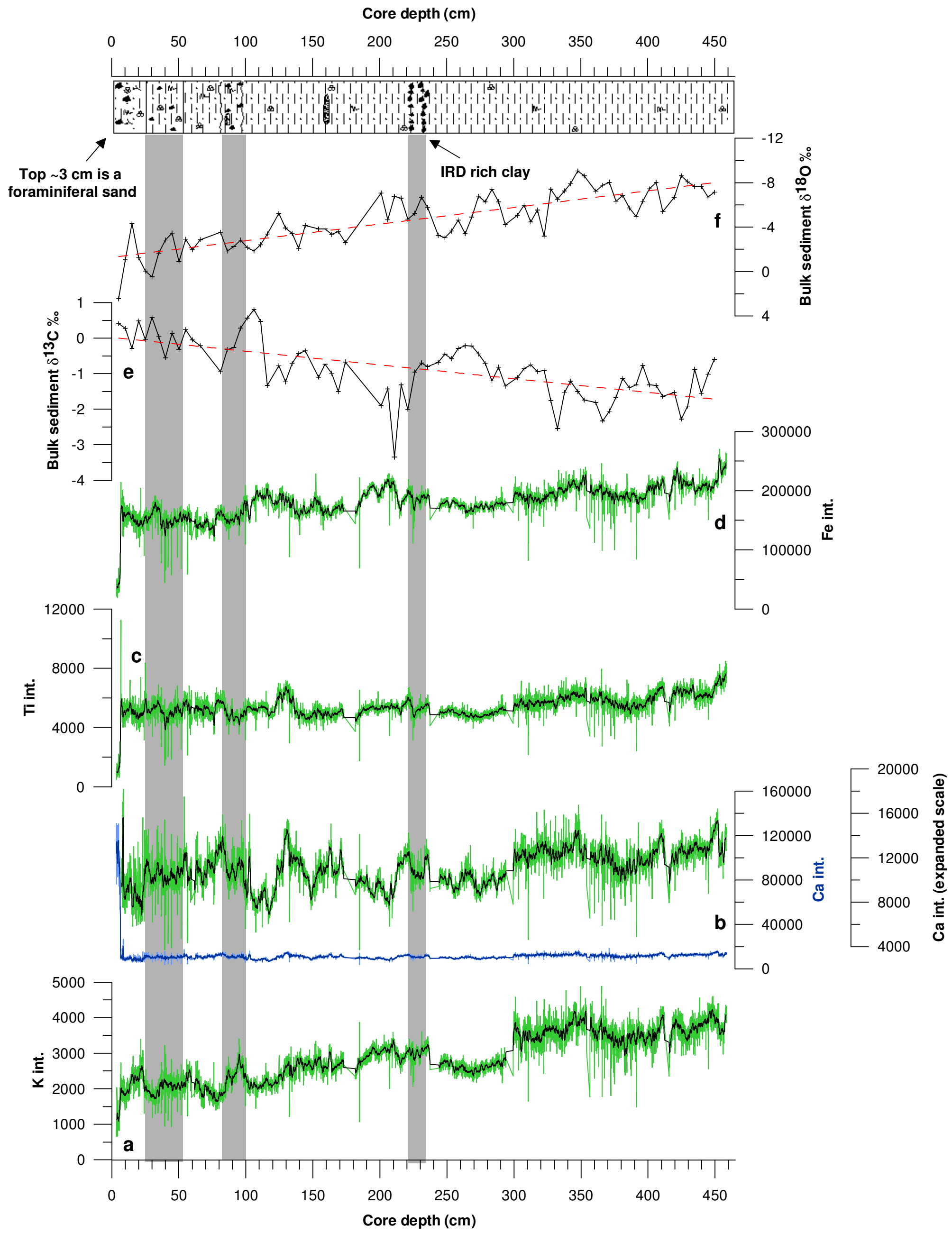

Figure 4.10. The key ITRAX-XRF core scanning results for the elements K, Ca, Ti and Fe (a-e), bulk sediment carbon ($\delta^{13}C$) and oxygen ($\delta^{18}O$) stable isotope ratios (f and g, respectively), and the core log (Kenyon *et al.*, 2004) for core TTR-451. In panels a to e, the data is shown in green/light blue and a 17-point running average through the data is shown in black/dark blue. Int. stands for intensity in counts per second (cps). Note that the bulk sediment $\delta^{18}O$ record is plotted on an inverted axis. Trend lines through the $\delta^{18}O$ and $\delta^{13}C$ records are shown as red dashed lines. Grey shaded bars indicate the key sedimentary transitions.

-4.56 ‰. Overall, the bulk sediment $\delta^{18}O$ record increase from a minimum value of around –8.5 ‰ at the base of the core to 2.46 ‰ at the core top. It is very unlikely that such extreme range and negative $\delta^{18}O$ values result from isotopic variation of foraminiferal calcite as it would imply unrealistic sea surface salinity or temperature changes (e.g., O'Neil *et al.*, 1969; Shackleton, 1974).

Figure 4.10e shows the bulk sediment stable carbon isotope ratio ($\delta^{13}C$) record for core TTR-451, which has a much smaller range of values in comparison to the $\delta^{18}O$ record, with a minimum of –3.35 ‰, a maximum of 0.80 ‰, and a mean value of –0.87 ‰. Similar to the $\delta^{18}O$ record, the $\delta^{13}C$ record increases up-core to more positive values (note the inverted axis for the $\delta^{18}O$ record). However, the gradient of this decrease (see trend line in red) is much shallower (note the smaller range on the $\delta^{13}C$ axis). Notable depletions in both the $\delta^{13}C$ and $\delta^{18}O$ records occur at around 210 cm and between 325 and 377 cm depth.

In order to investigate the possible cause of the extreme change in $\delta^{18}O$ and $\delta^{13}C$ values though core TTR-451, the reproducibility of the results were first tested. Widely spaced samples were re-analysed in a random order and the results are shown in Figure 4.11. The $\delta^{18}O$ re-runs are shown in red and suggest good reproducibility of results in the upper 250 cm of the core. In the lower portion of the core, however, results deviate by up to 1.94 ‰. The extreme negative values in the lower portion of TTR-451 are however, reproduced. The $\delta^{13}C$ duplicate data are shown in blue. The data show relatively good reproducibility in the upper 200 cm of the core; however, below this depth the reproducibility is poor, with deviations up to 1.96 ‰.

Despite the relatively large (nearly 2 ‰) deviations between original and duplicate analyses, the overall decrease to low $\delta^{18}O$ values was reproduced, indicating that laboratory or instrumental error cannot provide explanation for the large drift in the record. Because detrital carbonate can have relatively depleted $\delta^{18}O$ values due to the diagenetic processes of formation (e.g., Hendry *et al.*, 2000; Krajewski *et al.*, 2001; 2002; 2004), and an alternative explanation for the extremely negative $\delta^{18}O$ values in core TTR-451, would be if detrital carbonate was contained within the sediments. This hypothesis was investigated with thin section descriptions, and principally by analysing the mineralogical content of the bulk sediment samples using X-ray diffraction (XRD). The green circles in Figure 4.10 indicate the samples that were used for the XRD study.

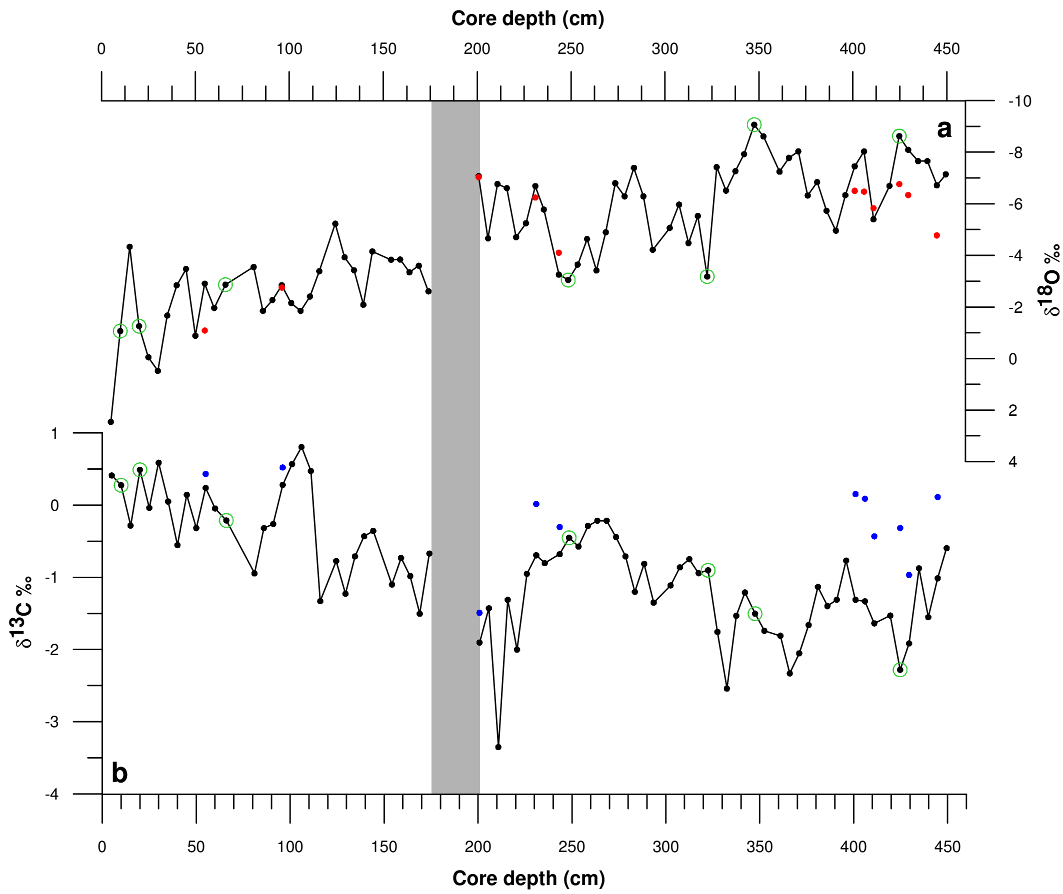

Figure 4.11. a. The bulk sediment stable oxygen isotope ($\delta^{18}O$) record for core TTR-451. Red dots represent the results from the re-analysis. b. The bulk sediment stable carbon isotope ($\delta^{13}C$) record for core TTR-451. Blue dots represent the results from the re-analysis. The grey shaded bar demarcates an interval of no data where the carbonate content was too low for analysis. The green circles indicate the samples that were used for XRD analyses.

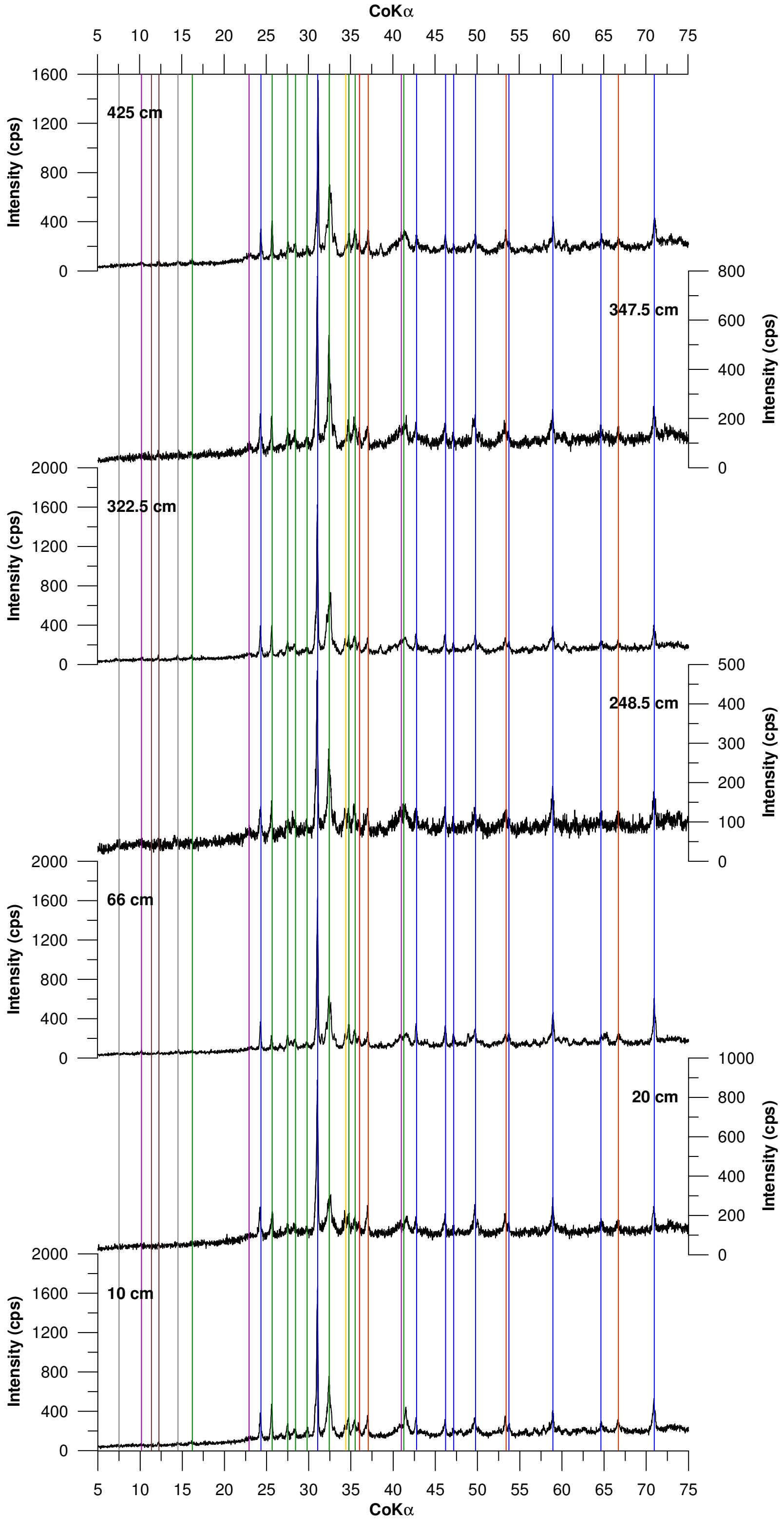

Figure 4.12. Mineral composition of bulk sediment samples from core TTR-451. Vertical lines indicate the characteristic d-spacings for minerals: blue = quartz, green = plagioclase feldspar, orange = halite, purple = mica, brown = amphibole, grey = chlorite, yellow = calcite and red = ankerite.

Analysis of thin sections using petrological microscope indicated that ferroan dolomite was present within the sediment samples, and the XRD results, revealed a peak with a d-spacing, characteristic of ankerite (Figure 4.12), which characteristically has extremely depleted $\delta^{18}O$ values (Hendry *et al.*, 2000; Krajewski *et al.*, 2001; 2002).

4.1.7. ITRAX-XRF core scanning results for core TTR-451

The ITRAX-XRF core scanning results for core TTR-451 are shown in Figure 4.10 and are presented in terms of intensities in counts per second (cps). Only records for the elements potassium, titanium, iron and calcium (K, Ti, Fe and Ca) are shown and discussed as these are considered to be the most reliable elemental data (e.g., Jansen *et al.*, 1998; Böning *et al.*, 2007). Note that data for the uppermost 3 cm of core TTR-451 were not measured, as it was not possible to sample the loosely consolidated core top.

The record of potassium intensity is shown in Figure 4.10a. Values of potassium intensity range from 660 to 4883 cps, with a mean of 2884 cps. In general, the record shows a trend to lower values up-core. Low potassium counts are centred around 32, 44, 53, 69, 79, 109, 120, 184 and 224 cm depth, and a broad low anomaly occurs between core depths of around 240 to 300 cm. A sharp shift to higher intensities occurs at around 300 cm depth. The uppermost few centimetres of core TTR-451 are characterised by low potassium intensities of around 1000 cps.

As previously discussed for core TTR-450, potassium is contained within terrigenous sedimentary fraction, and likely within the clay and silt grain size ranges. Variations in the intensity of potassium counts are interpreted to reflect changing abundances of continental, acidic sediment sources (Yaroshevsky, 2006). Therefore, the extremely low potassium intensity that is observed in the upper 10 cm of core TTR-451 can be attributed to the high foraminifera abundances, and hence relatively low clay and silt sediment content. Similarly, the sharp low in potassium counts at around 224 cm depth likely results from the increased abundance of IRD and reduced clay and silt sediment size fractions.

The intensity of the calcium counts is shown in Figure 4.10b. Changes in calcium intensity likely represent variations in the abundance of foraminifera; however, contribution from detrital carbonate (ankerite) may also be reflected in the calcium intensity record for core TTR-451. The uppermost 7 cm of sediment has exceedingly high calcium counts, with a peak value of 130812 cps. These high calcium counts are attributed to the sediment predominantly containing foraminifera in this portion of the core. Below 7 cm core depth, calcium intensities range between 3714 and 18632 cps around mean of 11046 cps.

The calcium intensity record below 304 cm core depth again shows high frequency and high amplitude variability, with prominent lows at around 309, 361 and 416 cm depth, and a broader anomaly between 475 and 402 cm depth. Broad lows in calcium intensity record occur between core depths of 101 and 124 cm depth, and 138 and 304 cm depth. It is also noteworthy that over the entire interval between 101 and 304 cm depth, the variability in the record is of a smaller amplitude and frequency. The calcium intensity in the upper 100 cm of core shows relatively high frequency and high amplitude variability, with prominent lows centred at around 20, 42 and 51 cm depth.

The relationship between the potassium (which is exclusively sourced from terrigenous sediments) and calcium (most likely a reflection of foraminiferal abundances) intensity records for core TTR-451 are assessed in a similar manner to core TTR-450. The potassium and calcium counts are cross-plotted, and reveals two clouds of data (Figure 4.13), similar to results from TTR-450. The linear least squares regression for cloud A has an R^2 of 0.49 (n = 77) and represents the uppermost 7 cm of core TTR-451; the winnowed foraminiferal sand. Conversely, cloud B, which represents the remainder of the data below 7 cm core depth, has a statistically weak correlation coefficient of 0.31 (n = 8443), and shows no response in calcium intensity with relatively large variation in the potassium intensity.

The record of Ca/K is shown in Figure 4.14. Below 200 cm depth, the Ca/K record shows very little structure and values remain relatively low. Between depths of 7 to around 200 cm, and especially down to 120 cm, the Ca/K record shows a high degree of variability with notable peak values at around 24, 79, 103 and 129 cm depth. Low Ca/K values in the uppermost 7 cm of core reflect the foraminiferal-rich core top.

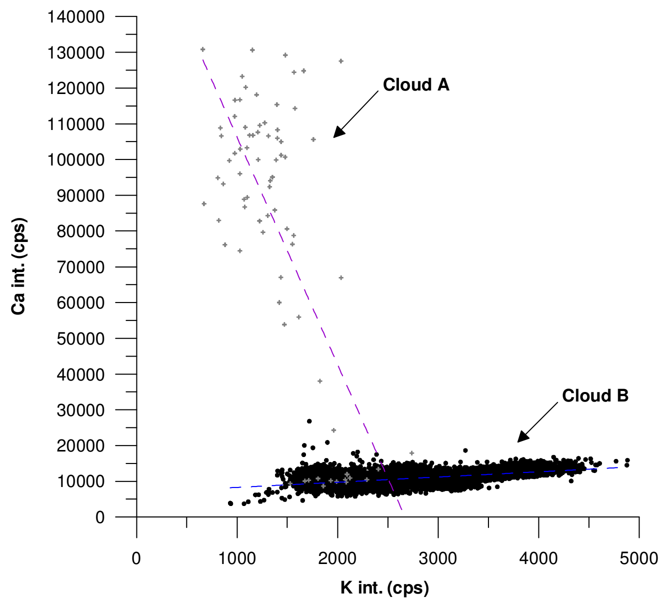

Figure 4.13. Cross-plot of the K and Ca intensities in counts per second (cps). Cloud A (grey crosses) has an R^2 value of 0.49 (Y = -63.57482616 * X + 169815.5733), n = 77, and cloud B (black dots) has an R^2 value of 0.31 (Y = 1.458257622 * X + 6826.960629), n = 8443.

Figure 4.10c & d shows the titanium and iron intensity records for core TTR-451. Similar trends are observed in both records, with good agreement in the lowermost 250 cm of TTR-450. Between core depths of 364 and 405 cm, a broad low is observed in both records, with sharp reductions centred at around 390 and 415 cm depth. Broad lows with reduced variability occur in both the iron and titanium counts between core depths of 131 to 190 cm and 240 to 301 cm. It is noteworthy that both records show a sharp low at around 225 cm depth, coincident with the IRD rich horizon. The sharp, relatively high frequency variability shows good visual correlation, with low counts centred at around 40, 60, 75 and 87 cm depth.

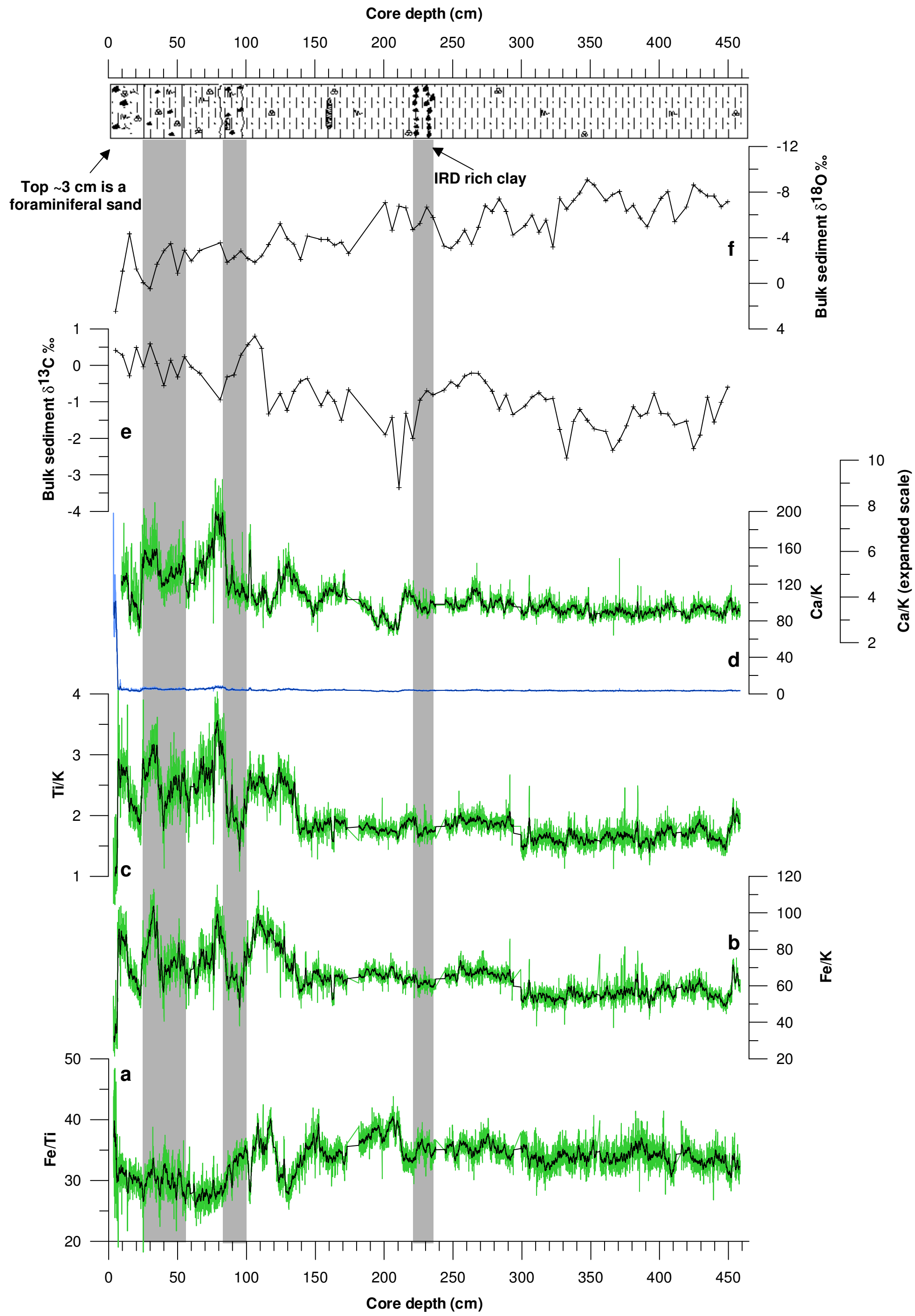

Figure 4.14. Ratios of Fe/Ti (a), Fe/K (b), Ti/K and Ca/K for core TTR-451. In green are the data and the black line shows a 17-point running average through the data. For the Ca/K record the data is shown on an expanded scale with the uppermost 9 cm of data removed. In blue is the complete dataset. (e) & (f) are the bulk sediment δ^{13}C and δ^{18}O records, respectively, for core TTR-451. In the top panel is the core log for TTR-451 (Kenyon *et al.*, 2004). The grey vertical bars show the key sedimentary boundaries.

Unlike the titanium record, the iron intensities are generally lower throughout this upper ~100 cm of the core, and the relative amplitude and sharpness of the shifts are reduced. Furthermore, a prominent low is observed in the titanium counts between core depths of 102 to 120 cm, whereas enhanced iron intensities occur at equivalent depths. The upper ~7 cm of core TTR-450 is characterised by extremely low counts in both the iron and titanium records, and possibly results from the high concentration of foraminiferal tests that are contained within the winnowed core top.

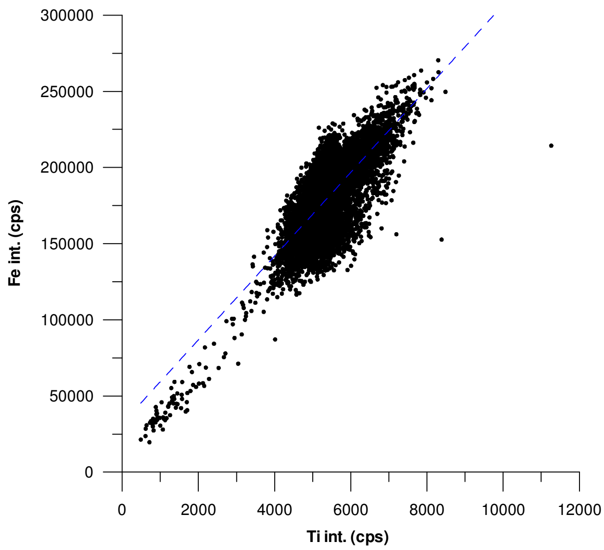

Figure 4.15. Cross-plot of the Ti and Fe intensities in counts per second (cps). A regression line is shown in blue and gives an R^2 value of 0.63 (Y = 27.47625192 * X + 31956.43593, n = 8519).

In a similar manner to results from core TTR-450, the relationship between the iron and titanium counts is investigated for core TTR-451 in order to ascertain their source and sediment pathway. The iron and titanium counts were cross-plotted and the result is shown in Figure 4.15. The ratio of iron over titanium (Figure 4.14a) identifies where discrepancies occur between the two records. The cross-plot (Figure 4.15) reveals a good positive correlation between the iron and titanium intensities, with an R^2 value of 0.63 (n = 8519), indicating that for the most part these two elements share the same sediment source. The source of titanium and iron in TTR-451 is likely to be (titano)magnetites, from the Nordic Basaltic Province (Kissel *et al.*, 1997; 1999a; Laj *et al.*, 2002).

The Fe/Ti record (Figure 4.14a) reveals prominent lows in the Fe/Ti sediment composition at around core depths of 63, 128, 165 and 220 cm. A gradual shift to lower Fe/Ti values occurs between 110 and 63 cm. This shift maybe due to a change in the source of the iron (i.e., iron oxides, pyrite), and IRD (i.e., hematite stained quartz). Alternatively, changes in the sediment porosity and interstitial water content may also provide explanation (Kido *et al.*, 2006). A relatively iron-rich core top is likely due to higher concentrations of iron oxide.

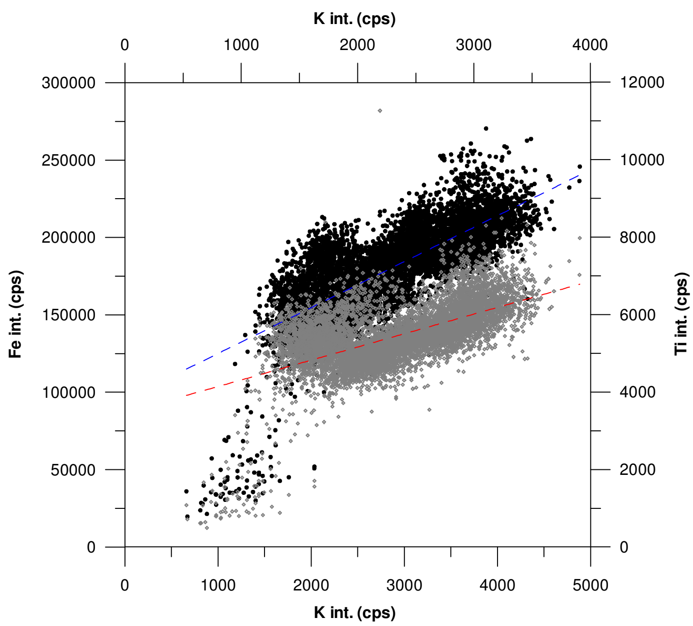

Figure 4.16. Cross-plots of the K intensity (cps) versus the Fe intensity (cps) (black dots), and the Ti intensity (cps) (grey open diamonds). Regression lines are shown in blue (K versus Fe) and red (K versus Ti) and reveal R^2 values of 0.59 (Y = 29.714643 * X + 95279.80246) and 0.37 (Y = 0.6808541864 * X + 3460.088055), respectively (n = 8519).

In Figure 4.16, the potassium, iron and titanium datasets are cross-plotted. This reveals relatively high correlation coefficients of 0.59 and 0.37 (n = 8519) for the iron and titanium counts, respectively. Such a good agreement between the datasets indicates that the potassium, iron and titanium are likely contained within the same sediment size fraction, i.e. the clay and silt (Kissel *et al*., 1997; Moros *et al*., 1997; Yaroshevsky, 2006). Note that the IRD enriched interval of core TTR-451 at around 225 cm depth has reduced counts of all three elements, validating the above assumption.

In order to show abundances of iron and titanium with respect to the total clay/silt fraction, the ratios of iron and titanium intensities versus potassium intensity are shown in Figures 4.13b and c, respectively. These records show remarkable similarity. Below 130 cm core depth, the records show only low amplitude changes; with only one notable shift to lower values at around 296 cm depth. An additional peak in the Ti/K record occurs at around 53 cm. The top 150 cm of core TTR-451 shows high amplitude variability, with peak Fe/K and Ti/K values at around 34 and 79 cm depth, and between 98 and 139 cm depth.

4.1.8. Conclusions

Core sediment descriptions, bulk oxygen and carbon stable isotope ratios and key ITRAX-XRF elemental data for core TTR-450 and TTR-451 are shown in this sub-chapter. The reproducibility of the ITRAX-XRF data is statistically tested, and results show that discrepancies between duplicate analyses likely results from the fine (500 μm) measurement intervals and offsets between point-to-point comparison. Relatively depleted bulk sediment $\delta^{18}O$ values at the base of core TTR-451 were investigated using thin section and XRD analyses. The presence of detrital carbonate (ankerite) was the most likely explanation for these extremely negative $\delta^{18}O$ values.

For both cores TTR-450 and TTR-451, analyses of the Ti and Fe intensity counts suggest that they likely reflect variation in the clay and silt sediment fractions and also probably have a common source – (titano)magnetite. These results are compared in the next sub-chapter with the environmental magnetic data from these cores.

4.2. Environmental Magnetic and Palaeomagnetic Results for marine sediment cores TTR-450 and TTR-451.

This sub-chapter presents the results from the environmental and palaeomagnetic measurements that were made on core material sampled from marine sediment cores TTR-450 and TTR-451. Results include magnetic susceptibility (κ), natural remanent magnetisation (NRM) and anhysteretic remanent magnetisation (ARM). The environmental magnetic results are also compared with the iron and titanium elemental data that was gained from the ITRAX core-scanning XRF, and with the bulk sediment $\delta^{18}O$ data and core logs that were previously described in section 4.1.

4.2.1. Background

Variation in magnetic susceptibility is predominantly controlled by both the quantity and grain size of the magnetic material present, while variation in ARM is produced by changes in the concentration of the ferrimagnetic mineral component (e.g., Verosub and Roberts, 1995; Stoner *et al*., 1996). The ratio of κ_{ARM} (the anhysteretic susceptibility) over κ is inversely correlated to changes in average magnetic mineral ((titano)magnetite) grain size (i.e., coarser grain sizes are represented by lower κ_{ARM}/κ values), and is particularly sensitive to variations in the 1 to 10 μm size range (Banerjee *et al*., 1981; Verosub and Roberts, 1995).

The intensity of NRM is determined by the intensity of the geomagnetic field at the time of, or just after sedimentary deposition, and by the concentration, mineralogy and grain size of the magnetic remanence carriers (e.g., Stoner *et al*., 2000). The ratios of NRM/ARM and NRM/κ provide records of relative palaeointensity with the effect of magnetic mineral concentration removed, and are used in palaeoceanographic study as a relative (correlation) dating tool (e.g., Opdyke *et al*., 1973; Levi and Banerjee, 1976; Tucker, 1981; Weeks *et al*., 1993; 1994; Laj *et al*., 2000; 2004).

Over time, the direction of the geomagnetic field also changes. For the purpose of the present study, we need to consider changes with duration of less than 10^5 years. These are known as geomagnetic secular variations, which can be completely described by two vector components: the angle of inclination and the angle of declination (e.g., Butler, 1998). The above magnetic parameters are more fully defined and described in section 3.3.

4.2.2. Environmental Magnetic Results for Core TTR-450

Low-field volumetric magnetic susceptibility (κ) and ARM were acquired at 2.35 cm intervals along core TTR-450, using discrete sediment samples (for details on methods see chapter 3) and the results are shown in Figure 4.18a & c. A distinct low in magnetic susceptibility occurs between 535 and 480 cm core depth, coincident with a similar magnitude low in the record of ARM. Between 250 and 480 cm depth, magnetic susceptibility values are relatively high, punctuated by small amplitude, high frequency lows. This interval is demarcated by the double headed arrow in Figure 4.18a. Above this level the magnetic susceptibility record has relatively low values, punctuated by small amplitude variations (Figure 4.18a). A marked low in magnetic susceptibility occurs between core depths of 249 and 208 cm, and similar amplitude lows, but over shorter intervals of core, are centred at around 138 and 45 cm core depths.

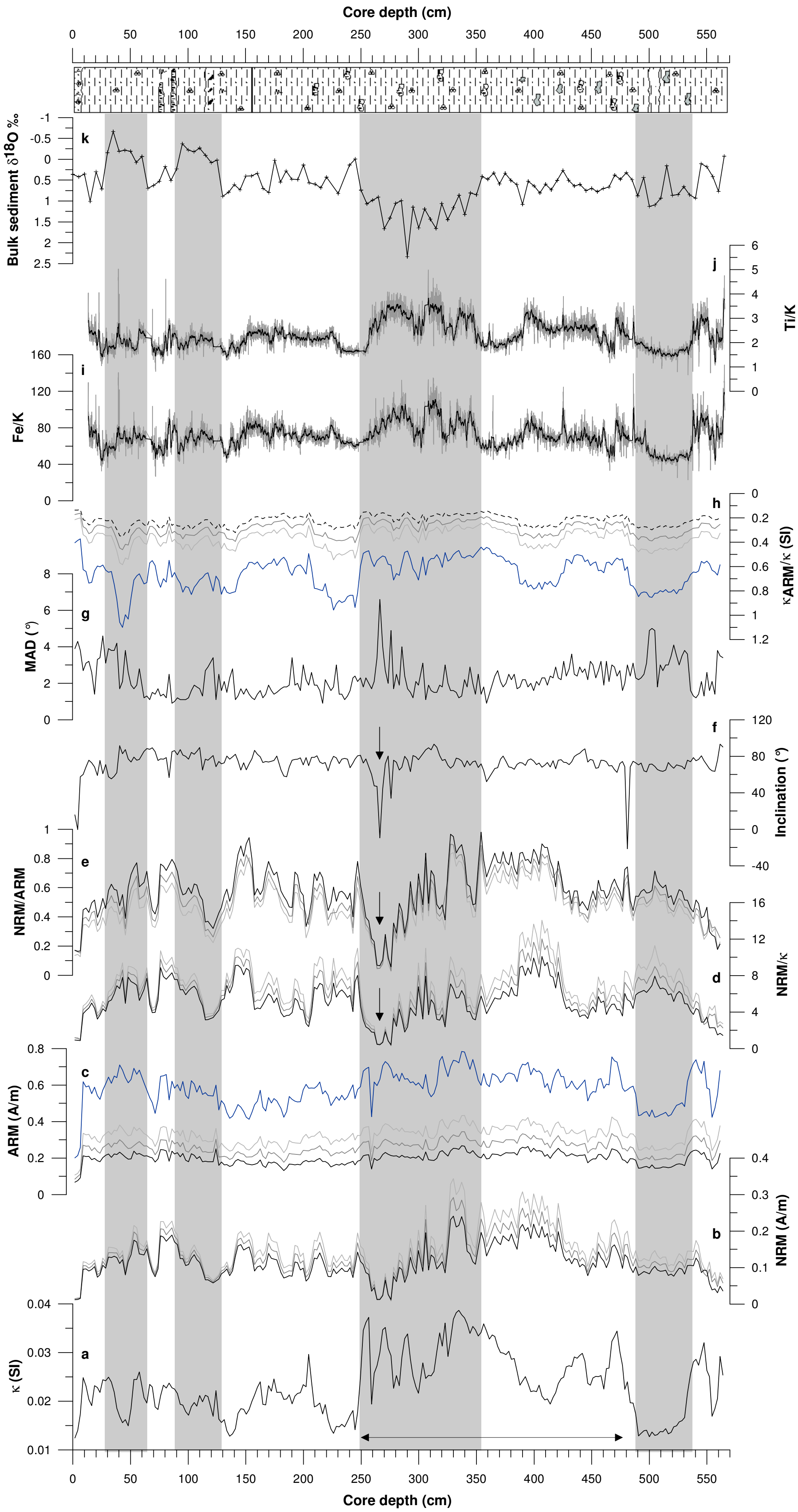
Core depth (cm)
Bulk sediment δ18O ‰
Ti/K
Fe/K
κARM/κ (SI)
MAD (°)
Inclination (°)
NRM/ARM
NRM/κ
ARM (A/m)
NRM (A/m)
κ (SI)
a
b
c
d
e
f
g
h
i
j
k

Figure 4.18. Environmental magnetic and palaeomagnetic records from core TTR-450 acquired from discrete sediment samples. Panel a = volumetric low-field magnetic susceptibility (κ), b = NRM, c = ARM, d = NRM/κ and e = NRM/ARM. The NRM and ARM measurements acquired after the application of Alternating Field (AF) demagnetisation levels of 0, 20, 25 and 30 mT are shown by blue, black, dark grey and light grey lines, respectively. Angles of inclination are shown in f and the MAD3 values in g. The κ_{ARM}/κ is shown in panel h. Note that lower values are interpreted to reflect coarser magnetic grain sizes (Banerjee *et al.*, 1981). Key ITRAX-XRF data, Fe/K and Ti/K, are shown in panels i and j, respectively, and the bulk stable oxygen isotope stratigraphy is shown in k. The sedimentary core log (Kenyon *et al.*, 2004) is shown in the top panel. The grey vertical bands demarcate excursions in the bulk sediment $\delta^{18}O$ record.

Two prominent lows occur in the ARM record (Figure 4.18c) towards the base of core TTR-450, one centred at around 554 cm depth and another between 532 and 487 cm depth. ARM values gradually increase up-core, peaking at around 340 cm depth, before decreasing gradually to a minimum at around 150 cm core depth. Two further sharp lows occur at around 258 cm and 71 cm. Lower amplitude variability occurs throughout the record. Similar to the magnetic susceptibility record, the core top is characterised by extremely low ARM intensities, likely due to reduced concentrations of ferrimagnetic grains within the foraminifera-rich, sandy horizon.

Cross-plotting of the magnetic parameter κ_{ARM} versus κ gives an indication of the suitability of the ratio of κ_{ARM}/κ as a magnetic grain size indicator. Data that cluster around a straight line with a constant slope indicate changes in concentration of the magnetic grains, whereas changes in the slope of the trend line are indicative of changes in magnetic grain size (Banerjee *et al.*, 1981; King *et al.*, 1982). The κ and κ_{ARM} values from core TTR-450 are cross-plotted in Figure 4.19. The linear trend of the data with R^2 = 0.54 indicates a limited change in average grain size. This finding is consistent with previous environmental magnetic studies of marine sediment cores recovered from beneath the North Atlantic Deep Water (NADW) pathway in the vicinity of Eirik Drift (Kissel *et al.*, 1997; 1999a, b; Moros *et al.*, 1997; Laj *et al.*, 2002; Snowball and Moros, 2003), if a constant magnetic mineralogy from a common source (the Nordic Basaltic Province) is assumed (Kissel *et al.*, 1999a; Laj *et al.*, 2002).

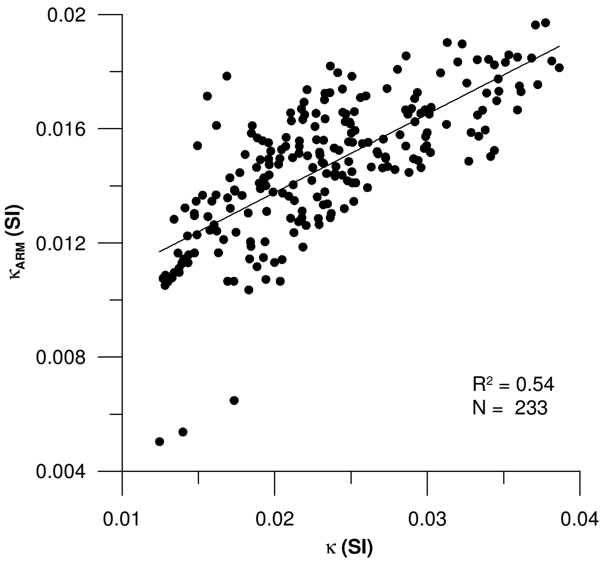

Figure 4.19. Cross-plot of κ and κ_{ARM} values of discrete sediment samples from core TTR-450. Equation for the regression line: Y = 0.2745972812 * X + 0.008272830852.

Figure 4.18h shows the down-core variations in the ratio of κ_{ARM} over κ for core TTR-450. The record shows four intervals where κ_{ARM}/κ is significantly elevated, i.e. relatively fine magnetic grain sizes (NB: note the inverted axis). These intervals are 536 - 482 cm, 425 - 387 cm, 249 - 208 cm, and 50 - 38 cm. The ITRAX elemental Fe/K and Ti/K data likely reflect variation in concentration of (titano)magnetite (for discussion see section 4.1). Comparison of the κ_{ARM}/κ record with the records of Fe/K and Ti/K (Figures 4.17i & j, respectively) show that only one of the κ_{ARM}/κ events (536 to 482 cm core depth) is coincident with reduced sediment concentrations of Fe and Ti, and is also coincident with significantly reduced ARM values. Therefore, it is likely that it is only in this portion of core that decreased concentrations of (titano)magnetite occur along with reduced magnetic grain sizes, whereas the other events only result from decreased average magnetic grain size. Note also that it is only this κ_{ARM}/κ event that is concurrent with a bulk sediment $\delta^{18}O$ anomaly, which is interpreted as a palaeoclimate indicator (Figure 4.18k). However, the sharp reduction in κ_{ARM}/κ between 50 and 38 cm depth is contemporaneous with a significant depletion in bulk sediment $\delta^{18}O$ (Figure 4.18k), although the κ_{ARM}/κ anomaly has shorter duration.

4.2.3. Palaeomagnetic and Directional Magnetic Records for core TTR-450

NRM was acquired from the same discrete sediment samples as the magnetic susceptibility and ARM was measured from. These samples were collected 2.35 cm intervals along a continuous strip of core TTR-450 (for further details see Chapter 3). The results from the NRM measurements are presented in Figure 4.18b.

NRM values for core TTR-450 demonstrate a gradual increase from relatively low values at the base of the core, to peak values at around ~330 cm depth (Figure 4.18b). Above 325 cm core depth, the NRM reduces to lower values, attaining a minimum at around 275 cm core depth and returning to moderate values at around 257 cm core depth. Above this level, the NRM record is dominated by relatively higher frequency and smaller amplitude variations. Low NRM values in the uppermost ~10 cm of the core correspond with the foraminifera-rich sandy top (low concentrations of magnetic carriers).

The records of NRM/κ and NRM/ARM are shown in Figure 4.18d & e. These two datasets show a high degree of structural similarity and correlate well with $R^2 > 0.72$ (Figure 4.20). In general, NRM/κ and NRM/ARM values increase from the base of the core, peaking at around 505 cm. The NRM/κ values subsequently decrease to a minimum at around 450 cm core depth, whereas the NRM/ARM record shows an additional peak at around 480 cm depth, prior to decreasing to a low at around 450 cm core depth.

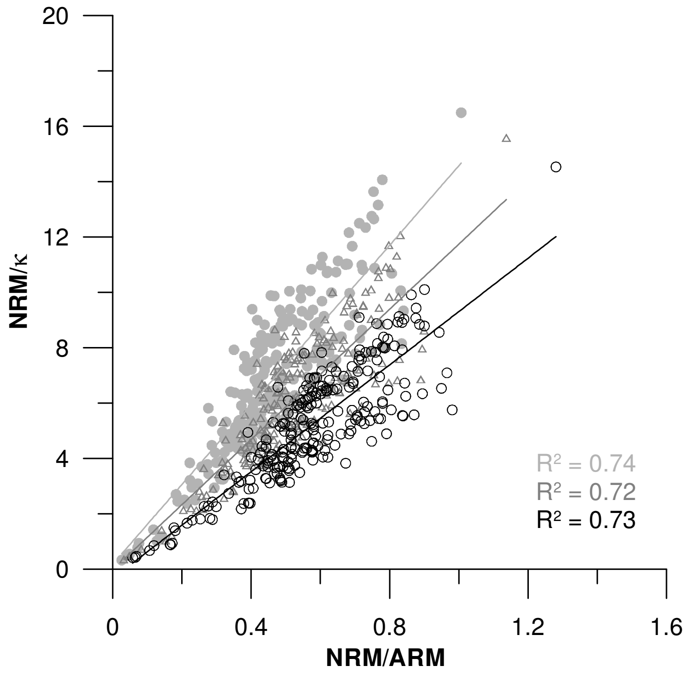

Figure 4.20. Cross plot of the NRM/ARM and NRM/κ data for core TTR-450. Light grey circles represent the NRM and ARM measured after AF demagnetisation at 20 mT, dark grey triangles are after AF demagnetisation at 25 mT, and black open circles are after AF demagnetisation at 30 mT. N = 231 for data collected after 20 and 30 mT AF demagnetisations and N = 207 for data collected after 25 mT AF demagnetisation.

Above 450 cm core depth, the NRM/κ and NRM/ARM records (Figure 4.18d & e) both increase to peak values at around 406 cm. The NRM/κ record (Figure 4.18d) sharply decreases at 387 cm depth, prior to gradually decreasing to a minimum at around 266 cm. The NRM/ARM record (Figure 4.18e) also has a minimum at 266 cm core depth, but the NRM/ARM values between 406 and 352 cm remain more or less constant.

Both NRM/κ and NRM/ARM values increase at around 253 cm core depth, recovering from their minima at 266 cm depth, and reaching peak values at around 247 cm depth (Figure 4.18d & e). Above this level, both records have peak values at around 153 cm core depth prior to decreasing to a minimum that is centred on ~120 cm depth. A sharp low occurs in both records, centred at 70 cm depth, after which values gradually decrease towards the core top. Above 8 cm core depth, NRM/κ and NRM/ARM values sharply decline, likely due to reduced concentration of magnetic carriers within the winnowed core top sediment (foraminiferal sand).

Component directions were calculated from the NRM measurements using the *Z-plot* programme. Maximum Angular Deviation (MAD) values are shown in Figure 4.18f and were generally less than 3°, with an average value of 2.3°, indicating that the magnetisation components were well defined (for further details see chapter 3.3.3).

The calculated component inclination values varied around a mean of 66°. Using the dipole equation (Equation 3.1), the expected inclination for the core site latitude was 72.8°. Therefore, the values for the component inclination were adjusted by +6.2° to fit the expected mean. The component declination values were highly variable, ranging between –289 and 307° and are therefore not presented.

The adjusted component inclination values are shown in Figure 4.18f. The low values calculated for the core top likely result from poor remanence stability (see section 3.3.3), an artefact of the foraminifera-rich sediment composition. Two further excursions to negative inclination values occur at 481 cm and 270 to 254 cm, with minimum values of –21.2° and –9.3°, respectively. The negative excursion at 254 cm is coincident with low values of relative palaeointensity (see arrows in Figure 4.18d, e & g), and likely represents the Laschamp palaeomagnetic event that is dated in the NAPIS-75 and GLOPIS-75 stacked palaeointensity record at around at around 41 ka BP (Laj *et al.*, 2000; Laj *et al.*, 2004).

4.2.4. Environmental Magnetic Results for Core TTR-451

Low-field volumetric magnetic susceptibility (κ) and ARM measurements were made at 2.35 cm intervals along a continuous strip of core TTR-451. The results are shown in Figure 4.24a. Higher resolution magnetic susceptibility was measured at 0.5 cm intervals with a *Bartington Instruments MS2E1* point sensor that was placed in contact with the surface of a split core, and is labelled as 'whole core' in Figure 4.24a. For further details on the methods see Chapter 3.

For the uppermost ~350 cm of core TTR-451, the discrete and whole core magnetic susceptibility data show good agreement and cross-validate each other (Figure 4.21a). However, in the lowermost portion of the core below ~350 cm, the two records bear little resemblance (see yellow shaded zone in Figure 4.21a). This disagreement between the discrete and whole core data may result from lateral variation within the core, as the discrete samples were taken from the edge of the core while the whole core data was measured down a central strip. Also, the point sensor data is only sensitive to the top few millimetres of sediments, so the whole core data only records variation in the sediment composition near the split core sediment surface. As the discrete dataset provides average values of a larger volume of sediment, these data are favoured over the whole core data.

Below 235 cm depth, the record of magnetic susceptibility for core TTR-451 shows only low amplitude variability (Figure 4.21a). At around 232 and 216 cm core depth, two spikes are observed. These are approximately coincident with two distinct horizons that are rich in coarse-grained lithics/ice-rafted debris (IRD) (see uppermost panel in Figure 4.21). A broad low in magnetic susceptibility is centred at ~198 cm core depth. A double peak is centred around 170 cm depth. However, the first of the peaks in the whole core data is not duplicated by the discrete sample data. This discrepancy may result from the difference in resolution of the datasets. Magnetic susceptibility values are reduced above this horizon at around 150 cm depth, and return to peak values at around 129 cm core depth. Over this portion of core (160 to 135 cm depth), some discrepancies exist between the whole core and discrete data, with higher frequency variability in the higher resolution point sensor record.

In the uppermost ~120 cm of core TTR-451, sharp variations in the magnetic susceptibility records are approximately coincident with sedimentary boundaries (see shaded regions in Figure 4.21). The magnetic susceptibility values gradually decrease over an interval spanning 37 cm of the core, attaining minimum values at around 92 cm (Figure 4.21a). This low is sharply terminated at around 84 cm.

Magnetic susceptibility values decrease from 84 cm and level out between 60 and 26 cm depth (Figure 4.21a), and a sharp low occurs above this level. At around 6 cm depth, magnetic susceptibility values return to higher values, although more abruptly in the whole core data than the discrete data. The uppermost 4 cm of core TTR-451, which comprises foraminiferal sand, was too unconsolidated to sample for discrete analysis. However, measurements could be made with the *Bartington Instruments MS2E1* point sensor, and the results show significantly lowered values.

The ARM record for core TTR-451 is presented in Figure 4.21c. Low amplitude variability dominates the ARM record below 220 cm core depth. Above this horizon the ARM record shares key features with the magnetic susceptibility record with a broad low between 210 and 182 cm, a significant peak at around 133 cm core depth, and two further distinct and sharper lows between 98 and 84 cm and 25 and 13 cm core depth.

The κ_{ARM} and κ data obtained from the discrete sediment samples are cross-plotted in Figure 4.22. As previously discussed with respect to core TTR-450, plots of κ_{ARM}/κ in which the data cluster around a straight line with a constant slope give an indication of changes in concentration of the magnetic grains (Banerjee *et al.*, 1981; King *et al.*, 1982; 1983). Conversely, changes in the slope of the trend line are indicative of changes in magnetic grain sizes (Banerjee *et al.*, 1981; King *et al.*, 1982; Snowball and Moros, 2003).

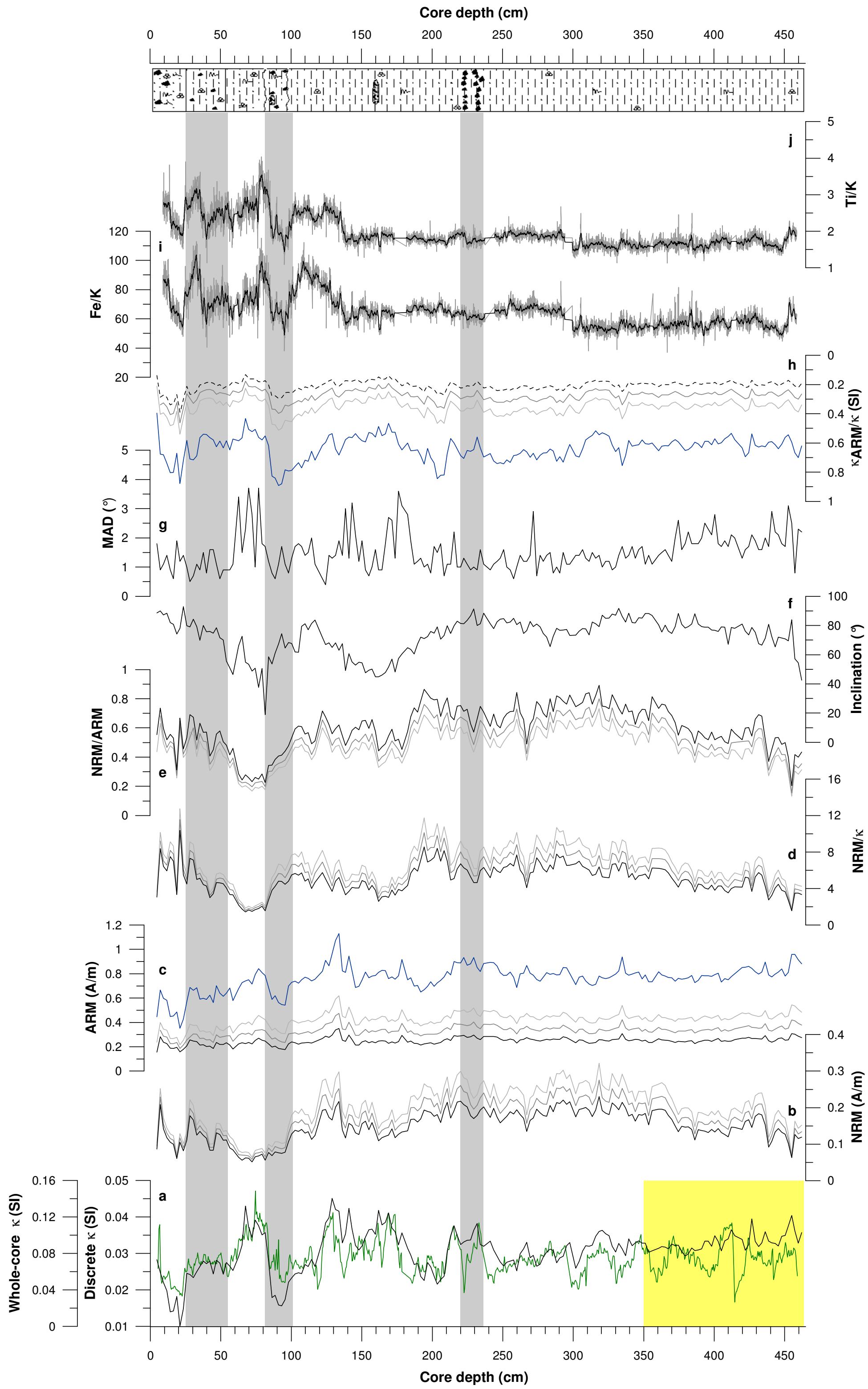

Figure 4.21. Environmental magnetic and palaeomagnetic records from core TTR-451 acquired from discrete sediment samples. Panel a = volumetric low-field (κ). In green are the whole core data and in black are the discrete data. The yellow shaded box demarcates where the two records

show disagreement. b = NRM, c = ARM, d = NRM/κ and e = NRM/ARM. The NRM and ARM measurements acquired after the application of Alternating Field (AF) demagnetisation levels of 0, 20, 25 and 30 mT are shown by blue, black, dark grey and light grey lines, respectively. Angles of inclination are shown in f and the MAD3 values in g. The κ_{ARM}/κ is shown in panel h. Note that lower values are interpreted to reflect coarser magnetic grain sizes (Banerjee *et al.*, 1981). Key ITRAX-XRF data, Fe/K and Ti/K, are shown in panels i and j, respectively. The sedimentary core log (Kenyon *et al.*, 2004) is shown in the top panel. Vertical shaded grey boxes represent the depths of sedimentary changes.

The linear trend of the κ_{ARM} versus κ data for core TTR-451 (Figure 4.27; R^2 = 0.60, N = 189) indicates a higher covariance between these data than for core TTR-450 (Figure 4.19), and is more consistent with previous environmental magnetic studies of marine sediment cores recovered from beneath the North Atlantic Deep Water (NADW) pathway (Kissel *et al.*, 1997; 1999a, b; Moros *et al.*, 1997; Snowball and Moros, 2003). A constant magnetic mineralogy with a common source (the Nordic Basaltic Province) has been previously assumed along the NADW flow path, transported via deep overflow through the Denmark Strait and the Iceland-Scotland Ridge (Kissel *et al.*, 1999a, b; Laj *et al.*, 2002). It is therefore likely that κ_{ARM}/κ data from TTR-451 record changes in grain size of the magnetic material carried out of the Nordic Basaltic Province by NADW.

Figure 4.21h shows the κ_{ARM}/κ record for core TTR-451. The record below ~240 cm shows only low amplitude variability. Two notable lows, indicative of coarser magnetic grain sizes, occur at 232 and 213 cm core depth (note the inverted axis), nearly coincident with two IRD rich horizons that were noted during the core logging (see top panel of Figure 4.21). Above this level, two distinct peaks (inferred relatively fine magnetic grain sizes) are observed in the record.

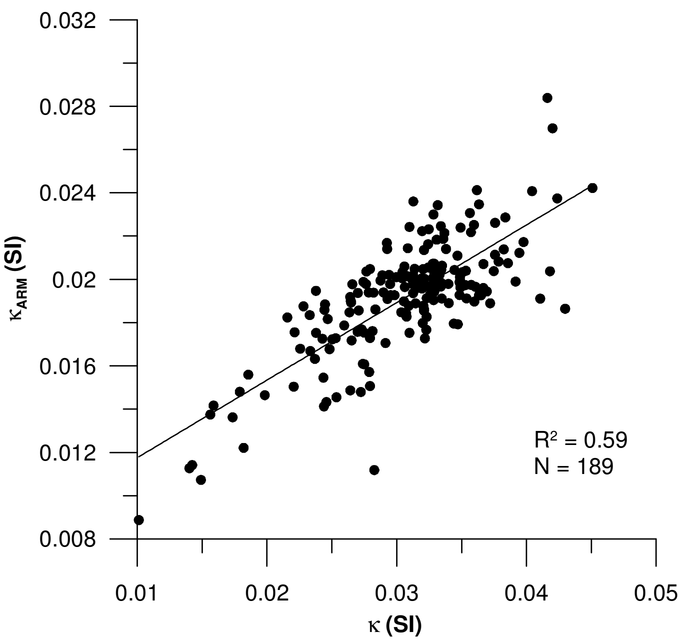

Figure 4.22. Cross-plot of κ and κ_{ARM} discrete sediment sample data from core TTR-451. Equation for regression fit line = Y = 0.3585979392 * X + 0.008171103605.

The first peak occurs at around 206 cm depth, and is characterised by a sharp reduction and gradual recovery of κ_{ARM}/κ values. The second peak is centred around 90 cm depth, and is conversely characterised by a gradual decline in κ_{ARM}/κ values and a sharp recovery. A much smaller amplitude low occurs at around 31 cm core depth, after which the κ_{ARM}/κ record only returns to higher values over a small interval of core, with a prominent low between 25 and 5 cm core depth. Comparison of the κ_{ARM}/κ results with the Fe/K and Ti/K ITRAX XRF data (Figure 4.21i & j, respectively) shows a fairly good degree of coherence in the upper 120 cm of core TTR-451 between the two sets of records. In particular, the sharp lows in the κ_{ARM}/κ record at around 90 and between 25 - 5 cm depth are also reflected in the Fe/K and Ti/K datasets, as well as the sharp increase at around 84 cm depth.

4.2.5. Palaeomagnetic and Directional Magnetic Results for core TTR-451

In a similar manner to core TTR-450, NRM was acquired from discrete sediment samples from core TTR-451 that were removed at 2.35 cm intervals along a continuous strip (for further details see section 3.3). The results from the NRM measurements are presented in Figure 4.21b. NRM values gradually increase from the base, attaining peak values at around 318 cm core depth. Between 318 and 220 cm, the NRM values level out before decreasing into a broad low between 220 and 134 cm. A second broad low in NRM values occurs between core depths of 134 and 31 cm, and a further sharp decrease occurs between 27 and 8 cm.

The palaeointensity records (NRM/κ and NRM/ARM) are shown in Figure 4.21d and e, respectively. These two datasets show a high degree of covariance and a cross-plot reveals R^2 values greater than 0.72 (Figure 4.23). NRM/κ and NRM/ARM values gradually increase from the base of core TTR-451 and peak at around 194 cm core depth (Figure 4.21d & e). A sharp low occurs close to the base of the core at around 456 cm, and a second is centred at around 267 cm. Above 194 cm, NRM/κ and NRM/ARM values decline, reaching minima at around 162 cm. The NRM/κ and NRM/ARM values gradually increase to a core depth of 101 cm, above which values decrease to form a minima between 85 and 58 cm. Above this level, three sharp lows punctuate the NRM/κ and NRM/ARM records at 42, 26 and 19 cm depth.

Component directions were calculated from the discrete sample NRM measurements using the *Z-plot* programme. A good stability of remanence is demonstrated in section 3.3.3. Maximum Angular Deviation (MAD)3 values are shown in Figure 4.21f and were generally less than 2°, with an average value of 1.5°, indicating well-defined magnetisation components. The calculated component inclination values vary around a mean of 67.2°. Using the dipole equation (Equation 3.1), the expected inclination for the core site latitude was 72.8°. The component inclination values were therefore adjusted by +5.6° to fit the expected mean.

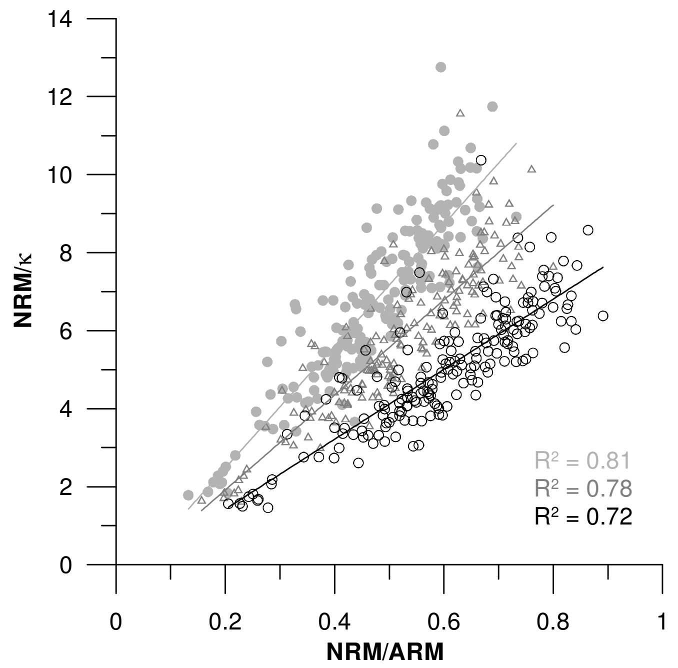

Figure 4.23. Cross plot of the NRM/ARM and NRM/κ data for core TTR-450. Light grey circles represent the NRM and ARM measured after AF demagnetisation at 20 mT, dark grey triangles are after AF demagnetisation at 25 mT, and black open circles are after AF demagnetisation at 30 mT. N = 231 for data collected after 20 and 30 mT AF demagnetisations and N = 207 for data collected after 25 mT AF demagnetisation.

The adjusted component inclination record is shown in Figure 4.21f. The record shows a very stable directional component, with only three notable anomalies. Low inclination values occur at the very base of core TTR-451. This may be an artefact of the base of the core as values recover to a higher angle of inclination by 457 cm depth. Two further broad lows occur between core depths of 189 and 122 cm, and 90 and 53 cm. The latter of the two anomalies shows a sharp recovery at around 66 to 63 cm core depth.

Figure 4.24 shows the unadjusted component declination record for core TTR-451. The angle of declination increases from –58 ° at the base of the core, to around 240 ° near the core top. Two sharp increases occur at around 165 cm and 22 cm core depth (red arrows in Figure 4.24). It is likely that the large range of values down core and these sharp changes result from the rotation of the sediment within the core liner during coring. Therefore, the component declination values are not used further.

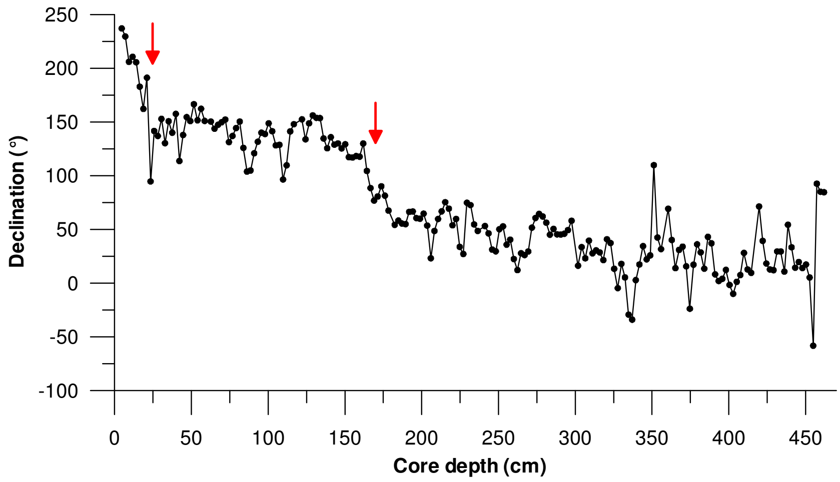

Figure 4.24. Record of component declination angles for core TTR-451. Red arrows show where sediments have likely rotated within the core liner.

4.2.6. Conclusions

Sediments from marine sediment cores TTR-450 and TTR-451 show a strong magnetic character and a good stability of remanence is demonstrated in section 3.3, which has allowed for the generation of robust records of palaeointenisty, a useful correlative and dating tool (e.g. Laj *et al.*, 2000; 2004). Large variations in the environmental magnetic records that indicate changes in magnetic grain size and concentration are observed in both TTR-450 and TTR-451. For the upper ~120 cm of core TTR-451, these variations occur at distinct sedimentary boundaries and are synchronous with changes in the ITRAX-XRF Fe/K and Ti/K records. These synchronous changes between the Fe/K and Ti/K records indicate that the key magnetic carrier likely is (titano)magnetite. These findings are consonant with previous studies around the northern North Atlantic that suggest a common source for the magnetic material at cores site located beneath the pathway of North Atlantic Deep Water (NADW), namely, the Nordic Basaltic Province (e.g., Kissel *et al*., 1997; Laj *et al*., 2002). Due to the aforementioned high-amplitude variations in the upper ~120 cm of core TTR-451, further environmental magnetic studies shall focus upon this interval of core.

4.3. Investigation of the magnetic parameter κ_{ARM}/κ as a measure of magnetic grain size, and comparison with sortable silt grain size data.

This subchapter describes the record of κ_{ARM}/κ for the upper ~120 cm of core TTR-451 in detail and the cross validates the measurements with additional κ_{ARM} (u-channel) and κ datasets. As briefly described in section 4.2.4, the uppermost 120 cm of core TTR-451 (for location see Figure 3.1) shows a number of sharp shifts in the environmental magnetic parameters magnetic susceptibility (κ) and susceptibility of Anhysteretic Remanent Magnetisation (κ_{ARM}), and hence also the ratio of κ_{ARM}/κ. These sharp shifts in the environmental magnetic records correspond to fluctuations in the ITRAX-XRF measurements of Ti/K and Fe/K, as well as changes in the core sedimentology (see section 4.1).

Next, magnetic hysteresis loops and their parameters, Saturated Isothermal Remanent Magnetisation (SIRM) and backfield remanence curves, are presented along with First Order Reversal Curve (FORC) diagrams for a selection of samples. Together, these analyses test the assumption of the (titano)magnetite dominated magnetic mineral content of the sediments from core TTR-451, and give indication of magnetic mineral, domain states, and hence, also magnetic mineral grain sizes.

Key results from Scanning Electron Microscopy (SEM) image analysis of polished thins sections are presented to validate the assumption of a (titano)magnetite magnetic mineral composition, and furthermore to 'ground-truth' the magnetic mineral grain size estimates that were gained from the environmental magnetic measurements.

Finally, a new record of mean sortable silt grain sizes, which is an established proxy for bottom current flow intensity (McCave *et al.* 1995a, b; 2006; Bianchi and McCave, 1999; Hall *et al.*, 2001), is presented for core TTR-451. These data were generated from subsamples of the same sediment on which κ and κ_{ARM} were measured, in order to test and corroborate the suggestion that magnetic mineral concentration (κ_{ARM}) and, especially, magnetic mineral grain size (κ_{ARM}/κ) variations reflect changes in NADW flow strength (Kissel *et al.*, 1999a; Laj *et al.*, 2002).

4.3.1. Background

The ratio of κ_{ARM} versus κ is a proxy for magnetic mineral grain size when the sediment's magnetic mineral content is dominated by (titano)magnetite (Banerjee *et al.*, 1981; Verosub and Roberts, 1995). Previous work supports the assumption of constant magnetic mineralogy along the NADW flow path in the vicinity of Eirik Drift (Kissel *et al.*, 1999a; Laj *et al.*, 2002). Eirik Drift represents a key region for deposition of suspended matter transported out of the Nordic Seas, especially for transportation via deep-water overflow through Denmark Strait (between Iceland and Greenland). The magnetic mineral content of sediments in that region originates from a single common source, the Nordic basaltic province (Kissel *et al.*, 1999a; Laj *et al.*, 2002). The new κ_{ARM}/κ record from core TTR-451 (Eirik Drift) therefore likely reflects variations in the size of the coarsest magnetic grains that can be carried by NADW out of the Nordic Seas and that settle out on Eirik Drift as NADW rounds the southern tip of Greenland. Lower κ_{ARM}/κ values represent coarser grain sizes (Banerjee *et al.*, 1981), and are suggested to reflect increased intensity of NADW formation (Kissel *et al.*, 1999a; Laj *et al.*, 2002; Snowball and Moros, 2003).

4.3.2. κ_{ARM}/κ record for the top ~120 cm of core TTR-451.

The records of low-field volumetric magnetic susceptibility, κ, κ_{ARM}, and κ_{ARM}/κ that were measured from the discrete sample set of core TTR-451 are shown for the upper ~120 cm of the core in Figure 4.25a, b & c, respectively. A high degree of covariance of the three magnetic records is apparent, and when the κ and κ_{ARM} records are cross-plotted (Figure 4.26) an R^2 value of 0.57 (N=48) is revealed.

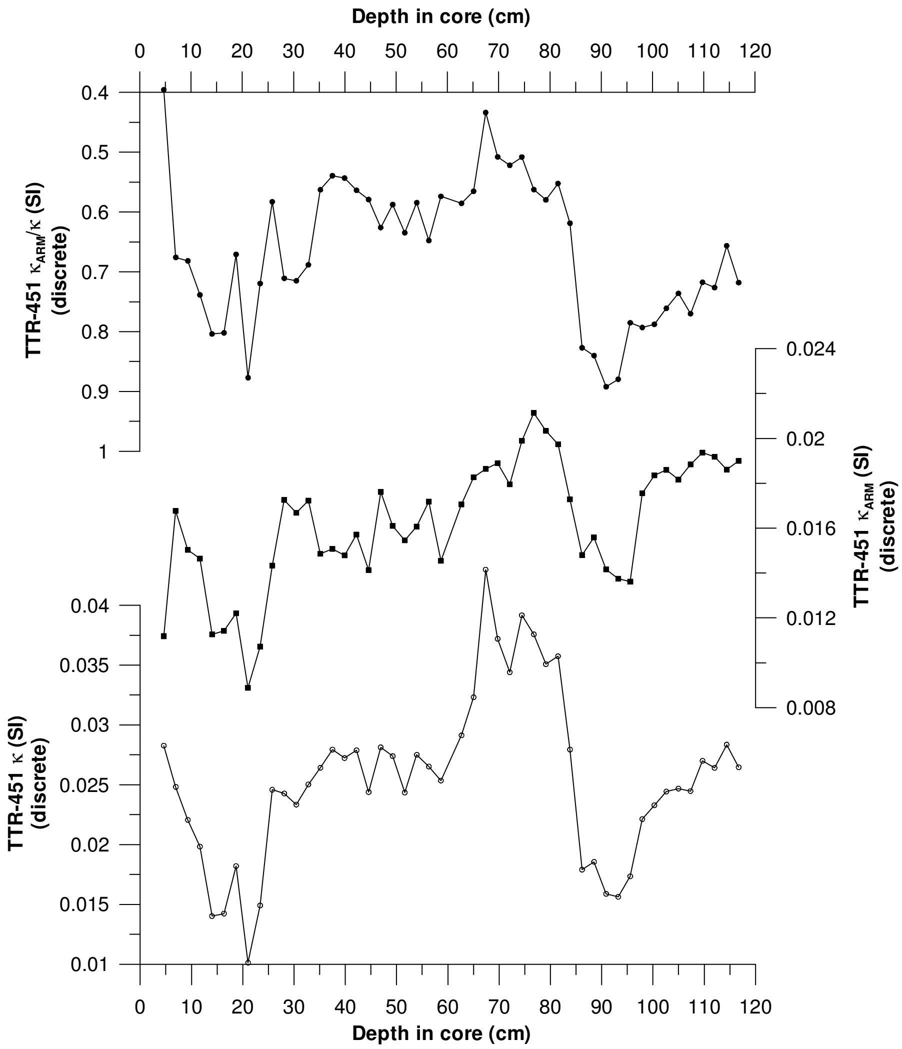

Figure 4.25. The low-field magnetic susceptibility (κ) record for the upper 120 cm of core TTR-451 is presented in (a), panel b shows the susceptibility of Anhysteretic Remanent Magnetisation (κ_{ARM}), and panel c shows the ratio of κ_{ARM}/κ. NB: note the inverted axis.

Significantly lowered magnetic susceptibility and κ_{ARM}, and correspondingly high (note the inverted axis) κ_{ARM}/κ values occur between core depths of 98 and 84 cm (Figure 4.25 a, b & c), indicative of sediments with relatively low concentrations of magnetic ((titano)magnetite) material and smaller magnetic mineral grain sizes. At around 84 cm core depth, a sharp increase in the magnetic susceptibility and κ_{ARM} records indicates an abrupt increase in magnetic mineral concentration, and a correspondingly sharp decrease in κ_{ARM}/κ values suggests a significant increase in magnetic mineral grain sizes.

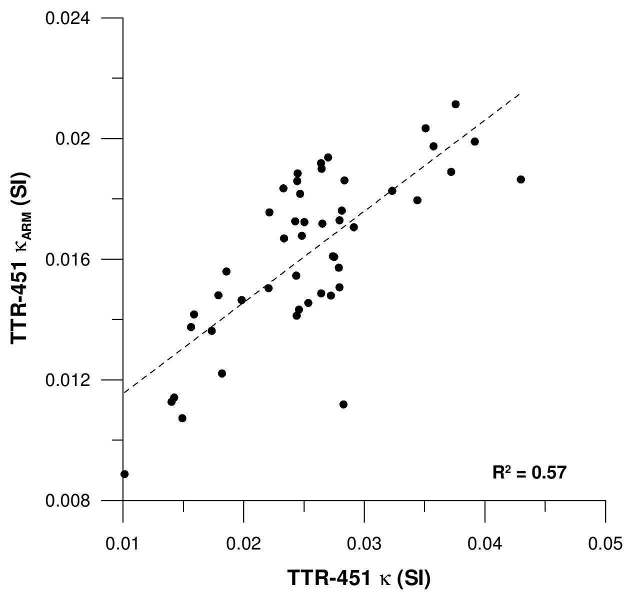

Figure 4.26. Cross-plot of the κ and κ_{ARM} data from discrete samples recovered from the upper 120 cm of core TTR-451 (N = 48). Equation for the regression fit line = Y = 0.3021837913 * X + 0.00852239289.

Peak κ_{ARM} values occur at 77.8 cm core depth (Figure 4.25b), whereas the magnetic susceptibility (Figure 4.25b) and κ_{ARM}/κ (Figure 4.25c) records have their maximum and minimum, respectively, later than this at 67.4 cm core depth. The magnetic susceptibility and κ_{ARM} values gradually decrease and near plateau between 58.6 cm and 27.9 cm core depth. Slightly higher κ_{ARM} values occur at 56.3, 47.0, and between 32.8 and 27.9 cm core depth. Above 67.4 cm depth, the κ_{ARM}/κ record indicates a gradual reduction of magnetic grain size, a maximum κ_{ARM}/κ value is reached at 56.3 cm depth after which values gradually decrease, attaining a minimum at 37.7 cm core depth. A further sharp increase in κ_{ARM}/κ values is centred on 30.6 cm depth.

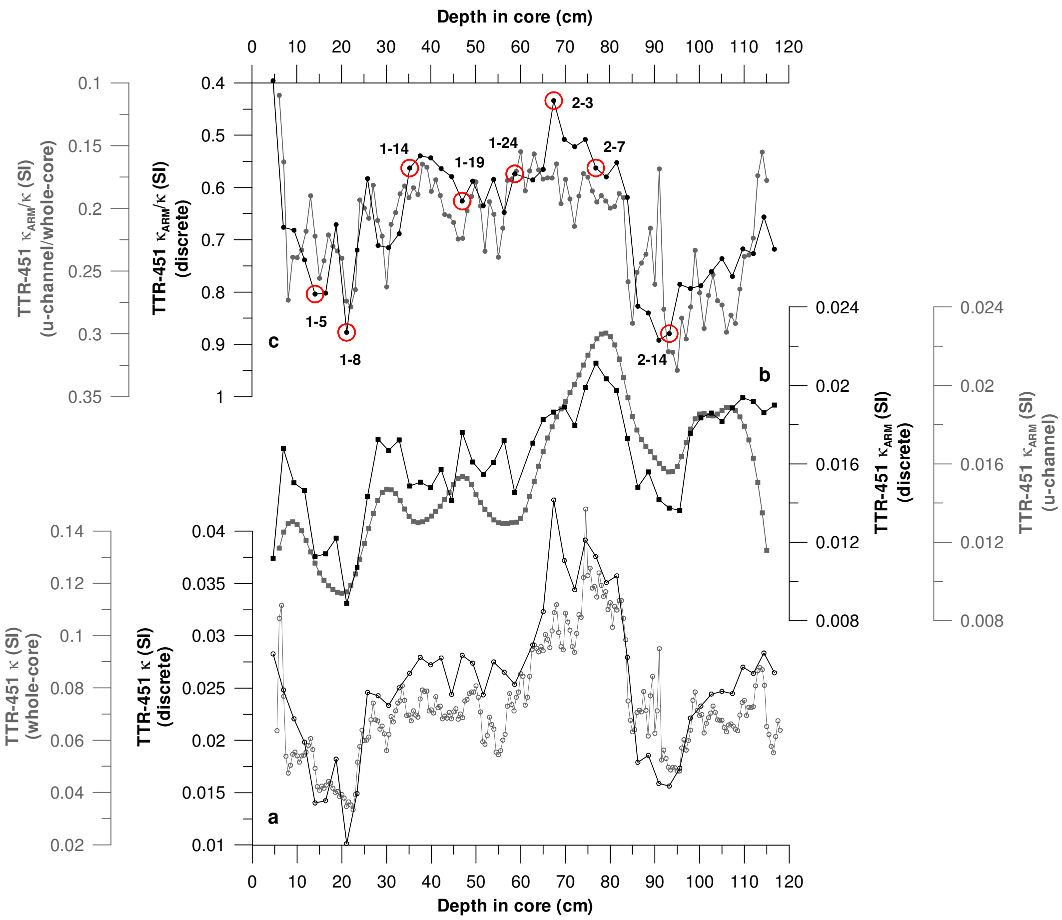

Figure 4.27. The magnetic susceptibility, κ_{ARM}, and κ_{ARM}/κ records for the upper ~120 cm of core TTR-451. The whole core and u-channel data, and the resultant 'hybrid' κ_{ARM}/κ record is shown in grey in cross-validation of the discrete sample data that is shown in black. The low-field magnetic susceptibility (κ) record is presented in (a), panel b shows the susceptibility of Anhysteretic Remanent Magnetisation (κ_{ARM}), and panel c shows the ratio of κ_{ARM}/κ. NB: note the inverted axis.

The κ_{ARM}/κ record shows a sharp decrease in values at 25.7 cm depth, prior to a similarly sharp increase, with maximum at 21.2 cm core depth. κ_{ARM}/κ values remain relatively high (inferred as reduced magnetic grain sizes) up to 7 cm core depth, after which values decline sharply. A significant and sharp low in the magnetic susceptibility (Figure 4.25a) and κ_{ARM} (Figure 4.25b) records occurs between ~24 and 11.4 cm core depth.

The discrete sample low-field volumetric magnetic susceptibility, κ_{ARM} and κ_{ARM}/κ records were cross-validated with higher resolution records made from 'whole-core' and continuous u-channel measurements (for further details see chapter 3). The whole-core magnetic susceptibility and κ_{ARM} records are shown in grey in Figure 4.27a &b, respectively, along with the resultant 'hybrid' u-channel κ_{ARM} versus whole core κ record which is shown in Figure 4.27c. These higher resolution duplicate records show excellent reproducibility and cross-validation of the discrete sample results.

Only two notable deviations are apparent between the discrete sample and the higher resolution hybrid κ_{ARM}/κ data. A relatively sharp shift to lower values is apparent exclusively in the hybrid κ_{ARM}/κ record between 92 and 86 cm depth and another occurs between 14 and 11 cm depth (Figure 4.27c). These likely result from normalising the smooth κ_{ARM} record by the relatively 'spiky' point sensor magnetic susceptibility data. Furthermore, the magnitude of the shift to lower values between 82 and 65 cm depth is greater in the discrete κ_{ARM}/κ record than in the hybrid κ_{ARM}/κ. Overall, however, with consideration of the difference in methods employed for generation of the higher-resolution datasets, the agreement with the far more robust discrete sample method is very good. Note, however, that the non-standard method used in creating the higher-resolution hybrid κ_{ARM}/κ record, allows its use only in validation of the overall trends in the discrete sample dataset, and not for interpretation.

4.3.3. Magnetic Grain Sizes: Hysteresis loops, SIRM and backfield remanence curves, and FORC Diagrams.

Eight discrete samples (encircled in red in Figure 4.27c) were subsampled for further magnetic measurements based on their very different κ_{ARM}/κ ratios, and include magnetic hysteresis loops, SIRM and backfield remanence curves, and First Order Reversal Curve (FORC) diagrams (for details on methods see chapter 3). These analyses were performed in order to better characterise the average magnetic grain size within the sediment samples.

Ferrimagnetic material (e.g., magnetite) becomes fully magnetically saturated (i.e., as magnetised as its mineralogical composition and the laws of thermodynamics permit) in applied magnetic fields of around 300 mT, whereas canted antiferrimagnetic minerals (e.g., hematite) saturate in fields in excess of 2.5 T (Verosub and Roberts, 1995). Where the magnetic content of a sediment sample is known to be magnetite, certain magnetic hysteresis parameters and their ratios, namely the saturation magnetisation (M_s) versus the saturation remanence (M_r) and the coercivity (B_c) versus coercivity of remanence (B_{cr}), can be used to determine the domain state and grain size of the magnetic material (Day *et al.*, 1977). The magnetic parameters, M_s, M_r, B_c and $B_{cr,}$ are defined in sub-chapter 3.3.4.

For samples containing coarse multi-domain (MD) grains, M_r/M_s <0.05 and B_{cr}/B_c >4, while samples dominated by fine grain single domain (SD) grains, M_r/M_s >0.5 and B_{cr}/B_c <1.5 (Day *et al.*, 1977). Pseudo single domain grains (PSD) are represented by values in between these two extremes. For magnetite, the SD/MD grain size transition is estimated primarily from theoretical calculations, at around 70 nm. For PSD grains, which show high remanence (SD), but low coercivity (MD) characteristics, the grain size range is estimated between 0.1 and 20 µm (Fabian *et al.*, 1996).

Interpretation of domain state and grain size from hysteresis parameters can be ambiguous due to magnetostatic interactions (e.g., Dunlop, 2002a, b), and where samples contain different admixtures of magnetic particles with variable domain states hysteresis parameters do not provide a detailed understanding of the individual components (Roberts *et al.*, 2000).

FORC diagrams provide a better way of characterising individual magnetic components, and were pioneered by Roberts *et al*. (2000). FORC diagrams have since been used to investigate a wide range of magnetic particle systems with both synthetic and natural samples (Pike *et al*., 1999; 2001; Roberts *et al*., 2000; Muxworthy and Dunlop, 2002; Carvallo *et al*., 2003; 2005; 2006). A FORC diagram is a contour plot of the First Order Reversal Curve (FORC) distribution and it is convenient to change the coordinates from H and H_r to $H_c = (H - H_r)/2$ and $H_b = (H + H_r)/2$, where H and H_r are the positive and reverse field in which the samples are magnetically saturated. For further explanation see sub-chapter 3.3.4.

The magnetic hysteresis loops and SIRM and backfield remanence curves for the eight samples selected from core TTR-451 are shown in the left hand panel of Figure 4.28, and the FORC diagrams for each sample are shown in the adjacent right hand panel. For the hysteresis loops and SIRM and backfield remanence curves, the magnetisation intensities have been mass normalised so that the vertical axis units are Am^2/kg. The magnetic parameters, M_s, M_r, B_{cr} and B_c that were acquired from the hysteresis loops are given in Table 4.2, and cross-plots of M_r/M_s versus H_r/H_c (Day plot) and κ_{ARM}/κ versus M_r/M_s values are shown in Figure 4.29 and 4.30, respectively.

Sample number	Depth (cm)	κ_{ARM}/κ	M_s (Am^2/kg)	M_r (Am^2/kg)	H_c*10^{-2} (T)	H_r*10^{-2} (T)	M_r/M_s	B_{cr}/B_c
TTR-451 1-5	14.00	0.8039	0.2579	0.05623	1.7035	4.7416	0.2180	2.7834
TTR-451 1-8	21.05	0.8771	0.2294	0.05287	1.8414	4.9326	0.2304	2.6787
TTR-451 1-14	35.15	0.5628	0.3611	0.05649	1.3624	4.2361	0.1565	3.1094
TTR-451 1-19	46.90	0.6260	0.3672	0.05998	1.4090	4.2767	0.1634	3.0352
TTR-451 1-24	58.65	0.5739	0.3847	0.05786	1.2387	3.4563	0.1504	2.7903
TTR-451 2-3	67.38	0.4337	0.4585	0.06373	1.1611	3.3653	0.1390	2.8984
TTR-451 2-7	76.78	0.5626	0.5649	0.08569	1.2456	3.4367	0.1517	2.7590
TTR-451 2-14	93.22	0.8796	0.2005	0.03650	1.4272	3.6609	0.1821	2.5651

Table 4.2. Magnetic properties of sediment samples from core TTR-451. The magnetic parameters are given to 4 significant figures.

a. TTR-451 1-5 14.00 cm **κ_{ARM}/κ = 0.839**

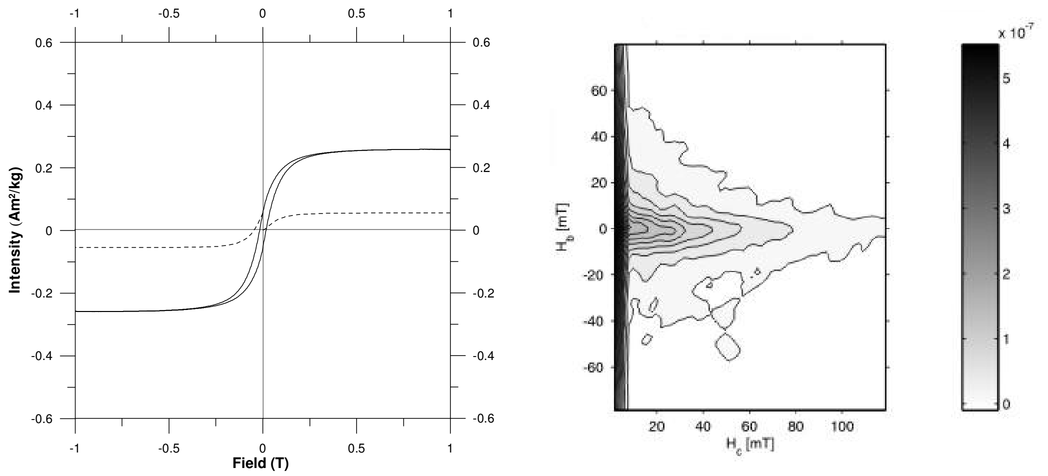

b. TTR-451 1-8 21.05 cm **κ_{ARM}/κ = 0.8771**

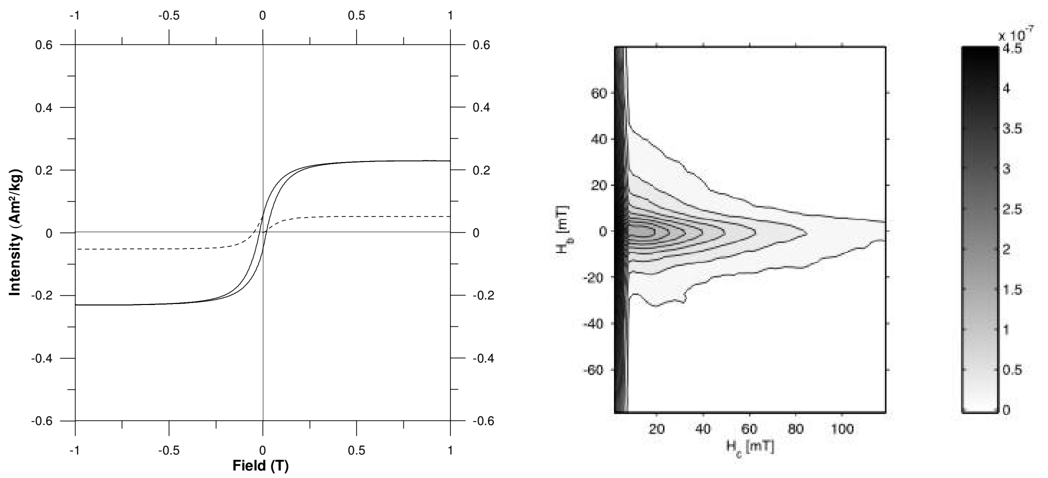

c. TTR-451 1-14 35.15 cm **κ_{ARM}/κ = 0.5628**

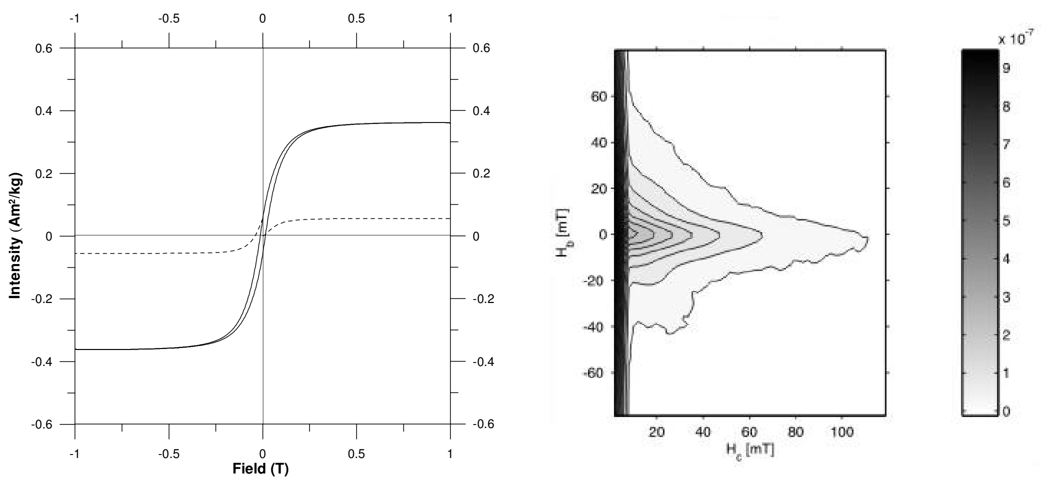

d. TTR-451 1-19 45.90 cm **κ_{ARM}/κ = 0.6260**

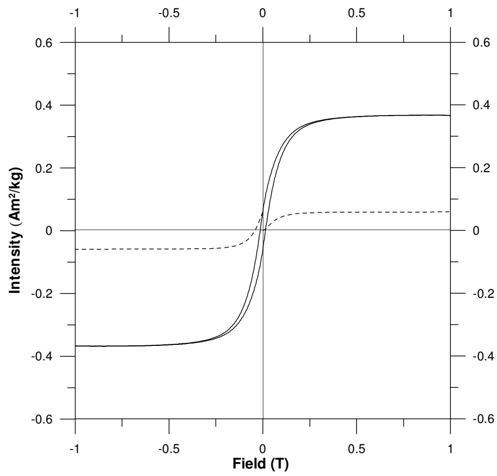

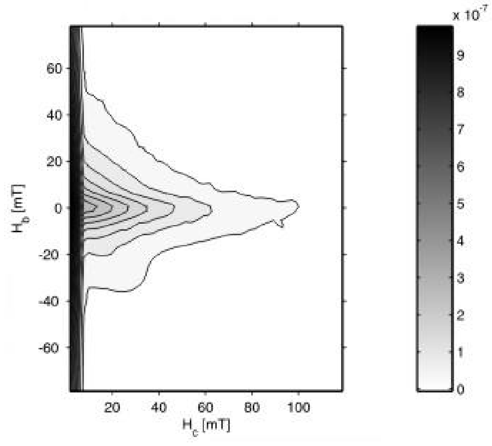

e. TTR-451 1-24 58.65 cm **κ_{ARM}/κ = 0.5739**

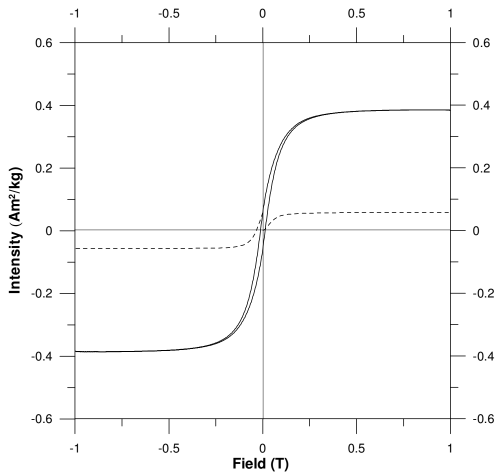

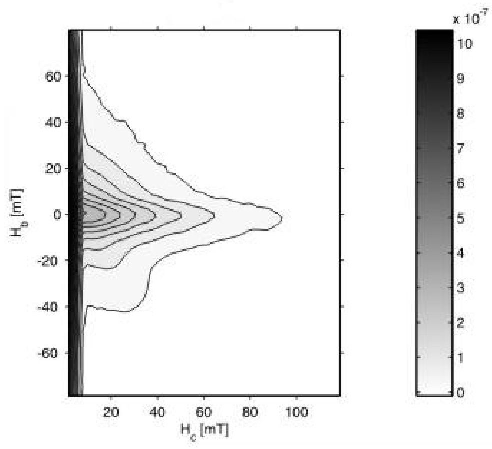

f. TTR-451 2-3 67.38 cm **κ_{ARM}/κ = 0.4337**

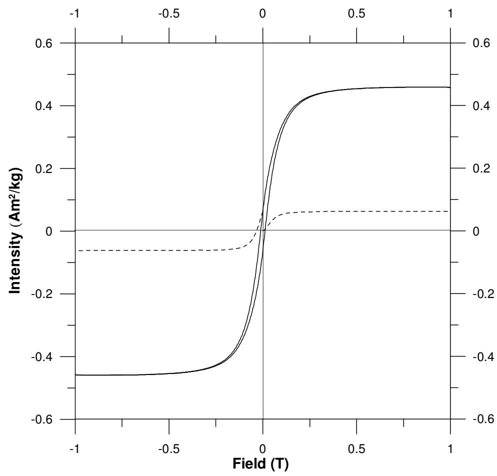

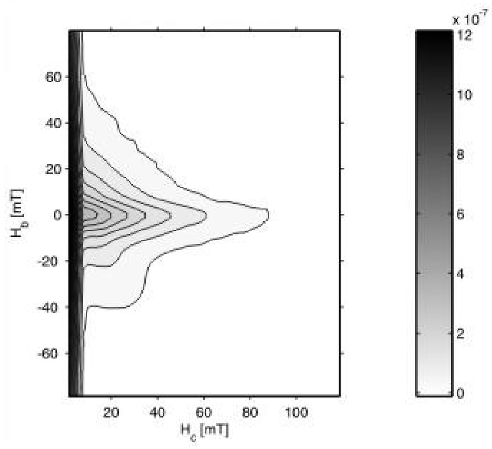

g. TTR-451 2-7 76.78 cm **$\kappa_{ARM}/\kappa = 0.5626$**

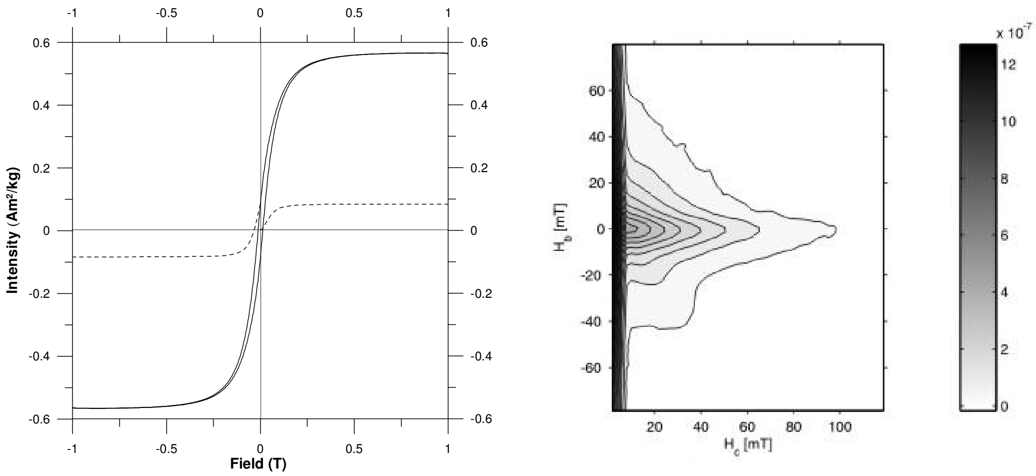

h. TTR-451 2-14 93.22 cm **$\kappa_{ARM}/\kappa = 0.8796$**

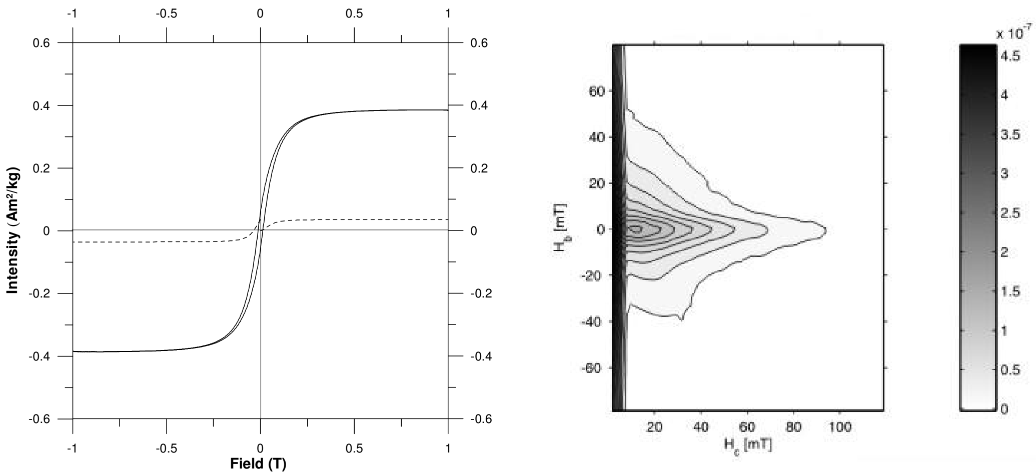

Figure 4.28. Magnetic mineral analyses of eight sediment samples from the top ~120 cm of core TTR-451. Magnetic hysteresis loops (solid line) and SIRM and backfield single remanence curves (dashed line) are shown in the left hand panel, and the corresponding FORC diagram is shown in the right hand panel. A smoothing factor of 4 is used for the generation of the FORC diagrams. Note that for the hysteresis curves and SIRM/backfield acquisition curves the data have been normalised by mass (i.e. Am^2/kg) for sample comparison. The κ_{ARM}/κ values are additionally given in the top right hand corner of the FORC diagram.

The magnetic hysteresis loops from TTR-451 all have a constricted (narrow waisted) shape, characteristic of PSD/MD magnetic grain sizes (Dunlop *et al.*, 1990; Roberts, *et al.*, 1995). Low SIRM magnetisations indicate a magnetic mineralogy of (titano)magnetite. Samples with higher κ_{ARM}/κ values (TTR-451 1-5, 1-8 and 2-14) have lower SIRM intensities, indicating that they predominantly contain finer magnetic grain sizes. For all samples, the hysteresis parameters give ratios M_r/M_s and H_r/H_c of between 0.1 to 0.3, and 2.5 to 3.2, respectively (Table 4.2), which suggests that all samples primarily contain magnetic grains with PSD sizes (Day *et al.*, 1977). A Day plot (Day *et al.*, 1977) of the hysteresis parameters M_r/M_s versus H_r/H_c (Figure 4.29) shows that the data cluster within the centre of the PSD grain size field and have similar distributions as data from other sediment samples recovered from the northern North Atlantic (Kissel *et al.*, 1997; 1999; Snowball and Moros, 2003).

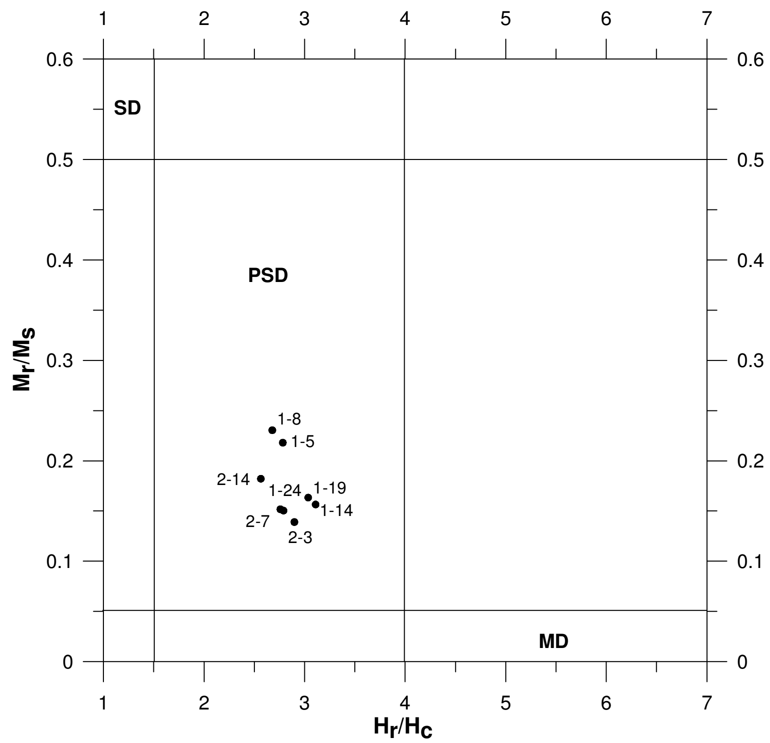

Figure 4.29. Magnetic hysteresis ratios M_r/M_s versus H_r/H_c reported on a Day diagram (Day *et al.*, 1977) for core TTR-451. A PSD average (titano)magnetite grain size is indicated. Sample numbers are given next to each data-point.

In order to investigate the relationship between the κ_{ARM}/κ values and the hysteresis parameters (both indicators of average magnetic grain sizes), the ratio of the magnetisations (M_r/M_s) is cross-plotted versus the κ_{ARM}/κ data (Figure 4.30). A positive linear relationship is observed between these two datasets, with an R^2 value of 0.78 (see dashed trend-line in Figure 4.30). Sample TTR-451 2-14, however, shows relatively high M_r/M_s values in comparison to its κ_{ARM}/κ value and deviates from the trend line. By removing this sample, the correlation coefficient is much improved (see solid trend-line in Figure 4.30) to give an R^2 value of 0.96.

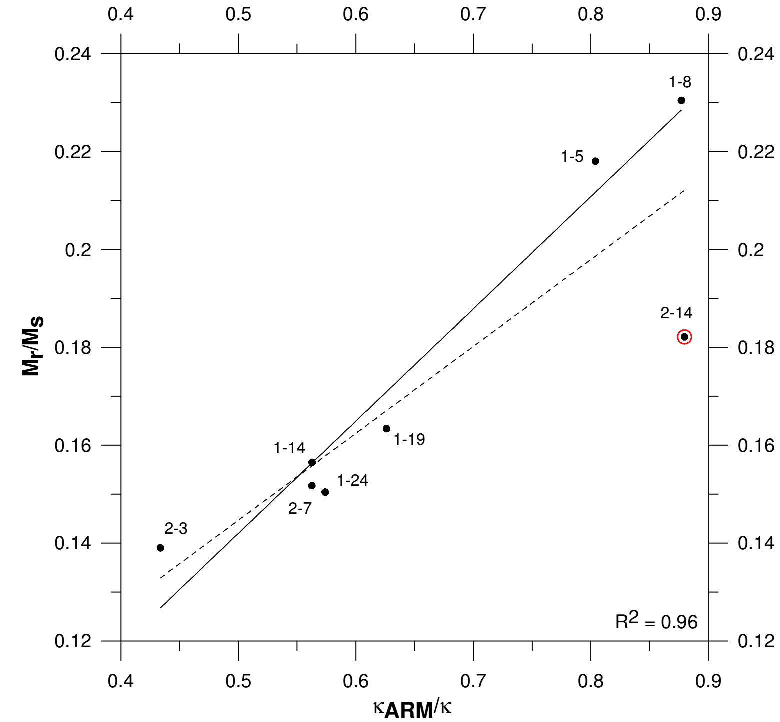

Figure 4.30. Cross-plot of average magnetic grain size indicators κ_{ARM}/κ versus the hysteresis parameters M_r/M_s. The dashed trend line is for all data, whereas the solid trend line is without sample TTR-451 2-14 (encircled in red).

The FORC diagrams (Figure 4.28) for all samples show divergent contour distributions which intersect the vertical H_b axis at $H_c = 0$. Following Roberts *et al*. (2000), these results indicate that the samples predominantly contain

PSD/MD magnetites and are therefore consistent with results from the magnetic hysteresis loop analyses. Samples with higher κ_{ARM}/κ values, lower SIRM acquisition intensity, and lower values of M_r and M_s magnetisations (Figure 4.28a, b & h), have FORC distributions with comparatively less spread along the vertical (H_b) axis (less divergent contours), and, for sample TTR-451 2-14, even closed contours. These closed contours at H_c <20 mT are indicative of the presence of non-interacting SD magnetic grains (Roberts *et al.*, 2000). It is also noteworthy that compared to the other FORC distributions, samples TTR-451 1-5 and 1-8 (Figures 4.28a & b) have contours which spread out more along the horizontal (H_c) axis (i.e. have higher peak coercivities). After Roberts *et al.* (2000), these samples, therefore, show behaviour of PSD/MD type magnetic particles, but are finer grained with the some non-interacting SD type grains present.

Conversely, samples that have the lowest κ_{ARM}/κ values, highest SIRM acquisition intensity and highest M_r and M_s values (e.g., TTR-451 2-3 and 2-7; Figures 4.28f & g) have FORC diagrams with contours that are more divergent, shallower and that are more spread out along the vertical (H_b) axis. Therefore, consistent with the inferences drawn from the κ_{ARM}/κ and hysteresis parameters, the FORC distributions for these samples indicate a magnetic grain assemblage comprising predominantly PSD/MD type grains, but display more MD like behaviour, i.e. they have coarser magnetic grain sizes (e.g., Carvallo *et al.*, 2003).

4.3.4. Scanning Electron Microscope (SEM) study of magnetic grain sizes.

Subsamples from discrete sediment samples TTR-451 1-5, 1-8, 1-14, 1-19, 1-24, 2-3, 2-7 and 2-14 were lightly ground, resin embedded and made into polished thin sections. Mosaics of 15 x 15 SEM images were collected for each sample at a magnification of x1000. In total 1800 separate images were collected. SEM – Electron Dispersal Spectroscopy (EDS) allowed for identification of (titano)magnetites, recognised by an elemental composition of only iron, titanium, silica and aluminium oxides. *PGT IMIX* image analysis software was calibrated using the acquired elemental data to automatically count and measure (titano)magnetite grains. The (titano)magnetites were the brightest grains within the sample (Figure 4.31) and easily identified. For details see Chapter 3.4.

Sample No.	Depth (cm)	κ_{ARM}/κ (SI)	Average number of grains	% Area	Average diameter (µm)	Longest diameter (µm)	Area equivalent diameter (µm)
TTR-451 1-5	14.00	0.804	9.36	0.047	2.66	3.29	2.06
TTR-451 1-8	21.05	0.877	9.75	0.078	2.76	3.43	2.13
TTR-451 1-14	35.15	0.563	16.67	0.155	3.16	3.91	2.40
TTR-451 1-19	46.90	0.626	20.83	0.212	3.06	3.77	2.41
TTR-451 1-24	58.65	0.434	24.50	0.204	3.10	3.81	2.42
TTR-451 2-3	67.38	0.574	24.82	0.342	3.22	3.93	2.54
TTR-451 2-7	76.78	0.563	27.42	0.279	3.20	3.92	2.49
TTR-451 2-14	93.22	0.880	61.75	0.244	2.36	2.91	1.85

Table 4.3. Selected results from the SEM image analyses.

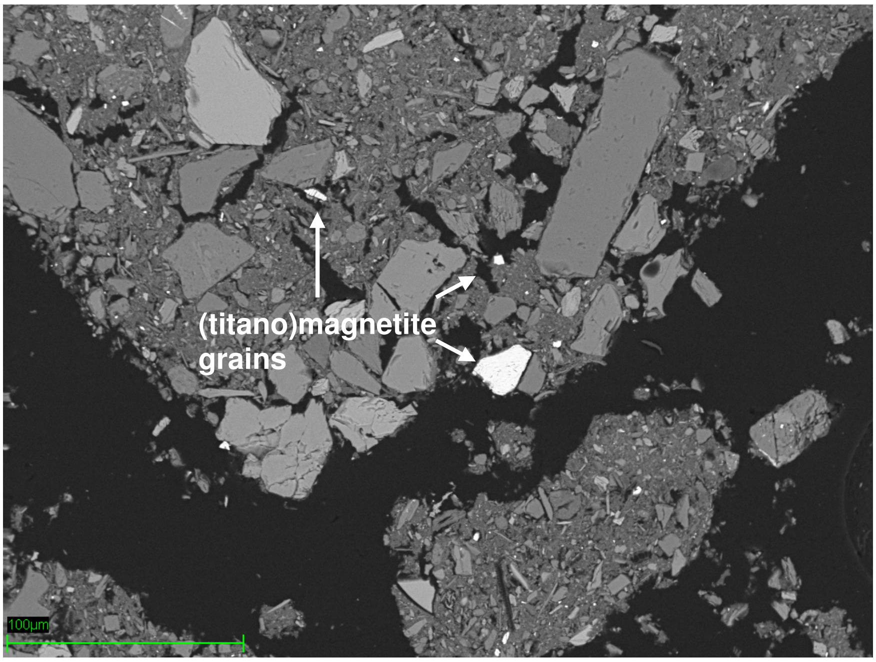

Figure 4.31. An example SEM image from sample TTR-451 2-14 (image number 1656) and shows characteristic (titano)magnetite grains. Magnification = x1000 and a scale bar is shown in the bottom left corner. 1 pixel = 0.359241 µm

Key results from the SEM image analysis are cross-plotted against the magnetic parameters κ_{ARM} and κ_{ARM}/κ, and shown in Figures 4.32 and 4.33. Firstly, the assumption is tested that κ_{ARM} for sediments from core TTR-451 is a measure of (titano)magnetite concentration. The cross-plot (Figure 4.32) shows a positive linear relationship, but reveals an R^2 value of only 0.40. This low correlation coefficient may result from bias introduced during the SEM image analysis, as areas of balsam resin without sediment coverage, were also included in the calculation. However, similar to previous magnetic investigations (see section 4.3.3), sample 1-24 appears to be an outlier. With this sample removed, the correlation coefficient is much improved, with an R^2 value of 0.69.

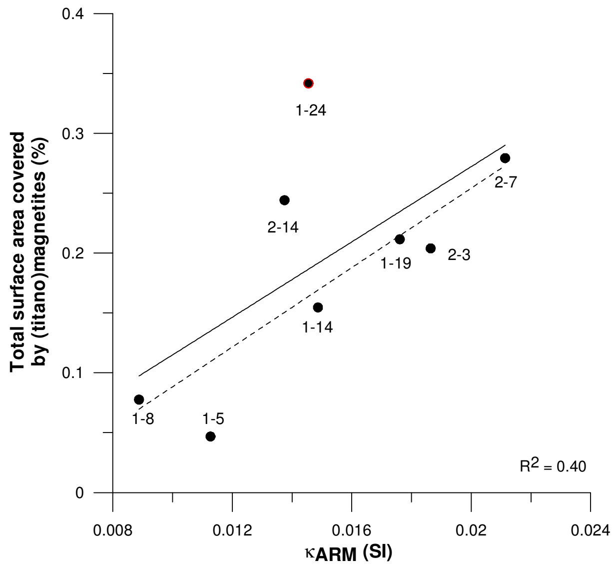

Figure 4.32. Cross-plot of the percentage area of the polished thin section covered by (titano)magnetites versus the magnetic measurement κ_{ARM}. Sample numbers are shown next to each data point. The dashed trend line is with sample 1-24 (encircled in red) removed.

Secondly, the assumption is tested that magnetic ratio κ_{ARM}/κ is a measure of average (titano)magnetite grain size for sediments from core TR-451. The cross-plot of κ_{ARM}/κ versus the calculated average (titano)magnetite grain size (Figure 4.33) shows an inverse linear relationship. Note that higher κ_{ARM}/κ values are interpreted as reflecting finer magnetic grain sizes (Banerjee *et al.*, 1981). Therefore, the SEM image analysis results from core TTR-451 (natural sediment samples) corroborate previous laboratory measurements of synthetic magnetite samples (Banerjee *et al.*, 1981). The cross-plot (Figure 4.33) gives an R^2 value of 0.76, indicating some correlation, although an F-test p-value of 0.12 suggests that the correlation is not classed significant with this low number of data points. Bias in the SEM image analysis was likely due to pitted grains being counted as multiple smaller grains (note the relatively high average number of grains per slide, yet fine grain sizes for sample TTR-451 2-14; Table 4.3). This error was reduced to some extent by manipulation of the software, but for differentiation between one or multiple grains remained difficult especially for the fine grains.

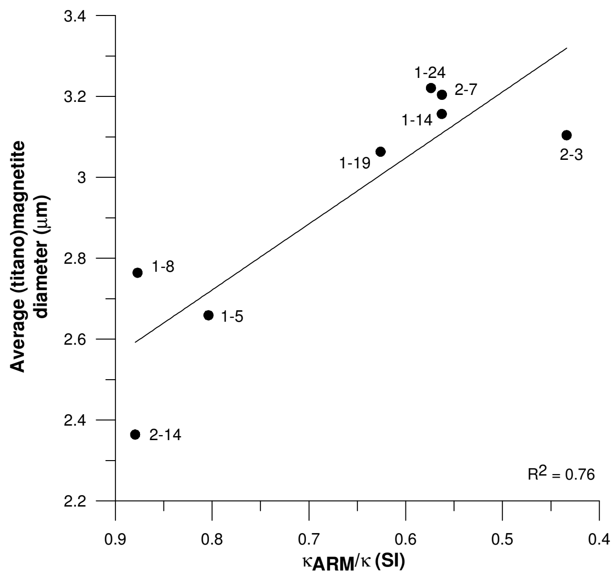

Figure 4.33. Cross-plot of the magnetic proxy κ_{ARM}/κ for (titano)magnetite average grain sizes versus measured (titano)magnetite grains sizes using SEM image analysis. Sample numbers are given next to each data point.

Overall, there appears to be reasonably good agreement between κ_{ARM}/κ for (titano)magnetite average grain size and the measured grain size from the SEM image analysis. The SEM results show that average (titano)magnetite diameters for the selected TTR-451 samples fall within a surprisingly narrow range, between 2.36 and 3.22 μm. These SEM results are therefore also in good agreement with the results from the hysteresis parameters and FORC diagrams (Figure 4.28 and 4.29), which are interpreted as representing a magnetic mineral composition of PSD type grains, with a grain size range of 0.1 to 20 μm (Fabian *et al*., 1996).

However, the measured narrow range of grain sizes could have implications if variations in κ_{ARM}/κ are interpreted to reflect average magnetic grain sizes that result from bottom current sorting, and thus used as a dynamic proxy for bottom current flow speed (e.g., Kissel *et al*., 1999a; Laj *et al*., 2002; Snowball and Moros, 2003). Firstly, one has to contemplate whether differences in the degree of bottom current sediment sorting would cause variation in such a narrow range of very small grain sizes. Secondly, it should be considered whether the variation in magnetic grain size may result not from the speed of current at the deposition site, but from the speed of current and ability to erode the bedrock at the source. Thirdly, the validity of these magnetic measurements as a near bottom flow speed indicator should be questioned as the magnetic grain size range falls below the grain size threshold for current sorting (McCave *et al*., 1995b), i.e., the magnetic grains have diameters that are less than 10 μm and therefore should behave cohesively. Therefore, the data from the κ_{ARM}/κ method in core TTR-451 are tested to establish this method's suitability to portray past bottom current flow speed. This is done by comparison with mean sortable silt grain size measurements made on subsamples of exactly the same sediment samples.

4.3.5. Mean sortable silt measurements versus the magnetic ratio κ_{ARM}/κ as near bottom current flow speed proxies.

The grain size distribution of terrigenous particles within the 10-63 μm size range, or sortable silt size range as defined by McCave *et al*. (1995b), is considered to be a sensitive index for near bottom current strength. Variations of the mean grain sizes within the sortable silt grain size window have been interpreted to reflect changes in intensity of near bottom strength (e.g., Bianchi and McCave, 1999) as more vigorous flow prevents deposition of the finer grains, biasing the mean grain size towards higher values (Ledbetter, 1984; McCave *et al.*, 1995b). For in-depth reviews on the background understanding, techniques and pitfalls of the sortable silt method, see McCave *et al.* (2006) and McCave and Hall (2006).

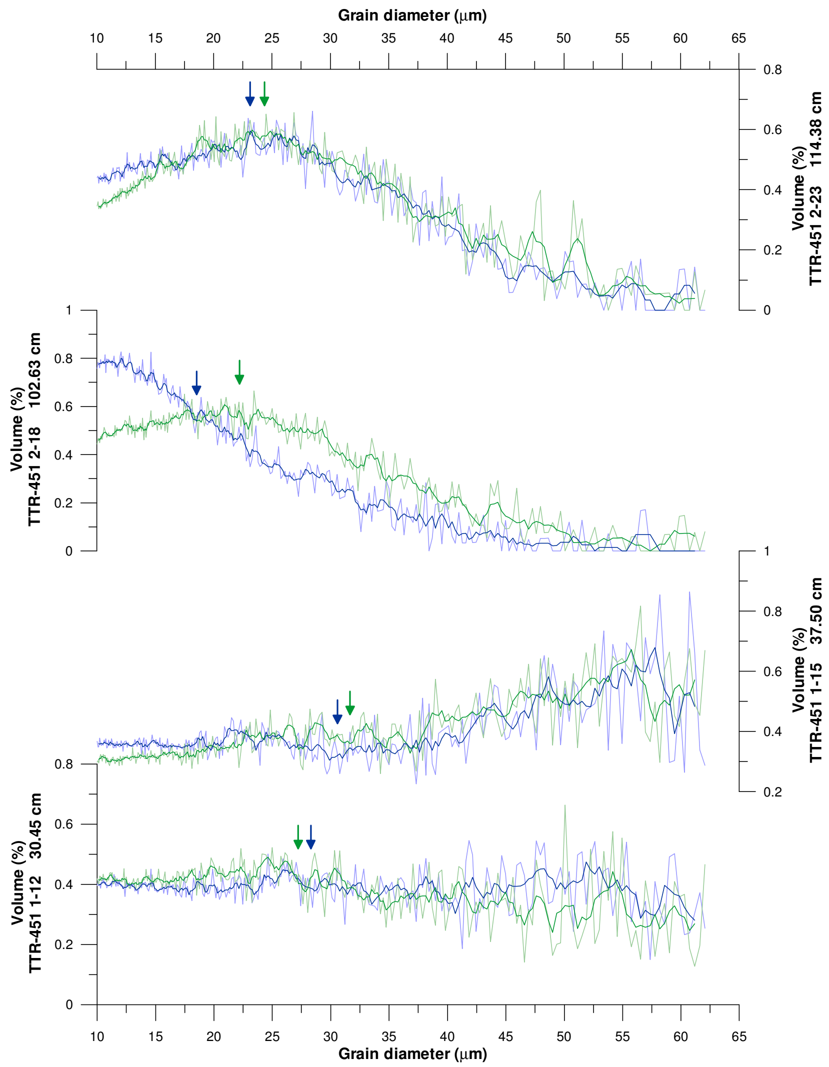

Figure 4.34. Comparison of sortable silt grain size distributions and mean sortable silt grain sizes of duplicate results for a selection of samples analysed at the beginning and end of each batch. The blue line represents the results from the first run and the green line represents the results from the second run. A 5-point running average is shown by the darker coloured blue and green lines, respectively. The mean sortable silt values are shown by blue and green arrows for the first and second runs, respectively.

The sortable silt grain size distributions were measured at the *School of Earth, Ocean and Planetary Sciences* in *Cardiff University* in collaboration with Dr. I. Hall, using a *Beckman Multisizer 3* Coulter Counter, and subsamples of the discrete sample-set for which the κ_{ARM}/κ measurements were made (for further details see chapter 3). Only the samples from the top ~120 cm of core TTR-451 were used in this study. Mean sortable silt values were calculated using the *Multisizer 3* software (see operator's manual; PN 8321681 Rev. B).

Samples were analysed in two batches. For procedural error identification purposes, the first few samples analysed were re-analysed at the end of sample batches. This was done as sediment samples were added to the electrolyte '*isoton*' solution after manual shaking of samples, and an aliquot taken using a pipette. Any delay between the shaking of the sample and removal of the aliquot may have biased the mean sortable silt grain sizes to finer diameters as coarser grains would have settled out first (for further discussion see section 3.5). It is likely that this process became faster with repetition, therefore biasing the first few samples analysed towards finer grain sizes. The measures described were used to identify any such bias.

Figure 4.34 compares the sortable silt grain size distributions and mean grain sizes (see arrows in Figure 4.34) for a selection of the duplicate sample analyses. For three of the samples (TTR-451 1-12, 1-15 and 2-23), very little difference is seen between the grain size distributions. Also, the mean sortable silt values between these duplicates differ by <1.29 µm. Sample TTR-451 2-18, however, shows a different grain size distribution for the duplicate analyses, with the first analysis (in blue) significantly biased towards the finer grain sizes, and a total difference in mean sortable silt grain size of 3.53 µm. Sample TTR-451 2-18 was the first analysed within the second batch of samples and these results probably indicate that error was introduced via an increased time lapse between the shaking and pipetting of the sediment for the first analysis. Sample TTR-451 1-12 was the next sample analysed, and the excellent agreement between the data for the duplicate analyses, with the second analysis having a finer mean grain size, would indicate that this error did not propagate through the batch analyses.

For sample TTR-451 2-18, the results from the second analysis were used for the down core record of mean sortable silt grain sizes, as the first is considered to be erroneous.

Figure 4.35 shows the mean sortable silt grain sizes along with the κ_{ARM}/κ record for core TTR-451. A good visual correlation is seen, with low grain sizes at the base of the interval of study, a sharp rise at around 84 cm depth, and lowered grain sizes in the top 34 cm of the core. However, the magnitude of the shift to larger grain sizes at 84 cm depth is not reflected in the mean sortable silt grain sizes. Instead the sharp jump in the sortable silt record between 86 and 79 cm depth is preceded by a gradual increase. The biggest difference between the two records is observed in sample TTR-451 2-4 (69.7 cm depth), where a low in mean sortable silt grain sizes is coincident with near minimum κ_{ARM}/κ values (maximum magnetic grain sizes). A large deviation between the two records is also observed at 28.1 cm depth (sample TTR-451 1-9), where a relatively large mean sortable silt grain size is coincident with a relatively high κ_{ARM}/κ value (inferred fine magnetic grain sizes).

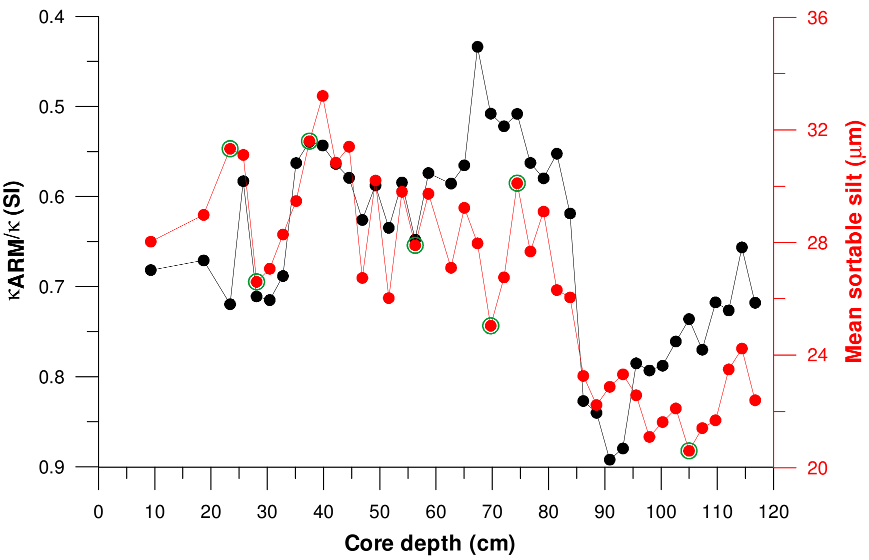

Figure 4.35. Comparison of the κ_{ARM}/κ record and mean sortable silt grain sizes for the top ~120 cm of core TTR-451. Data points highlighted in green are those presented in Figure 4.36.

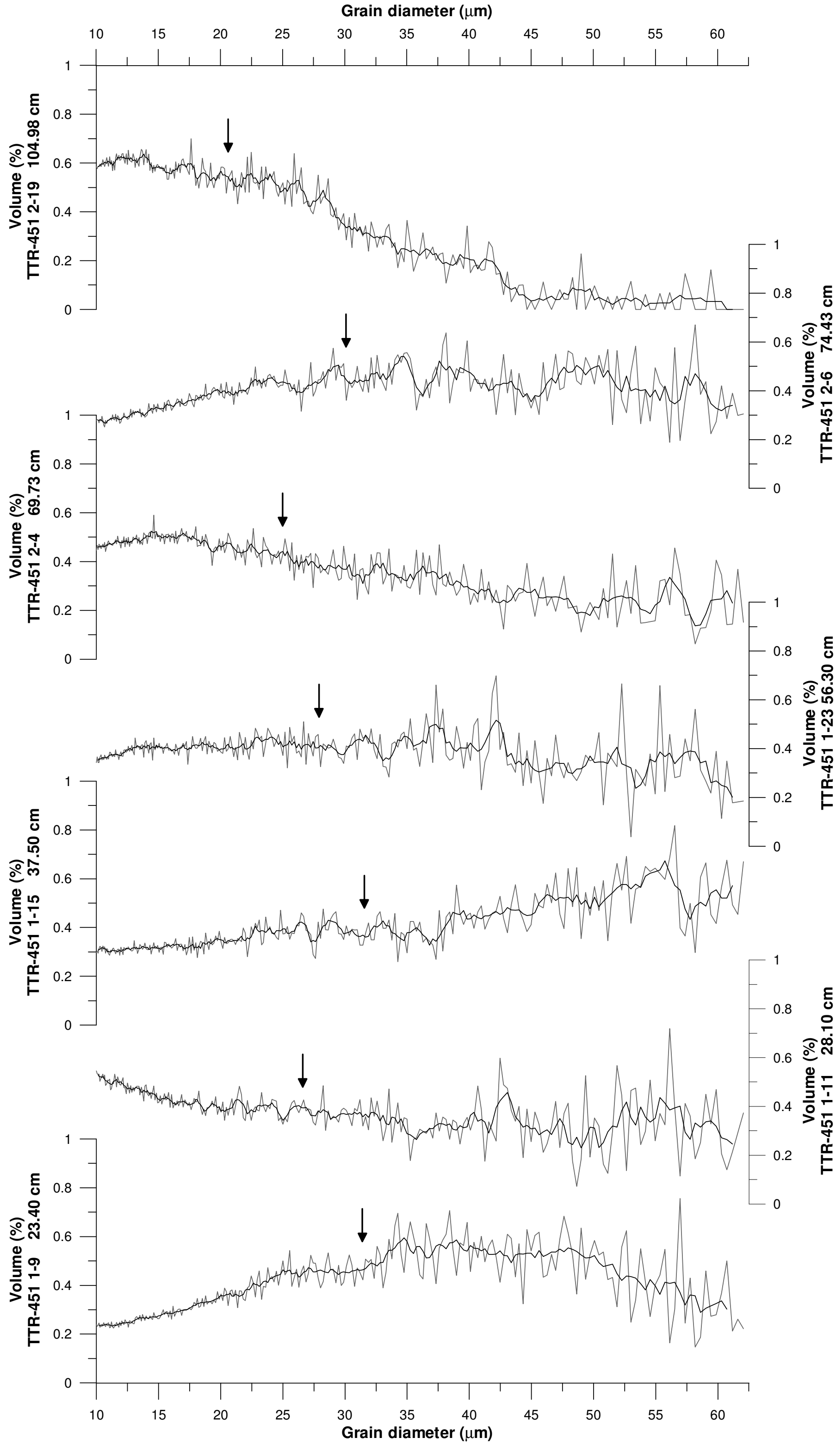

Figure 4.36. Results of the sortable silt grain sizes analyses for a selection of samples. The grain size distributions are shown in grey and a 5-point running average of the data is shown in black. Arrows represent the mean sortable silt grain size for each sample.

Figure 4.36 presents the sortable silt grain size distributions for the samples that are highlighted in green in Figure 4.35. The modality of the grain size distributions indicates how well sorted the sediments are. Samples that are well sorted have a uni-modal, narrow grain size distribution, and are normally indicative of stronger flowing near bottom currents (McCave *et al.*, 1995a, b).

Samples TTR-451 1-9 and 1-15 have distributions that are skewed towards coarser grain sizes and correspondingly coarser mean sortable silt grain sizes (Figure 4.36). Conversely, samples TTR-451 2-4 and 2-19 that have finer mean sortable silt grain sizes have distributions that are clearly skewed towards lower values. However, samples TTR-451 1-11 and 1-23 have poorly sorted grain size distributions and comparison of all the TTR-451 data to examples of grain size distributions in McCave and Hall (2006) would suggest relatively weak bottom currents over Eirik Drift.

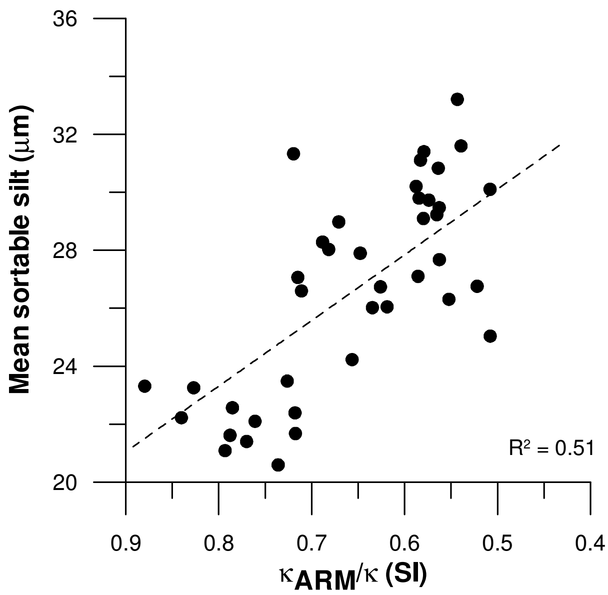

Figure 4.37. Cross-plot of the κ_{ARM}/κ and mean sortable silt values for the upper ~120 cm of core TTR-451. The dashed black line is the regression line (Y = -22.64802209 * X + 41.43328157) (N=42). Note that the κ_{ARM}/κ (x) axis is plotted on an inverted scale so that finer grain sizes are towards the y intercept (finer mean sortable silt grain sizes).

The statistical relationship between the κ_{ARM}/κ and mean sortable silt grain size record for core TTR-451 was tested by cross-plotting the two datasets (Figure 4.37). This reveals a linear, negative relationship (note the inverted x-axis), with an R^2 value which is relatively low at 0.51 (N = 42).

The robustness of the correlation between the κ_{ARM}/κ and mean sortable silt records is statistically tested using variance analyses. As the absolute values of the two dataset values are different by nearly three orders of magnitude, the variances are normalised by scaling the records between one and zero, where one represents the highest value for the sortable silt (coarsest grain size) and the lowest κ_{ARM}/κ value (inferred coarsest grain size). The two records are therefore shown in terms of their grain size variation. The scaling of one to zero is used to normalise the datasets rather than their standard deviation as for the latter, variance analyses would be invalid. Figure 4.38 shows the variance normalised κ_{ARM}/κ and mean sortable silt records.

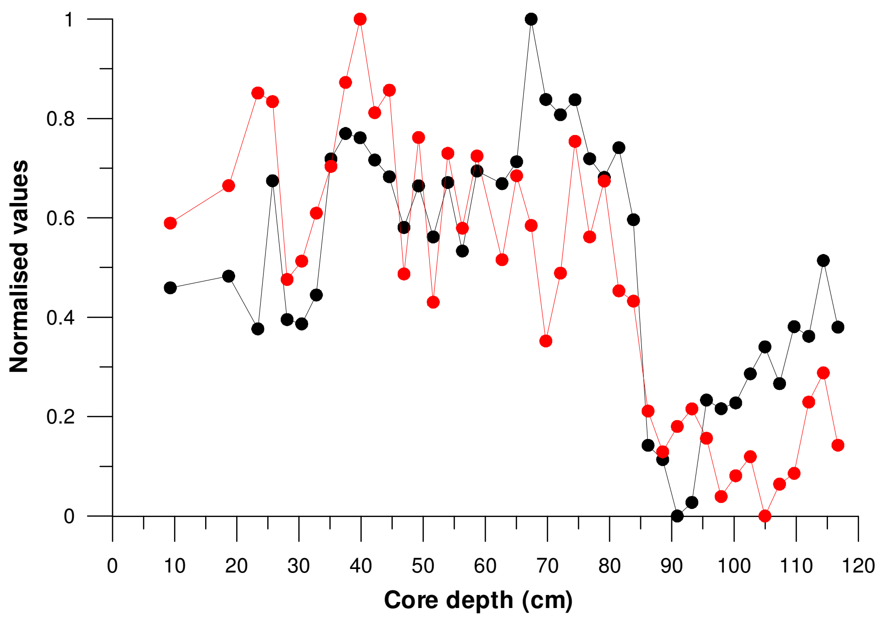

Figure 4.38. Normalised κ_{ARM}/κ (black) and mean sortable silt (red) records for the upper ~120 cm of core TT-451. Note that the κ_{ARM}/κ record has been inverted so that the two records are compared in terms of their relative grain size variations.

Figure 4.39 shows a histogram plot of the scaled κ_{ARM}/κ (black) and the mean sortable silt grain size (red) data. Figure 4.40 compares the cumulative probability distribution functions of the two datasets. Figures 4.39 and 4.40 demonstrate that the probability distributions of the κ_{ARM}/κ and mean sortable silt datasets are similar to one another. The cumulative probability function plot (Figure 4.40) indicates that the greatest difference between the two datasets occurs below normalised values of 0.4 (i.e., the finer grain sizes).

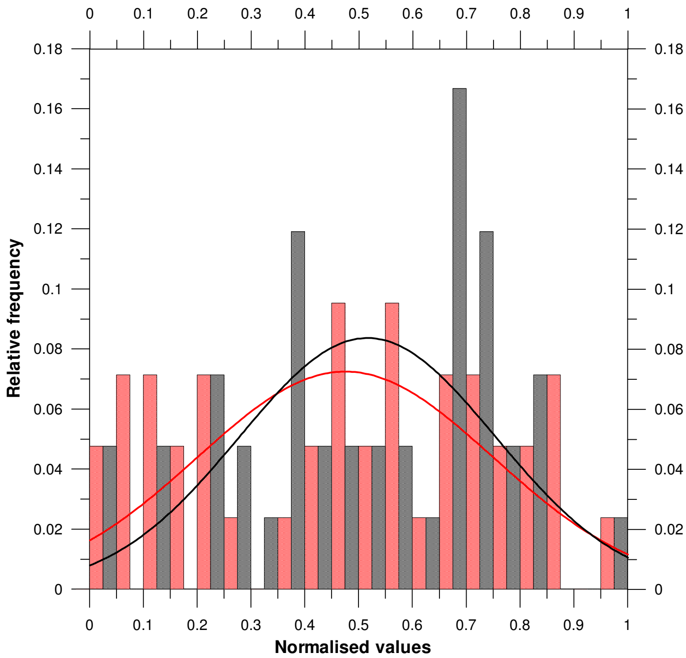

Figure 4.39. Histogram plot of the scaled κ_{ARM}/κ (black) and the mean sortable silt (red) data. The black and red lines show a Gaussian fit of the distributions for the κ_{ARM}/κ and mean sortable silt grain size data, respectively.

The correlation between the κ_{ARM}/κ and mean sortable silt grain size data is investigated using a two-sample Kolmogorov-Smirnov test in order to test the null hypothesis that the κ_{ARM}/κ and mean sortable silt data are drawn from the same distribution. A two-sample Kolmogorov-Smirnov test is an alternative non-parametric method for a two-sample t-test and uses the maximal distance

(D-value) between the two cumulative probability frequency distributions of these two populations of data as the statistic.

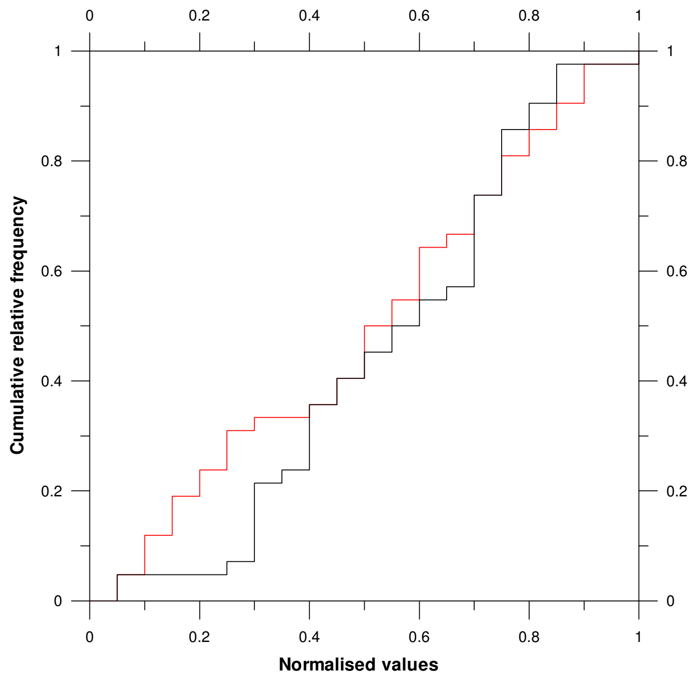

Figure 4.40. Cumulative probability distribution function of the κ_{ARM}/κ (black) and the mean sortable silt (red) data.

Table 4.4 presents the results of the two-sample Kolmogorov-Smirnov test between the κ_{ARM}/κ and mean sortable silt grain size data. A D-value of 0.1429 and a p-value of 0.7848 were obtained, indicating that the two datasets are correlated 78.48 % of the time. However, although the two-sample Kolmogorov-Smirnov test suggests a good degree of statistical correlation, a p-value of 0.7848 means that the null hypothesis cannot be rejected as there are not enough data to do so.

In summary, both the R^2 value and the two-sample Kolmogorov-Smirnov test indicate that there is some correlation between the κ_{ARM}/κ and mean sortable silt grain size data from core TTR-451, but that this correlation is statistically weak. However, based upon the good visual agreement of the two datasets and a p-value of 0.7848 from the two-sample Kolmogorov-Smirnov test, there is enough correlation between them for the validation of the κ_{ARM}/κ record as a proxy for near bottom current flow intensity.

	κ_{ARM}/κ	Sortable silt
Standard deviation	0.1105	3.509
N	42	
R^2	0.5090	
Kolmogorov-Smirnov test (D-value)	0.1429	
Kolmogorov-Smirnov test (p-value)	0.7848	

Table 4.4. Results of the statistical analysis of the κ_{ARM}/κ and mean sortable silt grain size data.

4.3.6. Comparison of core top mean sortable silt grain size measurements with near bottom current flow speed.

Mean sortable silt grain sizes of fine grained sediment from the Vema Channel could be successfully calibrated to current meter data (R^2 = 0.81, N = 13) (Ledbetter, 1986), and the suspended sediment concentrations have been linked to abyssal eddy kinetic energy and benthic storms (HEBBLE - Hollister and McCave, 1984). In order to 'ground-truth' the mean sortable silt grain size data, and so also the κ_{ARM}/κ measurements, as a near bottom current strength index for Eirik Drift, modern core top mean sortable silt grain size data were obtained from 4 sediment cores (TTR-451, TTR-450, D298-P1 and D298-P3). These data were compared with near bottom current velocity data that were acquired from Lowered Acoustic Doppler Current Profiler (LADCP) measurements during the D298 2005 cruise of *RRS Discovery*. The core top sortable silt grain size data were generated with the same methods as the down core record from core TTR-451, and all measurements were made in Cardiff at the same time (for further details see Chapter 3.5). Figure 4.41 presents the current velocity profiles for the nearest two CTD stations to each core site (for a map of the core sites and CTD stations see Figure 3.16).

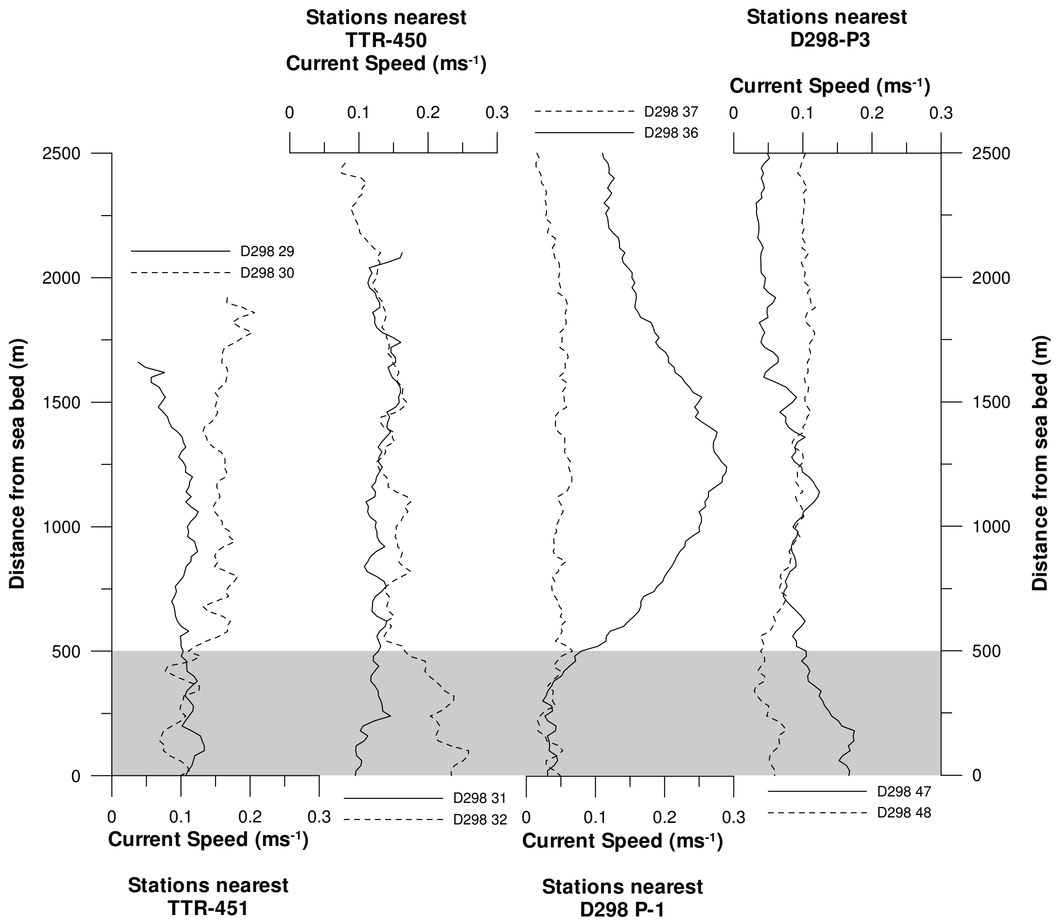

Figure 4.41. Velocity profiles calculated from LADCP data for the D298 CTD stations nearest the sites for cores TTR-451, TTR-450, D298-P1 and D298-P3

McCave *et al.* (1995b) recommend using geostrophic current velocities to compare with mean sortable silt grain size data, as these data give longer-term averages that would theoretically be more comparable to the long term averages represented in core top samples. However, geostrophic velocities can be subject to large error due to large temporal variability, and require interpolation methods in order to account for a sloping seabed (Hunter *et al.*, 2007b). Therefore, directly measured scalar velocities (gained from u and v) are used here for comparison with the core top mean sortable silt grain sizes. Values were obtained by averaging measurements from the nearest two CTD stations to each core site. Hunter *et al.* (2007b) show beam attenuation data which was also acquired during the D298 *Discovery* cruise. These data, which indicate the distribution of the sediment load, show a distinct bottom nepheloid layer that is around 300 m thick, and work by Clark (1984) suggested that the Deep Western Boundary Current (DWBC) in the vicinity of Eirik Drift is around 500 m thick. The LADCP data in Figure 4.41 show a distinct change in near bottom current speed at around 500 m from the sea floor in some of the profiles. Therefore, mean scalar current speeds from 0 to 40 m as well as 0 to 500 m above the sea floor are used to compare with core top mean sortable silt grain size data.

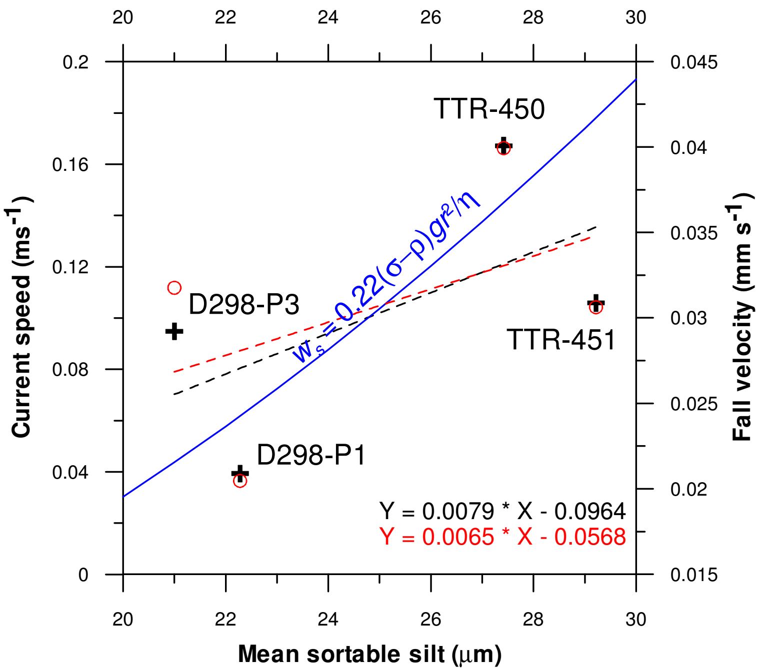

Figure 4.42. Cross-plot of the core top mean sortable silt grain sizes versus the mean scalar velocities of the two nearest CTD stations to the core sites. The black crosses and black trend-line concern scalar velocities averaged over the bottom 500 m and the red open circles and red trend-line concern scalar velocities averaged over the bottom 40 m. The blue line shows the calculated fall velocity of particles according to Stoke's Law.

Figure 4.42 cross-plots the mean scalar velocities versus the core top mean sortable silt grain size data. Also indicated is the predicted settling/fall velocities of particles (w_s) calculated from Stoke's law (Equation 4.2); where g is gravity, r is the radius of the particle, η is the molecular viscosity of seawater that is estimated to be 1.8 x 10^{-6} m^2 s^{-1} at 0°C (Soulsby, 1997), ρ is the density of seawater (1.03 g cm^{-3}), and σ is the density of the solid, which is assumed to be quartz (2.66 g cm^{-3}).

$$w_s = 0.22(\sigma\text{-}\rho)gr^2/\ \eta \qquad \text{(Equation 4.2)}$$

The relationship between current speed and the sorting of non-cohesive sediment is not only governed by the settling velocities of the particles transported, but also by the fluid shear stress (τ), which itself is controlled by three variables; the critical erosion stress, the critical suspension stress and the critical deposition stress. Sediment sorting results from grains being trapped in the viscous sublayer of the turbulent boundary layer; whereas other grains with smaller settling velocities are instead transported further downstream by being retained in turbulent suspension (e.g., McCave and Hall, 2006).

The deposition of sediment from suspension is more fully described by equations 4.3 and 4.4 (Sundborg, 1956; Einstein and Krone, 1962); where for deposition as a function of time (t), $K_t = (tp/h)$, and as a function of distance (x), $K_x = (xp/hU)$, where the probability of deposition (p) allows for the sorting of sediment through the suppression of deposition of slower settling particles under faster flows with higher boundary shear stress (τ_o) values. This is therefore an important term, which is defined by $p = (1 - \tau_o/\ \tau_d)$, where τ_d is the limiting stress for deposition and is less than $\tau_{o.}$ Parameter h is the thickness of suspension, U is the flow speed, and C_o is the concentration at a nominal size. Further explanation is beyond the scope of present study. For further discussions the reader is referred to McCave and Hall (2006).

$$C_t = C_o \exp\ (-K_t w_s) \qquad \text{(Equation 4.3)}$$

$$C_x = C_o \exp\ (-K_x w_s) \qquad \text{(Equation 4.4)}$$

Figure 4.42 shows that broadly speaking coarser core top mean sortable silt grain sizes correspond with faster flowing near-bottom currents over the core sites. The mean sortable silt grain sizes recorded in the core tops of D298-P1 and TTR-450 show positive relationship with current velocity, which supports the use of mean sortable silt grain size measurements from Eirik Drift as a near bottom current flow speed indicator. However similar current speeds were recorded above core sites D2980-P1 and TTR-451, and yet their mean sortable silt grain sizes are very different.

Previous study of profiler and seismic sections as well as regional modern hydrographies (e.g., Hunter *et al*., 2007a, b) may provide explanation of the discrepancy outlined above. Firstly, it is shown that today, the TTR-451 core site lies just above the main DWBC current core and, therefore, may reflect a relict measurements related to a previous faster flow regime. Secondly, core D298 lies to the southwest of a secondary ridge crest on Eirik Drift, and it is postulated in Hunter *et al*. (2007a) that this may cause flow separation of the DWBC. Additionally, one has to consider that varying interactions between the seafloor and the current flowing over it may also affect the relationship between mean sortable silt grain sizes and near bottom flow intensity, as boundary layer shear and critical stresses are affected by local topography (McCave and Hall, 2006). This would make the above relationship ambiguous over large distances. One also needs to be critical about the appropriateness of the use of scalar current velocities (see previous discussion). Finally, we acknowledge that four calibration points is a start, but by no means a substantial enough information resource for establishing robust relationships.

4.3.7. Conclusions

Within this sub-chapter κ_{ARM}/κ measurements from the top ~120 cm of core TTR-451 are compared with results from SIRM and backfield remanence curves, magnetic hysteresis loops and FORC diagrams to confirm that the κ_{ARM}/κ data provides an accurate record of mean (titano)magnetite grain sizes. It is assumed that the (titano)magnetites sourced from the Nordic Basaltic Province and transported within NADW, and therefore that their grain sizes reflect NADW flow intensity (Kissel *et al*., 1999a; Laj *et al*., 2002). These further magnetic measurements corroborates that the sediments contain a predominantly PSD magnetic mineral assemblage, as suggested previously by Kissel *et al*. (1997; 1999a) and Laj *et al*. (2002). Comparison with grain sizes of (titano)magnetites estimated from SEM image analysis validates the magnetic measurements, revealing grain sizes between 2-4 μm.

Mean sortable silt grain sizes, an established proxy for near bottom current strength (e.g., McCave *et al*., 1995a, b; 2006; Bianchi and McCave, 1999; Hall *et al*., 2001), were measured from the same sediment samples as the κ_{ARM}/κ and the two records show a good visual correlation. Statistical analysis shows correlation, but despite good visually agreement, is weak. Finally, mean sortable silt grain size data from core tops are compared with mean scalar velocities gained from LADCP data, which reveals a general positive trend that validates the use of mean sortable silt grain sizes, and hence also κ_{ARM}/κ, as near bottom current indices at Eirik Drift.

4.4. Records of planktonic foraminiferal $\delta^{18}O$ and $\delta^{13}C$, lithic counts and planktonic foraminiferal abundances for marine sediment core TTR-451.

This sub-chapter presents oxygen and carbon stable isotope ($\delta^{18}O$ and $\delta^{13}C$) records for the planktonic foraminiferal species *Neogloboquadrina pachyderma* (left coiling) through the top ~120 cm of marine sediment core TTR-451 (for the core location, see Figure 3.1). Using the global ice volume correction of Duplessy *et al.* (2002), the $\delta^{18}O_{npl}$ data were adjusted for the global ocean $\delta^{18}O$ change from preferential sequestration of ^{16}O relative to ^{18}O in the ice sheets. These ice volume corrected $\delta^{18}O_{npl}$ data are also presented within this sub-chapter. Where specimen abundances permitted, the *N. pachyderma* (left coiling) $\delta^{18}O$ and $\delta^{13}C$ data are compared to those obtained from planktonic foraminifera *Globigerina bulloides*.

A number of previous studies show that ice-rafted debris (IRD)-rich layers in North Atlantic marine sediment cores are often associated with light surface water $\delta^{18}O$ isotopic excursions (inferred surface water freshening), and reduction in planktonic foraminiferal abundances (*amongst others* Heinrich, 1988; Bond *et al.*, 1992; 1993; 1997; 1999; Broecker *et al.*, 1992; 1994; Grousset *et al.*, 1993; 2001; Hilliare-Marcel *et al.*, 1994; Knutz *et al.*, 2001; Darby *et* al., 2002; Elliot *et* *al*., 2002; Hemming and Hajdas, 2003; Jennings *et al*., 2006; Peck *et al*., 2006; 2007a, b). For further discussion see section 3.6 and the review by Hemming (2004).

Next in this sub-chapter, the planktonic foraminiferal $\delta^{18}O$ record for core TTR-451 is compared with total abundances of planktonic foraminifera >150 µm and counts of IRD/lithic grains >150 µm. The 150 µm diameter threshold for IRD is widely used, because larger grains cannot be carried by bottom currents (Bond and Lotti, 1995; Bond *et al*., 1997; 1999; Broecker, 1994; Grousset *et al*., 1993; 2000; 2001; Knutz *et al*., 2001; Darby *et* al., 2002; Elliot *et al*., 2002; Hemming and Hajdas, 2003; Peck *et al*., 2006; 2007a, b). As Icelandic volcanic glass shards >150 µm may be deposited at the TTR-451 core site as air-fall rather than as IRD, these are discounted in the 'ash-free' IRD counts also presented here.

IRD provenance studies of North Atlantic marine sediment cores have attributed the origin of hematite stained grains to the Greenland and British ice sheets, detrital carbonate to the Laurentide and Fennoscandian ice-sheets, and shards of volcanic glass to the vicinity of Iceland, transported by sea-ice (e.g., Bond *et al*., 1992; 1993; 1999; Bond and Lotti, 1995; Elliot *et al*., 1998; Grousset *et al*., 2000; 2001; Knutz *et al*., 2001; Peck *et al*., 2006; 2007a, b; review in Hemming, 2004). The above studies have also shown a phased pulsing of the circum-North Atlantic ice sheets just prior to and during the main IRD/Heinrich events. Therefore, this sub-chapter presents counts of the individual grain types that together form the total IRD abundances, in order to decipher the origin of the IRD in core TTR-451.

Significant changes in sedimentation rate result in variation in IRD and planktonic foraminiferal abundance records, in terms of numbers per gram of dry sediment, as a function of mass accumulation. For example, a reduction in the quantity of silts and clays being deposited with no change in IRD and planktonic foraminiferal fluxes would result in a relative increase in the numbers per gram of dried bulk sediment. Therefore, the age model which is described in sub-chapter 4.5 is used with the calculated bulk sediment mass accumulation rate (grams of total dried sediment yr^{-1}) to determine the fluxes of IRD and planktonic foraminferal counts (grains or planktonic foraminifera >150 µm cm^{-2} yr^{-1}). All records are shown in comparison with the magnetic susceptibility record for TTR-451 to provide stratigraphic reference to the previously described environmental and paleomagnetic records acquired for this core (sections 4.2 and 4.3).

4.4.1. Records of planktonic foraminiferal $\delta^{18}O$ and $\delta^{13}C$

Figure 4.43b & c present the $\delta^{18}O$ and $\delta^{13}C$ records for *N. pachyderma* (left-coiling) ($\delta^{18}O_{npl}$, $\delta^{13}C_{npl}$) for core TTR-451. The global ice volume corrected $\delta^{18}O_{npl}$ record is also shown in Figure 4.43b (grey). In addition, $\delta^{18}O$ and $\delta^{13}C$ data for the species *G. bulloides* ($\delta^{18}O_{gb}$, $\delta^{13}C_{gb}$) are shown in Figure 4.43b by red and blue crosses, respectively. The data obtained from *G. bulloides* are shown to cross-validate the $\delta^{18}O_{npl}$ data, but due to the different depth habitats between species, close agreement is considered unlikely.

At the base of the $\delta^{18}O_{npl}$ record (Figure 4.43b), a 0.8 ‰ shift to lighter values occurs at around 111 cm depth. From around 98 cm, a strong shift to lighter $\delta^{18}O_{npl}$ values develops, culminating in a broad peak of light values at around 87 cm depth. This $\delta^{18}O_{npl}$ change equates to -1.45 ‰ (Figure 4.43b) and around -1.5 ‰ in the ice volume corrected $\delta^{18}O_{npl}$ record. Above 87 cm, the $\delta^{18}O_{npl}$ record returns to heavier values and levels out at around 75 cm. Over this same interval of core, the $\delta^{13}C_{npl}$ values show a progressive increase, and they level out at around 61 cm. The data in the ice volume corrected $\delta^{18}O_{npl}$ record, however, do not level out, but instead show a progressive enrichment that culminates at around 31 cm depth, and with a total change of 1.23 ‰. Above 31 cm, a gradual shift to lighter $\delta^{18}O_{npl}$ develops, with a magnitude of around 0.7 ‰ (or 0.5 ‰ for the ice volume corrected $\delta^{18}O_{npl}$ data). Over this same interval of core, the $\delta^{13}C_{npl}$ record shows a relatively minor decrease by around 0.1 ‰.

The $\delta^{18}O_{gb}$ data (Figure 4.43b) plot closely around the $\delta^{18}O_{npl}$ values, which validates the $\delta^{18}O_{npl}$ record as being representative of the past surface water conditions above core TTR-451. A maximum difference of around 0.24 ‰ occurs between these two sets of data at around 93 cm depth, just prior to the peak light values at 98 cm. Because *N. pachyderma* (left-coiling) primarily lives within the pycnocline, but with ontogenic migration down to 600 m (Volkmann, 2000; Simstich *et al*., 2003), whereas *G. bulloides* tend to live within the upper 30 to 60 m of the water column (Schiebel *et al*., 1997; Barker and Elderfield, 2002), these deviations in $\delta^{18}O$ values during the light $\delta^{18}O$ event may reflect the different depth habitats of the two species. Alternatively, these lighter $\delta^{18}O_{gb}$ values may reflect the later season of growth for *G. bulloides* (Ganssen and Kroon, 2000). However, it is acknowledged that four data points do not provide substantial enough evidence for further interpretation. The $\delta^{13}C_{gb}$ data (Figure 4.43c) do not show agreement with the $\delta^{13}C_{npl}$ record, and deviate by up to 0.8 ‰. Due to the ambiguity in these $\delta^{13}C$ records, they are not interpreted further.

4.4.2. Records of planktonic foraminifera abundances and IRD (>150 µm)

The numbers of planktonic foraminiferal tests >150 µm per gram of dry sediment for core TTR-451 are presented in Figure 4.43d. This record shows a two-step increase from almost zero to around 1500 foraminifera g^{-1} between 107 and 95 cm depth, above which numbers gradually return to around 200 at around 79 cm. This interval of enhanced planktonic foraminiferal abundances spans the entire period of light $\delta^{18}O_{npl}$ values (Figure 4.43b). The planktonic foraminiferal abundances remain relatively low until around 41 cm depth. A sharp increase occurs between 29 and 25 cm depth when values increase from around 550 to 2500 foraminifera g^{-1}. Abundances gradually decrease to around 450 foraminifera g^{-1} until 11 cm. This sharp increase in planktonic foraminiferal concentration is approximately coincident with the $\delta^{18}O_{npl}$ light excursion which initiates at around 31 cm. The number of foraminifera (>150 µm) g^{-1} significantly increases from 1000 at around 7 cm to nearly 57,000 at the core top. These high concentrations of foraminiferal tests likely result from bottom current winnowing of the core top sediments.

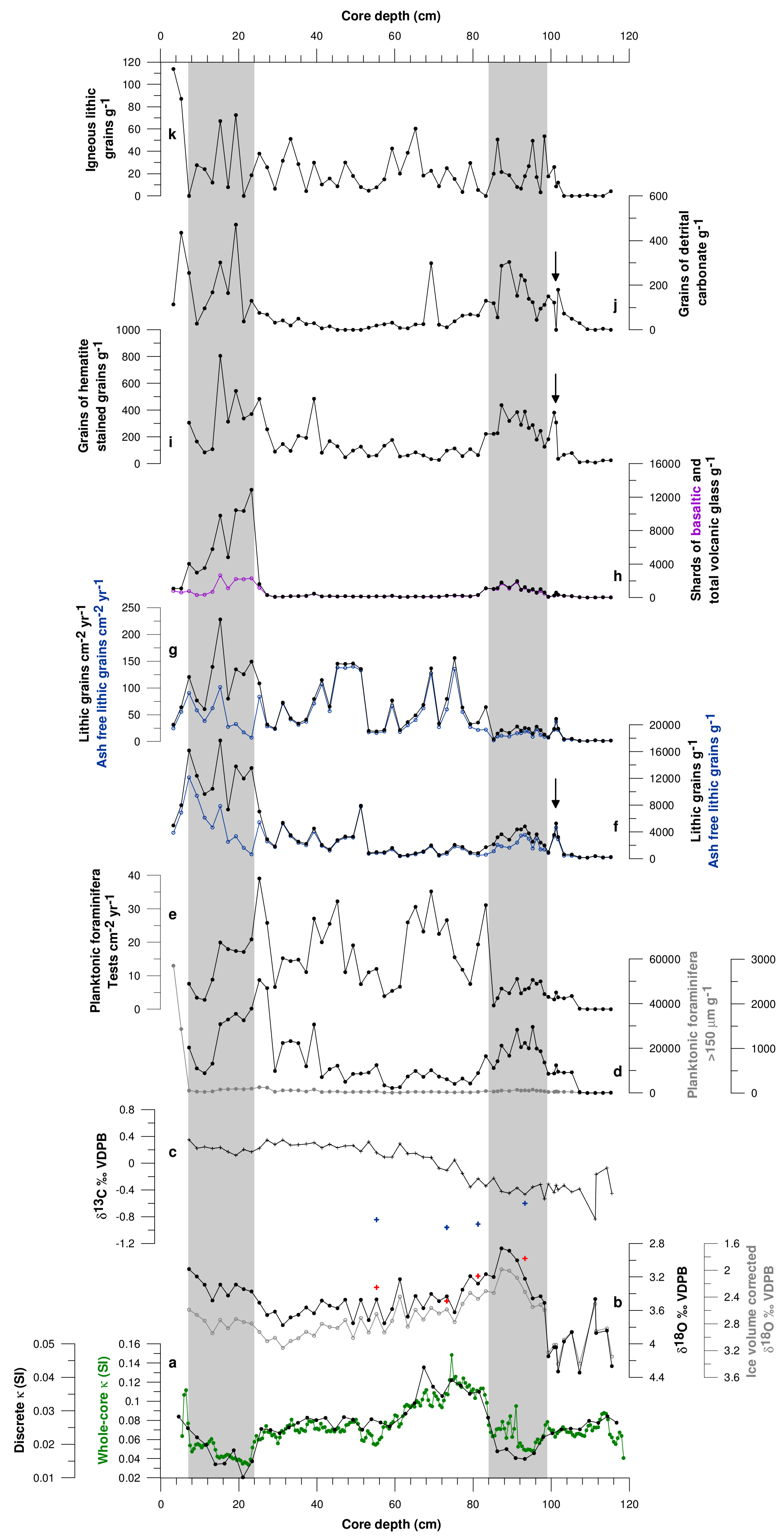
Core depth (cm)
Igneous lithic grains g^{-1}
k
Grains of detrital carbonate g^{-1}
j
Grains of hematite stained grains g^{-1}
i
Shards of basaltic and total volcanic glass g^{-1}
h
Lithic grains cm^{-2} yr^{-1}
Ash free lithic grains cm^{-2} yr^{-1}
g
Lithic grains g^{-1}
Ash free lithic grains g^{-1}
f
Planktonic foraminifera Tests cm^{-2} yr^{-1}
e
Planktonic foraminifera >150 μm g^{-1}
d
δ^{13}C ‰ VDPB
c
δ^{18}O ‰ VDPB
Ice volume corrected δ^{18}O ‰ VDPB
b
Discrete κ (SI)
Whole-core κ (SI)
a

Figure 4.43 a. Records of 'whole-core' and discrete sample magnetic susceptibility data for core TTR-451. b. The $\delta^{18}O_{npl}$ record (black) is compared to $\delta^{18}O_{gb}$ data (red crosses), as well as the global ice volume corrected $\delta^{18}O_{npl}$ record (grey). c. The $\delta^{13}C_{npl}$ record (black) is compared to $\delta^{13}C_{gb}$ data (blue crosses). d. The total number of planktonic foraminiferal tests >150 µm per gram of dried sediment. In black are the data are plotted on an expanded scale. e. The flux of planktonic foraminiferal tests >150 µm cm^{-2} yr^{-1}. f. The number of lithic grains (black) and ash free lithic grains (blue) >150 µm per gram of dried sediment. g. The flux of lithic grains (black) and ash free lithic grains (blue) >150 µm cm^{-2} yr^{-1}. h. The number of shards of volcanic glass (black) and basaltic glass (purple) >150 µm per gram of dried sediment. Panels i, j and k show the numbers of hematite stained grains, detrital carbonate and igneous grains >150 µm per gram of dried sediment. The black arrow shows the timing of a precursory IRD 'spike'.

Figure 4.43e presents the flux of foraminiferal tests (>150 µm) cm^{-2} yr^{-1}. The transformation from numbers per gram (Figure 4.43d) to fluxes (Figure 4.43e) considerably changes the shape of the records. Generally low fluxes occur towards the base of the studied section, with only a relatively small rise of up to 8 foraminifera (>150) µm cm^{-2} yr^{-1} between 107 and 97 cm depth. A sharp rise to around 31 foraminifera (>150 µm) cm^{-2} yr^{-1} occurs at around 83 cm, which declines to around 7 at approximately 79 cm depth. Above this depth, the record fluctuates between these two levels, with increases at around 73, 45 and 27 cm, and decreases at around 62, 38 and 23 cm depth. The flux of foraminifera (>150 µm) cm^{-2} yr^{-1} gradually declines until around 7 cm, after which abundances significantly increase to over 300 foraminifera (>150 µm) cm^{-2} yr^{-1}, likely due to bottom current winnowing of the core top sediments.

The record of IRD (>150) µm g^{-1} for core TTR-451 is shown in Figure 4.43f. Relatively low quantities of IRD occur at the base of the interval of study and a sharp increase, with short duration, occurs at around 101 cm depth, with a magnitude of change from near to zero to over 5000 grains g^{-1} (see arrow in Figure 4.43). Figures 4.43 h, i, j and k show the records of volcanic glass shards, hematite stained grains of quartz and feldspar, and detrital carbonate and igneous grains, respectively; and their percentage abundances of the total IRD content are presented in Figure 4.44d, e, f and g. Although a small increase in the abundance of hematite stained grains can be seen at the time of the IRD peak at 101 cm depth (see arrow Figures 4.43i), this IRD peak predominantly comprised quartz (note the relatively low percentage compositions in Figure 4.44).

A notable peak in IRD concentration occurs between 99 and 81 cm depth, where the number of grains (>150 μm) g^{-1} increases from around 1000 to nearly 5000 (3500 excluding volcanic glass). Following this, toward the end of the period, the IRD primarily contains basaltic volcanic glass (Figure 4.44d) with percentage compositions as high as 65 %. Although volcanic glass may be deposited directly as air-fall to the ocean surface, the observed basaltic glass in TTR-451 was blocky in appearance (see Figure 3.18). Therefore, the mechanism for its transportation is interpreted to have been air fall onto sea-ice and subsequent transport as IRD, consonant with previous suggestions (e.g., Bond and Lotti, 1995; Bond *et al*., 1997; 1999).

From about 80 cm depth, the total IRD g^{-1} (Figure 4.43d) levels out and remains below 1000 grains (>150 μm) g^{-1} until around 53 cm depth, when concentrations increase to around 1500 grains g^{-1}. Above 53 cm, the abundances of IRD remain at approximately the same level until ~25 cm depth, when the number of grains (>150 μm) g^{-1} sharply increases to over 13,000 grains g^{-1}. This lithic peak predominantly contains shards of rhyolitic volcanic glass, forming up to 95 % of the total IRD (Figure 4.43h and 4.44 d). A relatively smaller increase in basaltic grains occurs at the same time (Figure 4.43h and 4.44d). Other IRD grain types increase later at around 16 cm depth, with a rise from just over 5000 to 12,000 grains >150 μm g^{-1} (note the 'ash-free' IRD counts in Figure 4.43 f), before decreasing towards the core top (~3 cm depth) with abundances around 5000 grains >150 μm g^{-1}.

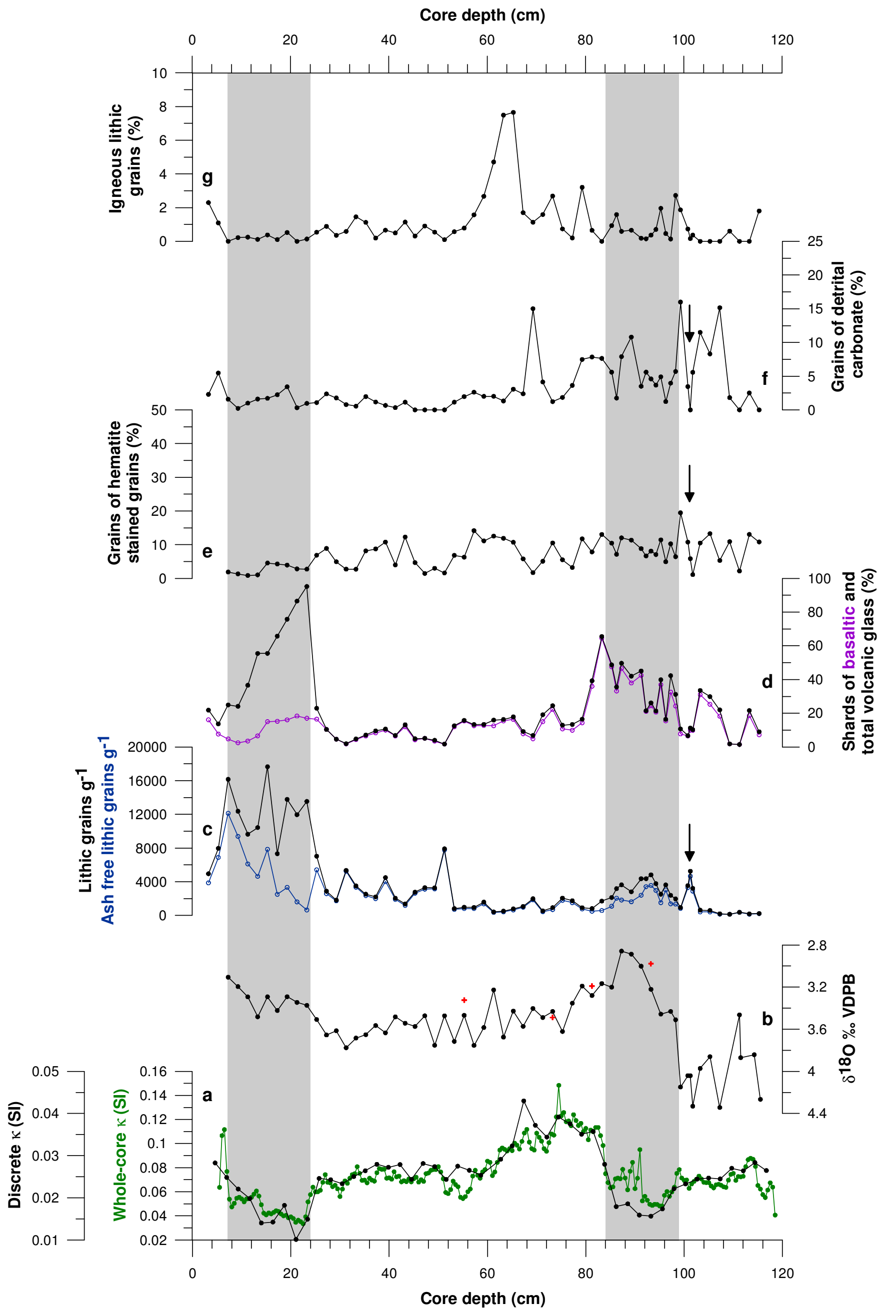

Figure 4.44 a. Records of 'whole-core' and discrete sample magnetic susceptibility data for core TTR-451. b. The $\delta^{18}O_{npl}$ record (black) is compared to $\delta^{18}O_{gb}$ data (red crosses). c. The numbers of lithic grains (black) and ash free lithic grains (blue) >150 µm per gram of dried sediment. The percentage compositions of the total lithic grains of volcanic glass, hematite stained grains, detrital carbonate and igneous grains are presented in panels d, e, f and g, respectively. The black arrow shows the timing of an early IRD 'spike'.

The total and ash-free IRD counts are corrected for the sediment mass accumulation rate (g yr^{-1}) and the resultant flux data (grains (>150 μm) cm^{-2} yr^{-1}) are presented in Figure 4.43g. The IRD flux for core TTR-451 shows no notable increase until around 77 cm depth, when the IRD flux rises from around 4 to 155 grains (>150 μm) cm^{-2} yr^{-1}, with only a minor peak at around 101 cm depth (from near zero to around 40 grains (>150 μm) cm^{-2} yr^{-1}). Between 77 and 26 cm depth, the flux of lithic grains >150 μm remains variable and range between 16 and 146 grains cm^{-2} yr^{-1}, with low values between 74 to 70 cm, 68 to 52 cm, and 39 to 26 cm. At 26 cm depth, a significant increase in flux in lithic grains >150 μm predominantly comprises rhyolitic glass, with peak values of 146 grains (>150 μm) cm^{-2} yr^{-1} (note the difference between the blue and black plots in Figure 4.43g). A second sharp increase in rhyolitic shards occurs at around 15 cm depth, with a peak total value of 230 lithic grains (>150 μm) cm^{-2} yr^{-1}. A moderate increase in flux of other IRD grain types also occurs at the same depth.

The flux of lithic grains >150 μm gradually decreases towards the top of the core, with a value of around 26 grains (>150 μm) cm^{-2} yr^{-1} at 3 cm depth, and a relatively small increase at around 7 cm depth, when the flux increases to around 120 grains (>150 μm) cm^{-2} yr^{-1}. The convergence of the graphs of the total and the ash-free lithic grains (>150 μm) cm^{-2} yr^{-1} shows a sharp decrease in the volcanic glass component. It is noteworthy that these relatively high deposition rates of lithics >150 μm are approximately coincident with the broad low in magnetic susceptibility and the light $\delta^{18}O_{npl}$ anomaly (Figures 4.43a & b).

4.4.3. Conclusions

The record of $\delta^{18}O_{npl}$ for core TTR-451 reveals two light isotopic anomalies; one between 98 and 87 cm, and the other from 31 cm depth and culminating towards the core top. These light $\delta^{18}O_{npl}$ events coincide with increases in both IRD and planktonic foraminiferal abundances. The uppermost peak in lithic grains >150 μm at 26 cm depth is dominated by volcanic glass, in particular rhyolitic shards. Adjustment of the planktonic foraminiferal and IRD counts for the sediment accumulation rate of the core has provided records of flux (cm^{-2} yr^{-1}).

These records show no discernable increase with the lowermost $\delta^{18}O_{npl}$ light anomaly, whereas large increases in both records coincide with the uppermost $\delta^{18}O_{npl}$ light excursion. The fluxes of IRD and planktonic foraminifera both show distinct increases at around 83 and 77 cm depth, respectively, not coincident with the $\delta^{18}O_{npl}$ anomalies.

4.5. Age-model and chronology of marine sediment core TTR-451

The chronology of the upper ~120 cm of core TTR-451 is primarily constrained by seven Accelerated Mass Sprectrometric (AMS)^{14}C datings of monospecific samples of *Neogloboquadrina pachyderma* (left coiling) that have been calibrated using Calib5.0.1 (Hughen *et al*., 2004; Reimer *et al*., 2004). Within these AMS^{14}C age constraints, the age model is further fine-tuned using a robust correlation between the TTR-451 magnetic susceptibility (κ) records and the GRIP and GISP2 ice-core stable oxygen isotope ratio (δ^{18}O) records (Grootes and Stuiver, 1997; Stuiver and Grootes, 2000; Johnsen *et al*., 2001; Andersen *et al*., 2006; Svensson *et al*., 2006; Rasmussen *et al*., 2006; 2007; Vinther *et al*., 2006).

Stable oxygen isotope ratios (δ^{18}O) of ice from Greenland ice cores reflect temperature and air mass variations over the ice sheet (e.g., Stuiver and Grootes, 2000). More negative values generally represent colder conditions, and less negative values represent warmer conditions. Recent layer-counting has provided a common timescale (the Greenland Ice Core Chronology 2005, or GICC05) for four key ice cores from the Greenland ice sheet back to 14.7 ka BP, and more recently, back to 42 ka BP (DYE-3, GRIP, and NorthGRIP) (Andersen *et al*., 2006; Svensson *et al*., 2006; Rasmussen *et al*., 2006; 2007; Vinther *et al*., 2006).

Within this sub-chapter, the AMS^{14}C results for core TTR-451 are presented, and the methods for age model construction are described, tested and discussed. Note that the published age-model for core TTR-451 in Stanford *et al*. (2006) is modified here for ages older the 14.7 ka BP (thousands of years Before Present, where Present refers to AD1950), due to extension of the GICC05 timescale into Marine Isotope Stage (MIS) 2, which was not available at the time of original publication (Andersen *et al*., 2006; Svensson *et al*., 2006; Rasmussen *et al*., 2007).

4.5.1. AMS^{14}C chronology of core TTR-451

Table 4.5 presents the raw and calibrated results of the AMS^{14}C datings for marine sediment core TTR-451, which were obtained from >8 mg of monospecific samples of *N. pachyderma* (left coiling) (for further details see 3.7). The AMS^{14}C radiocarbon conventional ages have been calibrated using Calib5.0.1, and with the Marine04.14c calibration curve (Hughen *et al*., 2004; Reimer *et al*., 2004). A time-dependent reservoir age correction for the global ocean of ~400 years (Austin *et al*., 1995) is incorporated into the Marine04.14c calibration curve. For core TTR-451, a local reservoir age correction $\Delta R = 0$ was used, as it was aimed instead to diagnose ΔR for Eirik Drift. The calibrated datings are presented in years Before Present (BP), and represent the maximum modal (or peak probable) ages.

The ^{14}C reservoir age of the oceans is strongly controlled by the carbon cycle and surface to deep water exchange, with sequestration of ^{14}C into the ocean interior. Past reductions in Atlantic Meridional Overturning Circulation (AMOC) intensity would have likely reduced the surface to deep water exchange, causing the ^{14}C reservoir age, of the ocean waters to have increased (e.g., Austin *et al*., 1995; Hughen *et al*., 2000; 2004; Muscheler *et al*., 2000; 2008; Waelbroeck *et al*., 2001; Laj *et al*., 2002; Robinson *et al*., 2005; Keigwin and Boyle, 2008; Marchitto *et al*., 2007). This increase in reservoir age throughout the water column (e.g., Robinson *et al*., 2005), results in ^{14}C age plateaus (e.g., Hughen *et al*., 2000; 2004; Cao *et al*., 2007).

KIA-sample number	Depth (cm)	species	AMS^{14}C age	Calibrated age (Calib 5.0.1.)	2σ age range	Inferred ΔR	2σ range for the ΔR
KIA-26998	12.0	*N. pachy.* (lc)	10905 ± 60 BP	12535 BP*	12213-12715	437	96-650
KIA-27856	40.0	*N. pachy.* (lc)	12220 ± 55 BP	13692 BP	13495-13800		
KIA-25853	57.5	*N. pachy.* (lc)	12690 ± 55 BP	14141 BP	13986-14527		
KIA-27857	76.0	*N. pachy.* (lc)	12825 ± 55 BP	14420 BP	14154-14843		
KIA-27858	83.5	*N. pachy.* (lc)	13460 ± 55 BP	15411 BP*	15136-15769	801	470-1204
KIA-27859	94.3	*N. pachy.* (lc)	14750 ± 60 BP	17196 BP*	16720-17568	1242	707-1688
KIA-25854	102.3	*N. pachy.* (lc)	14890 ± 60 BP	17432 BP*	16975-17839	647	107-1146

Table 4.5. AMS^{14}C measurements measured from monospecific samples of *N. pachyderma*, left-coiling (lc), and their calibrated (calendar) ages for core TTR-451. Inferred ΔR values are also presented for AMS^{14}C datings that represent the Younger Dryas and Heinrich event 1 (see 4.5.2.). * These datings have relatively large calibrated 2σ errors due to plateaus in the marine04.14c calibration curve (Hughen *et al.*, 2004). KIA = Kiel Institut für Altersbestimmungen.

Figure 4.45 shows the calibration plots for the sample in Table 4.5. The probability plots of ages from samples KIA-27998, KIA-27858, KIA-27859 and KIA-25854 (Figure 4.45a, e, f and g) have skewed, and even bi-modal, distributions that have relatively large 2σ uncertainties. These skewed distributions are due to plateaus in the Marine04.14c calibration curve, and the datings are bracketed by the Younger Dryas and Heinrich event 1 (H1) time periods, when the AMOC was in a state of near complete shutdown (e.g., Austin and Kroon, 2001; McManus *et al.*, 2004). In comparison, sample KIA-25853 (Figure 4.45c) for example has a uni-modal distribution with a relatively small 2σ range.

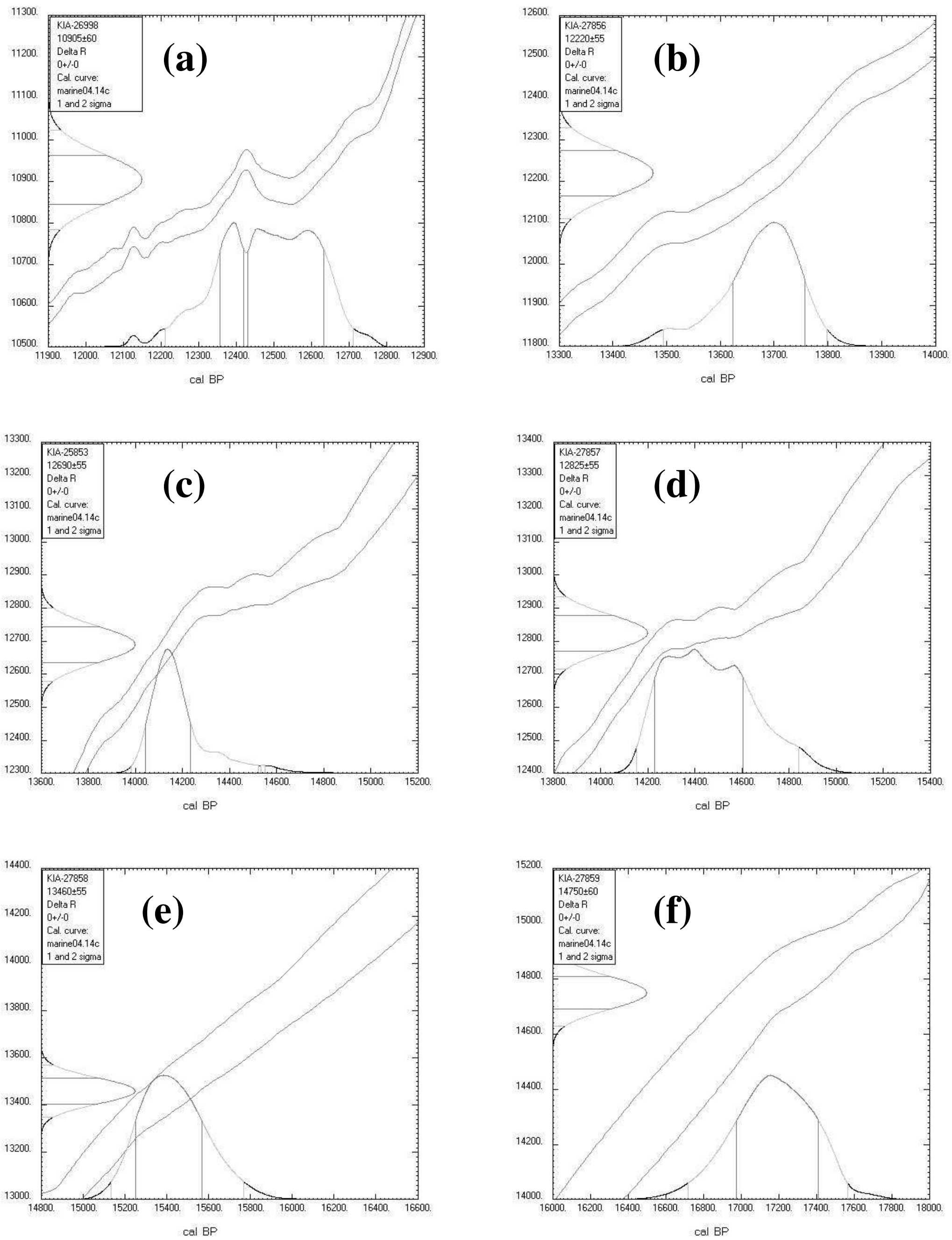

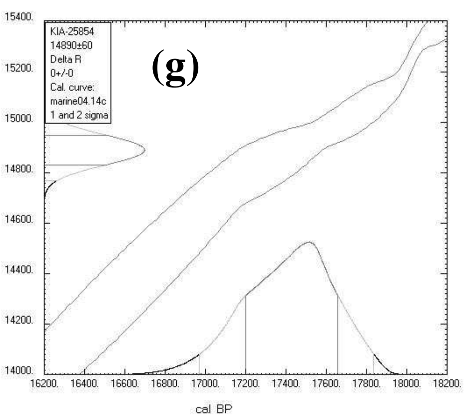

Figure 4.45. Conventional radiocarbon versus calibrated ages for core TTR-451. The plots were generated using Calib5.0.1., and y-axis values represent conventional radiocarbon ages.

4.5.2. Fine-tuning the age-model for core TTR-451

To reduce the relatively large AMS^{14}C dating uncertainties for the Younger Dryas and H1, the age-model for TTR-451 is fine-tuned to the GICC05 chronology, using a correlation between the magnetic susceptibility (κ) record for core TTR-451 and the δ^{18}O ice core record from GRIP and GISP2 on the GICC05 chronology (Grootes and Stuiver, 1997; Stuiver and Grootes, 2000; Johnsen *et al*., 2001; Andersen *et al*., 2006; Svensson *et al*., 2006; Rasmussen *et al*., 2006; 2007; Vinther *et al.,* 2006), similar to methods used previously (e.g., Dokken and Jansen, 1999; Kissel et al., 1999a, b). For further discussions on the construction of the GICC05 'Greenland Ice Core Chronology 2005' see section 5.1.

4.5.2.1. TTR-451 age-model between 11 and 15 ka BP

Figure 4.46 plots the initial age-model for core TTR-451, of which the upper 84 cm is primarily constrained by calibrated AMS^{14}C datings. Between 84 and 24 cm, TTR-451 sediments represent the Bølling and Allerød warm periods (GI-1e & c) (Björck *et al*., 1998), during which ΔR values are generally thought to have been close to zero (Hughen *et al*., 2000; Bondevik *et al*., 2006). Two AMS^{14}C datings are not used in the upper 90 cm of the core (see [1] and [2] in Figure 4.46), one has an age within the Younger Dryas period, and the other just prior to the Bølling transition.

The AMS^{14}C dating at 12.535 ka BP (KIA- 26998; Table 4.5) has a bi-modal and poorly calibrated probability distribution function due to a plateau in the marine04.14c calibration curve (Figure 4.45c). Visually robust tie points between the TTR-451 magnetic susceptibility (κ) and the Greenland ice core δ^{18}O stratigraphies (see correlation lines in Figure 4.52) indicates that this age is 'too old'. ΔR for this dating is approximated using the difference between the ages derived from the magnetic susceptibility tie points (absolute calendar ages) and the calibrated AMS^{14}C datings (Table 4.5). The inferred ΔR value for the Younger Dryas (ΔR = 437 yrs, Table 4.5) compares well (just within 1σ) with

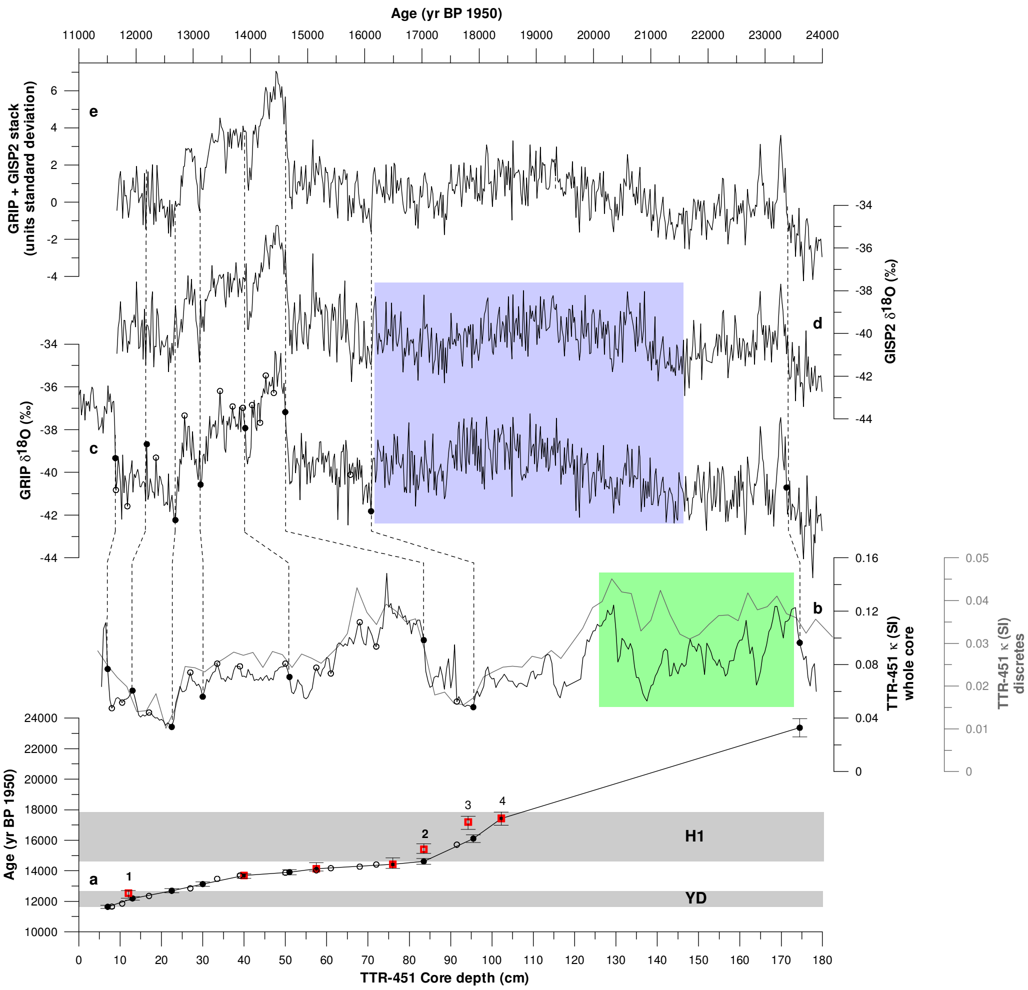

Figure 4.46. a. Depth versus age plot for core TTR-451. Open, red squares indicate calibrated AMS^{14}C datings, and error bars indicate the 2σ uncertainty range (Table 4.5). Numeric markers refer to the main text. Solid black dots indicate tie points from the correlation between the magnetic susceptibility and the GRIP ice-core δ^{18}O record, and open black circles represent extra correlation points between the magnetic susceptibility of core TTR-451 and the GRIP ice core record that are not used to construct the age model, but are shown for validation. 2σ error bars indicate the maximum counting error on the GICC05 timescale. The grey areas represent the times of reduced NADW ventilation associated with the Younger Dryas and Heinrich Event 1 (McManus *et al.*, 2004). b. Magnetic susceptibility records for TTR-451: black denotes the higher resolution whole core data, and grey denotes the lower resolution discrete sample measurements. The green shaded area highlights an interval with reduced

agreement between the magnetic susceptibility records form these two independent methods. The GRIP (c) and GISP2 (d) ice core $\delta^{18}O$ records plotted versus the new GICC05 timescale based on layer-counting (Andersen *et al.*, 2006; Svensson *et al.*, 2006; Rasmussen *et al.*, 2006; 2007; Vinther *et al.*, 2006). The blue shaded area highlights where the GRIP and GISP2 $\delta^{18}O$ records disagree. e. The GRIP and GISP2 $\delta^{18}O$ records are combined to form a regional air-temperature proxy in units standard deviation. YD = Younger Dryas, and H1 = Heinrich event 1

independently derived ΔR estimates of 371 yrs, based on cores from the Norwegian margin (Bondevik et al., 2006), and 300 yrs for the northern North Atlantic (Austin *et al.*, 1995). Note that the age-model for the Younger Dryas lies just within the 2σ bounds of this dating.

The relatively sharp jump in the TTR-451 magnetic susceptibility (κ) record at around 84 cm depth has a good visual correlation with the onset of the Bølling warming (GI-1e) (Björck *et al.*, 1998) in the GRIP and GISP2 ice core $\delta^{18}O$ records (see correlation lines in figure 4.46), which is dated at 14.6 ka BP (Rasmussen *et al.*, 2006). On the basis of this excellent visual correlation, the AMS^{14}C dating at 83.5 cm depth (KIA-27858, [2] in Figure 4.46a), with a calibrated age of 15.411 ka BP, has an inferred ΔR of around 800 yrs.

As the age-model for the upper ~90 cm of core is constructed primarily on the basis of the AMS^{14}C chronology, and where the age model deviates from its AMS^{14}C datings is on the basis of strong correlation tie points, it provides a test-bed for the robustness of the correlation for continuation of this method further down-core.

The TTR-451 magnetic susceptibility (κ) record and the GRIP $\delta^{18}O$ ice core record were interpolated onto the same time steps (Figure 4.47a) and cross-plotted during the time interval of 11.5 to 15 ka BP, and reveal a statistically significant R^2 value of 0.71 (N=116) (Figure 4.47b). On the basis of this correlation coefficient, this method of age-model construction is continued down core. This method of correlation is important for H1 and the Last Glacial Maximum (LGM), as during these periods its use becomes necessary because of the likely unreliability of AMS^{14}C datings due to enhanced ΔR values (Hughen *et al*., 2000; 2004; Laj *et al*., 2002; Robinson *et al*., 2005; Keigwin and Boyle, 2008; Muscheler *et al*., 2008).

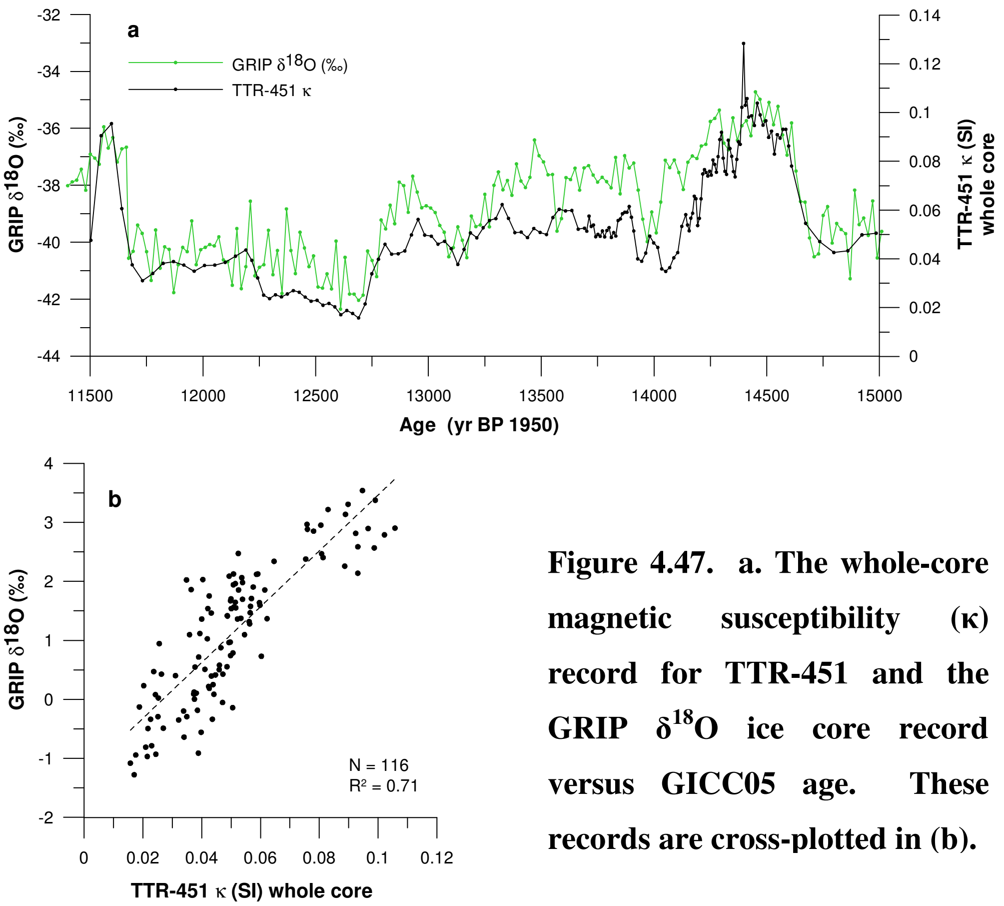

Figure 4.47. a. The whole-core magnetic susceptibility (κ) record for TTR-451 and the GRIP δ^{18}O ice core record versus GICC05 age. These records are cross-plotted in (b).

4.5.2.2. TTR-451 age-model below 15 ka BP

Comparison between calibrated ages of AMS^{14}C datings KIA-27859 and KIA-25854 (Table 4.5; [3] and [4] in Figure 4.46a) indicates that 8 cm of core TTR-451 represent only 250 yrs or less. This infers a sharp increase in sedimentation rates, which would be surprising as there is no correspondingly sharp change in the coarse sediment fraction concentration at around this depth (see section 4.4.2), as would be expected due to dilution changes. As AMS^{14}C dating KIA-27859 has a calibrated age of 17.196 ka BP, which is well within the H1 interval of AMOC collapse (McManus *et al.*, 2004; grey shaded bars in Figure 4.46a), a more likely explanation would be that it is affected by relatively old ^{14}C ventilation ages.

The correlation between the magnetic susceptibility (κ) record for TTR-451 and the GRIP/GISP2 ice core δ^{18}O records for ages older than ~16 ka BP is problematic due to (1) the lack of agreement between δ^{18}O signals between the two ice cores (see blue shaded region in Figure 4.46), and (2) a lack of agreement between the discrete sample and whole-core magnetic susceptibility (κ) records for TTR-451 (see green shaded region in Figure 4.46). As the GRIP and GISP2 δ^{18}O records provide a regional proxy for air temperatures above Greenland and, furthermore, are located in close proximity to one another, it would be incorrect to favour the correlation with one record over the other to TTR-451. To negate this problem, the GRIP and GISP2 δ^{18}O records are combined to form a hybrid Greenland air-temperature record in unit standard deviation (Figure 4.46e). The lack of agreement between the magnetic susceptibility records for core TTR-451 is resolved by the use of the discrete sample data for the correlation, as its methods are more robust than those for the generation of the whole-core data (for further discussions see section 4.2.4).

A distinct visual correlation can be made at 95.5 cm depth in the TTR-451 magnetic susceptibility (κ) record with the GRIP and GISP2 ice core δ^{18}O records at 16.110 ka BP (Figure 4.46). Using this correlation tie-point, sample KIA-27859 from core TTR-451 has an inferred ΔR of 1242 yrs. Keigwin and Boyle (2008) use paired bivalve and planktonic foraminifera AMS^{14}C ages for sediments from Bermuda Rise and estimate a ΔR of 1170 yrs for a foraminiferal sample with a conventional ^{14}C age of 14.800 +/- 0.06 ka BP. KIA-27859, with a conventional ^{14}C age of 14.750 +/- 0.06 ka BP, therefore, has a ΔR value that is in very close agreement.

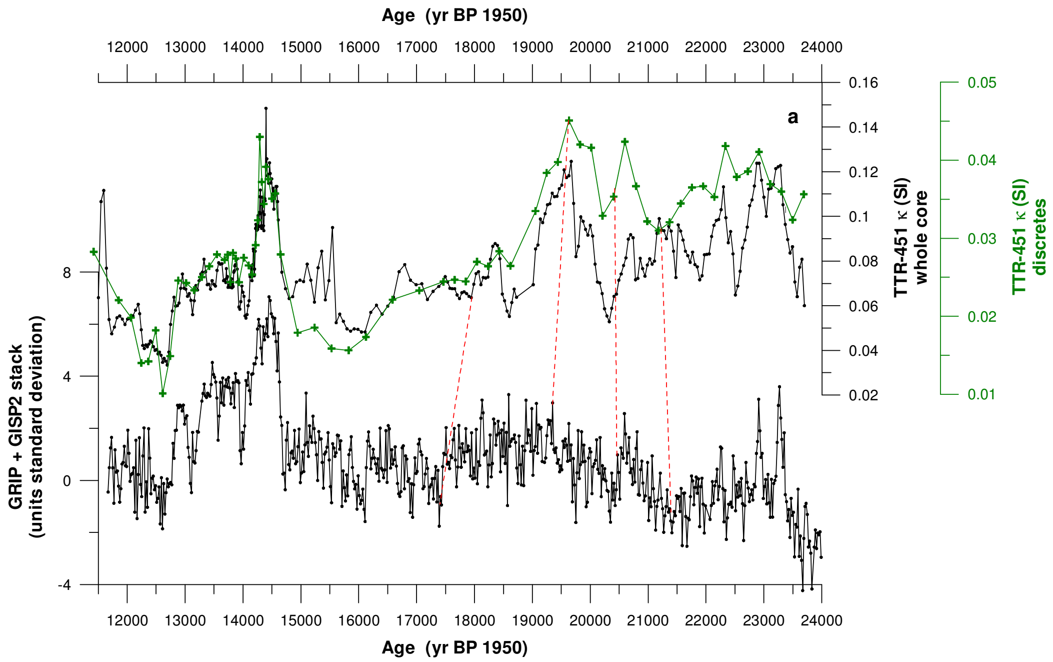

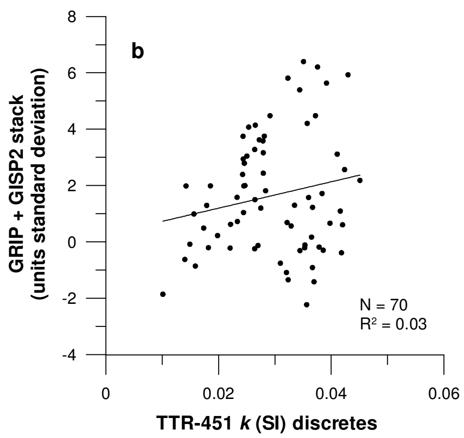

Figure 4.48. a. The magnetic susceptibility (κ) records for TTR-451 and the hybrid Greenland ice core air-temperature proxy record plotted versus GICC05 age. The red dashed lines represent correlation tie-points. b. The discrete sample magnetic susceptibility (κ) data are cross–plotted versus the GRIP + GISP2 hybrid ice core data.

Initially, the dating at 102.3 cm depth in TTR-451 (KIA-25854), with a calibrated age of 17.432 ka BP (Table 4.5), is used in the age model construction ([4] in Figure 4.46). Ages are interpolated between this AMS^{14}C dating and a relatively robust tie point between the TTR-451 magnetic susceptibility at 174.5 cm depth and 23.370 ka BP in the hybrid Greenland ice core temperature record. Figure 4.48a plots these records against age with only those limited age controls. A cross-plot of the discrete magnetic susceptibility data and the Greenland hybrid ice core record shows that there is no correlation (Figure 4.48b), with an $R^2 = 0.03$.

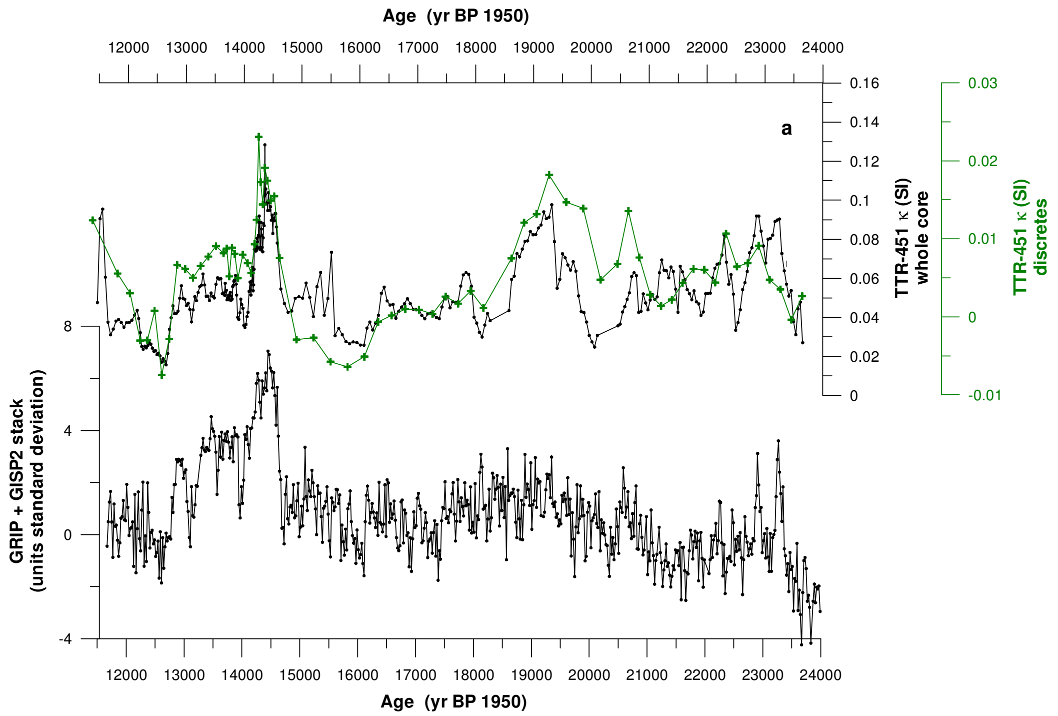

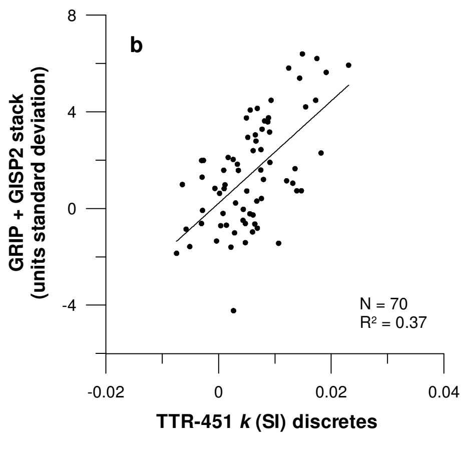

Figure 4.49. a. The de-trended magnetic susceptibility (κ) records for TTR-451 and the hybrid Greenland ice core air-temperature proxy record plotted versus GICC05 age. b. The de-trended discrete sample magnetic susceptibility (κ) data are cross–plotted versus the GRIP + GISP2 hybrid ice core data.

The red dashed lines in Figure 4.48 indicate four new tie-points between the TTR-451 magnetic susceptibility and the hybrid Greenland ice core temperature record, which considerably improve the correlation. The AMS^{14}C dating at

102.3 cm depth [KIA-25854, with a calibrated age of 17.432 ka BP; Table 4.5) is rejected as a strict control point on the basis of this correlation exercise, and a ΔR of 647 years is estimated. As this age lies just within the time of the H1 AMOC collapse (grey shaded bars in Figure 4.46a, McManus *et al*., 2004), an old ^{14}C ventilation age is not unsurprising. This now places the age model just outside the 2σ errors of the calibrated dating.

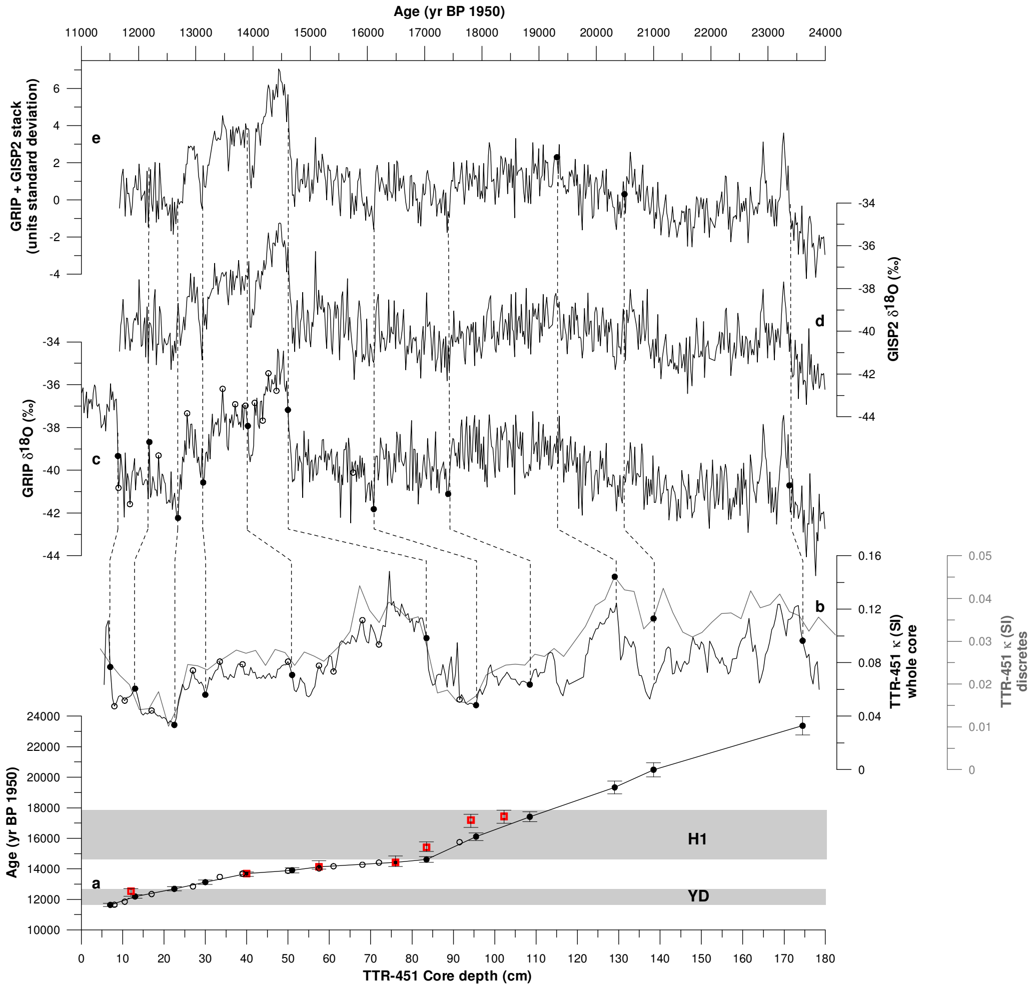

Figure 4.50. Depth versus age plot for core TTR-451. Open, red squares indicate calibrated AMS^{14}C datings, and error bars indicate the 2σ uncertainty range (Table 4.5). Solid black dots indicate tie points from the correlation between the magnetic susceptibility and the GRIP ice-core δ^{18}O record, and open black circles represent extra correlation points between the magnetic susceptibility of core TTR-451 and the GRIP ice core record

that are not used to construct the age model, but are shown for validation. 2σ error bars indicate the maximum counting error on the GICC05 timescale. The grey areas represent the times of reduced NADW ventilation associated with the Younger Dryas and Heinrich Event 1 (McManus *et al.*, 2004). b. The magnetic susceptibility records for TTR-451: black denotes the higher resolution whole core data, and grey denotes the lower resolution discrete sample measurements. The GRIP (c) and GISP2 (d) ice core $\delta^{18}O$ records plotted versus the new GICC05 timescale based on layer-counting (Andersen *et al.*, 2006; Svensson *et al.*, 2006; Rasmussen *et al.*, 2006; 2007; Vinther *et al.*, 2006). e. The GRIP and GISP2 $\delta^{18}O$ records are combined to form a regional air-temperature proxy in units standard deviation. YD = Younger Dryas, and H1 = Heinrich event 1

We note that also the TTR-451 magnetic susceptibility (κ) records show a progressive trend to lower values towards the core top. In order to better assess the correlation between the TTR-451 magnetic susceptibility and the hybrid Greenland temperature record, this trend needs to be removed, so the magnetic susceptibility data are de-trended using a linear fit. The results are plotted in Figure 4.49 and reveal a good visual correlation. A cross-plot of the discrete sample magnetic susceptibility (κ) data on the new age-model against the hybrid Greenland temperature record (Figure 4.49b) gives an R^2 of 0.37 (N = 70). Although the correlation coefficient is not statistically significant, a good visual correlation (Figure 4.49a) between these datasets suggests that these tie-points are appropriate to use in the final TTR-451 age-model construction, which is shown in Figure 4.50. The near linear sedimentation rate below 84 cm depth (Figure 4.50a) supports the likelihood that this solution offers an adequate TTR-451 age model.

4.5.3. Validation of the TTR-451 chronology

The relatively high correlation coefficient (0.71) between the TTR-451 magnetic susceptibility record and the GRIP $\delta^{18}O$ ice-core record for the time period 11.5

to 15 ka BP (Figure 4.5), during which period the TTR-451 chronology is primarily constrained by AMS^{14}C datings, indicates that the age-model for this portion of the core is robust. Further validation for this time interval is gained by comparing records of palaeointenisty (NRM/ARM) for TTR-451 and core PS 2644-5 that was recovered from the Denmark Strait (67° 52' N, 21° 46' W) (Voelker *et al*., 1998; 2000; Kissel *et al*., 1999a, b; Laj *et al*., 2000; 2002; 2003) (Figure 4.51d). The age-model of core PS 2644-5 is tied to the layer counted GISP2 chronology (Meese *et al*., 1997) i.e., not GICC05. However, the GISP2 δ^{18}O record agrees well with NGRIP and GRIP on the GICC05 chronology for ages younger than 14.7 ka BP (Rasmussen *et al*., 2006). Figure 4.51d plots the palaeointensity records for cores TTR-451 and PS 2644-5 and shows good agreement over the time interval 11.5 to 15 ka BP

Further validation of the TTR-451 age model comes from comparison of its κ_{ARM}/κ record (a bottom current intensity proxy – for further discussions and validation of this proxy see section 4.3) with another (independently dated) record of NADW flow rate, which is based on the ^{231}Pa/^{230}Th ratio in core GGC5 from Bermuda Rise (McManus *et al*., 2004) (Figure 4.51c). This empirically corroborates the age-model for TTR-451 by a high degree of signal structure similarity. Note that the apparent offset at the Bølling transition results only from sample resolution in the discrete sample κ_{ARM}/κ series of TTR-451, and is verified by a sharper shift in our higher resolution 'whole core' measurements (grey record in Figure 4.51c).

The IRD (grains >150 μm g^{-1}) record for core TTR-451 is plotted versus age (Figure 4.51b). A ~500 year IRD minimum reflects the Bølling warm period and IRD peaks represent H1 and the Younger Dryas cold intervals. This evidence lends further support to the age model for core TTR-451. Finally, figure 4.51e shows the ratio of right coiling versus left coiling *N. pachyderma*. A sharp increase at around 14.5 ka BP is indicative of increased sea surface temperatures (e.g., Darling and Wade, 2008), and provides additional evidence for the identification of the Bølling warming in core TTR-451. This independently corroborates that the sharp shift to higher magnetic susceptibility values at

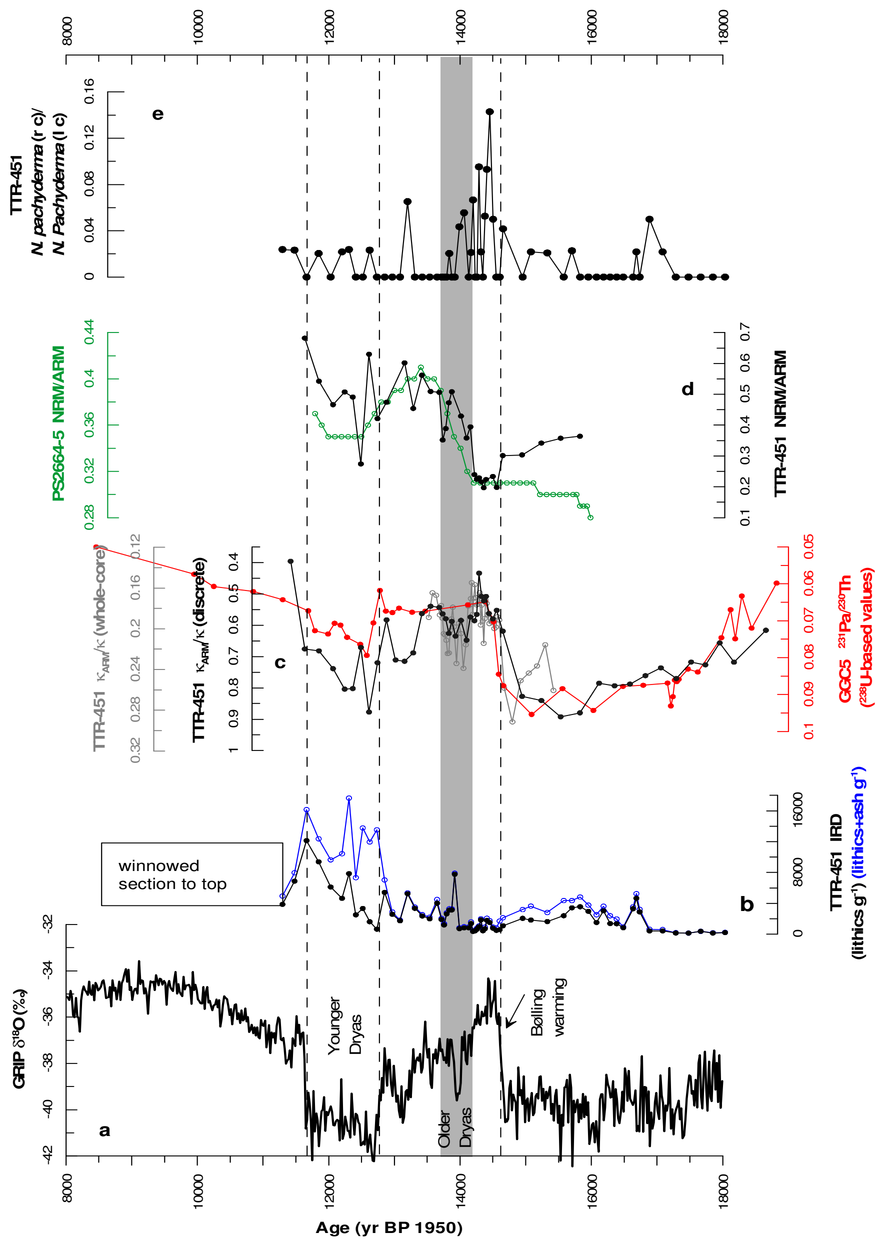

Figure 4.51 a. The GRIP ice core $\delta^{18}O$ record. plotted versus the new GICC05 timescale based on layer-counting (Andersen *et al.*, 2006; Svensson *et al.*, 2006; Rasmussen *et al.*, 2006; 2007; Vinther *et al.*, 2006). b. counts of lithic fragments, larger than >150 µm, per gram dry sediment weight in Eirik Drift core TTR-451. Black indicates lithic grains excluding volcanic glass, and blue indicates lithic grains including volcanic glass. The Holocene is represented in core TTR-451 by an intensely winnowed (sand) layer. c. Record of κ_{ARM}/κ for Eirik Drift core TTR-451 from discrete samples (in black) and whole core measurements (grey). The κ_{ARM}/κ data for TTR-451 are presented alongside the $^{231}Pa/^{230}Th$ record of core GGC5 from Bermuda

Rise (in red) (McManus *et al.*, 2004). d. Records of palaeointensity (NRM/ARM), after AF demagnetisation at 25 mT, for cores TTR-451 (black) and PS 2644-5 (Denmark Strait) (green). e. Ratio of right coiling (r c) versus left coiling (l c) *N. pachyderma* for core TTR-451.

---

around the same depth in core TTR-451 (Figure 4.50b), represents the sharp Bølling warming.

4.5.4. Summary

The chronology of TTR-451 is initially constrained by seven AMS^{14}C datings of monospecific samples of left-coiling *N. pachyderma* that have been calibrated using Calib5.0.1 with a regional reservoir age correction ΔR = 0 (Table 4.5). Within these constraints, the age model is fine-tuned using correlation between the TTR-451 magnetic susceptibility (κ) record and Greenland ice-core $\delta^{18}O$ records, similar to methods used previously (e.g., Dokken and Jansen, 1999; Kissel *et al.*, 1999a, b). The fine-tuned age model remains well within the 2σ bounds on three of the calibrated radiocarbon datings (red circles in Figure 4.50a), just within the 2σ bounds for one dating, and just outside the 2σ bounds for three datings. Note that the fine-tuned age model remains well within the 2σ bounds of the calibrated AMS^{14}C during intervals for which ΔR values is generally thought to have been close to zero (Hughen et al., 2000; Bondevik et al., 2006; Keigwin and Boyle, 2008).

The fine-tuned age model suggests somewhat enhanced ΔR values for the four radiocarbon datings from the Younger Dryas (YD) and Heinrich Event 1 (H1) intervals (Figure 3a), again in agreement with previous suggestions that ^{14}C reservoir ages were substantially increased during those times (Hughen et al., 2000; Bondevik et al., 2006; Keigwin and Boyle, 2008). ΔR values are approximated for these datings for core TTR-451, and these inferred ΔR values compare well with independently derived ΔR estimates (Austin *et al.*, 1995; Bondevik et al., 2006; Keigwin and Boyle, 2008).

CHAPTER 5

5. DISCUSSION

The temporal relationship between North Atlantic meltwater injections, and in particular meltwater pulse 1a (mwp-1a), and the climate history of the last deglaciation remains a subject of debate. This chapter aims to resolve and reconcile timing discrepancies between sea-level and climate records. With new evidence from core TTR-451 (Eirik Drift, south of Greenland; Figure 3.1), palaeoceanographic reconstructions of Heinrich event 1 (H1) and the last deglaciation provide information on the relationship between meltwater injections, NADW flow intensity and climate. The location of core TTR-451 and the methods are described in chapter 3, the results in section 4, and the age-model for the core in section 4.5.

First, this chapter presents the findings by Stanford *et al.*, which were published in *Palaeoceanography* in December, 2006. For reference, this paper is provided in its published format in the appendices of this thesis. Here, the timing of mwp-1a in the Barbados fossil coral sea level record is conclusively resolved, and placed in context with the climate history of the last deglaciation, as recorded in the GRIP $\delta^{18}O$ ice core stratigraphy on the latest GICC05 chronology. This is done with consideration of the well constrained uncertainties of both records. Also published in Stanford *et al.* (2006), and presented next in this chapter, is a high-resolution record of North Atlantic Deep Water (NADW) flow intensity from core TTR-451, Eirik Drift, which spans the time period of the last deglaciation. This provides a tool with which to evaluate whether there is a relationship between meltwater injections, NADW formation, and climate change.

Next in this chapter, the apparent timing discrepancies through the last deglaciation, and in particular mwp-1a, between the Sunda Shelf (^{14}C dated) and the Barbados fossil coral (U/Th) dated sea-level records are investigated. Within the context of their dating and depth uncertainties, the timing of mwp-1a is reconciled between these two records.

Finally in this chapter, high-resolution planktonic foraminiferal $\delta^{18}O$ data, lithic and foraminiferal abundance counts and the record of NADW flow intensity (κ_{ARM}/κ) are presented for core TTR-451. These new records are combined and compared with previously published datasets from marine sediment cores and terrestrial records, to give new reconstruction of the palaeoceanographic evolution of Heinrich event 1 in the North Atlantic, and to provide insight into the mechanism for the abrupt Bølling warming. These records also further elucidate the role of the Nordic Seas during these extreme climate transitions.

5.1. Timing of meltwater pulse 1a and climate responses to meltwater injections

Well-dated fossil corals (Fairbanks, 1989; 1990; Bard *et al.*, 1990a, b, 1996; Fairbanks *et al.*, 2005), and other methods (e.g., Rohling *et al.*, 1998; Hanebuth *et al.*, 2000; Siddall *et al.*, 2003), have documented that global sea level has risen by 120 m or more since the Last Glacial Maximum. The combined use of Accelerator Mass Spectrometry (AMS) ^{14}C and U/Th datings in fossil coral studies offers insight into the real time structure of the deglacial sea level rise, and also allows extension of the radiocarbon calibration curve beyond 10 ka BP (thousands of years Before Present, where Present refers to AD1950) (Bard *et al.*, 1990a, 1998; Reimer *et al.*, 2004: Fairbanks *et al.*, 2005). Fossil coral records contain evidence of a dramatic sea level rise in excess of 20 m at around the time of the last deglaciation, the so-called melt water pulse (mwp-1a) (Fairbanks, 1989; 2005; Bard *et al.*, 1990b; 1996; Hanebuth *et al.*, 2000; Weaver *et al.*, 2003). However, controversy remains about the precise age of mwp-1a, with published values varying from around 14.6 ka BP (Hanebuth *et al.*, 2000) to 14 ka BP (Bard *et al.*, 1996; Fairbanks *et al.*, 2005).

A marked step in the last deglaciation is recognised in Greenland ice core records by the sharp Bølling warming (GI-1e) (Björck *et al.*, 1998), dated at around 14.6 ka BP (Rasmussen *et al.*, 2006). At around 14 ka BP, the Bølling warm period was ended abruptly by the Older Dryas cold event (GI-1d) (Björck *et al.*, 1998; Rasmussen *et al.*, 2006). Based upon an inferred age of around 14.6 ka BP for mwp-1a, this meltwater event has been suggested as a trigger for the Bølling warming (Hanebuth *et al.*, 2000). Isostatic rebound calculations and ocean-climate modelling results have been used to support the suggestion that mwp-1a was derived from Antarctica and was the direct cause for the Bølling warming (Clark *et al.*, 1996; 2002; Kienast *et al.*, 2003; Weaver *et al.*, 2003). In contrast, earlier results from the Barbados fossil coral record were used to infer that mwp-1a should instead be associated with the Older Dryas cooling that terminated the Bølling warming (Bard, 1996; Kroon *et al.*, 1997).

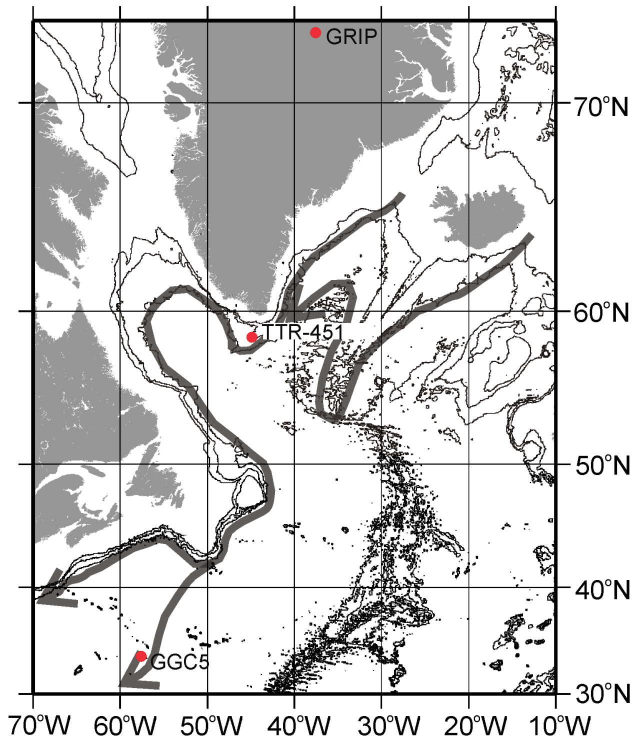

Figure 5.1. Location of core TTR-451. Also shown are the locations of marine core GGC5 and the GRIP ice core drill site. The dark grey arrows indicate the NADW flowpath (after Schmitz, Jr. and McCartney (1993)).

To resolve this controversy, we compare the Greenland ice core climate proxy record on the new layer-counted GICC05 time scale (Rasmussen *et al.*, 2006), with the latest U/Th-dated history of deglacial sea-level change (Fairbanks *et al.*, 2005; Peltier and Fairbanks, 2006). To evaluate the implications of the resolved relative timings between these records with respect to climate change mechanisms associated with meltwater injections, we present a new high-resolution record of NADW flow intensity during the last deglaciation, as recorded in core TTR-451 from Eirik Drift (south of Greenland) (Figure 5.1). The results are then placed within the context of recent suggestions about the location and depth-distribution of meltwater pulses (Aharon, 2005; Tarasov and Peltier, 2005). Modern observations of surface freshening and sea-ice reductions in the Arctic Ocean and Nordic Seas (Dickson *et al.*, 2002; Lindsay and Zhang, 2005) and reduced formation of NADW (Dickson *et al.*, 2002; Bryden *et al.*, 2005) underline the need for a better understanding of the potential ocean-climate responses to meltwater injections.

5.1.1. Revised ages of mwp-1a and Greenland climate events

The fossil reef series indicates a sharp global sea-level rise of about 20 m at around 14 ka BP (Figure 5.2b): meltwater pulse 1a (mwp-1a) (Fairbanks, 1990). Gaussian smoothing through the recently improved data series for Barbados (Fairbanks *et al.*, 2005; Peltier and Fairbanks, 2006) illustrates the history of sea-level change through time (Figure 5.2b), and its first time derivative offers insight into rates of sea-level change (Figure 5.2c). The latter clearly identifies mwp-1a between 14.17 and 13.61 ka BP, with a peak rate of 4.3 cm yr^{-1} sea-level rise close to 13.86 ka BP. The youngest indicator of low pre-mwp-1a sea level is sample RGF 9-8-2, which was originally U/Th-dated at 14.235±0.050 ka BP (1σ) (Bard *et al.*, 1990a; 1990b) and was recently re-dated at 14.082±0.028 ka BP (1σ) using higher precision mass spectrometry and new decay constants (Fairbanks *et al.*, 2005). This single young point has been questioned (Kienast *et al.*, 2003; Weaver *et al.*, 2003) since Sunda shelf data suggest that mwp-1a started considerably earlier, at around 14.6 ka BP (Hanebuth *et al.*, 2000). However, the Sunda Shelf record relies upon AMS^{14}C ages, which are subject to much greater uncertainty than U/Th chronologies, especially when corrections for variable ^{14}C reservoir ages are considered. Recent improvements in the resolution of the Barbados record have added 6 new low (pre-mwp-1a) sea-level points between 14.60 and 14.08 ka BP that comprehensively validate the age of sample RGF 9-8-2 (Table 5.1.) (Fairbanks *et al.*, 2005; Peltier and Fairbanks, 2006).

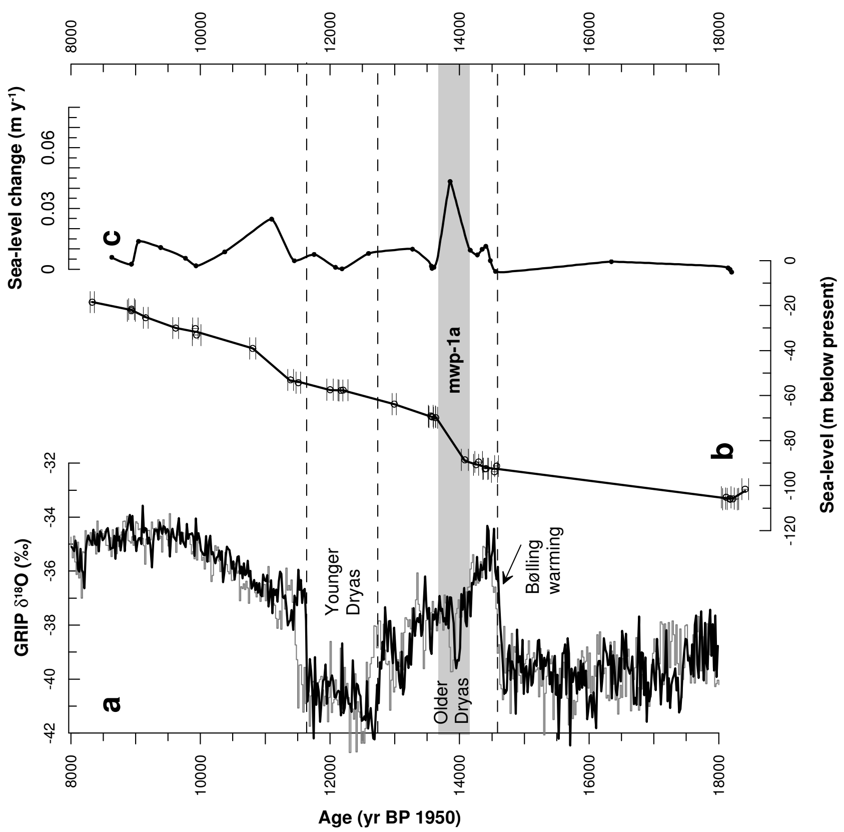

Figure 5.2 a. The GRIP ice core $\delta^{18}O$ record. The thin grey line is the record plotted versus the previous (modelled) ss09sea timescale (Johnsen *et al.*, 2001). The heavy black line is plotted versus the new GICC05 timescale based on layer-counting (Anderson *et al.*, 2006; Svensson *et al.*, 2006; Rasmussen *et al.*, 2006; 2007). b. The sea-level record based on U/Th-dated corals from Barbados (Fairbanks *et al.*, 2005; Peltier and Fairbanks, 2006) (see also Table 5.1). Error bars indicate 2σ limits. c. Record of rate of sea-level change, determined as the first time derivative of the solid line in (b).

Stable oxygen isotope ratios ($\delta^{18}O$) of ice from Greenland ice cores reflect temperature and air mass variations over the ice sheet. More negative values generally represent colder conditions, and less negative values represent warmer conditions. Recent layer-counting has provided a common timescale for three key ice cores from the Greenland ice sheet back to 14.73 ka BP (DYE-3, GRIP, and NorthGRIP) (Rasmussen *et al.*, 2006; Vinther *et al.*, 2006). The resultant new GICC05 timescale is in good overall agreement with that of the fourth key record from the Greenland ice sheet (GISP2) (Meese *et al.*, 1997). In the GRIP ice-core $\delta^{18}O$ record, a sharp $\delta^{18}O$ shift near the bottom of the layer-counted series (Figure 5.2a, black) marks the abrupt onset of the Bølling (GI-1e) (Björck *et al.*, 1998) warm period. In the GICC05 timescale this warming is dated at 14.64 ka BP, with a maximum error of 186 years (Rasmussen *et al.*, 2006), which is in close agreement with its layer-counted age of 14.65 ± 0.09 ka BP in Cariaco Basin (Lea *et al.*, 2003). These tight constraints place the warming some 60 years earlier than the previous, less certain, ss09sea ice-core timescale (Johnsen *et al.*, 2001) (Figure 5.2a, grey). Note that the total uncertainty of the GICC05 timescale, which amounts to only 186 years at around the Bølling warm transition, mainly consists of the maximum counting error (related to the number of annual layers that were difficult to interpret) and a possible bias (because the rules used for identifying annual layers cannot be independently validated). Comparison of the GICC05 timescale with the INTCAL04 radiocarbon calibration curve based on volcanic horizons (Rasmussen *et al.*, 2006) indicates that the maximum counting error in GICC05 is a conservative and adequate measure of the total uncertainty of the GICC05 timescale in this interval.

For the first time, the age models of both ice cores and sea-level evolution are constrained with sufficient accuracy to permit sensible comparisons. If the 186-year uncertainty in the GICC05 age of 14.64 ka BP for the Bølling onset were entirely systematically biased toward the younger bound, then its youngest possible age would be 14.45 ka BP. Note that it is unlikely that the errors in the GICC05 timescale are distributed in such a systematic manner, especially given the excellent agreement with ages from Cariaco Basin (Lea *et al.*, 2003). Based on RGF 9-8-2, the maximum age for the onset of mwp-1a would be 14.11 (1σ) or 14.14 ka BP (2σ) (Figure 5.2b). Hence, mwp-1a apparently lags the Bølling onset by 5 to 6 centuries. Even when pushing the edges of the confidence limits in the two timeframes, mwp-1a lags the Bølling onset by 3 centuries. This firmly corroborates the age offset suggested independently by radiocarbon results, which by themselves are insufficiently precise to be conclusive due to reservoir age uncertainties. Consequently, there is no longer a reasonable case to assume that mwp-1a coincided with the Bølling onset. We therefore reject the hypothesis that mwp-1a may have triggered the abrupt onset of the Bølling warm period (Kienast *et al.*, 2003; Weaver *et al.*, 2003).

sample code	species	RSL (m)	mean U/Th age (y BP)	2σ (y)	N	mean ^{14}C age (y BP)	2σ (y)	N
RGF 12-9-5	A. palmata	-57.59	12203	76	1	10485	70	1
RGF 12-15-4	A. palmata	-63.78	12993	34	2	11464	78	4
RGF 12-21-2	A. palmata	-69.06	13555	38	1	11903	56	2
RGF 12-21-6	A. palmata	-69.35	13574	52	1	11945	70	1
RGF 12-21-7	A. palmata	-69.57	13578	52	1	11909	88	4
RGF 12-21-10	A. palmata	-69.85	13632	32	1	12075	60	1
RGF 9-8-2	A. palmata	-88.60	14082	56	2	12615	80	1
RGF 9-11-2	A. palmata	-90.75	14255	40	3	12735	80	1
RGF 9-9-7	A. palmata	-89.51	14295	58	1	12795	80	1
RGF 9-12-7	A. palmata	-92.57	14396	36	2	12780	50	2
RGF 9-12-5	A. palmata	-92.49	14408	40	1	12780	80	2
RGF 15-5-3	A. palmata	-91.34	14573	30	1	12730	70	1
RGF 9-13-3	A. palmata	-93.89	14539	46	1	12680	60	1
RGF 9-21-11	A. palmata	-106.09	18176	112	1	15405	60	1

Table 5.1. U/Th and ^{14}C ages of the samples identifying meltwater pulse 1a in the Barbados coral record. Radiocarbon ages are reported without reservoir age subtraction. Ages are after Fairbanks *et al.* (2005). All reported ^{14}C ages are conventional ^{14}C ages before 1950 (5568 yr half life, corrected for fractionation). Errors are given at the 2σ level for both ^{14}C and ^{230}Th ages. All ^{230}Th ages are expressed as years before 1950. The relative sea levels (RSL) are the recovery depths of *Acropora palmata* relative to the present sea level. Mwp-1a is bracketed in Barbados between samples from cores 9 and 12.

The new time constraints instead confirm a previous suggestion (Bard *et al.*, 1996; Kroon *et al.*, 1997) that mwp-1a was associated with the termination of the Bølling warm period (Figures 2a-c). Meltwater addition started within the Bølling, possibly as a direct response to high-latitude warming during that period (McManus *et al.*, 2004), or due to increased heat transport in the Agulhas Current (Peeters *et al.*, 2004), and culminated in a meltwater peak at 13.9 ka BP that coincides with the sharp "Older Dryas" (GI-1d) (Björck *et al.*, 1998) cooling event. At issue however, is whether there was a change in NADW flow intensity coincident with mwp-1a and the Older Dryas.

5.1.2. Record of κ_{ARM}/κ from TTR-451 as a NADW flow intensity proxy

Previous studies have invoked a relationship between large meltwater pulses into the Atlantic Ocean and coincident cooling over large parts of the northern hemisphere, through reduction of deep-water formation in the Nordic Seas and the associated oceanic poleward heat transport (e.g., Broecker, 1991; Rahmstorf, 1995). Our new proxy record for the strength of NADW overflow from Eirik Drift (Figure 5.3e) allows us to test the hypothesis that mwp-1a may have caused the termination of the Bølling warm period.

The ratio of susceptibility of anhysteretic remanent magnetization (κ_{ARM}) to low-field magnetic susceptibility (κ) is a proxy for magnetic mineral grain size when sediments are magnetically dominated by (titano)magnetite (Banerjee *et al.*, 1981; Verosub and Roberts., 1995). Previous work supports the assumption of constant magnetic mineralogy along the NADW flow path in the vicinity of Eirik Drift (Kissel *et al.*, 1999a, b; Laj *et al.*, 2002). Eirik Drift represents a key region for deposition of suspended matter transported out of the Nordic Seas, especially for transportation via deep-water overflow through Denmark Strait (between Iceland and Greenland). The magnetic mineral content of sediments in that region originates from a single common source (the Nordic basaltic province) (Kissel *et al.*, 1999a, b; Laj *et al.*, 2002). Our new κ_{ARM}/κ record from Eirik Drift therefore reflects variations in the size of the coarsest magnetic grains that can be carried by NADW out of the Nordic Seas and that settle out on Eirik Drift as NADW rounds the southern tip of Greenland. Lower κ_{ARM}/κ values represent coarser grain sizes (Banerjee *et al.*, 1981), and therefore, increased intensity of NADW formation (Figure 5.3e; note the inverted scale).

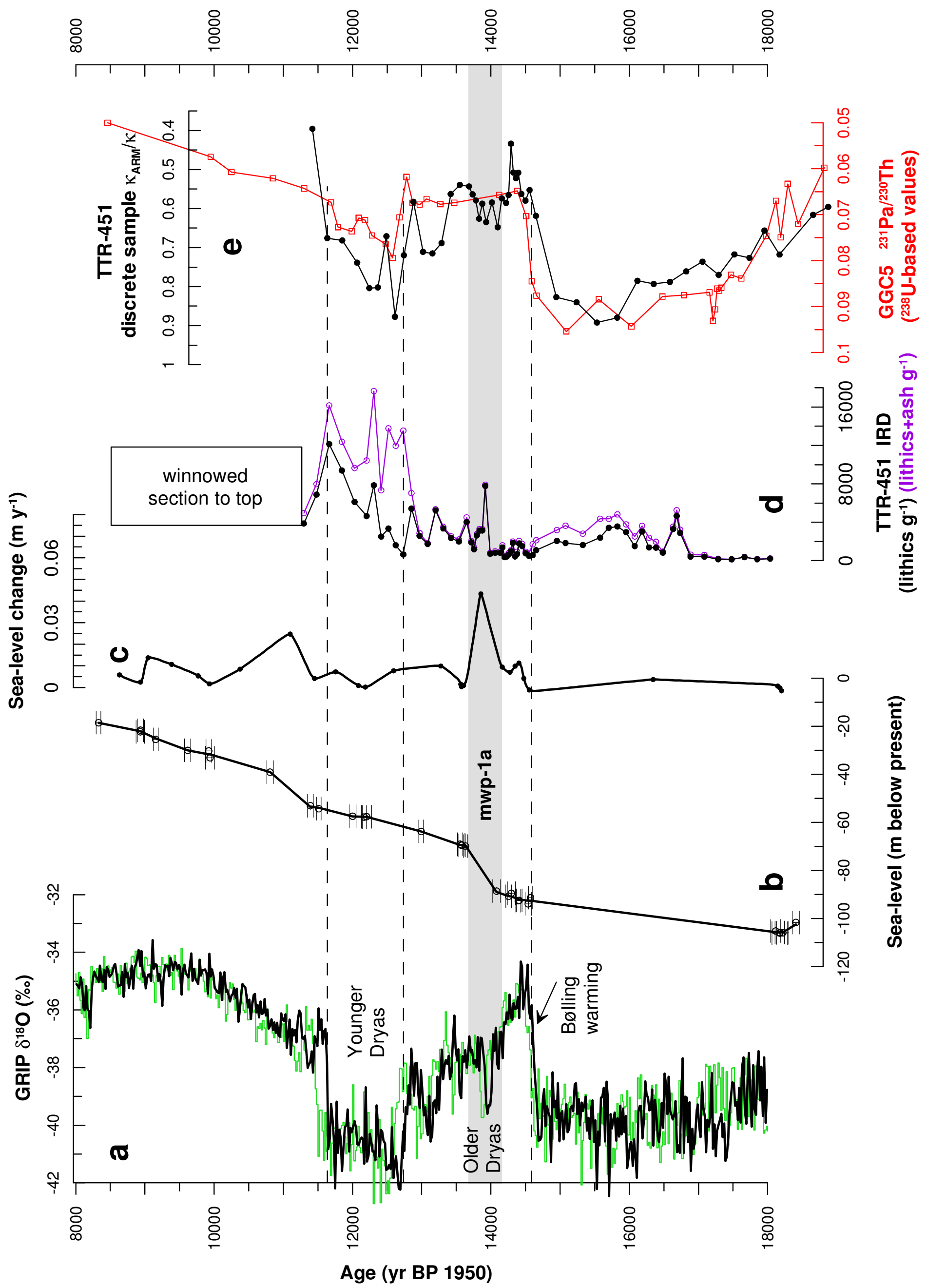

Figure 5.3 a. The GRIP ice core δ^{18}O record. The thin green line is the record plotted versus the previous (modelled) ss09sea timescale (Johnsen *et al.*, 2001). The heavy black line is plotted versus the new GICC05 timescale

based on layer-counting down to 14.73 ka BP (Rasmussen *et al.*, 2006). b. The sea-level record based on U/Th-dated corals from Barbados (Fairbanks *et al.*, 2005; Peltier and Fairbanks, 2006) (see also Table 5.1.). Error bars indicate 2σ limits. c. Record of rate of sea-level change, determined as the first time derivative of the solid line in (b). d. counts of lithic fragments, larger than >150 μm, per gram dry sediment weight in Eirik Drift core TTR-451. Black indicates lithic grains excluding volcanic glass, and purple indicates lithic grains including volcanic glass. The Holocene is represented in core TTR-451 by an intensely winnowed (sand) layer, suggesting a strong bottom-current regime. e. Record of κ_{ARM}/κ for Eirik Drift core TTR-451 from discrete samples (in black). The κ_{ARM}/κ data for TTR-451 are presented alongside the $^{231}Pa/^{230}Th$ record of core GGC05 from Bermuda Rise (in red) (McManus *et al.*, 2004).

The κ_{ARM}/κ record for core TTR-451 in shown in Figure 5.3e, along with another (independently dated) record of NADW flow rate, which is based on the $^{231}Pa/^{230}Th$ ratio in core GGC5 from Bermuda Rise (McManus *et al*., 2004). The suggestion that magnetic mineral concentration and grain size reflect changes in NADW flow strength (Kissel *et al*., 1999a, b; Laj *et al*., 2002) is empirically corroborated by the high degree of structural similarity between our κ_{ARM}/κ record and the $^{231}Pa/^{230}Th$ record from core GGC5 (Figure 5.3e). Note that the apparent offset at the Bølling transition results only from sample resolution (this is verified by a sharper shift in our higher resolution, 'whole core' measurements (not shown) that agrees closely with the $^{231}Pa/^{230}Th$ shift at that time; see Figure 4.58c). Compared to the $^{231}Pa/^{230}Th$ record, the TTR-451 κ_{ARM}/κ record offers a higher temporal resolution between the onset of the Bølling and the onset of the Younger Dryas (Figure 5.3e). A distinct NADW slowdown is suggested during the cooling from about 14.2 ka BP that culminated in the Older Dryas at around 14.0 ka BP. This suggests that the Bølling warm period may have been terminated by a reduction in deepwater formation in the Nordic Seas, and consequently reduced oceanic poleward heat transport, coincident with mwp-1a.

5.1.3. Wider implications

Our compilation of records demonstrates that direct climate impacts are not proportional to either the magnitude, or the rate, of meltwater addition (compare Figure 5.3a with 5.3b & c), and neither is the NADW flow intensity (compare Figure 5.3e with 5.3b & c). First, the dramatic mwp-1a event is found to be associated with only a slowdown (not shutdown) of NADW flow, and only a brief (100-150 year) direct climatic anomaly. Second, the widespread and long-lasting Younger Dryas cold reversal (Figure 5.3a) clearly lacks a discernible meltwater pulse (Figures 5.3b & c), but it was characterized by significant NADW slowdown (not shutdown) (Figure 5.3e). Third, there is little evidence (Hanebuth *et al.*, 2000) for rapid sea-level rise/meltwater addition during the 2-3 kyr interval centred on 16 ka BP ("Heinrich event 1" (Hemming, 2004; McManus *et al.*, 2004)), but this major cold period was marked by near NADW shutdown (McManus *et al.*, 2004) (Figure 5.3e).

Non-linear responses of ocean circulation to the magnitude and rate of meltwater additions may be expected in a system with different quasi-stable climate states and abrupt meltwater-driven transitions (Rahmstorf, 1995; Ditlevsen, 1999). However, it has also been argued that the location and nature of meltwater entry may be more important for NADW formation than the magnitude or rate (Moore, 2005; Tarasov and Peltier, 2005); smaller surface-bound additions in critical locations could outweigh large additions elsewhere and over greater depth ranges (hyperpycnal additions).

A considerable component of meltwater associated with mwp-1a is thought to have entered the ocean via the Gulf of Mexico (Flower *et al.*, 2004), in a hyperpycnal manner (Aharon, 2005), and strong mixing with seawater would have reduced its impact on NADW formation (Tarasov and Peltier, 2005; Aharon, 2005). Conversely, surface (iceberg) meltwater injection from Hudson Strait during Heinrich event 1, although not dramatically evident in the sea-level record (Fairbanks, 1989; Aharon, 2005; Peltier and Fairbanks, 2006) (Figures 4b,c), may have sufficiently affected the Nordic Seas to cause a collapse of

NADW formation (Figure 5.3e). The pronounced Younger Dryas event, associated with severely reduced NADW formation (Figure 5.3e), has also been ascribed to a surface (iceberg) meltwater flux, that was small enough to remain undetectable in terms of sea-level, into this critical region (from the Arctic (Moore, 2005; Tarasov and Peltier, 2005)). A meltwater signal into that region has been detected on the SE Greenland shelf (Jennings *et al.*, 2006).

The combined results presented here demonstrate that NADW formation and its associated climatic impacts are not simply governed by the magnitude and/or rate of meltwater addition. If indeed the climate forcing was dependent on freshwater input, then (small) freshwater additions targeted on the Arctic/Nordic Seas appear to carry a much greater risk of disrupting NADW formation. Alternatively, it should be considered that the inferred non-linear responses of ocean circulation to the magnitude and rate of meltwater additions indicate that meltwater input was not necessarily the primary driver. To evaluate this, new records are required that constrain other potential aspects of the ocean-climate interaction, such as sea-ice feedbacks (Li *et al.*, 2005; Wunsch, 2006).

5.1.4. Conclusions

Comparison of the GRIP ice core $\delta^{18}O$ record on the new layer-counted GICC05 time scale with the better constrained U/Th-dated sea-level record conclusively demonstrates that mwp-1a coincided with the Older Dryas and not the Bølling warming. By combining a new proxy record of NADW flow intensity from Eirik Drift with the Barbados sea-level and Greenland ice-core $\delta^{18}O$ records, we show that at the time of mwp-1a and the Older Dryas, there was a brief reduction (not a shutdown) in NADW flow intensity. However, our combination of proxy records also demonstrates that more extreme cooling events (Heinrich event 1 and the Younger Dryas), which were not associated with meltwater pulses large enough to significantly affect the sea-level record, were characterized by nearly collapsed NADW formation. This suggests either that there is a fundamental non-linearity between the rate and magnitude of meltwater injection and the rate of NADW formation, with perhaps a greater importance of the location and depth-distribution of melt-water injection, or that the primary mechanism for some climate transitions lies elsewhere in the ocean-climate-atmosphere system (e.g., sea-ice feedbacks).

5.2. Do the Sunda Shelf and Barbados timings for mwp-1a agree?

Deglacial meltwater pulse (mwp) -1a (about 20 m of sea-level rise in about 500 years) is the largest of the known well-constrained meltwater input events. Deglacial meltwater pulses are of great current interest, because these large-scale events offer ideal test-beds for numerical models of the responses of ocean circulation and climate to meltwater addition. As yet, however, such applications of mwp-1a are compromised by debate about its exact age in the Barbados and Sunda Shelf records. Here we show that careful scrutiny of the available data supports a mutually agreed timing and climatic scenario for mwp-1a.

Six recently added high-precision pre-mwp-1a U/Th datings were found to comprehensively validate the original U/Th age of 14.2 ka BP (re-dated at 14.082 ± 0.028 ka (1 σ)), for the onset of mwp-1a in the Barbados fossil coral record (Fairbanks *et al.*, 2005; Peltier and Fairbanks, 2006; Stanford *et al.*, 2006). However, a radiocarbon-dated record from the wide Sunda Shelf has been used to suggest that the sea-level rise of mwp-1a would be 300-500 years older (Hanebuth *et al.*, 2000). Although relatively small in view of systematic and random dating uncertainties, this timing offset has led to the development of two very different climate scenarios for mwp-1a, when these two datings scenarios are compared to the Greenland ice core $\delta^{18}O$ (temperature) records.

The first scenario relies on the younger (U-series) datings of around ~14 ka BP in the Barbados fossil coral record. These would imply that mwp-1a coincided in time with the Older Dryas cooling event that terminated the Bølling warm episode (Figure 5.4a-c) (Fairbanks, 1989; Bard *et al*., 1990a & b; 1996; Liu and Milliman, 2004; Fairbanks *et al*., 2005, Peltier and Fairbanks, 2006; Stanford *et al*., 2006). A reconstruction of North Atlantic Deep Water (NADW) flow intensity over Eirik Drift, offshore southern Greenland, indicates a coincident ~200 year weakening of the Atlantic Meridional Overturning Circulation (AMOC) (Stanford *et al*., 2006), coincident with the timing of the Older Dryas cooling.

The second scenario relies on the older (radiocarbon) datings of 14.6 to 14.3 ka BP for mwp-1a from the Sunda Shelf (Hanebuth *et al*., 2000). These would imply that mwp-1a coincided with the sharp Bølling warming, when Greenland temperatures rose from glacial to near present-day values in only a decade or two (Severinghaus and Brook, 1999; Rasmussen *et al*., 2006). The AMOC underwent a major abrupt intensification at that time (McManus *et al*., 2004; Stanford *et al*., 2006). An isostatic rebound model has been used to suggest that mwp-1a originated from Antarctica (Clark *et al*., 2002), and an ocean circulation model has used the Sunda Shelf ages for mwp-1a to suggest that a large meltwater event from Antarctica caused the sharp AMOC resumption and attendant Bølling warming event (Weaver *et al*., 2003).

Presented here is a critical assessment of the various datings for mwp-1a, to evaluate whether and how the sea level records from Barbados and Sunda Shelf might be reconciled with one another. Clearly, such reconciliation and a mutually agreed chronology for the event are essential for a better understanding of ocean/climate responses to the meltwater injection. Key to our assessment is a recalibration of the originally reported radiocarbon convention ages from Sunda Shelf, using the most recent iteration of the calibration curve, INTCAL04/CALIB 5.0.1. (Reimer *et al*., 2004) (Table 5.2), prior to comparison with the recently improved U-series datings from Barbados (Fairbanks *et al*., 2005; Peltier and Fairbanks, 2006; Stanford *et al*., 2006). The peak probability ages are calculated for the sea-level reconstruction, and ages with multiple peak 1 σ probabilities are considered insufficiently constrained (however, their 1 σ and 2 σ age ranges are listed in Table 5.2, and are represented by error bars only in Figure 5.4). For marine datings, we use the Marine04.14c calibration curve (Hughen *et al*., 2004), and we assume that ΔR=0. Plots of ^{14}C conventional ages versus calibrated/calendar ages are given in the appendix 1 of this thesis.

KIA-number	core number	core water-depth [m]	depth in core [cm]	sea-level (m below present)	type of facies	isolated material	age [^{14}C kyr BP]	1 σ [yr] (+) (-)	calibrated age using CALIB 4 [cal kyr BP] (Hanebuth et al. (4))	1 σ ranges [cal kyr BP]	calibrated age using CALIB 5.0.1 [cal kyr BP]	1 σ range [cal kyr BP]	2 σ range [cal kyr BP]
5620	18322-2	70	68	-70.68	shoreline	piece of wood	11.46	55	13.44	13.49 - 13.18	13.30	13.256-13.361	13.214-13.418
5608	18308-2	80	31	-80.31	mangrove	macro-fibres	12.36	70	14.32	15.04 - 14.60 14.42 - 14.12		14.128-14.493 (0.97) 14.549-14.566 (0.03)	14.053-14.781
5609	18308-2	80	34	-80.34	mangrove	woody branch	12.29	70	14.28	15.03 - 14.65 14.39 - 14.10	14.15	14.023-14.305	13.973-14.634
5610	18309-2	83	178	-84.78	mangrove	piece of root, in situ	12.415	55	14.34	15.17 - 15.15 14.99 - 14.54 14.46 - 14.15	14.31	14.225-14.597	14.147-14.834
5611	18309-2	83	178	-84.78	mangrove	macro-fibres	12.44	80	14.35	15.215 - 15.19 14.93 - 14.15	14.45	14.231-14.674	14.145-14.913
5986	18302-2	83	410	-87.1	mangrove	piece of wood	12.335	60	14.31	15.03 - 14.62 14.41 - 14.12	14.19	14.098-14.421	14.033-14.689
3113	18302-2	83	415	-87.15	mangrove	root-fibres, in situ	12.1	70	14.1	14.96 - 14.82 14.32 - 14.02 13.96 - 13.83	13.96	13.860-14.029	13.795-14.111
3530	18302-2	83	490	-87.9	mangrove	macro-fibres	12.23	60	14.15	15.025 - 14.69 14.36 - 14.08	14.09	14.010.14.162	13.890-14.308
3527	18300-2	91	61	-91.61	mangrove	macro-fibres	12.44	70	14.35	15.22 - 15.19 14.93 - 14.16	14.45	14.239-14.661	14.158-14.896
2567	18300-2	91	206	-93.06	mangrove	macro-fibres	12.65	60	15.29	15.52 - 15.19 14.77 - 14.35	14.95	14.779-15.063	14.632-15.189
2568	18300-2	91	223	-93.23	mangrove	macro-fibres	12.45	+100/ -90	14.92; 14.88; 14.36	15.24 - 15.19 14.915 - 14.155	14.50 (*on plateau*)	14.235-14.719	14.140-14.959
3111	18300-2	91	404	-95.04	mangrove	piece of wood	12.58	60	15.21; 14.63; 14.43	15.445 - 15.19 14.81 - 14.32	14.88	14.648-14.979	14.402-15.117
2569	18300-2	91	415	-95.15	mangrove	macro-fibres	12.56	100	15.18; 14.65; 14.42	15.42 - 15.19 14.82 - 14.31	14.84	14.477-14.972	14.225-15.092
3112	18300-2	91	428	-95.28	mangrove	root-fibres, in situ	12.44	80	14.35	15.22 - 15.19 14.93 - 14.16	14.45	14.231-14.674	14.145-14.913
2570	18300-2	91	431	-95.31	mangrove	piece of wood	12.47	60	15.015; 14.79; 14.37	15.30 - 15.17 14.90 - 14.23	14.62	14.288-14.716	14.200-14.919
5606	18301-2	93	277	-95.77	mangrove	piece of wood	12.41	110	14.34	14.95 - 14.13	14.29	14.173-14.668	14.065-14.934
5605	18301-2	93	277	-95.77	mangrove	piece of wood	12.37	55	14.32	15.035 - 14.59 14.425 - 14.13	14.23	14.147-14.492	14.088-14.752
5981	18301-2	93	331	-96.31	mangrove	piece of wood	12.51	55	15.10; 14.72; 14.39	15.36 - 15.18 14.86 - 14.28	14.69	14.453-14.871	14.248-14.972
4178. 02	18310-2	100	490	-104.9	shoreline	piece of wood	13.26	120	15.94	16.24 - 15.64	15.71	15.472-15.945	15.266-16.203
3535	18307-2	100	516	-105.16	tidal flat	macro-fibres	13.57	60	16.295	16.53 - 16.06	16.14	15.943-16.336	15.772-16.563
3536	18307-2	100	926	-109.26	delta plain	leach residue	15.41	90	18.41	18.70 - 18.12		18.110-18.383 (0.72) 18.431-18.536 (0.28)	18.023-18.618
5604	18299-1	102	285	-104.85	bay/lagoon	piece of wood	12.765	60	15.41	15.65 - 15.16 14.74 - 14.415	15.07	14.953-15.185	14.815-15.348
3532	18305-2	109	171	-110.71	shoreline	leach residue	15.25	150	18.23	18.55 - 17.91	18.03	17.887-18.489	17.467-18.623
3533	18305-2	109	511	-114.11	shoreline	leach residue	15.78	80	18.84	19.14 - 18.54	18.74	18.671-18.804	18.604-18.862
3533	18305-2	109	511	-114.11	shoreline	piece of wood	16.14	140	19.25	19.59 - 18.92	19.35	19.455-19.174	19.005-19.522
5980	18276-2	116	60	-116.6	tidal flat	leach residue	17.68	80	21.02	21.35 - 20.69	20.39	20.267-20.508	20.133-20.712
4754	18262-3	56	50	-56.5	bay/lagoon	maco-fibres	10.11	60	11.69; 11.67; 11.65	11.91 - 11.81 11.76 - 11.55 11.50 - 11.49 11.47 - 11.44 11.38 - 11.36		11.504-11.521 (0.04) 11.608-11.829 (0.75) 11.876-11.960 (0.21)	11.400-11.982
3146	18262-3	56	820	-64.2	mangrove	maco-fibres	10.93	70	12.97	13.12 - 13.08 13.03 - 12.88	12.88	12.846-12.923	12.815-13.000
3148	18262-3	56	840	-64.4	mangrove	maco-fibres	11.08	70	13.12; 13.08; 13.03	13.155 - 12.985	12.96	12.931-13.063	12.882-13.120
5201	18265-2	47	227	-49.27	shoreline	piece of wood	9.6	60	11.07; 10.94; 10.86; 10.82; 10.81	11.11 - 11.06 11.02 - 11.005 10.96 - 10.765		10.787-10.974 (0.71) 10.995-11.033 (0.13) 11.061-11.104 (0.16)	10.746-11.169
5202	18265-2	47	266	-49.66	shoreline	piece of wood	9.58	50	11.065; 10.94; 10.85; 10.83; 10.805; 10.80; 10.79	11.09 - 11.045 11.02 - 11.00 10.96 - 10.93 10.91 - 10.90 10.89 - 10.76		10.783-10.882 (0.42) 10.926 -11.040 (0.46) 11.052-11.083 (0.12)	10.733-11.134

Table 5.2. Sunda Shelf and Vietnamese Shelf AMS ^{14}C datings. *For dates with multiple 1 σ age distributions using CALIB5.0.1, the relative areas under the distributions are bracketed next to their 1 σ ranges. NB: No ages are assigned for these datings.

Figure 5.4a shows the GRIP ice-core $\delta^{18}O$ record on the latest, layer-counted GICC05 timescale (Andersen *et al.*, 2006; Svensson *et al.*, 2006; Rasmussen *et al.*, 2006; 2007), the Barbados fossil coral sea-level record (Fig. 5.4b - black), the rate of sea-level change as recorded in Barbados (Fig. 5.4c), and the re-calibrated Sunda Shelf sea-level data (Fig. 5.4b – green and red). Red symbols in Fig. 5.4b

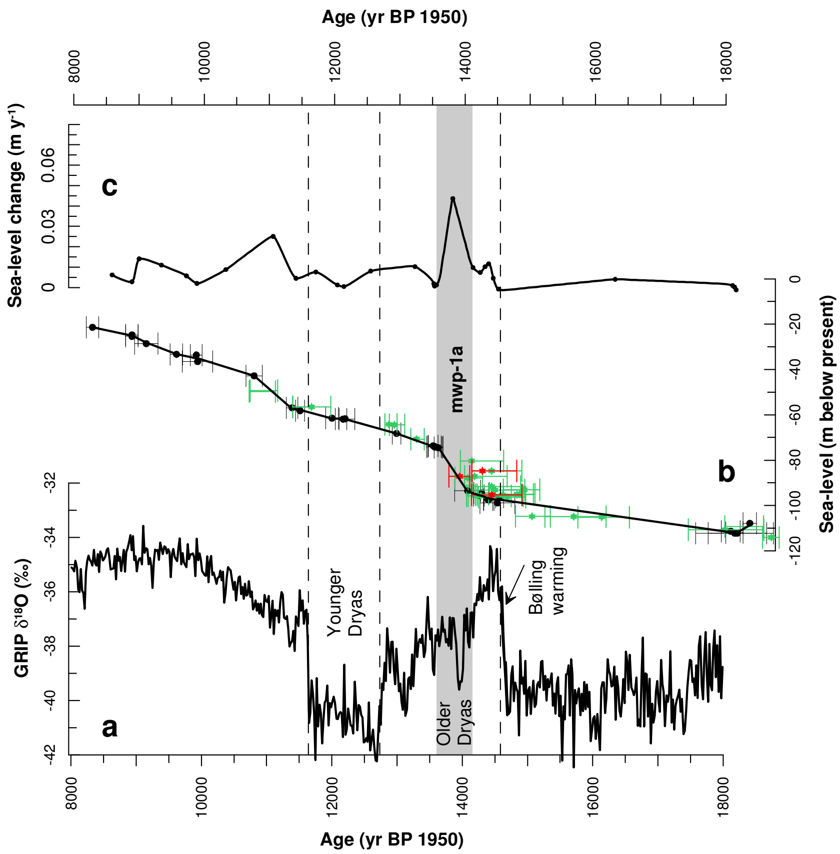

Figure 5.4a. The GRIP ice core δ^{18}O record on the GICC05 timescale on the basis of layer-counting (Andersen *et al.*, 2006; Svensson *et al.*, 2006; Rasmussen *et al.*, 2006; 2007). b. The U/Th-dated *Acropora palmata* corals from Barbados in black, which are corrected for a constant uplift of 0.34 m kyr^{-1} (^{230}Th ages are used for the uplift correction) (Fairbanks *et al.*, 2005; Peltier and Fairbanks, 2006) and the ^{14}C dated Sunda Shelf sea level record in green (re-calibrated from Hanebuth *et al.*, 2000). Datings on in situ roots and root fibres from the Sunda Shelf are shown in red, with their 2 σ error bars. c. Record of the rate of sea level change, determined as the first time derivative of the solid line in Figure 5.4b.

highlight results from in situ mangrove roots on Sunda Shelf (Hanebuth *et al.*, 2000). These are considered more reliable than the other results (green), which were described as loose wood fragments and macro-fibres and are more likely to have undergone reworking (Hanebuth *et al.*, 2000). Because of this reworking potential, we consider (after the in situ roots) the youngest ages from the wood fragments/macro-fibres to be the most accurate. Error may also result from compaction due to dewatering and coring, contamination by younger material, as well as the displacement of vegetation from higher elevations during spring tides (Toscano and Macintyre, 2003). We also consider the data comparison using a qualitative but obvious criterion, namely that sea-level cannot have resided at different levels at the same time.

Comparison of the Sunda Shelf and Barbados sea-level records by Hanebuth *et al.* (2000) suggested a near constant offset in the timings and/or sea-level depths throughout Termination 1. Figure 5.4b shows that the Sunda Shelf sea-level record on our recalibrated age frame instead agrees closely with the Barbados sea-level record. In Figure 5.5, we further scrutinise these records around the timing of mwp-1a, 13 to 15 ka BP. We here show that between ~15 and ~14.2 ka BP the re-calibrated sea-level points from the Sunda Shelf plot closely around the six new pre-mwp-1a U/Th dated sea-level points from Barbados (Fairbanks *et al.*, 2005; Peltier and Fairbanks, 2006). Using the above criteria for evaluating the Sunda Shelf datings, the timing of this pre-mwp-1a lowstand is validated by a dating on in situ mangrove root fibres at around 14.45 ka BP (14.145-14.913 ka BP 2σ). With the INTCAL98 curve, this sample had a calibrated age of 14.35 ka BP (Hanebuth *et al.*, 2000; Table 5.2). Further validation of the age of the pre-mwp-1a lowstand is given by two datings on separate pieces of mangrove wood taken from the same depth in core 18301-2, which yielded dates of 14.23 ka BP (14.088-14.752 ka BP, 2σ) and 14.29 ka BP (14.065-14.934 ka BP, 2σ). Given the reproducibility of the ^{14}C age, and the reworking potential of these loose fragments, we consider these youngest ages to be the most reliable dating for the pre-mwp-1a lowstand, and they agree closely with the Barbados sea level curve (Figure 5.5).

In situ mangrove root fibres that were dated at 13.96 ka BP, and with a 'tight' 2 σ range of 13.80-14.11 ka BP, give the first clear indication of the mwp-1a sea-level rise at Sunda Shelf. Two further datings of this sea-level rise were obtained from macro-fibres and a loose piece of wood, with slightly older ages of 14.09 ka BP (14.010-14.162, 2σ) and 14.19 (14.033-14.689 ka BP, 2σ), respectively. These observations validate the age of around ~14 ka BP suggested by the Barbados data for the onset of the mwp-1a sea-level rise.

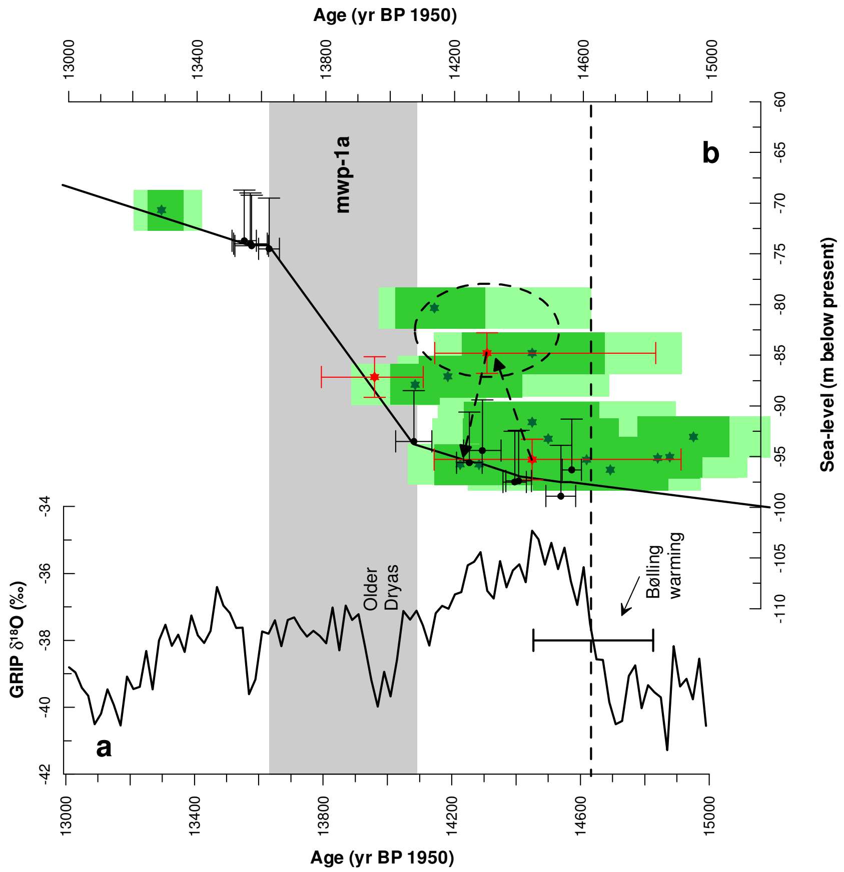

Figure 5.5a. The GRIP ice core δ^{18}O record on the GICC05 timescale on the basis of layer-counting (Andersen *et al.*, 2006; Svensson *et al.*, 2006; Rasmussen *et al.*, 2006; 2007). The horizontal error bar represents the total counting error at the Bølling warm transition. b. The U/Th-dated corals from Barbados in black, which are corrected for a constant uplift of 0.34 m kyr^{-1} (^{230}Th ages are used for the uplift correction) (Fairbanks *et al.*, 2005; Peltier and Fairbanks, 2006). The black vertical error bars represent the

5 m depth uncertainty of the *Acropora palmata* corals, and the horizontal black error bars represent the 2 σ dating uncertainty. The re-calibrated ^{14}C dated Sunda Shelf sea-level record is shown in green (re-calibrated from Hanebuth *et al.*, 2000) (the 2 σ error is shown in light green, and 1 σ is shown in dark green). The dark green stars represent the maximum modal (or peak probable) ages. The vertical shaded distance represents the estimated 2 m tidal range. Datings on in situ roots and root fibres from the Sunda Shelf are shown in red, with their 2 σ error bars. The dashed circle encloses three datings that are considered as anomalous, and the dashed arrows indicate the inferred sea-level fluctuations.

Three datings at depths above the initial mwp-1a sea-level rise have peak probability ages that range between 14.15 and 14.45 ka BP (encircled in Figure 2). We note that these are the only datings taken from core 18309-2 and sister core 18308-2. If we focus on in situ mangrove datings as the best constrained ages, then we would need to assume a rate of sea level rise of around 7.5 cm yr^{-1} between 14.45 and 14.31 ka BP (see dashed arrow in Figure 5.5), nearly double the minimum estimated rate for mwp-1a in Barbados of around 4.3 cm yr^{-1}. Two datings on mangrove wood fragments at a sea level depth of 95.77 m below present, however, have ages of 14.23 and 14.29 ka BP, therefore just postdating this inferred sea level jump. These datings concern woody fragments from core 18301-2 (the same site as core 18300-2), from which a large number of datings (including the oldest date for mwp-1a on the in situ mangrove root) were obtained. This date of 14.23 ka BP for a piece of mangrove wood would imply an astonishing rate of sea level lowering of around 13.14 cm yr^{-1} if the 14.15-14.45 highstand in cores 18309-2 and 18308-2 were real (see dashed arrow in Figure 5.5).

Given our criterion that sea level cannot have resided at different levels at the same time, that the three anomalous highstand datings (circled in Figure 5.5) are all from two rather poorly dated cores, and that the anomalous points would imply an extreme (unrealistic) sea-level fluctuation, we infer that these points (circled in Figure 5.5) are compromised. We therefore remove them from our final compilation of the recalibrated the Sunda Shelf record versus the Barbados fossil coral record (Figure 5.6).

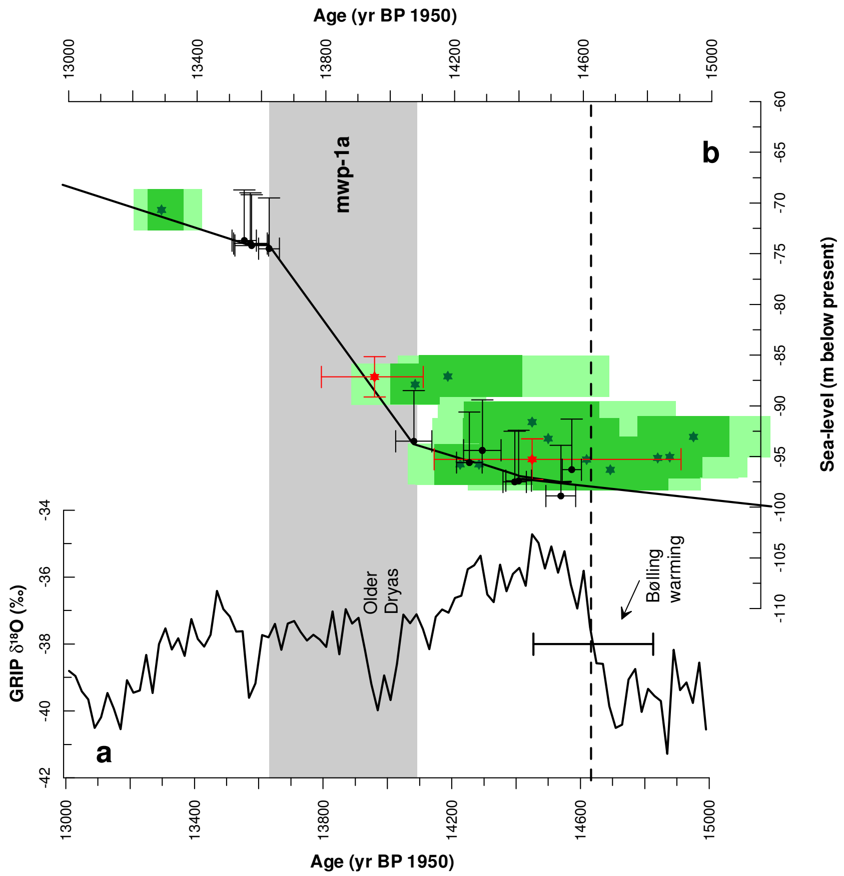

Figure 5.6a. The GRIP ice core δ^{18}O record on the GICC05 timescale on the basis of layer-counting (Andersen *et al.*, 2006; Svensson *et al.*, 2006; Rasmussen *et al.*, 2006; 2007). The horizontal error bar represents the total counting error at the Bølling warm transition. b. The U/Th-dated corals from Barbados in black, which are corrected for a constant uplift of 0.34 m kyr^{-1} (^{230}Th ages are used for the uplift correction) (Fairbanks *et al.*, 2005; Peltier and Fairbanks, 2006). The black vertical error bars represent the 5 m depth uncertainty of the *Acropora palmata* corals, and the horizontal black error bars represent the 2 σ dating uncertainty. The re-calibrated ^{14}C dated Sunda Shelf sea-level record is shown in green (re-calibrated from

Hanebuth *et al.*, 2000) (the 2 σ error is shown in light green, and 1 σ is shown in dark green). The dark green stars represent the maximum modal (or peak probable) ages. The vertical shaded distance represents the estimated 2 m tidal range. Datings on in situ roots and root fibres from the Sunda Shelf are shown in red, with their 2 σ error bars.

Our re-evaluation highlights some other relevant features in the Sunda Shelf data. The core logs for Sunda Shelf (Supplementary Information with Hanebuth *et al.*, 2000) show significant depositional hiatuses in most cores after about 13.96 ka BP (i.e. when the pre-mwp-1a lowstand mangrove forests drowned). A dating of around 13.30 ka BP in core 18322, taken after the transition from 'high glacial soils' to 'shoreline' deposits (Supplementary Information with Hanebuth *et al.*, 2000), represents the oldest Sunda Shelf evidence of a high post-mwp-1a sea level. Based on a conservative estimate from Barbados of a peak 4.3 cm yr^{-1} rate of sea-level rise during mwp-1a, we propose that mangrove forests/coastal swamps may not have been able to accrete fast enough to keep up with this rapid sea-level rise, so that mwp-1a may be represented on Sunda Shelf by a depositional hiatus. In this interpretation, mwp-1a is bracketed by the aforementioned datings of 13.96 ka BP and 13.30 ka BP (Figure 5.6b).

Alternatively, as the coral species *A. palmata* exhibit growth rates of up to 14 mm yr^{-1}, and can survive in waters deeper than 5 m (Toscano and McIntyre, 2003), one might consider that the last dated coral in the Barbados record prior to mwp-1a (RGF-9-8-2; Peltier and Fairbanks, 2006; Stanford *et al.*, 2006) was playing 'catch-up' with the sea-level rise, and might therefore not be truly representative of the onset of mwp-1a. If this was the case, then this would imply a date of mwp-1a in the Barbados records at 14.255 +/- 0.04 ka BP, which, using 2 σ uncertainties, is still separated from the Bølling warming by 159 yrs. However, the large depositional hiatus in the Barbados record after sample RGF 9-8-2 (14.082 ka BP) represents the main phase of mwp-1a, when the coral reef could no longer accrete at a fast enough rate to keep-up with the sea-level rise and drowned ('gave-up'). The excellent depth agreement between the Sunda Shelf and the Barbados sea-level record, prior to and after mwp-1a, would suggest that, if coral sample RGF 9-8-2 represented a reef playing catch-up, then it could not have been submerged at depths much greater than 5 m, without implication that the magnitude of mwp-1a in the Sunda Shelf sea level record is vastly underestimated.

5.2.1. Conclusions

Re-evaluation of the Sunda Shelf sea-level record would here imply that its dating for mwp-1a (13.96 ka BP, 2σ of 13.80-14.11 ka BP) post-dated the Bølling warming (14.64 ± 0.186 ka BP; Rasmussen *et al.*, 2006) by 680 yrs (Figure 5.6). When considering 2 σ errors on both the GICC05 layer counting and the Sunda Shelf radiocarbon dating, a minimum estimate of 343 yrs separates mwp-1a and the Bølling warming (Figure 5.6). This reconsidered timing for mwp-1a from the Sunda Shelf is in excellent agreement with the U/Th dated onset of mwp-1a of 14.082 ka BP from the Barbados fossil coral record (Fig. 5.6b). On this basis we now reject the hypothesis that mwp-1a could have been the trigger for the Bølling warming (Weaver *et al.*, 2003), and instead coincided with the Older Dryas cooling event that terminated the Bølling warm interval (Bard *et al.*, 1990a & b; 1996; Kroon *et al.*, 1997; Liu and Milliman, 2004; Peltier and Fairbanks, 2006; Stanford *et al.*, 2006).

5.3. The Palaeoceanographic evolution of Heinrich event 1 in the North Atlantic: A new perspective

Heinrich (H) events are characterised in North Atlantic sediment cores by horizons with increased IRD concentrations, low foraminiferal abundances, and light planktonic foraminiferal calcite $\delta^{18}O$ values (meltwater dilution), and they occurred quasi-periodically with a spacing of 5,000 –14,000 yr intervals (e.g., Heinrich, 1988; Broecker, 1991; 1994; Bond *et al.*, 1992; 1999; Bard *et al.*, 2000; Rohling *et al.*, 2003; Hemming, 2004). These layers are particularly distinct in marine cores recovered from the so-called “IRD belt” (40°N to 55°N), but can be recognised throughout most of the North Atlantic (e.g., Heinrich, 1988; Broecker, 1991; 1994; Bond *et al.*, 1992; 1999; Bond and Lotti, 1995; Cortijo *et al.*, 1997; Hemming *et al.*, 2000; 2002; Hemming and Hajdas, 2003 Grousset *et al*, 2000; 2001; for review see Hemming, 2004). For further discussions see chapter 2 of this thesis.

It is thought that H events mainly represent a periodic collapse of the Laurentide ice-sheet (MacAyeal, 1993), although there are strong indications that the Icelandic, Fennoscandian, and British ice sheets were also involved (e.g., Bond *et al.*, 1997; 1999; Scourse *et al.*, 2000; Knutz *et al.*, 2001; 2007; Grousset *et al.*, 2001; Hemming *et al*, 2002; Hemming, 2004; Julien *et al.*, 2006; Nygård *et al.*, 2007; Peck *et al.*, 2006; 2007b). Furthermore, records from around the North Atlantic, and even throughout the Northern Hemisphere, indicate dramatic marine and terrestrial temperature reductions and increased aridity during H events (e.g., Atkinson *et al.*, 1987; Alm, 1993; Bond *et al.*, 1992; Mayewski *et al.*, 1993; 1994; 1997; Vidal *et al*, 1999; Broecker, 2000a; Bard *et al.*, 2000; Gasse, 2000; Rohling *et al.*, 2003; Hemming, 2004). The most widely accepted theory holds that the low temperatures resulted from reduced oceanic poleward heat transport due to surface freshwater dilution in the North Atlantic and a consequent shutdown of the Atlantic Meridional Overturning Circulation (AMOC) (e.g., Broecker, 1991; Rahmstorf, 1994; Ganopolski *et al.*, 1998; Ganopolski and Rahmstorf, 2002; Rahmstorf, 2002; Schmittner *et al.*, 2002; Kim *et al.*, 2002).

Sediment cores recovered from the IRD Belt suggest a common age for H1 (the last major H event occurring at the onset of the deglaciation) of between 16 and 17.5 thousand years Before Present (ka BP, where Present refers to AD 1950) (e.g., Bond *et al.*, 1992; 1997; 1999; Bard *et al.*, 2000; Rohling *et al*, 2003; Grousset *et al.*, 2001; Hemming, 2004), and terminating well before the onset of the Bølling warming (14.64 ka BP) (Lea *et al.*, 2003; Rasmussen *et al.*, 2006). Coincident with this timing of H1, $^{231}Pa/^{230}Th$ ratios recorded in a Bermuda Rise sediment core GGC5 suggest a phase of virtually complete AMOC shutdown (McManus *et al.*, 2004). However, this proxy for AMOC intensity suggests a gradual slowdown from around 19 ka BP into the AMOC collapse, and a sharp AMOC resumption coincident with the timing of the Bølling warming (McManus *et al.*, 2004). This full picture of AMOC changes has been independently corroborated with magnetic grain size measurements in core TTR-451, recovered from Eirik Drift, offshore S. Greenland (Stanford *et al.*, 2006; sub-chapters 4.3 and 5.1 of this thesis). The timing presented by McManus *et al.* (2004) of the gradual slowdown from around 19 ka BP to full collapse at around 17.5 ka BP has also been corroborated by a record of $^{231}Pa/^{230}Th$ from a drift deposit in the Rockall Trough (Hall *et al.*, 2006). Reduced deep water ventilation and, hence, also decreased AMOC intensity during H1 has also been inferred from records of $\delta^{13}C$, as well as from deep water ^{14}C ages and Cd/Ca ratios (e.g., Boyle and Keigwin, 1987; Boyle *et al.*, 1992; Sarnthein *et al.*, 1994; Curry *et al.*, 1999; van Kreveld *et al.*, 2000; Robinson *et al.*, 2005; Marchitto *et* *al*., 2007; Boyle and Keigwin, 2008).

Marine sediment core TTR-451 from Eirik Drift (for the core location and details see section 3.1; and Figure 5.7) is located beneath the modern pathway of the East Greenland Current (EGC), which today, constitutes the main mechanism for the export of cold and relatively fresh surface waters out of the Arctic (Aagaard and Carmack, 1989; Bacon *et al*., 2002; Wilkinson and Bacon, 2005). Eirik Drift is a contourite formed from the deposition of suspended sediment in NADW as it rounds the southern tip of Greenland (Chough and Hesse, 1985), and therefore, sediments from core TTR-451 also record changes in the North Atlantic Deep Water (NADW) flow intensity (see also section 4.3 and 5.1).

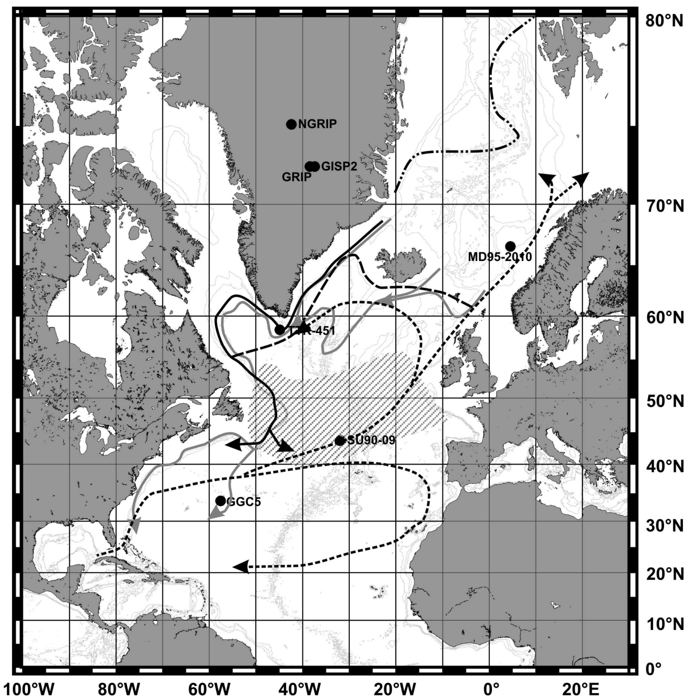

Figure 5.7. Map of the North Atlantic showing the core sites and the likely surface and deep hydrographies for the LGM after Bard *et al.* (2000) and Pflaumann *et al.* (2003). The IRD (hashed area) is after Hemming (2004). The deep currents are shown in grey, the warm surface currents are shown as dashed black arrows, and the cold surface currents as continuous black arrows. The summer and winter sea-ice margins, after Pflaumann *et al.* (2003) are shown by a 'dash-dot' line, and a dashed line, respectively.

Here, we investigate co-registered records of stable oxygen isotope analyses of the calcite tests of the planktonic foraminiferal species *Neogloboquadrina pachyderma* (left-coiling), IRD/lithic counts of grains (>150 μm) per gram of dried sediment, numbers of planktonic foraminifera (>150 μm) per gram of dried sediment, and the ratio of susceptibility of anhysteretic remanent magnetization (κ_{ARM}) to low-field magnetic susceptibility (κ) for core TTR-451. This combination provides an opportunity to study changes in both the surface and deep water currents that exited the Nordic Seas during H1. Note that the methods and age-model for core TTR-451 are described in sections 3 and 4.5 of this thesis, respectively, and the results in sections 4.3 and 4.4.

These results from Eirik Drift are combined with proxy records from around the North Atlantic and Nordic Seas for the interval that spans H1, from marine sediment cores SU90-09 (43°05N, 31°05W, 3375 m water depth), MD95-2010 (66º41N, 04º34E, 1226 m water depth), and GGC5 (33º42N, 57º35W, 4550 m water depth). These were published previously by Grousset *et al*. (2004), Dokken and Jansen (1999), and McManus *et al*. (2004), respectively, and their locations are shown in Figure 5.7. Also presented here is a re-evaluation of timings of ice-sheet and glacier advances and retreats, and their datings are compared with sea-level and circum-North Atlantic terrestrial temperature proxy records, for the time period of the Last Glacial Maximum (LGM), H1 and through the Bølling warming. These datings are then placed in the context of changes in the North Atlantic surface and deep-water hydrographies. We aim to thus elucidate the evolution of H1 in the northern North Atlantic, with specific attention to the involvement of the Nordic Seas.

5.3.1. Re-evaluation of terrestrial records of ice-sheet and glacier extent, and temperature for the LGM, H1 and the Bølling warming.

Reported (Accelerated Mass Spectrometric (AMS)^{14}C) radiocarbon convention ages for terrestrial temperature proxy records (Atkinson *et al*., 1987; Alm, 1993), terminal moraines, and for marine sediment horizons (Benson *et al*., 1998; McCabe and Clark, 1998; Giraudi & Frezzotti, 1997; Bowen *et al*., 2002; Dyke *et al.*, 2002; Marks, 2002; Ivy-Ochs *et al.*, 2006) are re-calibrated here using Calib5.0.1 (Reimer *et al.*, 2004). These re-calibrated datings are used along with previously published calendar ages (e.g., McCabe *et al.*, 2005; 2007) and ^{36}Cl boulder exposure ages (e.g., Bowen *et al.*, 2002; Dyke *et al.*, 2002; Licciardi *et al.*, 2004; Rinterknecht *et al.*, 2006). These combined timings of glacial advances and retreats are compared to ice core records of stable oxygen isotope ratios ($\delta^{18}O$) from Greenland and Antarctica, which reflect temperature and air mass variations over the ice sheet (e.g., Severinghaus *et al.*, 1998; Severinghaus and Brook, 1999; Stuiver and Grootes, 2000), and are shown on the GICC05 time-scale (Andersen *et al.*, 2006; Svensson *et al.*, 2006; Rasmussen *et al.*, 2006; 2007; EPICA community members, 2006). Because the GRIP and GISP2 ice core $\delta^{18}O$ records show significantly different values for the LGM/H1 transition despite their close proximity (Figures 5.7 and 5.8b), we consider (Figure 4.8a) a composite Greenland ice core $\delta^{18}O$ (temperature) record in units standard deviation.

From around 26 to 21 ka BP most of the circum-North Atlantic ice sheets had reached their maximum (LGM) extents, as shown by the sea-level records (e.g., Fairbanks, 1989; Bard, 1990a & b; Hanebuth *et al*, 2000; Yokoyama *et al.*, 2000; Lambeck *et al.*, 2002; Peltier and Fairbanks, 2006), and by datings on terminal moraines (e.g., Bowen *et al.*, 2002; Dyke *et al.*, 2002; Rinterknecht *et al.*, 2006; Figure 5.8e & f). The newly recalibrated radiocarbon convention ages for terrestrial records reveal surprising results. The LGM was a period of relative warmth, evident in Scandinavian pollen records (Alm, 1993) (Figure 5.8f), as well as *Coleoptera* abundances from the British Isles (Atkinson *et al.*, 1987). However, the Greenland ice core $\delta^{18}O$ records show the LGM to have been relatively cold, followed by warming from around 21 ka BP that likely reflects the change to increased summer insolation (Figure 5.8a), and the nearly coincident onset of warming in Antarctica (figure 5.8a). Onset of a southern hemisphere warming trend at this time has also been inferred from marine sediment records (e.g., Arz *et al.*, 1999; Sachs *et al.*, 2001; Kim *et al.*, 2002).

At around 21 ka BP, the British and Laurentide ice sheets underwent the first retreat from their LGM position (Bowen *et al.*, 2002; Dyke *et al.*, 2002 and references therein). Glaciers in the Austrian Alps, the Apennines, and the western US also started to retreat (Giraudi and Frezzotti, 1997; Licciardi *et al.*, 2004; Ivy-Ochs *et al.*, 2006). Although it is tempting to attempt reconstruction of phase relationships from Figure 5.8f, this is not warranted in view of the dating uncertainties on boulder exposure ages that can exceed 1000 yrs, and of the vast differences in the number of regional datasets. However, the continued 'early' activation of the British ice sheet is further corroborated by a record of terrestrial organic matter content (branched and isoprenoid tetraether (BIT)-index) in a marine core located in the Bay of Biscay (Menot *et al.*, 2006). The BIT-index serves as a proxy for freshwater discharge and indicates high discharge rates at around 19.5 ka BP.

Nearly 2000 yrs after the initial circum-North Atlantic retreat from the LGM extent that is described above, the Scandinavian ice sheet started its northward retreat at around 19 ka BP (Marks, 2002; Rinterknecht *et al.*, 2006; Figure 5.8f). Seismic mapping and marine sediment cores recovered from the Nordic Seas show that up to 20 m of fine-grained sediment was deposited over an area that exceeded 1600 km^2 (e.g., Hjelstuen *et al.*, 2004; Lekens *et al.*, 2005), which Lekens *et al.* interpreted to represent glacial outwash plume deposits. With a basal date in this depositional sequence of around 18.6 ka BP (Lekens *et al.*, 2005), these sediments give evidence of wide-spread and rapid glacial retreat along the Scandinavian ice-margin coeval with the timing of the terrestrial evidence of retreat (see pink line in Figure 5.8f). Further glacial retreats at with similar timing have been documented for the northwest American Cordilleran ice sheet (Clague and James, 2002), the southeast Appalachian margin (Dyke *et al.*, 2002), and for glaciers in the Austrian Alps (Ivy-Ochs *et al.*, 2006) (Figure 5.8f). Although poorly constrained, the ~500 yr duration Eerie interstadial is also dated at around 18.8 ka BP in the southern Laurentide region (Dyke *et al.*, 2002 and references therein). On a global scale, these datings of glacial retreat bracket a time interval when ice volume appears to have begun a first substantial decrease, as suggested by a first rapid step of sea-level rise (Hanebuth *et al.*, 2000; Yokoyama *et al.*, 2000; Figure 5.8e).

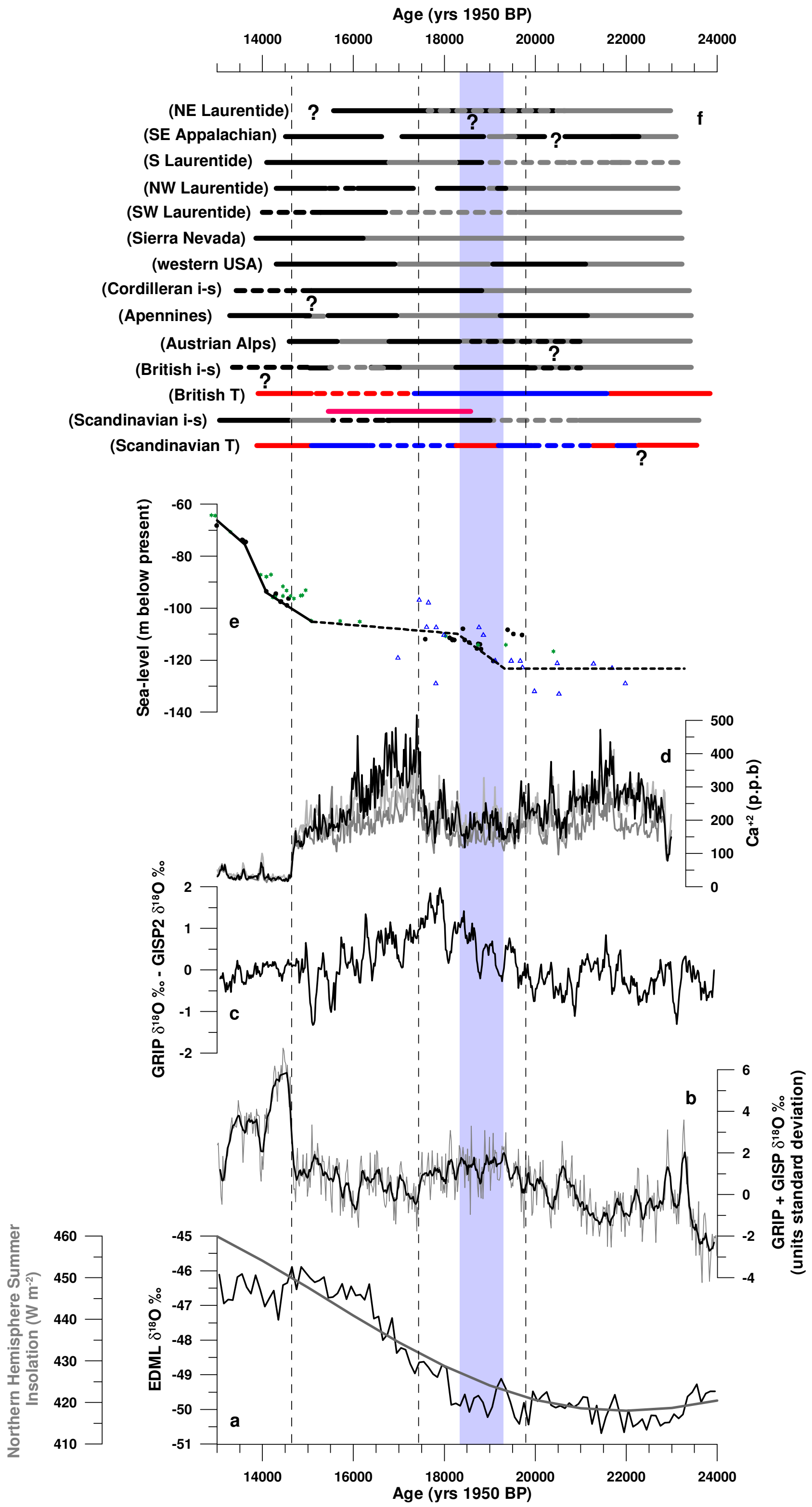

Figure 5.8 a. In black the EPICA Dronning Maud Land record on the GICC05 time scale (EPICA community members, 2006) and in grey, the northern hemisphere summer (July) insolation at 65 °N (Berger *et al*., 1999). b. The GRIP + GISP2 composite $\delta^{18}O$ ice core record in unit standard

deviation on the GICC05 timescale. c. The difference between the GRIP and NGRIP ice core $\delta^{18}O$ records (‰). d. The concentration of Ca^{2+} (p.p.b.) in the Greenland ice cores. GRIP is shown in black, GISP2 in dark grey and NGRIP in light grey (Fuhrer *et al.*, 1993; Mayewski *et al.*, 1994; Bigler *et al.*, 2004). e. Composite sea-level record. Black dots = the Barbados fossil coral record (Peltier and Fairbanks, 2006), green dots = the Sunda Shelf sea level record (Hanebuth *et al.*, 2000), blue triangles = the Bonaparte Gulf (Yokoyama *et al.*, 2000). The blue shaded area shows the timing of rapid sea level rise at around 19 ka BP. f. Recalibrated temperature records from Scandinavia (Alm, 1993) and Britain (Atkinson *et al.*, 1987); blue = cold, blue dashed = gradual cooling, red = warm, and red dashes = gradual warming. Grey lines show glacial advances, and retreats in black. Dashed lines are where there are no datings. Data is after Marks (2002), Rinterknecht *et al.* (2006), McCabe and Clark (1998), McCabe *et al.*, (2007) Bowen *et al.* (2002), Giraudi and Frezzotti (1997), Clague and James (2002), Licciardi *et al.* (2004) Dyke *et al.* (2002) and references therein Ivy-Ochs *et al.* (2006). The pink line represents the timing of extreme rates of sediment deposition in the Nordic seas (Lekens *et al.*, 2005).

After ~ 21 ka BP, a gradual cooling is inferred across Scandinavia (Alm, 1993), while a dramatic disappearance of *Coleoptera* in the British Isle suggests a rapid deterioration in climate (Atkinson *et al.*, 1987). Between 19.5 and 18.5 ka BP, a lack of ^{36}Cl boulder exposure ages in the British Isles may suggest that the British ice sheet re-advanced in response to the strong cooling (Bowen *et al.*, 2002). AMS^{14}C datings of marine mud from around the British Isles suggest a younger age for this re-advance of around 18.5 to 17 ka BP (McCabe and Clark, 1998; McCabe *et al.*, 2007 and references therein). This re-advance is broadly matched by a 2000 yr advance of glaciers within the Apennines that initiated at around 19.2 ka BP and continued to around 17 ka BP (Giraudi and Frezzotti, 1997). Within the southern Laurentide region the ice-sheet margin began to re-advance at around 18.3 ka BP (e.g., Dyke *et al.*, 2002). As a consequence of these glacial re-advances, at around 18.3 ka BP, the rate of global sea-level rise would appear to have been significantly reduced (Hanebuth *et al*., 2000; Yokoyama *et al*., 2000; Peltier and Fairbanks, 2006; Figure 5.8e). Note, however, that the Scandinavian ice-sheet continued to retreat (Lekens *et al*., 2005; Rinterknecht *et al*., 2006).

At around 17.5 ka BP, cooling is indicated in the Greenland ice core $\delta^{18}O$ records (Figure 5.8a), with a concomitant sharp increase in the Ca^{2+} ion concentration (Andersen *et al*., 2006; Svensson *et al*., 2006; Rasmussen *et al*., 2006; 2007). This sharp increase in the Ca^{2+} ion series is suggestive of a rapid intensification of the polar atmospheric circulation (Mayewski *et al*., 1997; Rohling *et al*., 2003 and references therein). Despite the onset of this cooling in Greenland at around 17.5 ka BP, coeval widespread and significant glacial retreat occurred on a near global scale (e.g., Giraudi and Frezzotti, 1997; McCabe and Clark, 1998; Denton *et al*., 1999; Dyke *et al*., 2002 and references therein; Bowen *et al*., 2002; Clague and James, 2002; Licciardi *et al*., 2004; Ivy-Ochs *et al*., 2006; Rinterknecht *et al*., 2006; McCabe *et al*., 2007; Figure 5.8f). Ice-free conditions in the Gulf of St. Lawrence by ~16.7 ka BP indicate the scale of this phase of retreat at the southeastern Laurentide margin, and a drawdown of the ice centre around the Hudson Bay region is thought to reflect an important reorganisation of the ice-streams (Dyke *et al*., 2002).

Conversely to the cooling trend shown in the Greenland ice core records (Figure 5.8b), a slight amelioration is evident in the British climate from the re-appearance of *Coleoptera* at around 17.2 ka BP. Their species abundances indicate that temperatures were at similar levels to the LGM, with winter temperatures around -25˚C (Atkinson *et al*., 1987). A short lived retreat of the British ice sheet was initiated at around this time (e.g., McCabe *et al*., 2007). However, by ~16.5 ka BP, the British ice-sheet had advanced back to its LGM (H1) extent before making its final retreat (McCabe and Clark, 1998; McCabe *et al*., 2007). A similar pattern is evident in the Austrian Alps (Ivy-Ochs *et al*., 2006), and a shorter duration re-advance occurred in the Apennine region, from around 15.5 ka BP (Giraudi and Frezzotti, 1997).

A gradual reduction in the Ca^+ ion series in the Greenland ice cores from around 16.2 ka BP suggests that the atmospheric polar circulation intensity decreased slightly at around this time, although remaining relatively intense (Figure 5.8b). However, relatively depleted $\delta^{18}O$ values recorded in the Greenland ice-cores indicate that temperatures in Greenland did not significantly improve at this time.

From around 15.5 ka BP, significant climate amelioration has been observed in records from the British Isles (Atkinson *et al*., 1987) and retreat from their H1 glacial maximum extent was well underway on a near global scale (Giraudi and Frezzotti, 1997; Benson *et al*., 1998; McCabe and Clark, 1998; Clague and James, 2002; Dyke *et al*., 2002 and references therein; Ivy-Ochs *et al*., 2006; McCabe *et al*., 2007; Hendy and Cosma, 2008). Intriguingly, planktonic foraminiferal faunal records from the Gulf of Cadiz indicate a more northward penetration of the Azores Front from around 16 ka BP (Rogerson *et al*., 2004). Hence, ~1000 yrs prior to the Bølling warming, it would appear that the atmospheric circulation was starting to rearrange back to a position more comparable to the present day, which may have been related to the sustained retreat of the Northern Hemisphere ice sheets.

The southern Scandinavian ice sheet, however, re-advanced at around 15.5 ka BP, most likely owing to positive mass balance due to increased moisture availability (Rinterknecht *et al*., 2006). However, both the Scandinavian pollen records (Alm, 1993) and the reduced Greenland ice core $\delta^{18}O$ values (Andersen *et al*., 2006; Svensson *et al*., 2006; Rasmussen *et al*., 2006; 2007) suggest that warming at northern high-latitudes may not have occurred until the sharp Bølling warming at 14.6 ka BP (Rasmussen *et al*., 2006). At the Bølling warming, when Greenland temperatures are estimated to have risen by up to 15ºC (Severinghaus *et al*., 1998; Severinghaus and Brook, 1999), even ice-sheets that were in positive mass balance, were overwhelmed by the climatic improvement and on a global scale ice-sheets rapidly retreated (Rinterknecht *et al*., 2006). Glacial retreat of the Scandinavian ice sheet is evident at around this time in Sweden (Lundqvist and Wohlfarth, 2001).

Low latitude sea-surface temperature (SST) estimates from Mg/Ca analyses (Lea *et al*., 2003) and shifts in the Inter-tropical Convergence Zone (ITCZ) from grey-scale data (Hughen *et al*., 1996) from Cariaco Basin, along with an East Asian monsoon intensification index from speleothem $\delta^{18}O$ records (Wang *et al*., 2001) show that relatively cold climatic conditions continued until the abrupt Bølling warming at 14.6 ka BP. These well-dated records show excellent signal comparison with the ice core $\delta^{18}O$ changes in Greenland (Rasmussen *et al*., 2006; Vinther *et al*., 2006), which likely record a predominantly winter signal. Denton *et al*. (2005) suggest that the records that show a close similarity to the Greenland $\delta^{18}O$ records may also be biased toward winter conditions, and speculate that improving summer conditions likely caused the apparent 'mismatch' with datings on snowline variations. Denton *et al*. (2005) also suggest that increased winter sea ice coverage at northern high latitudes likely caused this increased seasonality, consonant with suggestions by Broecker *et al*. (1999) and Seagar and Battisti (2006).

A more recent study of SST variations from paired Mg/Ca and $\delta^{18}O$ analyses on the planktonic foraminiferal species *Neogloboquadrina pachyderma* (left-coiling) and *Globigerina bulloides* from a NE Atlantic sediment core shows distinctly different temperature estimates between these tow species, with *G. bulloides* indicating much warmer SSTs during H events, than *N. pachyderma* (Peck *et al*., 2008). Peck *et al*. (2008) suggest that discrepancies between these two species result from *G. bulloides* recording a later and enhanced summer signal, and hence, indicate increased seasonality during H events. Peck *et al*. (2008) also suggest that this divergence in SST estimates may have resulted from increased meltwater stratification, or the formation of a shallow halocline, similar to the Arctic (Björk *et al*., 2002). However, evidence of intensified storminess over the North Atlantic (Rashid and Boyle, 2007), would preclude these hypotheses, as this would have likely resulted in increased rates of vertical mixing. We note however, that the divergence in planktonic foraminiferal SST proxy records does not extend towards the end of H events, but instead span the entire period of climate deterioration in the North Atlantic, including H1.

5.3.2. The records of Eirik Drift core TTR-451

Figure 5.9h shows the previously published environmental palaeomagnetic record of anhysteretic remanent magnetization (κ_{ARM}) to low-field magnetic susceptibility (κ), for core TTR-451 (Stanford *et al.*, 2006; see sections 4.3 and 5.1), along with the $^{231}Pa/^{230}Th$ record of core GGC5, Bermuda Rise (McManus *et al.*, 2004). These records offer two independent proxies for North Atlantic Deep Water (NADW) flow intensity that corroborate each other by a strong empirical relationship. Note that the chronologies of both records have also been developed independent from one another (McManus *et al.*, 2004; Stanford *et al.*, 2006). Both records show a virtually complete collapse of the AMOC initiating at around 18.8 ka BP and an abrupt AMOC resumption at the Bølling warming at around 14.6 ka BP (figure 5.9a & h). Note that the AMOC resumption in both records therefore does not coincide with the 'conventional' end of H1 (as recorded in sediment cores from the IRD belt) at around 16 ka BP (e.g., Grousset *et al.*, 2004; Hemming, 2004; Figure 5.9e). This timing for the AMOC flow intensity increase at around 14.6 ka BP underlines previous suggestions that the AMOC "switch on" and the Bølling warming were intrinsically linked (McManus *et al.*, 2004; Stanford *et al.*, 2006).

Figures 5.9e & g show the $\delta^{18}O$ record for the planktonic foraminiferal species *Neogloboquadrina pachyderma* (left-coiling) ($\delta^{18}O_{npl}$) from TTR-451, Eirik Drift. From around 16.7 ka BP a strong shift to lighter values develops (increased freshening), culminating in a broad peak of light values at around 15.1 ka BP. The magnitude of this $\delta^{18}O$ change equals -1.45 ‰. The IRD flux for TTR-451 (figure 5.9d) shows no notable increase during this time interval. Based on the generally low IRD flux during the interval of the main $\delta^{18}O_{npl}$ shift, the change in $\delta^{18}O_{npl}$ does not seem to be primarily derived from an iceberg event. Instead, we interpret this shift in $\delta^{18}O_{npl}$ during the H1 time period to have originated from iceberg-free freshened surface waters.

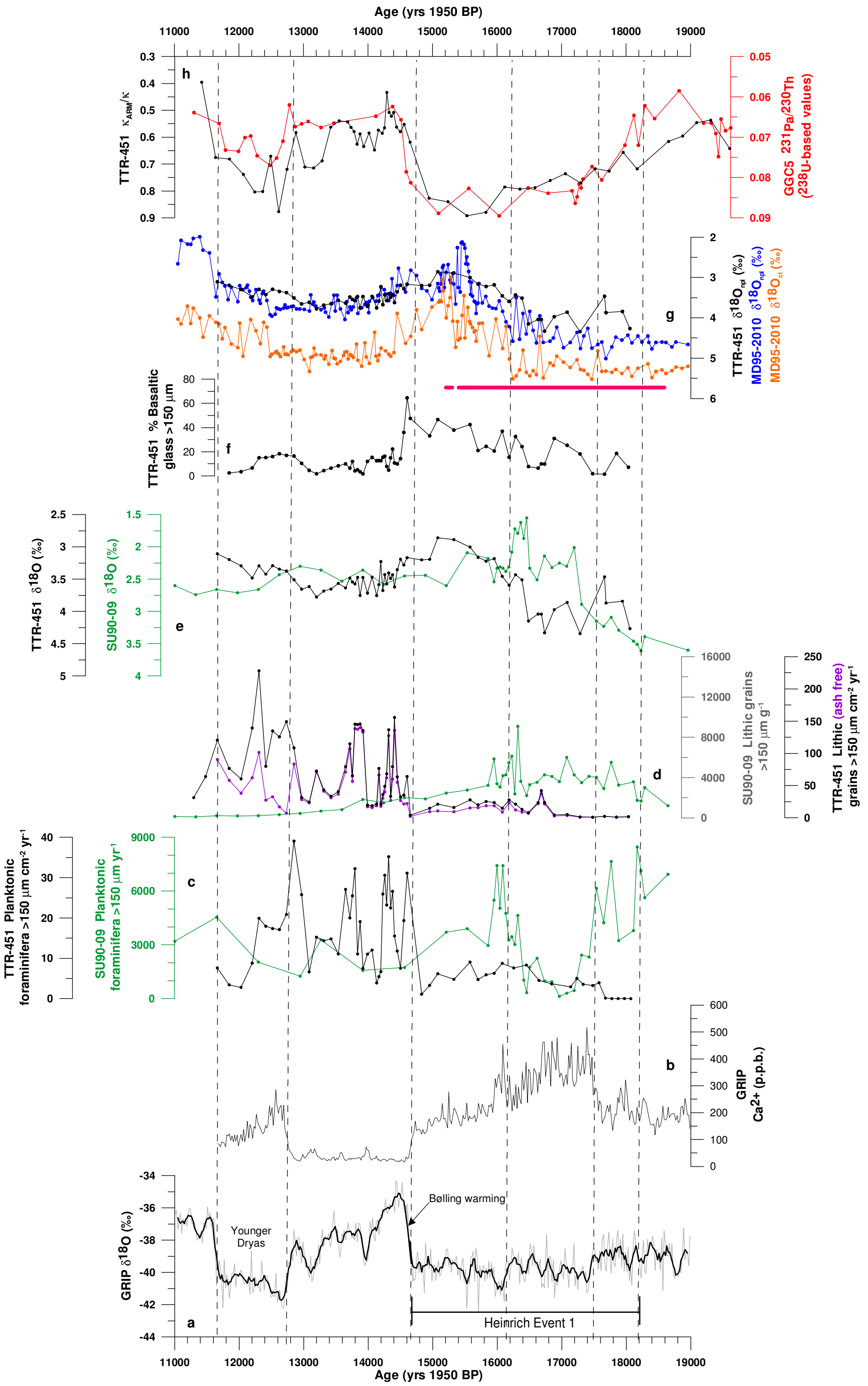

Figure 5.9a. The GRIP ice core $\delta^{18}O$ record plotted versus the GICC05 timescale (Rasmussen *et al.*, 2006; Andersen *et al.*, 2006; Svensson *et al.*, 2006; Vinther *et al.*, 2006). c. Records of the flux of planktonic foraminifera >150 μm cm^{-2} yr^{-1} for core TTR-451 (black) and the number of planktonic

foraminifera >150 μm per gram of dry sediment for core SU90-09 (green). d. Records of the flux of ash free lithic grains cm^{-2} yr^{-1} (purple) and total lithic grains cm^{-2} yr^{-1} (black) for core TTR-451. The number of lithic grains >150 μm per gram of dry sediment for core SU90-09 (green). e. $\delta^{18}O_{npl}$ records for TTR-451 (black) and SU90-09 (grey) f. Abundance of basaltic grains in core TTR-451. g. $\delta^{18}O_{npl}$ records for TTR-451 (black) and MD95-2110 (blue). Record of $\delta^{18}O_{ct}$ is shown in orange. The pink line represents the timing of extreme rates of sediment deposition in the Nordic seas (Lekens *et al.*, 2005). h. Record of κ_{ARM}/κ for Eirik Drift core TTR-451 (in black). The κ_{ARM}/κ data for TTR-451 are presented alongside the $^{231}Pa/^{230}Th$ record of core GGC05 from Bermuda Rise (in red). The record for κ_{ARM}/κ reflects variations in the magnetic mineral grain size (Banjeree *et al.* 1981; Verosub and Roberts, 1995), transported by NADW from a single source of fine-grained minerals, the Nordic Basaltic Province (Kissel *et al.*, 1999a, b; Laj *et al.*, 2000).

Grains of basaltic glass have been previously interpreted as an index for ice rafting from around Iceland (e.g, Bond and Lotti, 1995; Grousset *et al.*, 2001). Figure 4.9f plots the percentage basaltic glass composition of the total IRD in core TTR-451. A broad percentage increase, despite the low overall magnitudes, spans the entire interval of the H1 light $\delta^{18}O_{npl}$ event. The planktonic foraminiferal accumulation flux in TTR-451 (figure 5.9c) records generally low values during the H1 interval, with a notable minimum between 17.2 and 16.5 ka BP.

After the Bølling warm transition at around 14.6 ka BP, a return to heavier $\delta^{18}O_{npl}$ values is observed. Just prior to the Younger Dryas cold period, at around 12.9 ka BP, a gradual shift to lighter $\delta^{18}O_{npl}$ develops (Figure 5.9e & f). The fluxes of lithic and planktonic foraminifera dramatically increase at around 14.6 ka BP (Figure 5.8d & c) and remain highly variable until the top of core TTR-451 (about the termination of the Younger Dryas).

5.3.3. Comparison of the TTR-451 records from Eirik Drift through H1 with coeval data from the IRD Belt and the Nordic Seas

Figures 5.9c, 5.9d and 5.9e show the $\delta^{18}O_{npl}$, numbers of planktonic foraminifera and lithic grains >150 µm per gram of dried sediment for SU90-09, respectively (Grousset *et al.*, 2001). Core SU90-09 was recovered from the central IRD belt. Consonant with previous studies from the IRD belt (e.g., Bond *et al.*, 1992; Broecker *et al.*, 1993; Cortijo *et al.*, 1997; Hemming, 2004), core SU90-09 shows a maximum increase in surface water dilution with isotopically light freshwater during the time period from 17.3 to 16.4 ka BP, including with a $\delta^{18}O_{npl}$ shift of 0.9 ‰ in just over 100 years, at around 17.3 ka BP. This rapid shift followed a more gradual freshening (0.7 ‰ in 900 years), which started at around 18.3 ka BP. The numbers of lithic grains g^{-1} (IRD concentration) increase at around the same time as the surface water dilution – a ‘typical’ Heinrich layer signature of a massive iceberg derived meltwater discharge (e.g., Hemming, 2004). The numbers of planktonic foraminifera g^{-1} decrease from 8000 to just a few hundred, with a minimum centred on the timing of the maximum surface water dilution (17.3 to 16.4 ka BP), when *N. pachyderma* (left-coiling) became the dominant surface dweller (Grousset *et al.*, 2001).

In comparison to core SU90-09, and also previous descriptions of Heinrich layers in cores recovered from the heart of the IRD belt (Bond *et al.*, 1992; 1999; Grousset *et al.*, 2000; 2001; review in Hemming, 2004), the records of $\delta^{18}O_{npl}$, IRD and planktonic foraminiferal fluxes from core TTR-451 (Eirik Drift) display distinctly different patterns and timings. Instead, our results from Eirik Drift suggest a predominantly non-iceberg (IRD free) freshwater impact.

Figure 5.9g plots the $\delta^{18}O_{npl}$ data and the benthic $\delta^{18}O$ record for the species *Cassidulina teretis* ($\delta^{18}O_{ct}$), for the Nordic Seas marine sediment core MD95-2010 (Dokken and Jansen, 1999). On the basis of an excellent agreement of ΔR estimates for the Younger Dryas obtained from TTR-451 with those from the Norwegian margin (Bondevik *et al.*, 2006), the inferred TTR-451 ΔR values for H1 are used here to convert ages for core MD95-2010 onto the GICC05 chronology.

Consonant with previous studies of sediment cores from the Nordic Seas (e.g., Duplessy *et al*., 1991; van Kreveld *et al*., 1999; Rasmussen *et al*., 2002a, b; Rasmussen and Thomsen, 2004; 2008), the MD95-2010 record shows a strong freshwater dilution signal (up to -2 ‰ $\delta^{18}O_{npl}$ excursion) that spans across the later phase of H1 (~16.1 to ~15 ka BP) (Figure 5.9g). Comparison of our $\delta^{18}O_{npl}$ records from Eirik Drift and the Nordic Seas (figure 5.9g) shows that, apart from the difference in resolution, these records are near identical in both long-term variability and absolute values. This is a strong indication for direct water mass communication between the Nordic Seas and Eirik Drift during H1.

Light $\delta^{18}O_{npl}$ and benthic $\delta^{18}O$ excursions, with nearly identical pattern, timing and magnitude as seen in cores TTR-451 and MD95-2010, have been described for marine sediment cores from the Nordic Seas, the northern North Atlantic (in particular, the Faroe-Shetland Gateway), and in the vicinity of Eirik Drift (Vidal *et al*., 1998; Dokken and Jansen, 1999; Rasmussen *et al*., 2002a; Rasmussen and Thomsen, 2004; Lekens *et al*., 2005; Hilliare-Marcel and de Vernal, 2008; Meland *et al*., 2008). There are four current theories to explain this light $\delta^{18}O$ isotopic event. The first involves ice-berg derived, low salinity meltwater pulses and deepening of the halocline (e.g., Hilliare-Marcel and Bilodeau, 2000; Rashid and Boyle, 2007). Based upon the generally low H1 IRD flux at Eirik Drift, this is here considered to be unlikely. The second hypothesis involves a reversed thermocline as a result of sea-surface capping, and warming of the subsurface layer (e.g., Mignot *et al*., 2007; Peck *et al*., 2008). However, Hilliare-Marcel and deVernal (2008) show measurements of $\delta^{18}O$ *N. pachyderma* sub-populations based upon size in core MD95-2024 (Labrador Sea), which show a negative temperature gradient along the thermocline which led Hilliare-Marcel and deVernal (2008) to reject the above hypothesis. The third theory involves the sinking of isotopically light brines as a result of intense sea ice formation (e.g., Vidal *et al*., 1998; Dokken and Jansen, 1999; Risebrobakken *et al*., 2003; Millo *et al*., 2006; Hilliare-Marcel and de Vernal, 2008; Meland *et al*., 2008). Finally, the fourth theory suggests the penetration of relatively warm (4-8˚C) waters into the Nordic Seas at intermediate depths (<1700 m), which is suggested to represent the North Atlantic Drift (NAD) that flowed subsurface into the Nordic Seas (Rasmussen and Thomsen, 2004). Based upon the new records from Eirik Drift, these latter two theories are here investigated further.

5.3.4. Investigation of the H1 $\delta^{18}O$ light excursions in the Nordic Seas and at Eirik Drift.

Firstly, we shall consider the sea-ice hypothesis for the generation of the H1 light $\delta^{18}O$ event in the Nordic Seas and at Eirik Drift. Reconstructions of the LGM in the northern North Atlantic would suggest that seasonal sea-ice likely extended down to around 40ºN (Mix *et al*., 2001; Pflaumman *et al*., 2003). However, a regional $\delta^{18}O_{npl}$ value of around +4.5 ‰ indicates that the Nordic Seas and the northern North Atlantic likely were sea-ice free in summer (e.g., Weinelt *et al*., 1996; 2003; de Vernal *et al*., 2002; Meland *et al*., 2005; Millo *et al*., 2006). Sedimentation rates, sediment composition and $\delta^{18}O_{npl}$ records from western Fram Strait marine cores suggest that seasonally 'open' conditions extended to this region during the LGM (Nøgaard-Pederson *et al*., 2003).

Dokken and Jansen (1999) propose that freshwater additions into the North Atlantic and weakening of the AMOC would have resulted in high-latitude cooling and rapid extension of the sea-ice margin across the Nordic Seas during H1. Because sea-ice forms from the freezing of surface waters, which at this time were affected by freshwater dilution, the rejected brines would have had relatively light $\delta^{18}O$. Dokken and Jansen (1999), and more recently Meland *et al*. (2008), propose that brine rejection would have resulted in the convection of the 'pooled' isotopically light surface waters to intermediate depths (base of the halocline), accounting for the light H1 $\delta^{18}O$ signal recorded in both surface waters and at intermediate depths. On the basis of very similar $\delta^{18}O$ trends, Dokken and Jansen (1999) extend this hypothesis to account for the Nordic Seas $\delta^{18}O$ during other Heinrich events (Figure 5.10).

Comparison of the $\delta^{18}O_{npl}$ and $\delta^{18}O_{ct}$ data from the Nordic Seas for Heinrich events 4 and 6 (Figure 5.10), however, show a larger $\delta^{18}O$ shift to lighter values at intermediate depths than for the surface waters. For Heinrich event 6, this difference is approximately double. Furthermore, for H6, the $\delta^{18}O_{ct}$ values become lighter some 400 yrs prior to the $\delta^{18}O_{npl}$. This timing offset is even more pronounced for H3 as recorded in core ENAM93-21 from the southern Nordic Seas (Dokken and Jansen, 1999).

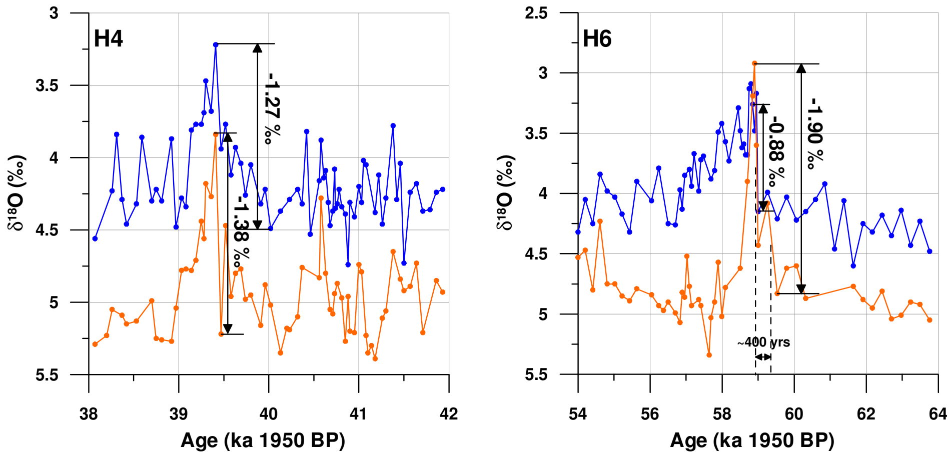

Figure 5.10. Benthic (orange) and planktonic (blue) δ^{18}O records for core MD95-2010 for H4 and H6. The records are generated from *C. teretis* (benthic foraminifera) and *N. pachyderma* (left coiling) (planktonic foraminifera) (Dokken and Jansen, 1999).

Because sea-ice formation and resultant brine release, mixes the light $\delta^{18}O$ signal in the halocline from the surface down through the water column, it would be expected that the greatest freshening would be seen in the $\delta^{18}O_{npl}$ data than in the $\delta^{18}O_{ct}$ data, and if there were any temporal offsets, the $\delta^{18}O_{npl}$ record would shift to lighter values first. Therefore, it is difficult to account for how the $\delta^{18}O_{ct}$ isotopic light episode could have had a greater magnitude than the $\delta^{18}O_{npl}$ in the Nordic Seas, or have occurred prior to the $\delta^{18}O_{npl}$ light event (Figure 5.10). Furthermore, as core TTR-451 records near identical absolute $\delta^{18}O_{npl}$ values as core MD95-2010 (Figure 5.9g), a near instantaneous and rapid growth of the sea ice margin would be needed across the entire Nordic Seas and northern North

Atlantic to account for these observations. Such a rapid and instantaneous sea ice growth across such a vast area is considered to have been unlikely. On the basis of these arguments, the hypothesis that brine rejection due to sea-ice formation caused the H1 $\delta^{18}O_{npl}$ light excursion observed in cores from the Nordic Seas and at Eirik Drift is here rejected.

Next we consider the fourth theory that accounts for these light $\delta^{18}O$ isotopic excursions in the Nordic Seas. Rasmussen *et al*. (1996) and Rasmussen and Thomsen (2004) find that in a number of cores (including ENAM93-21) recovered from the Nordic Seas and the Faroe-Shetland Gateway, a distinct abundance increase occurs of the benthic foraminifera 'Atlantic species' group (which include, *Sigmoilopsis schlumbergi, Egerella bradyi, Alabaminella weddellensi, Epistominella decorata, Bulimina costata. Sagrina subspinescens, Gyroidina spp*.), at the same time as the H1 $\delta^{18}O$ light excursion in the Nordic Seas. From these data, Rasmussen and Thomsen (2004) suggest a weak subsurface invasion of relatively warm (4-8ºC) Atlantic Waters, at depths greater than 1 km, into the Nordic Seas during H1, which they interpret as a subsurface expression of the North Atlantic Drift (NAD). Differences in the abundance of this 'Atlantic species' group have been used to infer that intermediate water depth temperatures were greater in the Nordic Seas during the latter part of H1 than during Dansgaard-Oeschger interstadials (Rasmussen and Thomsen, 2004). Rasmussen and Thomsen (2004) then suggest that the benthic and planktonic $\delta^{18}O$ shift to lighter values in the Nordic Seas during H events is due to a temperature increase caused by the invasion of this relatively warm subsurface watermass.

Similar to suggestions by Meland *et al*. (2008), we find the above interpretation by Rasmussen and Thomsen (2004) problematic, since these relatively warm inflowing waters would need to acquire a density to enter the Nordic Seas at greater than 1 km water depth. Meland *et al*. (2008) also suggest that although model experiments show that deep waters may be warmed by a few degrees Celsius (Weaver *et al*., 1993; Winton, 1997; Paul and Schulz, 2002), they do not account for the shallow Iceland-Scotland Ridge that these waters would need to cross. Moreover, Meland *et al*. (2008) note that Mg/Ca temperature reconstructions from benthic foraminifera for core MD95-2010 do not show increased temperatures at intermediate depths in the Nordic Seas during this time period (Dokken and Clark, *unpublished data*). Finally, relatively large temporal offsets are apparent for nearly all the Nordic Seas cores between the peak 'Atlantic species' abundances and the $\delta^{18}O$ minima (Rasmussen and Thomsen, 2004).

Our observation of identical absolute $\delta^{18}O_{npl}$ values in cores TTR-451 and MD95-2010, strongly suggest that there was direct watermass communication between the Nordic Seas and Eirik Drift during H1. Given that the warm intermediate water hypothesis during H1 (Rasmussen and Thomsen, 2004) cannot satisfactorily explain the $\delta^{18}O$ patterns within the Nordic Seas (see above), we now develop an alternative explanation for the light $\delta^{18}O$ excursion that extends over Eirik Drift.

Seismic mapping of the Nordic Seas and study of marine sediment cores have revealed that, coeval with the timing of H1, high rates of sediment accumulation occurred within the Nordic Seas (Hjelstuen *et al*., 2004; Sejrup *et al*., 2004; Lekens *et al*., 2005). These sediments are characterised in core MD99-2291 from the Vøring Plateau, southeastern Norwegian Sea, by laminated/partly laminated fine grained clay and silt (with individual laminae between 1mm–150 µm thick), with generally low planktonic foraminiferal abundances and occasional IRD (Lekens *et al*., 2005). Seismic mapping has revealed that these fine-grained sediments cover an area of around 1600 km^2 of the Norwegian sea floor, with an approximate volume of 1000 km^3 and attaining a thickness that in places exceeds 20 m (Hjelstuen *et al*., 2004; Sejrup *et al*., 2004; Lekens *et al*., 2005). However, since the Storegga Slide (ca. 8 ka BP; Bondevik *et al*., 2003) removed a large part of this deposit, calculations of volume are problematic and the cited value represents a minimum estimate (Lekens *et al*., 2005).

Radiocarbon dating at the base of the fine-grained sedimentary sequence indicates an age of around 18.6 ka BP, and a $\delta^{18}O_{npl}$ record through these sediments shows the same absolute values as those in MD95-2010 and TTR-451, and places the timing of the termination of these laminated deposits at 15.1 ka BP, coincident with peak light $\delta^{18}O_{npl}$ values in the Nordic Seas (Lekens *et al.*, 2005). Given the close agreement between the timing of emplacement of these sediments and the rapid retreat of the Fennoscandian ice-sheet (e.g., Rinterknecht *et al.*, 2006), Lekens *et al.* (2005) suggest that the sediments had a meltwater origin. Based upon the presence of >2 mm IRD and pristine fully articulated bivalves, Lekens *et al.* (2005) suggest that the sediments were deposited hemipelagically, and classify them as 'plumites' (i.e., surface water freshwater events). Lekens *et al.* (2005) also tentatively suggest that the laminations, which comprise two units (dark fine-grained laminae and lighter coloured coarser-grained laminae), represent winter sea-ice coverage and summer plume deposition, respectively.

Based upon the detailed sedimentary descriptions provided by Lekens *et al.* (2005) and the volume of sediment that was being delivered into the Nordic Seas over a relatively short time interval (over 1000 km ^{3} in around ~2000 yrs), we question whether these sediments would have spread into the Nordic Seas at the surface. Instead, due to the relatively high sediment concentrations within the meltwater plumes, we suggest that it is more likely that the sediments entered the Nordic Seas subsurface, and thus represent low-velocity hyperpycnal deposits resulting from glacial melting and outwash.

A hyperpycnal flow is defined by Mulder and Syvitski (1995) as a quasi-steady flow of a negatively buoyant watermass, which flows along the basin floor due to its density that is in excess of that of the ambient watermass, owing to the particle load that it carries. This means that hyperpycnal flows can carry sediments finer than medium sand over very large distances (Mulder *et al.*, 2003). Hyperpycnites – (the deposits from hyperpycnal flows) can be generated today from 'dirty' rivers, flood events, dam breaks, or Jökulhaups. Lekens *et al.* (2005) reject the hypothesis that these sediments represent subsurface turbidity current generated deposits based upon the rhythmic nature of the sediments, a lack of erosional contacts and the presence of fully articulated bivalves and IRD

(Rashid *et al.*, 2003). However, the low-velocity, quasi-steady regime of a hyperpycnal flows from low-velocity floods may not have erosional contacts (Mulder *et al.* 2003), and we suggest that such processes do not preclude the occurrence of IRD or fully intact bivalves.

Hyperpycnite deposits that form at river mouths during floods are characterised by two units; a coarsening-up sequence as the discharge increases, followed by a fining-up unit as the discharge wanes (Mulder *et al.*, 2001; 2003), and laminae have previously been described (Chough and Hesse, 1980). We suggest that the rhythmic, laminated deposits described in Lekens *et al.* (2005) may represent annual changes in flow regime, with the lighter coloured coarser grained portions resulting from high summer melt discharges. We note that very similar laminated sedimentary sequences, containing relatively large IRD have been previously described for H1 from the northwestern Bay of Biscay (Zaragosi *et al.*, 2001), and from the North Atlantic (Hesse & Khodabakhsh, 1998; Hesse *et al.*, 1996; Hesse *et al.*, 2004), where they have been interpreted as hyperpycnal deposits that resulted from sediment laden meltwater from the European and Laurentide ice-sheets, respectively. In addition, similar sequences have described in deglacial infill of an East Greenland fjord (Hansen, 2004).

A hyperpycnal method of freshwater delivery into the Nordic Seas provides a mechanism for supplying isotopically ($\delta^{18}O$) light meltwaters to intermediate depths. As the hyperpycnal flows de-watered, relatively fresh, low density, highly buoyant meltwaters would have risen towards the surface (while strongly mixing with ambient waters) (e.g., Hansen, 2004), which would have caused planktonic $\delta^{18}O$ anomalies similar to the benthic $\delta^{18}O$ anomalies. Evidence from $\delta^{18}O_{npl}$ suggests that large amounts of meltwater were supplied to the Nordic Seas during previous H events (Lekens *et al.*, 2006). The proposed hyperpycnal mechanism for delivering the freshwater allows for the observed greater magnitude and earlier timing of the $\delta^{18}O$ shift in the benthic data versus that in planktonic $\delta^{18}O$ data.

We note, however, that the basal dating of this thick sedimentary deposit suggests that deposition started some 1000 yrs prior to the light $\delta^{18}O_{npl}$ isotopic excursion (pink line in Figure 5.9g). Therefore, prior to the AMOC collapse (Figure 4.9h), and whilst there was still open convection in the Arctic (Nørgaard-Pederson *et al.*, 2003), we suggest the $\delta^{18}O$ signal in the Nordic Seas was not able to develop due to circulation through the Nordic Seas and strong mixing with the inflowing Atlantic waters. With the AMOC in a nearly completely collapsed state from around 17.5 ka BP (McManus *et al.*, 2004; Figure 5.9h) and a further collapsed state from around 16.1 ka BP (record of κ_{ARM}/κ in Figure 5.9h; see also Gheraudi *et al.*, 2005; Peck *et al.*, 2007b), and the Fram Strait 'closed' due to resultant significant cooling and extension of the sea ice margin (Nørgaard-Pederson *et al.*, 2003), the freshened waters would have 'pooled' towards the surface in the Nordic Seas.

Given these conditions that the Nordic seas overflow and resultant NADW flow had more or less collapsed from around 17.5 ka BP, and that the Bering Strait (today at ~50 m water depth) would have been closed due to the low sea level position (-110 m), mass balance requires that for any additions into the Nordic Seas and Arctic Basin, the same volume needs to have been expelled via surface waters. The majority of these exits through the Denmark Strait by means of the East Greenland Current (EGC). Hence, the $\delta^{18}O_{npl}$ signals observed at Eirik Drift in TTR-451 would likely have resulted from net freshwater (diluted surface water) export from the Nordic Seas, in a configuration reminiscent of the modern Arctic outflow through the Fram Strait.

Figure 5.9f shows the percentage composition of basaltic grains from the total IRD that was deposited at Eirik Drift. High percentage values occur through the entire period of H1 freshwater dilution recorded in TTR-451. As basaltic grains are thought to represent melt of sea ice that had formed around Iceland (e.g., Bond and Lotti, 1995), this evidence lends support to our hypothesis that the light $\delta^{18}O_{npl}$ signal at TTR-451 reflects a significant freshwater (and sea ice) export from the Nordic Seas.

An alternative hypothesis for the apparent mismatch of timings between the increased rates of sediment accumulation in the Nordic seas and the light $\delta^{18}O$ excursion in the Nordic Seas and at Eirik Drift may be gained from closer scrutiny of the sedimentary description of core MD99-2291. Lekens *et al.* (2005) describe a coarsening of sediments, with increased concentrations of planktonic foraminifera, decreased sedimentation rates, and a fewer laminations, which is coincident with the start of the $\delta^{18}O_{npl}$ event recorded in the same core. This may indicate that the rate of meltwater injection into the Nordic Seas was increased at this time, with the reduced sedimentation rates and increased proportions of coarser sediment reflecting the more distal transport of finer-grained sediments.

Based upon measurements of modern rivers that produce at least one hyperpycnal flow each year, Mulder and Syvitski (1995) estimate the critical threshold particle concentration required for a watermass to plunge subsurface. Calculated values range from around 38.9 kg m^{-3} for low latitude rivers to around 43.5 kg m^{-3} for high-latitude rivers. Measured annual average suspended particle concentrations are, however, somewhat lower (e.g., 20.7 kg m^{-3} for the Rioni in Russia) as hyperpycnal flows occur during peak discharge. Mulder *et al.* (2003) suggest that rivers with initial suspended particle threshold concentrations as low as 5 kg m^{-3} can produce hyperpycnal flows during flood.

We test the hypothesis that meltwater may have entered the Nordic Seas hyperpycnally during H1 by calculating average suspended particle concentrations, assuming a particle density of 2650 kg m^{-3} (Mulder and Syvitski, 1995). We calculate this for three different scenarios, and we then consider mixing this sediment load with incrementally increasing volumes of freshwater.

Scenario 1 uses the minimum estimated volume of sediment, which were deposited during H1 in the Nordic Sea. This equals 1000 km^3 (Hjelstuen *et al.*, 2004; Sejrup *et al.*, 2004; Lekens *et al.*, 2005). Scenario 2 takes into account that the $\delta^{18}O$ light isotopic anomaly in MD99-2291 only spans the upper 1.4 m of the 10.5 m thick laminated section. We therefore reduce the 1000 km^3 sediment volume by 87 %. Since the Storegga Slide (*ca.* 8.2 ka BP; Bugge *et al.*, 1987;

Bondevik *et al.*, 1997), which post-dated H1 by nearly 8000 years, removed a large proportion of the H1 sediment deposits in the Norwegian Sea, the derived 1000 km^3 estimate for the H1 deposit is only a minimum (Hjelstuen *et al.*, 2004; Sejrup *et al.*, 2004; Lekens *et al.*, 2005). Although rather unrealistic, scenario 3 calculates the maximum possible sediment load of the H1 meltwaters by including the volume of sediments that were contained within the Storegga Slide (3500 km^3 – Bondevik *et al.* (2003)). Therefore, scenario 3 uses a total sediment volume of 4500 km^3. The results from the three scenarios are given in Table 5.3, and mixing curves for scenarios 1 and 2 are shown in Figure 5.11.

	Volume of sediment (km^3)	Volume of fresh water (km^3)	Equivalent global sea level rise (m)	C_c (kg m^{-3})
Scenario 1	1000	61009 (C^1)	0.169	43.5 (A^1)
Scenario 2	133	8303 (C^4)	0.023	43.5 (A^1)
Scenario 3	1000 + 3500 (Storegga)	273999	0.759	43.5

Table 5.3. Volumes of freshwater required to be mixed with the sediment loads in order for the meltwaters to plunge subsurface (ie., for the average suspended particle loads to exceed the critical particle concentration (C_c)). C_c = 43.5 kg m^{-3} (Mulder and Syvitski, 1995; Mulder *et al.*, 2003). In brackets are the points denoted in Figure 5.11.

Assuming that the -1.45 ‰ $\delta^{18}O_{npl}$ shift at Eirik Drift ($\delta^{18}O_{npl}^{a-b}$) represents a mixed signal out of the Nordic Seas, we use a glacial meltwater endmember $\delta^{18}O$ of -35 ‰ ($\delta^{18}O_g$) to calculate the volume of freshwater that likely entered the Nordic Seas during H1. A volume of 2145900 km^3 (V_1) is used for the Nordic Seas, as we assume that mixing was constrained to the Norwegian Sea, Iceland Sea, and only the southern most sector of the Greenland sea (Nørgaard-Pederson *et al.*, 2003). We use the modern volume estimates minus the volume associated with a -110 m sea level change. The $\delta^{18}O_{npl}^{a-b}$ is solved from the following equation, where $\delta^{18}O_{npl}^{a}$ is the initial $\delta^{18}O$ value and V_2 is the volume of meltwater. We calculate that V_2 equals ~89000 km^3, or 0.246 m of equivalent sea level rise

$$(\delta^{18}O_{npl}^{a\text{-}b}) = [(V_1 \times \delta^{18}O_{npl}^{a}) + (V_2 \times \delta^{18}O_g)]/(V_1 + V_2) \qquad \text{(Equation 5.1)}$$

We then mix the derived volume of meltwater (V_2) with the sediment loads used in scenarios 1, 2 and 3. The results are given in Table 5.4, and the mixing curves for scenarios 1 and 2 are shown in Figure 5.11.

	Volume of sediment (km^3)	Volume of fresh water (km^3)	Equivalent global sea level rise (m)	C_{sav} ($kg\ m^{-3}$)
Scenario 1	1000	88806 ($C^{2,3}$)	0.246	29.84 (A^2)
Scenario 2	133	88806 ($C^{2,3}$)	0.246	3.98 (A^3)
Scenario 3	1000 + 3500 (Storegga)	88806	0.246	134.28

Table 5.4. Average suspended particle concentrations values (C_{sav}) calculated from mixing the estimated sediment volumes for each scenario with the meltwater volume derived from Equation 5.1. In brackets are the points denoted in Figure 5.11.

For scenario 1, a meltwater volume of 61009 km^3 is required for the flow to acquire the critical threshold particle concentration of 43.5 $kg\ m^{-3}$ (Table 5.3). By mixing the 1000 km^3 of sediment with the calculated meltwater volume, an average suspended particle concentration of nearly 30 $kg\ m^{-3}$ is revealed (Table 5.4). This value of 30 $kg\ m^{-3}$ is similar the observed average suspended particle concentrations of high latitude rivers today, which produce hyperpycnal flows (Mulder *et al.*, 2003). On this basis we consider that for scenario 1, the meltwaters injected into the Nordic Seas during H1 would have done so hyperpycnally.

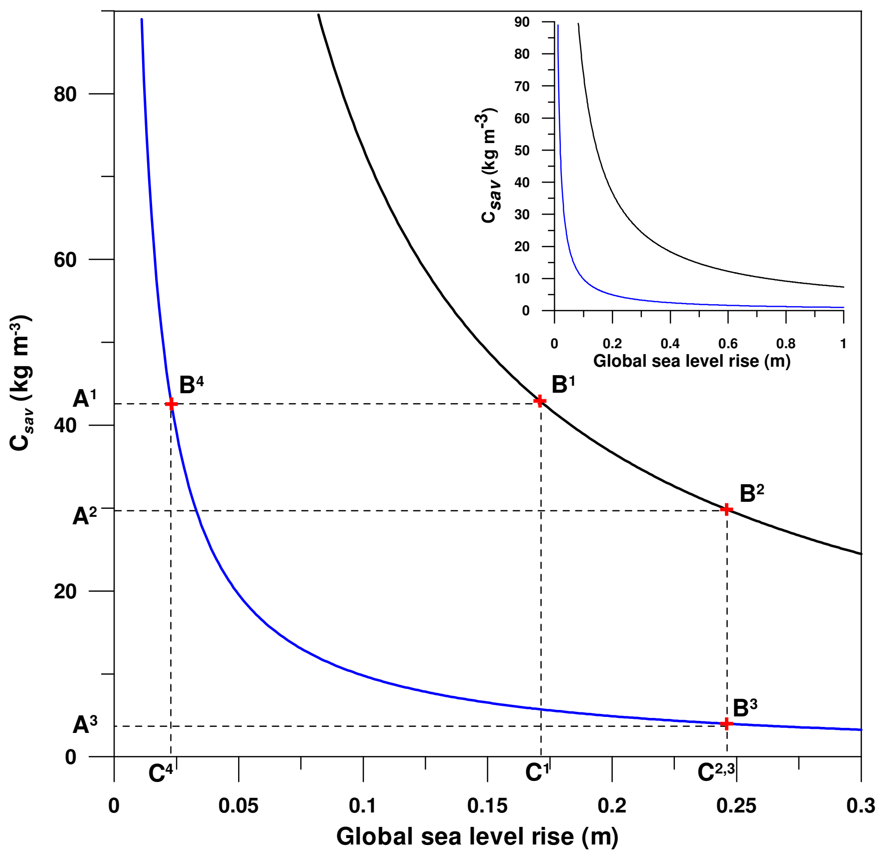

Figure 5.11. Melt water volume, in terms of its contribution to global sea level rise, versus its average suspended particle concentration values (C_{sav}) for scenarios 1 (black) and 2 (blue). The scenarios are defined in the main text. The plot shows how C_{sav} changes, with incrementally increased meltwater for these two scenarios. C_{sav} sediment particle density of 2650 kg m^{-3}. Points A$^{1-3}$ and C$^{1-4}$ are defined in Tables 5.3 and 5.4. B$^{1-4}$ show their intersect with the two curves.

Scenario 2, with the 87 % reduced sediment estimate, requires a volume of metlwater of only 8303 km^3 in order for the sediment load to cause the meltwater flow to exceed its critical particle concentration (43.5 kg m^{-3}) (Table 4.3). This meltwater volume is an order of magnitude less than the calculated meltwater volume (V_2). Mixing this relatively small sediment volume for scenario 2, with calculated meltwater volume, gives an average suspended particle concentration of 3.98 kg m^{-3}, less than the required >5 kg m^{-3} reported in Mulder *et al.* (2003). Note, however, that for scenario 2, a minimum sediment load is mixed with a maximum meltwater volume, and moreover, is averaged over an interval of time which spans around 1000 yrs. Because hyperpycnal flows occur during periods of peak flood discharge for modern rivers, and these rivers can have annual average suspended particle concentrations as low as 5 kg m^{-3} (Mulder *et al.*, 2003), and additionally, given the long duration of time (~1000 yrs) that our average estimates from the Nordic Seas brackets, during times of peak discharge (i.e., the short duration seasonal melt) the sediment load used in scenario 2 would have caused the meltwaters to enter the Nordic Seas subsurface.

For scenario 3, where the volume of the Storegga slide is added to the volume of laminated sediments in the Nordic Seas, a maximum average suspended particle concentration is estimated. To achieve a critical suspended particle concentration of 43.5 kg m^{-3}, a mixed freshwater volume of nearly 274000 km^3 (Table 5.3) far exceeds the meltwater volume (V_2) derived from the $\delta^{18}O_{npl}$ values of ~89000 km^3. When the sediment volume for scenario 3 (4500 km^3) is mixed with V_2, a C_{sav} of 134 kg m^{-3} is revealed. For scenario 3, the meltwater would be injected hyperpycnally into the Nordic Seas. Considering the outcomes for all three scenarios, we conclude that the laminated sediments deposited in the Nordic Seas during H1, represent hyperpycnites formed from hyperpycnal flows, generated from melt of the Scandinavian ice sheet.

At around 15.5 ka BP, intense northern high-latitude cooling (Alm, 1993; Figure 5.8f) caused a re-advance of the Scandinavian ice-sheet (Rinterknecht *et al.*, 2006). Coincident with this timing, the $\delta^{18}O$ records from the Nordic Seas and Eirik Drift return to heavier values, and finely laminated silt and clay were no longer being deposited in the Nordic Seas. The gradual return to heavier $\delta^{18}O_{npl}$ values in the Nordic Seas and at Eirik Drift indicate that the freshened waters were being purged out of the Nordic Seas, possibly due to wind driven circulation and/or the density gradient had developed between the Nordic Seas and the North Atlantic (e.g., Millo *et al.*, 2006). Only a few centuries after the meltwater purging began to decrease, the AMOC underwent a sharp recovery at the time of (and possibly causing (McManus *et al.*, 2004)) the abrupt Bølling warming (figure 5.9g, h).

5.3.5. A new conceptual model for the Nordic Seas and northern North Atlantic during H1

In this section, a new concept is proposed for the sequence of events associated with the H1 iceberg/meltwater perturbation in the North Atlantic. The sequence is discussed as a succession of three phases, and is placed within the context of previous studies in both the marine and terrestrial realm. Phase 1 (~19–17.5 ka BP) represents the onset of the AMOC collapse, phase 2 (17.5-16.5 ka BP) represents the main phase of H1 in the IRD belt, and phase 3 (16.5-14.6 ka BP) covers H1 in the Nordic Seas and at Eirik Drift and the termination of H1 cooling and resumption of the AMOC at the Bølling warm transition.

5.3.5.1. Phase 1. The onset of AMOC collapse (~19 – 17.5 ka BP)

The AMOC began a gradual slowdown from around 18.8 ka BP, culminating in a collapse from around 17.5 ka BP (McManus *et al*., 2004; Figure 5.9h; Hall *et al*., 2006), which coincided with the onset of the main phase of H1 in the IRD belt (e.g., Bond *et al*., 1992; 1999; Bard *et al*., 2000; Grousset *et al*., 2001; Hemming, 2004; Figures 5.9d-f; 5.12a). The AMOC slowdown clearly predates the start of H1 as identified by peak IRD in the IRD belt, by more than 1000 years. Therefore, the widespread iceberg (IRD) event of H1, as identified in the IRD belt, could not be invoked as the root cause of AMOC weakening from around 18.8 ka BP. Instead, precursory freshwater events form a more likely mechanism for the AMOC slowdown.

Precursor IRD events with ages up to 1500 yrs prior to the main H1 IRD event have been identified in North Atlantic sediment cores from the IRD belt, and provenance studies indicate a significant contribution of sediment derived from the European and Scandinavian ice sheets (e.g., Bond *et al*., 1992; 1997; 1999; Bond and Lotti, 1995; Darby and Bischof, 1999; Grousset *et al*., 2000; 2001; Knutz *et al*., 2002; Scourse *et al*., 2000; Hemming *et al*., 2000, 2002; Hemming and Hajdas, 2003; Hemming, 2004; Peck *et al*., 2006; 2007a, b; Knutz *et al*., 2002; 2007; Walden *et al*., 2007). This observation of a European/Scandinavian origin has been validated by the contemporaneous increase in fluvial input found in the northern Bay of Biscay (Menot *et al.*, 2006). This has lead to the suggestion that early surging from European ice sheets likely acted as a stimulus for the reaction of the Laurentide ice sheet (e.g., Grousset *et al.*, 2000; 2001), the 'key-player' in the main Heinrich events (e.g., Marshall and Koutnik, 2006). Precursor IRD-rich layers have also been identified within the Arctic, with a possible source from the Canadian Arctic Archipelago (Darby *et al.*, 1997; 2002; Stokes *et al.*, 2005).

Primarily on the basis of model simulations, a number of scenarios have been proposed for the generation of Heinrich event type ice-surges. These models range from a 'binge-purge' mechanism due to over-sized and unstable ice-sheets (e.g., MacAyeal, 1993), ice-shelf growth and instabilities (Hulbe *et al.*, 1997), ice-stream surges due to basal instabilities due to reversed ice-air pressure gradients (Alley *et al.*, 2006) and catastrophic jökulhaup outflow events (Johnson and Lauritzen, 1995; Alley *et al.*, 2006), steric warming beneath ice-shelves (Flückiger *et al.*, 2006) and increased tidal ranges (Arbic *et al.*, 2008) causing ice-shelf instabilities.

From around 21 ka BP glacial retreat was occurring on a near global scale (e.g., Dyke *et al.*, 2002; Bowen *et al.*, 2002; Licciardi *et al.*, 2004), and at around 19 ka BP, a ~10 m jump is seen in sea-level records (e.g., Yokoyama *et al.*, 2000; Lambeck *et al.*, 2002). From around 19 ka BP significant warming is inferred from both the Scandinavian pollen records (Alm, 1993) and the Greenland $\delta^{18}O$ ice core records (Andersen *et al.*, 2006; Svensson *et al.*, 2006; Rasmussen *et al.*, 2007). Based upon the presented compilation of recalibrated terrestrial temperature records presented in here, along with the datings of glacial retreats, and the Greenland and Antarctic temperature records (Figure 5.8), it would appear that these precursory IRD events likely resulted from the post LGM warming.

This timing of northern high-latitude warming (~19 ka BP) coincides with start of the inferred warming trend in the EPICA Antarctic ice core record (EPICA community members, 2006), and increased northern summer insolation (Berger, 1991; 1999). Consequent warming in the southern hemisphere, sea ice reduction and enhanced global warming due to greenhouse gas and albedo feedbacks (e.g., Bender *et al.*, 1997; Alley and Clark, 1999) may have promoted the carving of the relatively 'small' ice sheets from Europe and Scandinavia (e.g., Stocker and Wright, 1991; McCabe and Clark, 1998; Stocker, 2003). A model simulation of freshwater perturbation (~10 m of sea level rise) in the southern hemisphere shows that from an LGM state of overturning, the AMOC would have been enhanced, and would have promoted further warming (Knorr and Lohmann, 2007). We suggest here however, that warming induced northern hemisphere meltwater perturbations at around 19 ka BP caused reduced AMOC intensity (similar to suggestions by Ganopolski and Rahmstorf, 2002), as seen in the record of $^{231}Pa/^{230}Th$ ratios from the Bermuda Rise (McManus *et al.*, 2004), which is corroborated by the record of κ_{ARM}/κ form Eirik Drift (Figure 5.9h). Alternatively, Peeters *et al.* (2004) show increased SST in the Cape Basin during the late glacial, and suggest that increased heat flow between the Indian and Atlantic Oceans via enhanced 'Agulhas leakage' may have triggered this North Atlantic warming. In response to the cooling associated with the AMOC slowdown (Figure 5.8f; 5.9h), a short duration re-advance of the British and southern Laurentide ice-sheet occurred from around 18.2 ka BP (Bowen *et al.*, 2002; Dyke *et al.*, 2002).

5.3.5.2. Phase 2. The 'main' phase of H1 (17.5 – 16.5 ka BP)

The main phase of H1 in the IRD belt (~17.5 to ~16.5 ka BP) is characterised by maximum freshening in the IRD belt, along with intense IRD deposition, and as a result, significantly reduced numbers of foraminifera (Bond *et al.*, 1992; 1999; Bond and Lotti, 1995; Grousset *et al.*, 2000; 2001; Knutz *et al.*, 2002; Scourse *et al.*, 2000; Hemming *et al.*, 2000, 2002; Hemming and Hajdas, 2003; Hemming, 2004; Peck *et al.*, 2006; 2008; Knutz *et al.*, 2002; 2007; Figure 5.9b-d), when there is a sustained and complete shutdown of the AMOC from around 17.5 ka BP (e.g., McManus *et al.*, 2004; Hall *et al.*, 2006) (Figure 5.9h). Significant northern hemisphere cooling at this time is indicated in the Greenland

$\delta^{18}O$ record (Andersen *et al.*, 2006; Svensson *et al.*, 2006; Rasmussen *et al.*, 2007), along with enhanced cooling in Britain (Atkinson *et al.*, 1987) and Scandinavia (Alm, 1993), and significantly reduced North Atlantic SSTs (Bard *et al.*, 2000). It is accompanied by a concomitant sharp increase in the concentration of Ca^{2+} in the Greenland ice cores (Andersen *et al.*, 2006; Svensson *et al.*, 2006; Rasmussen *et al.*, 2007).

Coeval with this 'main' phase of H1, at around 17.5 ka BP, widespread and significant glacial retreats occurred on a near global scale (e.g., Giraudi and Frezzotti, 1997; Denton *et al.*, 1999; Dyke *et al.*, 2002 and references therein; Bowen *et al.*, 2002; Clague and James, 2002; Licciardi *et al.*, 2004; Ivy-Ochs *et al.*, 2006; Menot *et al.*, 2006; Rinterknecht *et al.*, 2006), and a drawdown of the ice centre around the Hudson bay region most likely led to reorganisation of the northeastern Laurentide ice-streams (Dyke *et al.*, 2002; Figure 5.12b). Significantly increased sedimentation rates along the western Norwegian margin indicate that large volumes of freshwater were being delivered into the Nordic Seas at this time (Hjelstuen *et al.*, 2004; Sejrup *et al.*, 2004; Lekens *et al.*, 2005). We re-interpret these deposits as the result of meltwater that was injected at depth (i.e., hyperpycnally) (Figure 5.12b).

Based upon previous suggestions (e.g., Broecker, 1991; 1994; Rahmstorf, 1994; Manabe and Stouffer, 2000; Ganopolski and Rahmstorf, 2001; Knorr and Lohmann, 2003; 2007; McManus *et al.*, 2004; Rahmstorf *et al.*, 2005), we suggest that the significant freshwater perturbation associated with the iceberg discharges into the North Atlantic (as inferred from the light planktonic $\delta^{18}O$ isotope values and thick layers of IRD) (e.g., Hemming, 2004; Figure 5.9 c-e) likely kept the AMOC in a collapsed state of overturn (Figure 5.9h). This would have resulted in the significantly reduced northern hemisphere temperatures, and likely increased seasonality (Atkinson *et al.*, 1987; Broecker, 1991; Alm, 1993; Bond *et al.*, 1999; Bard *et al.*, 2000; review in Seager and Battisti, 2006; Andersen *et al.*, 2006; Svensson *et al.*, 2006; Rasmussen *et al.*, 2007; Peck *et al.*, 2008) (Figure 5.8a, f).

5.3.5.3. The H1 'clean-up' and resumption of the AMOC (16.5 – 14.6 ka BP)

The final phase of H1 started at 16.5 ka BP with a rapid reduction in surface-water freshening and IRD deposition in the IRD belt (Figures 5.9c, d, 5.12c). However, sustained cooling is apparent in the Greenland ice core $\delta^{18}O$ records (Figure 5.9a), Britain and Scandinavia (Figure 5.8f), while the Greenland Ca^{2+} ion series suggests that the atmospheric polar circulation intensity although decreases, remains relatively intensified (Figure 5.8b), and the AMOC remained in a collapsed state (Figure 5.9h). The British ice sheet and glaciers in the Apennine region re-advanced at around this time (Girraudi and Frezzotti, 1997; McCabe and Clark, 1998; McCabe *et al.*, 2007). Well-dated records from Cariaco Basin (Hughen *et al.*, 1996; Lea *et al.*, 2003), and speleothem records from China (Wang *et al.*, 2001), also show similar deteriorated climate conditions.

Unlike the decreased freshening inferred from records of IRD and $\delta^{18}O_{npl}$ for cores in the IRD belt, there were no signs of decreased surface water freshening at Eirik Drift or in the Nordic Seas (Figures 5.9e, g). Instead, the surface water freshening at Eirik Drift and in the Nordic Seas in both benthic and planktonic records started to increase at around 16.1 ka BP (Figure 5.9e, g). Given that the $\delta^{18}O_{npl}$ records at Eirik Drift have the same absolute values as those recorded in the Nordic Seas (Figure 5.9e, g), we suggest that this indicates direct watermass communication between the Nordic Seas and Eirik Drift during this latter phase of H1.

Maximum surface freshening at Eirik Drift is suggested at around 15.1 ka BP (Figure 5.9g). Thereafter, surface $\delta^{18}O_{npl}$ values progressively returned to heavier values, coincident with the termination of exceptionally high rates of deposition of fine grained sediments in the Nordic Seas (Lekens *et al.*, 2005). We interpret these sediments to represent hyperpycnal flows, which would have injected significant amounts of freshwater to intermediate depths in the Nordic Seas. As these sediments were deposited and the flows dewatered, the low density, highly buoyant, freshwater contained within these flows would have surfaced, transferring the light $\delta^{18}O$ signal from intermediate depths to the surface. As the AMOC was in a collapsed state (McManus *et al*., 2004; Figure 5.9h) and the Fram Strait was closed (Nøgaard-Pederson *et al*, 2003), these relatively fresh waters would have likely 'pooled' in the Nordic Seas and may thus have probably maintained the AMOC in its collapsed state (Figure 5.9h).

Given that NADW flow had more or less collapsed, and that the Bering Strait would have been closed, the relatively fresh waters that had pooled in the Nordic Seas would have been expelled via the Denmark Strait. Hence, the $\delta^{18}O_{npl}$ signals observed at Eirik Drift appear to record the same purged waters from the Nordic Seas. A hyperpycnal delivery of freshwater into the Nordic Seas provides the most plausible mechanism for invoking the benthic and planktonic $\delta^{18}O$ light excursion recorded in the Nordic Seas, as it can account for the greater magnitude of shift to lighter values observed in the benthic $\delta^{18}O$ records relative to the planktonic $\delta^{18}O$ records, as well as the temporal offsets between the two (Figure 5.9g; Figure 5.10). This hypothesis also gives explanation for the widespread distribution of this exact same signal in surface waters across not only the Nordic Seas, but the northern North Atlantic, which other hypotheses such as subsurface warming and sea-ice formation cannot.

From around 15.1 ka BP, the $\delta^{18}O_{npl}$ record at Eirik Drift, and in the $\delta^{18}O_{npl}$ and $\delta^{18}O_{ct}$ records in the Nordic Seas trend to heavier values (Figure 5.9g), concomitant with the termination of the deposition of laminated sediments in the Nordic Seas (Lekens *et al*., 2005; pink line in Figure 5.9g) and the re-advance of the Scandinavian ice sheet (Marks, 2002; Rinterknecht *et al*., 2006; Figure 5.8f). These heavier $\delta^{18}O$ values suggest a reduction in fresh water admixture in the Nordic Seas, which would have resulted from this reduction in meltwater input. This reduction in fresh water admixture would have aided by the purging of this relatively fresh watermass out of the Nordic Seas.

Also from around 15.5 ka BP, significant climate amelioration is recorded in the British Isles (Atkinson *et al*., 1987) and retreat from the H1 glacial maximum extent was well underway on a near global scale (Giraudi and Frezzotti, 1997;

Benson *et al*., 1998; McCabe and Clark, 1998; Clague and James, 2002; Dyke *et al*., 2002 and references therein; Ivy-Ochs *et al*., 2006; McCabe *et al*., 2007; Hendy and Cosma, 2008). However, warming at northern high-latitudes (Alm, 1993; Rasmussen *et al*., 2006) and climatic improvement in well-dated low latitude records (e.g., Hughen *et al*., 1996; Wang *et al*., 2001; Lea *et al*., 2003) is not inferred until sharp Bølling (15ºC) warming at 14.6 ka BP (Severinghaus *et al*., 1998; Severinghaus and Brook, 1999; Rasmussen *et al*., 2006). This apparent 'mismatch' between datings on snowline variations and winter dominated climate records is interpreted to reflect increased seasonality i.e., much cooler winter temperatures and warmer summer temperatures (Broecker *et al*., 1999; Denton *et al*., 2005; Seager and Battisti, 2006).

Previous model investigations have suggested that perturbations from the Southern Ocean may have caused the AMOC 'switch on' at the Bølling warming (e.g., Weaver *et al*., 2002; Knorr and Lohmann, 2003). However, these models cannot account for the sharp recovery that is seen in the proxy records (e.g., McManus *et al*., 2004; Stanford *et al*., 2006; Rasmussen *et al*., 2006; Figure 5.9a, h). An ocean-circulation model has also shown that low latitude salt promotion in the North Atlantic whilst the AMOC was in its collapsed state, preconditioned the AMOC for its kick start at the Bølling warming by advecting more saline surface waters to areas of NADW formation (Knorr and Lohmann, 2007). This model outcome agrees well with sea surface salinity estimates in the Caribbean during this final phase of H1 (Schmidt *et al*., 2004) and the Mediterranean salinity input (Rogerson *et al*., 2004).

However, in this study, we suggest that the trend to heavier $\delta^{18}O_{npl}$ values in the Nordic Seas and at Eirik Drift after 15.5 ka BP represents the termination of freshwater injection from the Scandinavian ice sheet into the Norwegian Sea (Lekens *et al*., 2005), and the purging of the accumulated freshwater out of the Nordic Seas that would have allowed the salinity of the basin to gradually increase. A few centuries after the freshwater signal/purging began to decrease, the AMOC underwent a sharp recovery (McManus *et al*., 2004; Stanford *et al*., 2006; Figure 5.9h) at the time of the abrupt Bølling warming (14.6 ka BP)

(a) Phase 1: 19-17.5 ka BP **(b) Phase 2: 17.5-16.5 ka BP**

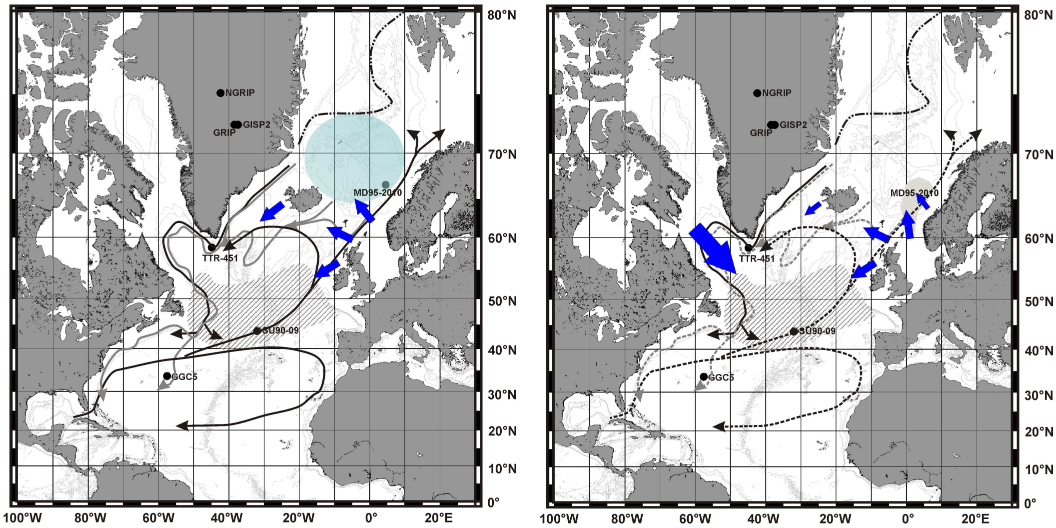

(c) Phase 3: 16.5-14.6 ka BP **(d) Phase 4: 14.6 ka BP**

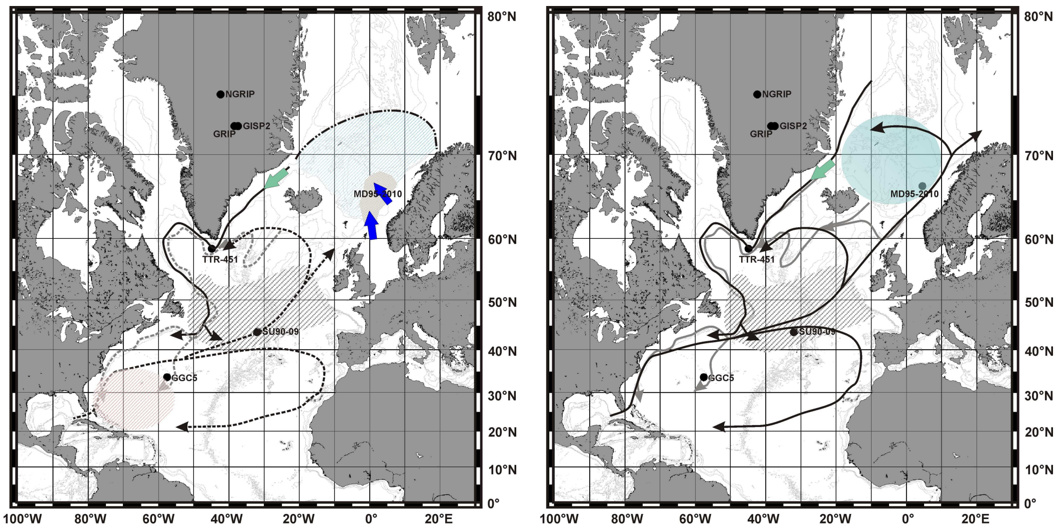

Figure 5.12. Schematic diagrams of the evolution of H1 in the Nordic Seas and the North Atlantic. Black lines indicate surface water currents, and dashed black lines indicate when the thermohaline surface currents may have had less flow intensity. Solid grey lines represent bottom currents and dashed grey lines indicate when bottom current flow intensity was significantly decreased. Solid blue arrows = inferred ice sheet surges. Solid

green arrow = the Nordic Seas/Eirik Drift surface water mass communication. Light blue shaded zone = sites of NADW. Hashed black zone = IRD belt (after Hemming, 2004). Dot/dashed line represents the summer sea-ice margin. Blue hashed area = subsurface freshening in the Nordic Seas. Brown hashed area = area of high rates of sediment accumulation (Lekens *et al.*, 2005). Orange hashed area represents an area of inferred increased surface water salinity (Schmidt *et al.*, 2004).

(Figure 5.9a). We therefore suggest that by increasing the salinity of the Nordic Seas, this key region of NADW formation (e.g., Dickson and Brown, 1994; Bacon, 1998; 2002) was prepared for the sharp AMOC recovery (Figure 5.12d).

5.3.6. Conclusions

We identify four key oceanographic changes during H1, namely: (1) a slowdown of NADW formation and small-scale precursor events; (2) a large-scale iceberg release and melting in the 'IRD Belt' and a shutdown of deep-water formation (3) pooling of hyperpycnally injected freshwater in the Nordic Seas, and sustained AMOC collapse and (4) the subsequent purging of the pooled meltwater out of the Nordic Seas.

The termination of this final meltwater 'clean-up' phase is near coincident with the AMOC recovery that accompanied the Bølling warming. The entire sequence of events extends the duration of H1 to almost 4000 years, rather than several centuries as suggested previously (Dowdeswell *et al.*, 1995; Rohling *et al.*, 2003; Hemming, 2004; Roche *et al.*, 2004a, b). This longer duration of the H1 episode now agrees with the entire previously established period of collapsed deep-water formation in the Nordic Seas (McManus *et al.*, 2004; Hall *et al.*, 2006; Stanford *et al.*, 2006).

CHAPTER 6

6. CONCLUSIONS AND WIDER IMPLICATIONS

Since it is speculated that freshwater additions into the North Atlantic may result in decreased rates of North Atlantic Deep Water (NADW) formation, and reduced poleward heat transport (e.g., Stommel, 1961; Broecker, 1991), the remit of study was to further elucidate the role of past freshwater forcing on the rate of NADW formation, the vigour of Atlantic Meridional Overturning Circulation (AMOC), and its impact upon climate, and also to evaluate the linearity of the ocean-climate system response.

This has been achieved through multi-proxy reconstruction from marine sediment core TTR-451, Eirik Drift, south of Greenland, and comparison of these findings with other, well-dated palaeo-proxy records. This study has focussed upon the time period of the last deglaciation (20 – 11 ka BP), which encompasses the climate deterioration and ice-berg discharge event of Heinrich event 1, the abrupt Bølling warming (when Greenland temperatures rose by more than 10ºC in only a couple of centuries (Severinghaus and Brook, 1999)), meltwater pulse (mwp)-1a, (a sea-level rise of around 20 m in around 500 yrs (e.g., Bard *et al*., 1996; Hanebuth *et al*., 2000; Peltier and Fairbanks, 2006)) and the sharp climate deterioration of the Younger Dryas.

Firstly, the much debated timings of the Bølling and mwp-1a are conclusively resolved by comparison of the GRIP ice core $\delta^{18}O$ record on the new layer-counted GICC05 time scale (Rasmussen *et al*., 2006) with the better constrained U/Th-dated Barbados fossil coral sea-level record (Fairbanks *et al*., 2005; Peltier and Fairbanks, 2006). This record comparison confirms previous suggestions (e.g., Bard *et al*., 1996; Liu and Milliman, 2004) that mwp-1a occurred at around 14.1 ka BP, culminating in a meltwater peak at around 13.9 ka BP. Therefore, mwp-1a was coincident with sharp "Older Dryas" (GI-1d) (Björck *et al.*, 1998) cooling event and not the Bølling warming (14.6 ka BP). Even when considering the 2σ uncertainties of these two ages, mwp-1a lags behind the Bølling warming by over 3 centuries. On this basis, the hypothesis that mwp-1a coincided with, and moreover was the trigger of, the Bølling warming (e.g., Hanebuth *et al*., 2000; Clark *et al*., 2002; Kienast *et al*., 2003; Weaver *et al*., 2003) is now rejected.

Also presented in this thesis is a re-evaluation of recalibrated accelerated mass spectrometric (AMS)^{14}C dated submerged flood terraces and mangroves from the Sunda Shelf (South China Sea). The Sunda Shelf sea level record has been used previously to question the Barbados dating of 14.1 ka BP for mwp-1a, since it dates mwp-1a at around 14.6 ka BP, co-incident with the Bølling warming (Hanebuth *et al*., 2000). Careful scrutiny and critical assessment of these recalibrated ages shows a significant depositional hiatus at around 14 ka BP, which most likely represents the rapid sea-level rise of mwp-1a (i.e., when it would have been unlikely for accretion of the mangrove forests to have kept pace with the sea level rise). This re-evaluation of datings of the Sunda Shelf sea level record therefore now supports the dating of mwp-1a from Barbados, at around 14.1 ka BP. The new time constraints that now place mwp-1a at the termination of the Bølling warming suggests that meltwater addition started within the Bølling, possibly as a direct response to high-latitude warming during that period (McManus *et al.*, 2004). At question, however, was whether there was a change in NADW flow intensity coincident with mwp-1a and the Older Dryas, since a previous record of AMOC intensity from the Bermuda Rise does not fully resolve this time period (McManus *et al*., 2004).

Presented within this thesis is a new record from marine sediment core TTR-451 of NADW flow intensity derived from the ratio of the susceptibility of anhysteretic remanent magnetisation (κ_{ARM}) versus low-field magnetic susceptibility (κ); a proxy for average (titano)magnetite grain size (Banerjee *et al.*, 1981; Verosub and Roberts, 1995). Since previous studies have suggested that the magnetic mineral content of sediments along the flowpath of NADW originates from the Nordic basaltic province (Kissel *et al.*, 1999a; Laj *et al.*, 2002), and deposition on Eirik Drift is dominated by suspended matter transported via deep-water overflow through Denmark Strait, the κ_{ARM}/κ record from Eirik Drift is interpreted to reflect variation in the size of magnetic grains that can be carried by NADW, and which settle out on Eirik Drift as the watermass rounds the southern tip of Greenland.

This interpretation of κ_{ARM}/κ values from Eirik Drift as a magnetic grain size indicator is tested by further environmental magnetic measurements, namely; the generation of saturated remanent magnetisation and backfield curves, magnetic hystersis loops and First Order Reversal Curve (FORC) diagrams, and Scanning Electron Miscroscope (SEM) image analysis of bulk sediments. Together, these studies confirm that the magnetic composition of sediments from TTR-451 is dominated by (titano)magnetite, and validates the inverse relationship between κ_{ARM}/κ and average (titano)magnetite grain size.

In order to test whether κ_{ARM}/κ is a sensitive index for NADW flow intensity, mean sortable silt grain size which is an established proxy for near bottom current strength (e.g. McCave *et al.*, 1995a, b; 2006; Bianchi and McCave, 1999; Hall *et al.*, 2001), was measured from the same sediment samples as the κ_{ARM}/κ. Comparison of these two records shows a good visual correlation. Statistical analyses reveal correlation, but despite good visual agreement, the correlation is weak. Next, the use of mean sortable silt grain sizes, and hence also κ_{ARM}/κ, as near bottom current indices at Eirik Drift, were tested by comparison of mean sortable silt grain size data from marine sediment core tops from Eirik Drift, with mean scalar velocities obtained from Lowered Acoustic Doppler Current Profiler (LADCP) data. A general positive trend was revealed and validates the use of mean sortable silt grain sizes, and hence also κ_{ARM}/κ, as near bottom current indices at Eirik Drift.

Combining the new (κ_{ARM}/κ) proxy record of NADW flow intensity from Eirik Drift with the Barbados sea-level and Greenland ice-core $\delta^{18}O$ records, shows that at the time of mwp-1a there was a ~500 yr reduction in NADW flow intensity. This slowdown was coincident with the brief Older Dryas cold period. This compilation of records also served to demonstrate the characteristic near-collapsed NADW formation during more extreme cooling events which were not associated with meltwater pulses large enough to significantly affect the sea-level record (Heinrich event 1 and the Younger Dryas). These data therefore suggest a fundamental non-linearity between the rate and magnitude of freshwater forcing in the form of meltwater injection and the AMOC intensity as witnessed by the rate of NADW formation, which is summarised in Figure 6.1.

Finally, a new reconstruction for Heinrich event 1 (H1) (16-17.5 ka BP; Bard *et al.*, 2000; Hemming, 2004) is presented, with focus upon the northern North Atlantic and the Nordic Seas. Records of IRD, planktonic foraminiferal counts and *N. pachyderma* (left-coiling) foraminiferal $\delta^{18}O$ for TTR-451, are compared with records from the IRD belt and the Nordic Seas, and their event stratigraphy is placed in context with re-evaluated terrestrial records of temperature and glacial extent. Identified are four key oceanographic changes. Firstly a slowdown of NADW formation from around 19 ka BP is associated with small-scale precursor events (e.g., Grousset *et al.*, 2000; 2001; Hemming, 2004; Knutz *et al.*, 2001; 2007; Peck *et al.*, 2006; 2007a, b; 2008) and the first significant jump in sea-level (e.g., Yokoyama *et al.*, 2000; Lambeck *et al.*, 2002). A short duration warming at high-latitudes is evident at this time (e.g., Alm, 1993; Andersen *et al.*, 2006; Svensson *et al.*, 2006; Rasmussen *et al.*, 2007), near coincident with warming in the Southern Hemisphere (e.g., Arz *et al.*, 1999; Sachs *et al.*, 2001; Kim *et al.*, 2002; Peeters *et al.*, 2004; EPICA community members, 2006). Increased insolation at this time (e.g., Berger *et al.*, 1999), has been suggested as the cause for this post Last Glacial Maximum (LGM) warming due to enhanced global temperatures as a result of greenhouse gas and albedo

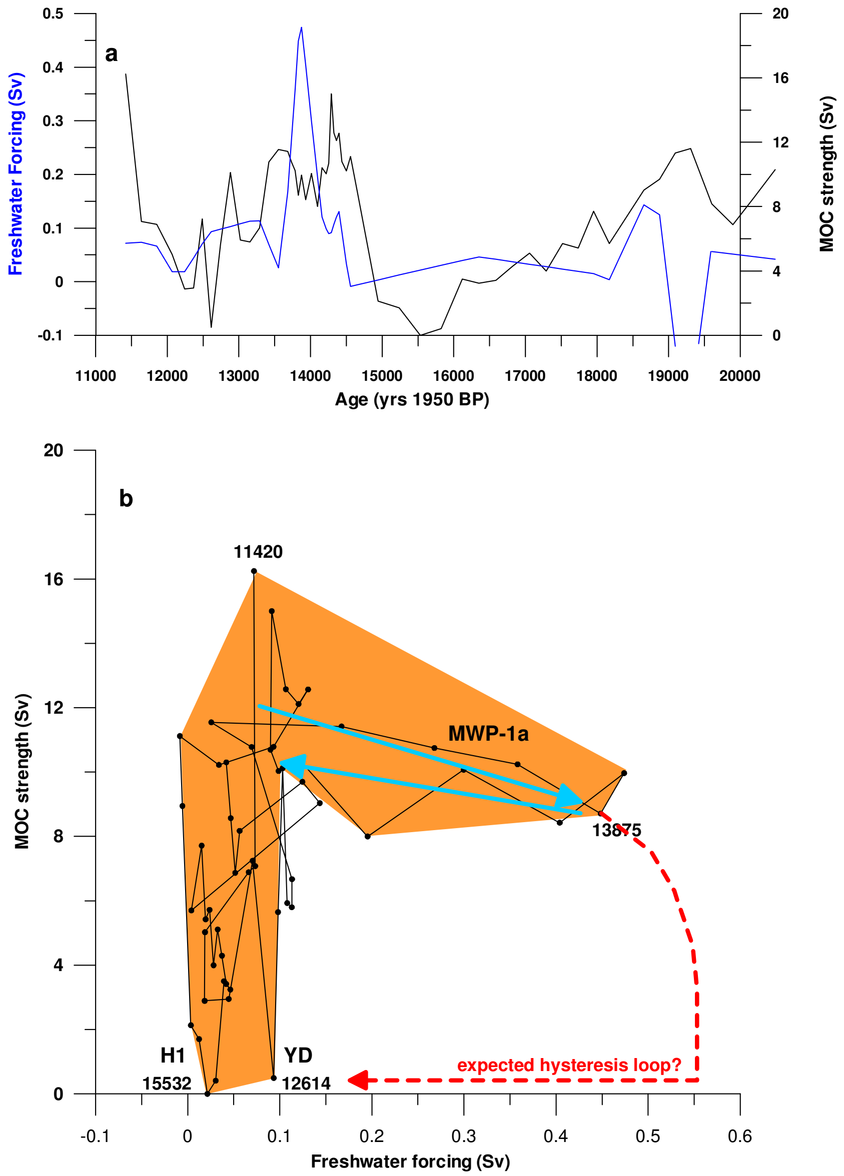

Figure 6.1. a. In black is the κ_{ARM}/κ record for NADW intensity from TTR-451, scaled to AMOC strength, assuming that the Bølling AMOC intensity equals 75 % of the modern AMOC strength (~15 Sv; McManus *et al.*, 2004). In blue is the freshwater forcing in Sv derived from the Barbados sea level record (Peltier and Fairbanks, 2006) and interpolated onto the same time steps as the κ_{ARM}/κ record. b. A cross-plot of the derived AMOC intensity versus freshwater forcing. Ages are given in yrs 1950 BP. In red is drawn the extrapolated hysteresis loop of mwp-1a. H1 = Heinrich event 1 and YD = Younger Dryas.

feedbacks (Bender *et al*., 1997; Alley and Clark, 1999). Advection of relatively warm waters from the Southern Ocean into the North Atlantic could have caused this warming in the North Hemisphere, ice sheet melt and consequent AMOC slowdown (e.g., Stocker and Wright, 1991; Bender *et al*., 1997; McCabe and Clark, 1998).

These early precursor meltwater events were followed at around 17.5 ka BP by a large-scale iceberg release and melting in the 'IRD Belt' (e.g., Bond and Lotti, 1995; Bond *et al*., 1999; Bard *et al*., 2000; Grousset *et al*., 2000; 2001; Hemming, 2004; Knutz *et al*., 2001; 2007) that likely caused the shutdown of deep-water formation, which is seen in the Eirik Drift (TTR-451) and Bermuda Rise records (e.g., McManus *et al*., 2004). At around 16.5 ka BP, IRD deposition ceased in the IRD belt and yet the κ_{ARM}/κ record for TTR-451 shows that the AMOC remained in a collapsed state, similar to previous suggestions (McManus *et al*., 2004; Peck *et al*., 2007b).

From around 16.5 ka BP, a light $\delta^{18}O$ excursion developed in both benthic and planktonic records from the Nordic Seas (e.g., Dokken and Jansen, 1999; Rasmussen and Thomsen, 2004). This light $\delta^{18}O$ event is also recorded in $\delta^{18}O$ records for *N. pachyderma* (left coiling) in core TTR-451. On the basis of the character and the widespread nature of the $\delta^{18}O$ light excursion observed across the Nordic Seas and the northern North Atlantic, hypotheses of either iceberg release (e.g., Rashid and Boyle, 2007), subsurface warming (e.g., Rasmussen *et al*., 2006; Rasmussen and Thomsen, 2004), or sea-ice formation (e.g., Dokken and Jansen, 1999) as the cause for this $\delta^{18}O_{npl}$ signal, are rejected.

Since the record of $\delta^{18}O_{npl}$ from Eirik Drift shares not only the same trends, but absolute values as a $\delta^{18}O_{npl}$ record from the Nordic Seas (Dokken and Jansen, 1999), direct surface water communication is suggested. Given that sedimentation rates of fine-grained laminated sediments in the southern Norwegian Sea were greatly enhanced at this time (Lekens *et al*., 2005), coincident with the timing of rapid glacial retreat from the Scandinavian ice sheet (e.g., Rinterknecht *et al*., 2006), the $\delta^{18}O$ light event in the Nordic Seas is ascribed here to meltwaters that were likely injected hyperpycnally into the Nordic Seas. Similar to previous suggestions (e.g., McManus *et al.*, 2004; Peck *et al.*, 2007b), the κ_{ARM}/κ record for TTR-451 indicates that the AMOC was in a state of complete collapse at this time and, due to significantly reduced ocean circulation, these meltwaters likely 'pooled' in the Nordic Seas, possibly maintaining the AMOC in its collapsed state. The agreement between the $\delta^{18}O_{npl}$ records from the Nordic Seas and at Eirik Drift, as the records return to heavier values, are interpreted to reflect a purging of these relatively freshened waters out of the Nordic Seas in a configuration analogous with the modern Arctic outflow through the Fram Strait via the East Greenland Current (EGC) (e.g., Rudels *et al.*, 2002).

A few centuries after the $\delta^{18}O_{npl}$ values in the Nordic Seas and at Eirik Drift returned to these heavier values, and the cessation of Scandinavian ice sheet retreat (Lekens *et al.*, 2005; Rinterknecht *et al.*, 2006), the AMOC underwent a sharp recovery at the Bølling warming (14.6 ka BP). The entire sequence of events extends the duration of H1 to almost 4000 years, rather than several centuries as previously suggested (Dowdeswell *et al.*, 1995; Rohling *et al.*, 2003; Hemming, 2004; Roche *et al.*, 2004a, b). This longer composite duration of H1, presented here, agrees with the entire previously established period of collapsed deep-water formation in the Nordic Seas (McManus *et al.*, 2004; Hall *et al.*, 2006).

In summary, this study shows that mwp-1a, the largest documented meltwater pulse of the last deglaciation, coincided with only a short lived and minor reduction in NADW flow intensity, and the relatively minor climate deterioration of the Older Dryas, which terminated the Bølling warming. However, much more extreme climate events (namely, H1 and the Younger Dryas), which are characterised by almost complete collapse of the AMOC have no discernable metlwater pulse associated with them. As summarised in Figure 6.1., this indicates a distinct non-linearity between the rate and magnitude of meltwater injections and the AMOC and climate response. Hysteresis loops of AMOC intensity in response to freshwater forcing produced by coupled ocean-climate models suggest AMOC shutdown would result from between 0.15 and 0.5 Sv of freshwater forcing (e.g., Rahmstorf *et al.*, 2005) and, moreover, instantaneous AMOC collapses for mwp-1a with only 0.1 Sv meltwater injection (e.g., Manabe and Stouffer, 1997). The freshwater forcings applied in these models are therefore apparently overestimated for H1 and the Younger Dryas, and yet underestimated for mwp-1a (Figure 6.1.). Clearly, reconciliation is required between the palaeo-data and modelled outcomes to better understand the ocean-climate response to meltwater perturbations.

Model simulations have suggested that non-linear responses of ocean circulation to the magnitude and rate of freshwater perturbations could occur in a system with different quasi-stable climate states (Rahmstorf, 1995; Ditlevsen, 1999). Alternatively, it may be that the nature or the location of meltwater entry into the oceans are more important for NADW formation than the magnitude or rate (Moore, 2005; Tarasov and Peltier, 2005). It has been suggested that a considerable component of mwp-1a may have hyperpycnally entered the ocean via the Gulf of Mexico (Flower *et al.*, 2004; Aharon, 2005), and strong mixing with ambient seawater may have reduced its impact on NADW formation (Tarasov and Peltier, 2005; Aharon, 2005). It has also been suggested that although mwp-1a occurred ~1000 yrs prior to the Younger Dryas, it may have pre-conditioned the North Atlantic later AMOC shutdown, by reduction of the Greenland-Scotland Ridge overflow (e.g., Lohmann and Schultz, 2000), and/or by shifting the ocean-climate system to conditions where more than one AMOC state might co-exist (Knorr and Lohmann, 2007). Alternatively, contributions to the mwp-1a sea level rise may also have come from the Southern Hemisphere (e.g., Clark *et al.*, 2002; Weaver *et al.*, 2003; Knorr and Lohmann, 2007).

Conversely, meltwater (iceberg) injections during Heinrich event 1 and the Younger Dryas, are not dramatically evident in the sea-level records (Fairbanks, 1989; Hanebuth *et al.*, 2000; Aharon, 2005; Peltier and Fairbanks, 2006) and yet may have sufficiently affected the Nordic Seas to cause a collapse of NADW formation. Moore (2005) and Tarasov and Peltier (2005) have proposed that if a small meltwater flux, not large enough to discern in sea level records, was injected into this critical region for NADW formation, it may have triggered the NADW formation collapse associated with the Younger Dryas. Furthermore, the new reconstruction presented here in this thesis for the Nordic Seas and northern North Atlantic for the end of H1, suggests that meltwater injected at intermediate depths into the Nordic Seas may have had a catastrophic impact upon the rate of NADW formation, possibly stabilising the AMOC in its ‘off’ mode.

It is clear from this study (as summarised in Figure 6.1) and from previous model investigations (e.g., Knorr and Lohmann, 2007; Huang and Tian, 2008) that climatic impacts are not simply governed by the magnitude and/or rate of meltwater addition. It would appear that, if indeed the climate forcing was dependent on freshwater input, then (small) freshwater additions targeted on the Arctic/Nordic Seas (a key region of NADW formation today (e.g., Dickson and Brown, 1994; Bacon, 1998; 2002a)) and in interstadial modes of AMOC (e.g., Rahmstorf, 2002) may represent a much greater risk of disrupting NADW formation. Alternatively, it should be considered that the inferred non-linear responses of ocean circulation to the magnitude and rate of meltwater additions indicate that meltwater input was not necessarily the primary driver in AMOC and climate transitions. To evaluate this, new palaeo-proxy records are required that constrain other potential aspects of the ocean-climate interaction, such as sea-ice feedbacks and important seasonality changes (Broecker, 2001; Gildor and Tziperman, 2003; Li *et al.*, 2005; Denton *et al.*, 2005; Wunsch, 2006; Peck *et al.*, 2008).

7. References

Aagaard, K. and E. C. Carmack (1989), The role of sea ice and other fresh water in the Arctic Circulation. *Journal of Geophysical Research*, *94*, 14485-14498.

Aharon, P. (1983), 140,000 yr. Isotope Climatic Record from Raised Coral Reefs in New Guinea. *Nature*, *304*, 720-724.

Aharon, P. (2005), Entrainment of meltwaters in hyperpycnal flows during deglaciation superfloods in the Gulf of Mexico, *Earth Planet. Sci. Lett.*, *241*, 260-270.

Aksu, A. E., A. de Vernal, and P. J. Mudie (1989), High-resolution foraminifer, palynologic, and stable isotopic records of Upper Pleistocene sediments from the Labrador Sea: Paleoclimatic and Paleoceanographic trends, *Proceeding of the Ocean Drilling Program, Scientific Results*, *105*, 617-652.

Allen, J. R. M., U. Brandt, A. Bauer, H.-W. Hubberten, B. Huntley, J. Keller, M. Kram, A. Mackensen, J. Mingram, J. F. W. Negendank, N. R. Nowaczyk, H. Oberhänsli, W. A. Watts, S. Wulf, and B. Zolitschka (1999), Rapid environmental changes in southern Europe during the last glacial period, *Nature*, *400*, 740-743.

Alley, R. B. and P. U. Clark (1999), The deglaciation of the Northern hemisphere: A global perspective, *Annu. Rev, Earth Planet Sci.*, *27*, 149-182.

Alley, R. B. (2000), the Younger Dryas cold interval as viewed from central Greenland, *Quaternary Science Reviews*, *19*, 213-226.

Alley, R. B., S. Anandakrishnan, P. Jung, and A. Clough (2001a), Stochatsic Resonance in the North Atlantic: Further Insights, *The Oceans and rapid climate change: past, present and future*, edited by Seidov, D., Haupt, B.J. & Maslin, M., pp. 57-68, American Geophysical Union, 2001, Washington, D.C.

Alley, R. B., S. Anandakrishnan, and P. Jung (2001b), Stochastic Resonance in the North Atlantic, *Paleoceanography*, *16*, 2, 190-198.

Alley, R. B., J. Marotzke, W. D. Nordhaus, J. T. Overpeck, D. M. Peteet, R. A Pielke Jr., R. T. Pierrehumbert, P. B. Rhines, T. F. Stocker, L. D. Talley, J. M. Wallace (2003), Abrupt Climate Change, *Science*, *299*, 2005-2010.

Alley, R. B., T. K. Dupont, B. R. Parizek, S. Anandakrishnan, D. E. Lawson, G. J. Larson, and E. B. Evenson (2006), Outburst flooding and the initiation of ice-stream surges in response to climatic cooling: A hypothesis, *Geomorphology*, *75*, 76-89.

Alm, T. (1993), Øvre Æråsvatn – palynostratigraphy of a 22,000 to 10,000 BP lacustrine record on Andøya, northern Norway, *Boreas*, *22*, 171-188.

Alvarez, M., F. F. Perez, H. Bryden and A. F. Rios (2004), Physical and Biogeochemical transport structure in the North Atlantic Sub-Polar Gyre. *Journal of Geophysical Research, 109,* doi: 10.1029/2003JC002015.

Andersen, K.K., A. Svensson, S.J. Johnsen, S.O. Rasmussen, M. Bigler, R. Röthlisberger, U. Ruth, M.-L. Siggaard-Andersen, J.P. Steffensen, D. Dahl-Jensen, B.M. Vinther, and H.B. Clausen (2006), The Greenland Ice Core Chronology 2005, 15-42 ka. Part 1: Constructing the time scale, *Quaternary Science Reviews*, *25*, Shackleton special issue 24.

Andrews JT, H. Erlenkeuser, K. Tedesco, A. E. Aksu, A. J. T. Jull (1994), Late Quaternary (Stage 2 and 3) meltwater and Heinrich events, Northwest Labrador Sea. *Quaternary Research*, *41*, 26–34.

Andrews, J. T., J. Hardadottir, J. S. Stoner, M. E. Mann, G. B. Kristjansdottir, and N. Koc (2003), Decadal to millennial-scale periodicities in North Iceland shelf sediments over the last 12 000 cal yr: long-term North Atlantic oceanography variability and solar forcing, *Earth and Planetary Science Letters*, *210*, 453-465.

Arbic, B. K., J. X. Mitrovica, D. R. MacAyeal, and G. A. Milne (2004), Ocean tides and Heinrich events, *Nature*, *432*, 460.

Arbic, B. K., J. X. Mitrovica, D. R. MacAyeal, and G. A. Milne (2008), On the factors behind large Labrador Sea tides during the last glacial cycle and the potential implications for Heinrich events, *Paleoceanography*, *23*, PA3211, doi:10.1029/2007PA001573.

Arnold, A. J., and W. C. Parker (1999), *Biogeography of planktonic Foraminifera* In: Sen Gupta, B. K. (Ed) Modern Foraminifera, *Kluwer Academic Publishers*, 103-122.

Arthur, M. A., S. P. Srivastava, M. Kaminiski, R. Jarrad, and J. Osler (1989), Seismic stratigraphy and history of deep circulation and sediment drift development in Baffin Bay and the Labrador Sea, *Proceedings of the Ocean Drilling Program, Scientific Results*, *105*, 957-988.

Arz, H. W., J. Patzold, and G. Wefer (1999), The deglacial history of the western tropical Atlantic as inferred from high resolution stable isotope records off northeastern Brazil, *Earth Planet. Sci. Lett*., *167*, 105–117.

Atkinson, T. C., K. R. Briffa, and G. R. Coope (1987), Seasonal temperatures in Britain during the past 22,000 years, reconstructed using beetle remains, *Nature*, *325*, 587-592.

Austin, W. E. N., E. Bard, J. B. Hunt, D. Kroon, and J. D. Peacock (1995), The ^{14}C age of the Icelandic Vedde Ash: Implications for Younger Dryas marine reservoir age corrections, *Radiocarbon*, *37*, 53-62.

Austin, W. E. N., and D. Kroon (2001), Deep sea ventilation of the northeastern Atlantic during the last 15,000 years, *Global and Planetary Change*, *30*, 13-31.

Bacon, S. (1998), Decadal variability in the outflow from the Nordic seas to the deep Atlantic Ocean, *Nature*, *394*, 871-874.

Bacon, S. (2002), The dense overflows from the Nordic Seas into the deep North Atlantic, *ICES Marine Science Symposia*, *215*, 148-155.

Bacon, S., G. Reverdin, I. G. Rigor and H. M. Snaith (2002), A freshwater jet on the East Greenland Shelf, *Journal of Geophysical Research, 107(C7),* 3068, doi: 10.1029/2001JC000935.

Bacon, S., W. J. Gould and Y. Jia, (2003), Open-ocean convection in the Irminger Sea. *Geophysical Research Letters, 30,* 1246.

Bäckström, D. L., A. Kuijpers, and J. Heinemeier (2001), Late Quaternary North Atlantic paleoceanographic records and stable isotopic variability in four planktonic foraminiferal species, *Journal of Foraminiferal Research*, *31*, 25-32.

Banerjee, S. K., J. W. King, and J. Marvin (1981), A rapid method for magnetic granulometry with applications to environmental studies, *Geophys. Res. Lett.*, *8,* 333-336.

Bard, E., B. Hamelin, R.G. Fairbanks, and A. Zindler (1990a), Calibration of the ^{14}C timescale over the past 30,000 years using mass spectrometric U-Th ages from Barbados corals, *Nature*, *345*, 405-410.

Bard, E., B. Hamelin, and R. G. Fairbanks (1990b), U/Th ages obtained by mass spectrometry in corals from Barbados - sea level during the past 130,000 years, *Nature*, *346*, 456-458.

Bard, E., B. Hamelin, M. Arnold, L. Montaggioni, G. Cabioch, G. Faure, and F. Rougerie (1996), Sea level record from Tahiti corals and the timing of deglacial meltwater discharge, *Nature*, *382*, 241-244.

Bard, E., F. Rostek, and C Sonzogni (1997), Interhemipsheric synchrony of the last deglaciation inferred from alkenone paleothermometry, *Nature*, *385*, 707-710.

Bard, E., M. Arnold, B. Hamelin, N. Tisnerat-Laborde, and G. Cabioch (1998), Radiocarbon calibration by means of mass spectrometric $^{230}Th/^{234}U$ and ^{14}C ages of corals. An updated data base including samples from Barbados, Mururoa and Tahiti, *Radiocarbon*, *40*, 1085-1092.

Bard, E., F. Rostek, J.-L. Turon, and C. Sonzogni (2000), Interhemispheric synchrony of the last deglaciation inferred from alkenone paleothermometry, *Nature*, *385*, 707-710.

Barker, S., and H. Elderfield (2002), Foraminiferal calcification response to glacial-interglacial changes in atmospheric CO2, *Science*, *297*, 833–836, doi:10.1126/science.1072815.

Bartov, Y., S. L. Goldstein, M. Stein, and Y. Enzel (2003), Catastrophic arid episodes in the Eastern Mediterranean linked with the North Atlantic Heinrich events, *Geology*, *31*, 439-442.

Basset, S. E., G. A. Milne, J. X. Mitrovica, and P. U. Clark (2005), Ice sheet and solid Earth influences of far-afieled sea-level histories, *Science*, *309*, 925-928.

Bauch, D., P. Schlosser, and R. G. Fairbanks (1995), Freshwater balance and the sources of deep and bottom waters in the Arctic Ocean inferred from the distribution of H218O, *Progress In Oceanography*, *35*, *1*, 53-80.

Bauch, D., H. Erlenkeuser, and N. Andersen (2005), Water mass processes on Arctic shelves as revealed from $\delta^{18}O$ of H_2O, *Global and Planetary Change*, *48*, 165-174.

Bemis, B. E., H. J. Spero, J. Bijma, and D. W. Lea (1998), Reevaluation of the oxygen isotope composition of planktonic foraminifera: Experimental results and revised paleotemperature equations, *Paleoceanography*, *13*, 150-160.

Bender, M., T. Sowers, M. –L. Dickson, J. Orchardo, P. Grootes, P. A. Mayewski, and D. A. Meese (1994), Climate correlations between Greenland and Antarctica during the past 100,000 years. Nature 372, 663–666.

Bender, M., T. Sowers, and E. Brook (1997), Gases in ice cores, *Proc. Natl. Acad. Sci*., *94*, 8343-8349.

Bender, M. L., B. Malaize, J. Orchardo, T. Sowers, and J. Jouzel, (1999), High precision correlations of Greenland and Antarctic ice core records over the last 100 kyr. In: Clark, P.U., et al. (Eds.), Mechanisms of Global Climate Change at Millennial Time Scales, Geophysical Monograph 112. American Geophysical Union, pp. 149–164.

Benson, L. V., H. M. May, R. C. Antweiler, T. I. Brinton, M. Kashgarian, J. P. Smoot, and S. P. Lund (1998), Continuous Lake-Sediment Records of Glaciation in the Sierra Nevada between 52,600 and 12,500 14C yr B.P. *Quaternary Research*, *50*, 113–127.

Benson, L., J. Liddicoat, J. Smoot, A. Sarna-Wojcicki, R. Negrini, and S. Lund (2003), Age of the Mono Lake excursion and associated tephra, *Quaternary Science Reviews, 22, 2-4,* 135-140.

Berger, W. H. (1971), Sedimentation of planktonic foraminifera, *Marine Geology*, *11*, 325-358.

Berger, A. (1991), Insolation values for the climate of the last 10 million of years, *Quaternary Science Reviews*, *10(4)*, 297-317, doi:10.1016/0277-3791(91)90033-Q.

Berger, A. (1999), Parameters of the Earths orbit for the last 5 Million years in 1 kyr resolution, PANGAEA, doi:10.1594/PANGAEA.56040.

Bianchi, G. G., and I. N. McCave (1999), Holocene periodicity in North Atlantic climate and deep-ocean flow south of Iceland, *Nature*, *397*, 515-517.

Bianchi, G. G., I. R. Hall, I. N. McCave, and L. Joseph (1999), Measurement of the sortable silt current speed proxy using the Sedigraph 5100 and Coulter Multisizer IIe: precision and accuracy, *Sedimentology*, *46*, 1001-1014.

Bigler, M. (2004), Hochauflösende Spurenstoffmessungen an polaren Eisbohrkernen: Glaziochemische und klimatische Prozessstudien, Ph.D. dissertation, University of Bern, Switzerland.

Bijma, J., B. Hönisch, and R. E. Zeebe (2002), Impact of the ocean carbonate chemistry on living foraminiferal shell weight: Comment on "Carbonate ion concentration in glacial-age deep waters of the Caribbean Sea" by W.S. Broecker and E. Clark. – *Geochemistry Geophysics Geosystems*, *3*, 1064, doi:10.1029/2002GC000388.

Billups, K., and H. J. Spero (1995), Relationship between shell size, thickness and stable isotopes in individual planktonic Foraminifera from 2 Equatorial Atlantic cores, *Journal of Foraminiferal Reserarch, 25, 1,* 24-37.

Billups, K., and D. P. Shrag (2000), Surface ocean density gradients during the Last Glacial Maximum, *Paleoceanography*, *15*, 1, 110-123.

Bischof, J. F., and D. A. Darby (1999), Quaternary ice transport in the Canadian Arctic and extent of late Wisconsinan glaciation in the Queen Elizabeth Islands, *Can. J. Earth Sci.*, *36*(12), 2007–2022.

Björck, S., M. J. C. Walker, L. C. Cwynar, S. Johnsen, K-L. Knudsen, J. Lowe, B. Wohlfarth, and Intimate Members (1998), An event stratigraphy for the Last Termination in the North Atlantic region based on the Greenland ice-core record: A proposal by the INTIMATE group, *J. Quat. Sci.*, *13*, 283-292.

Björk, G., J. Söderqvist, P. Winsor, A. Nikolopoulos, and M. Steele (2002), Return of the cold halocline layer to the Amundsen Basin of the Arctic Ocean: Implications for the sea ice mass balance, *Geophys. Res. Lett.*, *29*(11), 1513, doi:10.1029/2001GL014157.

Blunier, T., J. Schwander, B. Stauffer, T. Stocker, A. Dällenbach, J. Indermühle, J. Tschumi, D. Chappellaz, D. Raynaud, and J.-M. Barnola (1997), Timing of the Antarctic Cold Reversal and the atmospheric CO_2 increase with respect to the Younger Dryas event, *Geophys. Res. Lett., 24*, 2683-2686.

Blunier, T., J. Chappellaz, J. Schwander, A. Daellenbach, B. Stauffer, T. Stocker, D. Raynaud, J. Jouzel, H. B. Clausen, C. U. Hammer, and S. J. Johnsen (1998), Asynchrony of Antarctic and Greenland climate change during the last glacial period, *Nature*, *394*, 739-743.

Blunier, T, J., and E. J. Brook (2001), Timing of Millennial-Scale Climate Change in Antarctica and Greenland During the Last Glacial Period, *Science*, *291*, 109-112.

Bodén, P., R. G. Fairbanks, J. D. Wright, and L. H. Burckle (1997), High-resolution stable isotope records from southwestern Sweden: The drainage of the Baltic Lake and Younger Dryas ice margin oscillations, *Paleoceanography*, *12*, 1, 39-49.

Bond, G. W., H. Heinrich, W. Broecker, L. Labeyrie, J. McManus, J. Andrews, S. Huon, R. Jantschik, S. Clasen, C. Simet, K. Tedesco, M. Klas, G. Bonani and S. Ivy (1992), Evidence for massive discharges of icebergs into the North Atlantic ocean during the last glacial period, *Nature*, *360*, 245–249.

Bond, G., W. Broecker, S. Johnsen, J. McManus, L. Labeyrie, J. Jouzel, and G. Bonani (1993), Correlations between climate records from North Atlantic sediments and Greenland ice, *Nature*, *365*, 143-147.

Bond, G. C., and R. Lotti (1995), Iceberg Discharges into the North Atlantic on Millennial Time Scales During the Last Glaciation, *Science*, *267*, 1005-1009.

Bond, G., W. Showers, M. Cheseby, R. Lotti, P. Almasi, P. deMenocal, P. Priore, H. Cullen, I. Hajdas, and G. Bonani (1997), A Pervasive Millennial-Scale Cycle in North Atlantic Holocene and Glacial Climates, *Science*, *278*, 1257-1266.

Bond, G., W. Showers, M. Elliot, M. Evans, R. Lotti, I. Hajdas, G. Bonani, and S. Johnson (1999), The North Atlantic's 1-2 kyr Climate Rhythm: Relation to Heinrich Events, Dansgaard/Oeschger Cycles and the Little Ice Age. In *Mechanisms of Global Climate Change at Millennial Time Scales*, edited by Clark, P. U., Webb, R.S. & Keigwin, L.D., pp. 35-58, American geophysical Union, Washington, D.C.

Bondevik, S. J., J. Mangerud, S. Dawson, A. Dawson, and Ø. Lohne (2003), Record-breaking Height for 8000-Year-Old Tsunami in the North Atlantic, *Eos,Transactions, American Geophysical Union*, *84*, 31, 289-300.

Bondevik, S., J. Mangerud, H. H. Birks, S. Gulliksen, and P. Reimer (2006), Changes in North Atlantic radiocarbon reservoir ages during the Allerød and Younger Dryas, *Science*, *312*, 1514-1517.

Böning, P., E. Bard, and J. Rose (2007), Toward direct, micron-scale XRF elemental maps and quantitiative profiles of wet marine sediments, *Geology, Geophysics, Geosysetms*, *8*, 5 Q05004 doi: 10.1029/2006GC001480.

Bowen, D. Q., F. M. Phillips, A. M. McCabe, P. C. Knutz, and G. A. Sykes (2002), New data for the Last Glacial Maximum in Great Britain and Ireland, *Quaternary Science Reviews*, *21*, 89-101.

Boyle, E. A., and L. Keigwin (1987), North Atlantic thermohaline circulation during the past 20,000 years linked to high-latitude surface temperature, *Nature*, *330*, 35-40.

Boyle, E. A. (1992), Cadnium and $\delta^{13}C$ Paleochemical Ocean Distributions during the Stage 2 Glacial Maximum, *Annu. Rev. Earth Planet. Sci*, *20,* 245-287.

Boyle, E. A. (2000), Is ocean thermohaline circulation linked to abrupt stadial/interstadial transitions? *Quaternary Science Reviews*, *19*, 255-272.

Brachfeld, S.A., C. Kissel, C. Laj, A. Mazaud (2004), Behavior of u-channels during acquisition and demagnetization of remanence: implications for paleomagnetic and rock magnetic experiments. *Phys. Earth Planet. Inter*, *145*, 1–8.

Broecker, W. S. (1982), Glacial to interglacial changes in ocean chemistry. *Progress in Oceanography, 11*, 151-197.

Broecker, W.S., and T. H. Peng (1982), Tracers in the sea, *Eldigio Press*, *Palisades*, *New York.*

Broecker, W. S. (1991), The great ocean conveyor, *Oceanography*, *4*, 79-89.

Broecker, W. S., G. Bond, M. Klas, E. Clark, and J. McManus (1992), Origin of the northern Atlantic's Heinrich events, *Climate Dynamics*, *6*, 265-273.

Broecker, W. S. (1994), Massive iceberg discharges as triggers for global climate change, *Nature*, *372*, 421-424.

Broecker, W. S., S. L. Peacock, S. Walker, R. Weiss, E. Fahrbach, M. Schroeder, U. Mikolajewicz, C. Heinze, R. Key, T.-H. Peng, and S. Rubin (1998), How much deep water is formed in the Southern Ocean?, *Journal of Geophysical Research*, *103*, C8, 15,833-15, 843.

Broecker, W. S. (2000a), Abrupt climate change: causal constraints provided by the paleoclimate record, *Earth-Science Reviews*, *51*, 137-154.

Broecker, W. S. (2000b), Was a change in thermohaline circulation responsible for the Little Ice Age, *Proceedings of the National Academy of Sciences of the United States of America*, *97*, 1339-1342.

Broecker, W. S. (2001), The Big Climate Amplifier Ocean Circulation-Sea-Ice-Storminess-Dustiness-Albedo. In *The Oceans and Rapid Climate Change: Past. Present, and Future*, edited by Seidov, D., Haupt, B.J. & Maslin, M., pp. 53-56, American Geophysical Union, 2001, Washington, D.C.

Broecker, W. S. (2006), Was the Younger Dryas triggered by a flood?, *Science*, *312*, 1146-1148.

Brook, E. J., T. Sowers, and J. Orchardo (1996), Rapid variations in atmospheric methane concentration during the past 110 ka, *Science*, *273*, 1087–1091.

Brook, E. J., J. W. C. White, A. S. M. Schilla, M. L. Bender, B. Barnett, J. P. Severinghaus, K. C. Taylor, R. B. Alley, E. J. Steig (2005), Timing of millennial-scale climate at Siple Dome, West Antarctica, during the last glacial period, *Quaternary Science Review*, *24*, 1333-1343.

Bryden, H. L., H. R. Longworth, and S. Cunningham (2005), Slowing of the Atlantic meridional overturning circulation at 25ºN, *Nature*, *438*, 655-657.

Bugge, T., S. Befring, R. H. Belderson, T. Eidvin, E. Jansen, N. H. Kenyon, H. Holtedahl, and H. P. Sejrup (1987), A giant three-stage submarine slide off Norway, *Geo-Marine Letters*, *7*, 191-198.

Burns, S. J., D. Fleitmann, A. Matter, J. Kramers,. A. A. Al-Subbary (2003), Indian Ocean Climate and an Absolute Chronology over Dansgaard/Oeschger Events 9 to 13, *Science*, *301*, 1365-1367.

Butler, R. F. (1992), *Paleomagnetism: Magnetic Domains to Geologic Terrains* Blackwell Scientific Publications, Boston, MA, 319, pp1-15.

Cacho, I., J.O. Grimalt, C. Pelejero, M. Canals, F.J. Sierro, J.A. Flores, and N. J. Shackleton (1999), Dansgaard–Oeschger and Heinrich event imprints in Alboran Sea temperatures, *Paleoceanography*, *14*, 698–705.

Calov, R., A. Ganopolski, V. Petoukhov, M. Claussen, and R. Greve (2002), Large-scale instabilities of the Laurentide ice sheet simulated in a fully coupled climate-system model, *Geophysical Research Letters, 29*, 24 2216, doi:10.1029/2002GL016078.

Came, R. E., D. W. Oppo, W. B. Curry, and J. Lynch-Stieglitz (2008), Deglacial variability in the surface return flow of the Atlantic meridional overturning circulation, *Paleoceanography*, *23*, PA1217, doi:10.1029/2007PA001450, 2008

Cao, L., R. G. Fairbanks, R. A. Mortlock, and M. J. Risk (2007), Radiocarbon reservoir age of high latitude North Atlantic surface water during the last deglacial, *Quaternary Science Reviews*, *26*, 732–742.

Carvallo, C., A. R. Muxworthy, D. J. Dunlop, and W. Williams (2003), Micromagnetic modeling of First-order reversal curve (FORC) diagrams for single-domain and pseudo-single-domain magnetite, *Earth and Planetary Science Letters*, *213*, 375-390.

Carvallo, C., D. J. Dunlop, and O. Özdemir (2005), Experimental comparison of FORC and remanent Preisach diagrams, *Geophysical Journal Intational, 162*, 747–754.

Carvallo, C., A. P. Roberts, R. Leohardt, C. Laj, C. Kissel, M. Oerrin, P. Camps (2006), Increasing the efficiency of paleointensity analyses by selection of samples using first-order reversal curve diagrams, *Journal of Geophysical Research*, *111*, B12103, doi:10.1029/2005JB004126, 2006.

Chappell, J., and N. J. Shackleton (1986), Oxygen isotopes and sea level, *Nature*, *324*, 137-140.

Chappell, J. (2002), Sea-level changes forced ice breakouts in the last glacial cycle: New results from coral terraces. *Quaternary Science Reviews*, *21*, 1229–1240.

Chappellaz, J. M., T. Blunier, D. Ratnaud, J. M. Barnola, J. Schwander, and B. Stauffer (1993), Synchronous changes in atmospheric CH_4 and Greenland climate between 40 and 8 kyr BP, *Nature*, *366*, 227-241.

Chough, S. K., and R. Hesse (1985), Contourites from Eirik Ridge, South of Greenland, *Sedimentary Geology*, *41*, 185-199.

Clague, J. J., and T. S. James (2002), History and isostatic effects of the last ice sheet in southern British Columbia, *Quaternary Science Reviews*, *21*, 71–87.

Clarke, R. A. (1984), *Transport through the Cape Farewell Flemish Cap section*, International Council for the Exploration of the Sea Report, *185*, 120-130.

Clark, P.U., R. B. Alley, L. D. Keigwin, J. M. Licciardi, S. J. Johnsen, and H. Wang (1996), Origin of the first global meltwater pulse following the last glacial maximum, *Paleoceanography, 11,* 563-577.

Clark, P. U., J. X. Mitrovica, G. A. Milne, and M. E. Tamisiea (2002), Sea-level fingerprinting as a direct test for the source of global meltwater pulse 1a, *Science, 295*, 2438-2441.

Clemens, S. C. (2005), Millennial-band climate spectrum resolved and linked to centennial-scale solar cycles, *Quaternary Science Reviews*, *24*, 521-531.

Coplen, T. B. (1988), Normalisation of oxygen and hydrogen isotope data, *Chemical Geology (Isotope Geoscience Section), 72,* 293-297.

Coplen, T. B. (1994), Reporting of stable hydrogen, carbon, and oxygen isotopic abundances, *Pure and Applied Chemistry, 66,* 273-276.

Cortijo, E., L. Labeyrie, L.Vidal, M. Vautravers, M. Chapman, J.-C. Duplessy, M. Elliot, M. Arnold, J.-L.Turon, and G. Auffret, G. (1997), Changes in sea surface hydrology associated with Heinrich event 4 in the North Atlantic Ocean between 40° and 60°N. *Earth and Planetary Science Letters*, *146***,** 29–45.

Cortijo, E., L. Labeyrie, M. Elliot, E. Balbon, and N. Tisnerat (2000), Rapid climatic variability of the North Atlantic Ocean and global climate: a focus of the IMAGES program, *Quaternary Science Reviews*, *19*, 227-241.

Craig, H. (1957), Isotopic standards for carbon and oxygen and correction factors for mass-spectrometric analysis of carbon dioxide, *Geochimica et Cosmochimica Acta, 12,* 53-92.

Craig, H., and L. I. Gordon (1965), Isotope oceanography: deuterium and oxygen 18 variations in the ocean and the marine atmosphere. *University of Rhode Island Occasional Publications, 3,* 277-374.

Croudace, I.W., A. Rindby, and R. G. Rothwell, (2006) ITRAX: description and evaluation of a new multi-function X-ray core scanner. In, Rothwell, R.G. (ed.) *New techniques in sediment core analysis.* London, UK, Geological Society of London, 51-63. (Geological Society Special Publication 267).

Cuffey, K. M., and G. D. Clow (1997), Temperature, accumulation, and ice sheet elevation in central Greenland through the last deglacial transition, *Journal of Geophysical Research*, *102*, 383-396.

Curry, W. B., T. M. Marchitto, J. F. McManus, D. W. Oppo, and K. L. Laarkamp (1999), Millennial-scale Changes in Ventilation of the Thermocline, Intermediate, and Deep Waters of the Glacial North Atlantic. In *Mechanisms of Global Climate Change at Millennial Time Scales*, edited by Clark, P. U., Webb, R.S. & Keigwin, L.D., pp. 59-76, American Geophysical Union, New York.

Cutler, K. B., R. L. Edwards, F. W. Taylor, H. Cheng, J. Adkins, C. D. Gallup, P. M. Cutler, G. S. Burr, and A. L. Bloom (2003), Rapid sea-level fall and deep-ocean temperature change since the last interglacial Period, *Earth and Planetary Science Letters*, *206*, 253–271.

Dahl-Jensen, D., K. Mosegaard, N. Gundestrup, G. D. Clow, S. J. Johnsen, A. W. Hansen, and N. Balling (1998), Past Temperatures Directly from the Greenland Ice Sheet, *Science*, *282*, 268-271.

Dansgaard, W., J. W. C. White, and S. J. Johnsen (1989), The abrupt termination of the Younger Dryas climate event, *Nature*, *339*, 532-534.

Dansgaard, W., S. J. Johnsen, H. B. Clausen, D. Dahl-Jensen, N. S. Gundestrup, C. U. Hammer, C. S. Hvidberg, J. P. Steffensen, A. E. Sveinbjörnsdottir, J. Jouzel, and G. Bond (1993), Evidence for general instability of past climate from a 250-kyr ice-core record, *Nature*, *364*, 218–220.

Darby, D. A., J. F. Bischof, and G. A. Jones (1997), Radiocarbon chronology of depositional regimes in the western Arctic Ocean, *Deep Sea Res*., *Part II*, *44*, 1745– 1757.

Darby, D. A., J. F. Bischof, R. F. Spielhagen, S. A. Marshall, and S. W. Harman (2002), Arctic ice export events and their potential impact on global climate during the late Pleistocene, *Paleoceanography*, *17*, 2, 1025, doi: 1029/2001PA000639/

Darby, D. A. (2003) Sources of sediment found in sea ice form the western Arctic Ocean, new insights into processes of entrainment and drift patterns, *Journal of Geophysical Research*, *108*, doi: 10.129/2002JC001350.

Darling, K. F., and C. M. Wade (2008), The genetic diversity of planktic foraminifera and the global distribution of ribosomal RNA genotypes, *Marine Micropaleontology*, *67*, 216–238

Day, R., M. Fuller, and V. A. Schmidt (1977), Hysteresis properties of titanomagnetites: Grain size and composition dependence, *Phys. Earth Planet. Inter.*, *13*, 260– 267.

Denton, G. H., C. J. Heusser, T. V. Lowell, P. I. Moreno, B. G. Andersen, L. E. Heusser, C. Schülchter, and D. R. Marchant (1999), Interhemispheric linkage of paleoclimate during the last glaciation, *Geografiska Annaler*, *81*, 107-153.

Denton, G. H., R. B. Alley, G. C. Comer, and W. S. Broecker (2005), The role of seasonality in abrupt climate change, *Quaternary Science Reviews*, *24*, 1159-1182.

deMenocal, P., J. Ortiz, T. Guilderson, J. Adkins, M. Sarnthein, L. Baker, and M. Yarusinsky (2000), Abrupt onset and termination of the African Humid Period: rapid climate responses to gradual insolation forcing, *Quaternary Science Reviews*, *19*, 347-361.

de Vernal, A., and C. Hilliare-Marcel (2000), Sea-ice cover, sea surface salinity and halo-/thermocline structure of the northwest North Atlantic: Modern versus full glacial conditions, *Quaternary Science Reviews*, *19*, 65-85.

de Vernal, A., C. Hillaire-Marcel, W. R. Peltier, A. J. Weaver (2002), The structure of the upper water column in the northwest North Atlantic: modern vs. Last Glacial Maximum conditions. *Paleoceanography*, *17*, 1050.

de Vernal, A., E. Eynaud, M. Henry, C. Hilliare-Marcel, L. Londeix, S. Magin, J. Matthiessen, F. Marret, T. Radi, A. Rochon, S. Solignac, J.-L. Turon (2005) reconstruction of sea-surface conditions at middle to high latitudes of nthe Northern Hemipshere during the Last Glacial Maximum (LGM) based on dinoflagellate cyst assemblages, *Quaternary Science Reviews*, *24*, 897-924.

Dickson, R. R., and J. Brown (1994), The production of North Atlantic Deep Water: Sources, rates and pathways, *Journal of Geophysical Research,* 99, C6, 12,319-12,341.

Dickson, B., I. Yashayaev, J. Meincke, B. Turrell, S. Dye, and J. Holfort (2002), Rapid freshening of the deep North Atlantic Ocean over the past four decades, *Nature*, *416*, 832-837.

Ditlevsen, P. D. (1999), Observation of α-stable noise induced millennial climate changes from an ice-core record, *Geophys. Res. Lett.*, *26*, 1441-1444.

Dittert, N., K. H. Baumann, T. Bickert, R. Henrich, R. Huber, H. Kinkel, and H. Meggers (1999), Carbonate dissolution in the deep-sea, Methods, quantification and paleoceanographic application, In *Fischer, G. & Wefer, G., (Eds.), Use of proxies in paleoceanography, Berlin (Springer)*, 255-284.

Dokken, T. M. J., and E. Jansen (1999), Rapid change in the mechanism of ocean convection during the last glacial period, *Nature*, *401*, 458-461.

Dokken, T. M. J., and K. H. Nisancioglu (2004), Fresh angle on the polar seesaw, *Nature*, *430*, 842-843.

Dowdeswell, J. A., M. A. Maslin, J. T. Andrews, and I. N. McCave (1995), Iceberg production, debris rafting, and the extent and thickness of Heinrich layers (H-1, H-2) in North Atlantic sediments, *Geology*, *23*, 301-304.

Dowdeswell, J. A., A. Elverhoi, J. T. Andrews, and D. Hebbeln (1999), Asynchronous deposition of ice rafted layers in the Nordic Seas and North Atlantic Ocean, *Nature*, *400*, 348-351.

Dunlop, D. J. (1979), On the use of Zijderveld vector diagrams in multicomponent paleomagnetic studies, *Physics of The Earth and Planetary Interiors, 20, 1,* 12-24.

Dunlop, D. J. (1986), Hysteresis properties of magnetite and their dependence on particle size: A test of pseudo-single-domain remanence models, *Journal of Geophysical Research, 91(b9),* 9569-9584.

Dunlop, D. J., M. F. Westcott-Lewis, and M. E. Bailey (1990), Preisach diagrams and anhysteresis: do they measure interactions?, *Physics of The Earth and Planetary Interiors, 65,* 1-2, 62-77.

Dunlop, D. J. (2002a), Theory and application of the Day plot (M_{rs}/M_s versus H_{cr}/H_c) 1. Theoretical curves and tests using titanomagnetite data, *Journal of Geophysical Research*, *107*, B3, doi:10.1029/2001JB000486.

Dunlop, D. J. (2002b), Theory and application of the Day plot (M_{rs}/M_s versus H_{cr}/H_c) 2. Application of data to rocks, sediments and soils, *Journal of Geophysical Research*, *107*, B3, doi:10.1029/2001JB000487, 2002.

Duplessy, J. C., P. Blanc, and A. W. H. Bé (1981), Oxygen-18 enrichment of planktonic foraminifera due to gametogenic calcification below the euphotic zone, *Science, 213,* 1247-1250.

Duplessy, J.-C., N. J. Shackleton, R. K. Matthews, W. Prell,W. F. Ruddiman, M. Caralp, and C. H. Hendy (1984), $\delta^{13}C$ record of benthic foraminifera in the last interglacial ocean: Implications for the carbon cycle and the global deep water circulation, *Quaternary Research*, *21*, 225–243.

Duplessy, J.-C., N. J. Shackleton, R. G. Fairbanks, L. Labeyrie, D. Oppo, and N. Kallel (1988), Deep water source variations during the last climatic cycle and their impact on the global deepwater circulation, *Paleoceanography*, *3*, 343–360.

Duplessy, J. -C., L. Labeyrie, A. Julliet-Leclerc, F. Maitre, J. Duprat and M. Sarthein (1991), Surface salinity reconstruction of the North Atlantic Ocean during the last glacial maximum, *Oceanologica Acta*, *14*, *4*, 311-324.

Duplessy, J.-C., L. Labeyrie, and C. Waelbroeck (2002), Constraints on the ocean oxygen isotopic enrichment between the Last Glacial Maximum and the Holocene: Paleoceanographic implications, *Quaternary Science Reviews*, *21*, 315–330.

Dyke, A. S., J. T. Andrews, P. U. Clark, J. H. England, G. H. Miller, J. Shaw, and J. J. Veillette (2002), The Laurentide and Innuitian ice sheets during the Last Glacial Maximum, *Quaternary Science Reviews, 21*, 9-31.

Ebbesen, H., and M. Hald (2004), Unstable Younger Dryas climate in the northeast North Atlantic, *Geology*, *32*, 673-676.

Edwards, R. L., J. W. Beck, G. S. Burr, D. J. Donahue, J. M. A. Chappell, A. L. Bloom, E. R. M. Druffel, and F. W. Taylor, (1993), A large drop in atmospheric $^{14}C/^{12}C$ and reduced melting in the Younger Dryas, documented with ^{230}Th ages of corals, *Science*, *260*, 962–968.

Einstein, H. A., and R. B. Krone (1962), Experiments to determine modes of cohesive sediment transport in salt water, *Journal of Geophysical Research*, *67*, 1451–1461.

Elliot, M., L. Labeyrie, G. Bond, E. Cortijo, J.-L. Turon, N. Tisnerat, and J.-C., Duplessy (1998), Millennial-scale iceberg discharges in the Irminger Basin during the last glacial period: Relationship with Heinrich events and environmental settings, *Paleoceaongraphy*, *13*, 433-446.

Elliot, M., L. Labeyrie, and J.-C. Duplessy (2002), Changes in North Atlantic deep-water formation associated with Dansgaard-Oeschger temperature oscillations (60-10 ka), *Quaternary Science Reviews*, *21*, 1153-1165.

Emiliani, C. (1955), Pleistocene temperatures, *Journal of Geology, 63,* 538-578

EPICA Community Members (2006), One-to-one coupling of glacial climate variability in Greenland and Antarctica, *Nature*, *444*, 195-198, doi:10.1038/nature05301.

Epstein, S., R. Buchsbaum, H. A. Lowenstam, H. C. Urey (1953), Revised carbonate-water isotopic temperature scale. *Geological Society of America Bulletin*, *64*, 1315-1325.

Evans, M. E., and F. Heller (2003), *Environmental Magnetism: Principles and Applications of Enviromagnetics*, Academic Press, 2003, ISBN 0122438515, 9780122438516 pp. 66-69.

Fabian, K., A. Kirchner, W. Williams, F. Heider, T. Leibl, and A. Huber (1996), Three-dimensional micromagnetic calculations for magnetite using FFT, *Geophysical Journal International, 124, 1,* 89-104.

Fairbanks, R. G. (1989), A 17,000-year glacio-eustatic sea level record: Influence of glacial melting rates on the Younger Dryas event and deep-ocean circulation, *Nature*, *342*, 637-642.

Fairbanks, R. G. (1990), The age and origin of the Younger Dryas climate event in Greenland ice cores, *Paleoceanography*, *5*, 937-948.

Fairbanks, R. G., R. A. Mortlock, T.-C. Chiu, L. Cao, A. Kaplan, T. P. Guilderson, T. W. Fairbanks, A. L. Bloom, P. M. Grootes, and M.-J. Nadeau (2005), Radiocarbon calibration curve spanning 0 to 50,000 years BP based on paired $^{230}Th/^{234}U/^{238}U$ and ^{14}C dates on pristine corals, *Quat. Sci. Rev.*, *24*, 1781-1796.

Flower, B. P., D. W. Hastings, H. W. Hill, and T. M. Quinn (2004), Phasing of deglacial warming and Laurentide Ice Sheet meltwater in the Gulf of Mexico, *Geology, 32,* 597-600.

Flückiger, J., R. Knutti, and J. W. C. White (2006), Oceanic processes as potential trigger and amplifying mechanisms for Heinrich events, *Paleoceanography*, *21*, PA2-14, doi:10.1029/2005PA001204.

Friedrich, M., B. Kromer, K. F. Kaiser, M. Spurk, K. A. Hughen, and S. J. Johnsen (2001), High-resolution climate signals in the Bølling/Allerød Interstadial (Greenland Interstadial 1) as reflected in European tree-ring chronologies compared to marine varves and ice-core records, *Quaternary Science Reviews*, *20*, 1223-1232.

Fuhrer, K., A. Neftel, M. Anklin, and V. Maggi (1993), Continuous measurements of hydrogen peroxide, formaldehyde, calcium and ammonium concentrations along the new GRIP ice core from Summit, Central Greenland. *Atmospheric Environment*, *27A*, 12, 1873–1880.

Ganopolski, A., S. Rahmstorf, V. Petoukhov, and M. Claussen (1998), Simulation of modern and glacial climates with a coupled global model of intermediate complexity, *Nature*, *391*, 351-356.

Ganopolski, A., and S. Rahmstorf (2001), Rapid changes of glacial climate simulated in a coupled climate model, *Nature*, *409*, 153–158.

Ganopolski, A., and S. Rahmstorf (2002), Abrupt glacial climate changes due to stochastic resonance, *Phys. Rev. lett.*, *88*, 3, 038501, doi:10.1103/PhysRevLett.88.038501.

Ganachaud, A., and C. Wunsch (2000), Improved estimates of global ocean circulation, heat transport and mixing from hydrographic data, *Nature*, *389*, 453-457.

Ganssen, G. M., and D. Kroon (2000), The isotopic signature of planktonic foraminifera from NE Atlantic surface sediments: implications for the reconstruction of past oceanic conditions, *Journal of the Geological Society*, *157*, 693-699

Garlick, G. D. (1974), The stable isotopes of oxygen, carbon, and hydrogen in the marine environment, *The Sea, v. 5 (ed. E. D. Goldberg), John Wiley & Sons, New York,* 393-425.

Gasse, F., and E. van Campo (1994), Abrupt post-glacial climate events in West Asia and North Africa monsoon domains, *Earth and Planetary Science Letters*, *126*, 435-456.

Gasse, F. (2000), Hydrological changes in the African tropics since the Last Glacial Maximum, *Quaternary Science Reviews*, *19*, 189-211.

Genty D., D. Blamart, R. Ouahdi, M. Gilmour, A. Baker, J. Jouzel, and S. Van-Exter (2003), Precise dating of Dansgaard–Oeschger climate oscillations in western Europe from stalagmite data, *Nature*, *421*, 833-837.

Gherardi, J. M., L. Labeyrie, J. F. McManus, R. Francois, L. C. Skinner, and E. Cortijo (2005), Evidence from the Northeastern Atlantic basin for variability in the rate of the meridional overturning circulation through the last deglaciation, *Earth Planetary Science Letters*, *240*, 710–723.

GEBCO Digital Atlas: IOC, IHO, and BODC (2003), "Centenary Edition of the GEBCO Digital Atlas", published on CD-ROM on behalf of the Intergovernmental Oceanographic Commission and the International Hydrographic Organization as part of the General Bathymetric Chart of the Oceans; British Oceanographic Data Centre, Liverpool.

Gildor, H., and E. Tziperman (2003), Sea ice switches and abrupt climate change, *Philosophical Transactions of the Royal Society A*, *361*, 1935-1944.

Giraudi, C., and Frezzotti, M. (1997) Late Pleistocene glacial events in the Central Apennines, Italy, *Quaternary Research, 48*, 280-290.

Goree,W.S., and M. Fuller (1976), Magnetometers using RF-driven squids and their applications in rock magnetism and paleomagnetism, *Reviews of Geophysics, Space Physics, 14*, 591–608.

Gregory, J. M., O. A. Saenko, and A. J. Weaver (2003), The role of the Atlantic freshwater balance in the hysteresis of the meridional overturning circulation, *Climate Dynamics*, *21*, 707-717.

Grimm, E. C., G. L Jacobson Jr., W. A. Watts, B. C. S. Hansen, and K. A. Maash (1993), A 50,000-yr record of climate oscillations from Florida and its temporal correlation with the Heinrich events, *Science*, *261*, 198-200.

Grootes, P. M., M. Stuiver, J. W. C. White, S. Johnson, and J. Jouzel (1993), Comparison of oxygen isotope records from the GISP2 and GRIP Greenland ice cores, *Nature*, 366, 552-554.

Grootes, P. M., and M. Stuiver (1997), Oxygen 18/16 variability in Greenland snow and ice with 10^{-3}-10^{-5}-year resolution, *Journal of Geophysical Research*, *102*, 455-426, 470.

Grossman, E. L. (1987), Stable isotopes in modern benthic foraminifera: a study of vital effect. *Journal of Foraminiferal Research*, *17*, *1*, 48-61.

Grousset, F. E., L. Labeyrie, J. A. Sinko, M. Cremer, G. Bond,J. Duprat, E. Cortijo, and S. Huon (1993), Patterns of icerafted detritus in the glacial North Atlantic (40 – 55°N), *Paleoceanography*, *8*, 2, 175–192.

Grousset, F. E., C. Pujol, L. Labeyrie, G. Auffret and A. Boelaert (2000), Were the North Atlantic Heinrich events triggered by the behaviour of the European ice sheets? *Geology*, *28*; 123-126.

Grousset, F. E., E. Cortijo, L. Herve, T. Richter, D. Burdloff, J. Duprat, and O. Weber (2001), Zooming in on Heinrich layers, *Paleoceanography*, *16*, 240-259.

Guillou, H., B. S. Singer, C. Laj, C. Kissel, S. Scaillet, and B. R. Jicha (2004), On the age of the Laschamp geomagnetic excursion, *Earth and Planetary Science Letters*, *227*, 331– 343.

Hagen, S., and M. Hald (2002), Variation in surface and deep water circulation in the Denmark Strait, North Atlantic, during marine isotope stages 3 and 2, *Paleoceanography*, *17*, 4, 1061, doi:10.1029/2001PA000632.

Hall, I. R., I. N. McCave, N. J. Shackleton, G. P. Weedon, and S. E. Harris (2001), Intensified deep Pacific inflow and ventilation during Pleistocene glacial times, *Nature*, *412*, 809–812.

Hall, I. R., S. B. Moran, R. Zahn, P. C. Knutz, C.-C. Shen, and R. L. Edwards (2006), Accelerated drawdown of meridional overturning in the late-glacial Atlantic triggered by transient pre-H event freshwater perturbation, *Geophysical Research Letters*, *33*, L16616 doi:10.1029/2006GL026239.2006.

Hamilton, C.P., H. J. Spero, J. Bijma, and D. W. Lea (2008), Geochemical investigation of gametogenic calcite addition in the planktonic foraminifera *Orbulina universa*, *Marine Micropaleontology, 68, 3-4*, 256-267.

Hanebuth, T., K. Stattegger, and P. M. Grootes (2000), Rapid flooding of the Sunda shelf: A late-glacial sea-level record, *Science*, *288*, 1033-1035.

Hansen, L. (2004), Deltaic Infill of a deglaciated Arctic Fjord, East Greenland: Sedimentary Facies and Sequence Stratigraphy, *Journal of Sedimentary Research*, *74*, 3, 422-437.

Hansen, J., M. Sato, P. Kharecha, G. Russell, D. W. Lea, and M. Siddall (2007), Climate change and trace gases, *Phil. Trans. R. Soc. A*, *365*, 1925–1954.

Haug, G. H., K. A. Hughen, D. M. Sigman, L. C. Peterson, U. Rohl (2001), Southward Migration of the Intertropical Convergence Zone Through the Holocene, *Science*, *293*, 1304.

Heinrich, H. (1988), Origin and Consequences of Cyclic Ice Rafting in the Northeast Atlantic Ocean during the Past 13,000 Years, *Quaternary Research*, *29*, 142-152.

Hemming, S. R., and I. Hajdas (2003), Ice rafted detritus evidence from 40Ar/39Ar ages of individual hornblende grains for evolution of the southeastern Laurentide ice sheet since 43 ^{14}C ky, *Quat. Int.*, *99–100*, 29–43.

Hemming, S. R., G. C. Bond, W. S. Broecker, W. D. Sharp, and M. Klas-Mendelson (2002), Evidence from $^{40}Ar/^{39}Ar$ Ages of Individual Hornblende Grains for Varying Laurentide Sources of Iceberg Discharges 22,000 to 10,500 yr B.P., *Quaternary Research*, *54*, 372-383.

Hemming, S. R. (2004), Heinrich Events: Massive Late Pleistocene detritus layers of the North Atlantic and their global imprint, *Rev. Geophys.*, *42*, 1-43.

Hendy, I. L., and J. P. Kennett (1999), Latest Quaternary North Pacific surface-water responses imply atmosphere-driven climate instability, *Geology*, *27*, 4, 291-294.

Hendy, I. L., and J. P. Kennett (2003), Tropical forcing of North Pacific intermediate water distribution during Late Quaternary rapid climate change?, *Quaternary Science Reviews*, *22*, 673-689.

Hendy, I. L., and T. Cosma, (2008), Vulnerability of the Cordilleran Ice Sheet to iceberg calving during late Quaternary rapid climate change events, *Paleoceanography*, 23, PA2101, doi:10.1029/2008PA001606.

Hendry, J. P., M. Wilkinson, A. E. Fallick, and R. S. Haszeldine (2000), Ankerite Cementation in Deeply Buried Jurassic Sandstone Reservoirs of the Central North Sea, *Journal of Sedimentary Research*, *70*, 1, 227-239.

Hesse, R., and S. K. Chough (1980), The Northwest Atlantic Mid-Ocean Channel of the Labrador Sea: II. Deposition of parallel laminated levee mud from the viscous sublayer of low-density turbidity currents, *Sedimentology*, 27, 697–711.

Hesse, R., and S. Khodabakhsh (1998), Depositional facies of late Pleistocene Heinrich events in the Labrador Sea, *Geology*, *26*, 2, 103-106.

Hesse, R., I. Klauke, W. B. F. Ryan, M. B. Edwards, D. J. W. Piper, and NAMOC Study Group (1996), Imaging Laurentide ice sheet drainage into the deep sea: impact on sediments and bottom water, *Geological Society of America Today*, 3–9.

Hesse R., I. Klauck, S. Khodabakhsh, and D. Piper (1999), Continental slope sedimentation adjacent to an ice margin. III. The upper Labrador Slope, *Marine Geology*, *155*, 249–276.

Hesse R., H. Rashid, and S. Khodabakhsh (2004), Fine-grained sediment lofting from meltwater-generated turbidity currents during Heinrich events, *Geology*, *32*, 5, 449-452.

Hill, H. W., B. P. Flower, T. M. Quinn, D. J. Hollander, and T. P. Guilderson (2006), Laurentide Ice Sheet meltwater and abrupt climate change during the last glaciation, *Paleoceanography*, *21*, PA1006, doi:10.1029/2005PA001186.

Hilliare-Marcel, C., A. de Vernal, G. Bilodeau, and G. Wu (1994), Isotope stratigraphy, sedimentation rates, deep circulation, and carbonate events in the Labrador Sea during the last ~200 ka, *Canadian Journal of Earth Science*, *31*, 63-89.

Hilliare-Marcel, C., and G. Bilodeau (2000), Instabilities in the Labrador Sea water mass structure during the last climatic cycle, *Canadian Journal of Earth Science*, *37*, 795-809.

Hilliare-Marcel, C. and A. de Vernal (2008), Stable clue to episodic sea ice formation in the glacial North Atlantic, *Earth and Planetary Science Letters*, *268*, 143-150.

Hjelstuen, B. O., H. P. Sejrup, H. Haflidason, A. Nygård. I. M. Berstad, and G. Knorr (2004), Late Quaternary seismic stratigraphy and geological devolpment of the south Vøring margin, Norwegian Sea, *Quaternary Science Reviews*, *23*, 1847-1865.

Hollister, C. D., and I. N. McCave (1984), Sedimentation under deep-sea storms, *Nature*, *309*, 220–225.

Huang, E., and J. Tian (2008), Melt-Water-Pulse (MWP) events and abrupt climate change of the last deglaciation, *Chinese Science Bulletin*, *53*, 18, 2867-2878.

Hughen, K.A., J. T. Overpeck, L. C. Peterson, S. Trumbore (1996), Rapid climate changes in the tropical Atlantic region during the last deglaciation, *Nature 380*, 51-54.

Hughen, K. A., J. Overpeck, S. J. Lehman, M. Kashgarian, J. Southon, L. C. Peterson, R. Alley, and D. M. Sigman (1998), Deglacial changes in ocean circulation from an extended radiocarbon calibration, *Nature*, *391*, 65-68.

Hughen, K. A., J. Southon, S. J. Lehman, and J. Overpeck (2000), Synchronous radiocarbon and climate shifts during the last deglaciation, *Science, 290*, 1951-1954.

Hughen, K. A., S. J. Lehman, J. Southon, J. Overpeck, O. Marchel, C. Herring, and J. Turnbull (2004), ^{14}C activity and global carbon cycle changes over the past 50,000 years, *Science*, *303*, 202-207.

Hulbe, C. L. (1997), An ice shelf mechanism for Heinrich layer production, *Paleoceanography*, *12*, 5, 711–717.

Hulbe, C. L., D. R. MacAyeal, G. H. Denton, J. Kleman, and T. V. Lowell (2004), Catastrophic ice shelf breakup as the source of Heinrich event icebergs, *Paleoceanography*, *19*, PA1004, doi:10.1029/2003PA000890.

Hunter, S. E., D. Wilkinson, J. D. Stanford, D. A. V. Stow, S. Bacon, E. J. Rohling, A. M. Akhetmetzhanov, and N. H. Kenyon (2007a), *The Eirik Drift: a long-term barometer of North Atlantic deepwater flux south of Cape Farewell, Greenland*. In: Viana, A. R., and M. Rebesco (Eds) *Economic and Palaeoceanographic Significance of Contourite Deposits*, Geological Society Special Publications, *276*, 245-263.

Hunter, S. E., D. Wilkinson, E. Louarn, I. N. McCave, E. J. Rohling, D. A. V. Stow, and S. Bacon (2007b), Deep western boundary current dynamics and associated sedimentation on the Eirik Drift, Southern Greenland Margin, *Deep-Sea Research I*, *54*, 2036-2066.

Huybers, P. (2004), Comments on 'Coupling of the hemispheres in observations and simulations of glacial climate changes' by A. Schmittner, O. A. Saenko and A. J. Weaver', *Quaternary Science Reviews*, *23*, 207-212.

Imbrie, J., Boyle, E., S. Clemens, A. Duffy, W. Howard, G. Kukla, J. Knutzbach, D. Martinson, A. McIntyre, A. Mix, B. Molfino, J. Morley, L. Peterson, N. Piais, W. Prell, M. Raymo, N. Shackleton, and J. Toggweiler (1984), On the Structure and Origin of Major Glaciation Cycles. Linear responses to Milankovitch forcing, *Paleoceanography*, *7*, 701-738.

Imbrie, J., A. C. Mix, and D. Martinson, G. (1993), Milankovitch theory viewed from Devil's Hole, *Nature*, *363*, 531-533.

Ivy-Ochs S., J. Schäfer, P. W. Kubik, H. –A. Synal, C. Schlüchter (2004), The timing of deglaciation on the northern Alpine foreland (Switzerland), *Eclogae Geologicae Helvetiae*, *97*, 47–55.

Ivy-Ochs, S., H. Kerschener, P. W. Kubik, and C. Schlüchter (2006), Glacier response in the European Alps to Heinrich event 1 cooling: the Gschnitz stadial, *Journal of Quaternary Science*, *21*, 2, 115-130.

Jansen, J. H. F., S. J. Van der Gaast, A. J. Vaars (1998), CORTEX, a shipboard XRF-scanner for element analyses in split sediment cores, *Marine Geology*, *151*, 143-153.

Jenkins, R., and J. L. De Vries, (1970), *Practical X-ray Spectrometry*, MacMillan, London, pp. 1–190.

Jennings, A. E., M. Hald, M. Smith, and J. T. Andrews (2006), Freshwater forcing from the Greenland Ice Sheet during the Younger Dryas: Evidence from southeastern Greenland shelf cores, *Quaternary Science Reviews*, *25*, 282-298.

Johnsen, S. J., D. Dahl-Jensen, N. Gundestrup, J. P. Steffensen, H. B. Clausen, H. Miller, V. Masson-Delmotte, A. E. Sveinbjörndottir, and A. J. White (2001), Oxygen isotope and palaeotemperature records from six Greenland ice-core stations: Camp Century, Dye-3, GRIP, GISP2, Renland and NorthGRIP, *Journal of Quaternary Science*, *16*, 299-307.

Johnson, R.G., and S. E. Lauritzen (1995), Hudson Bay–Hudson Strait jokulhlaups and Heinrich events—a hypothesis, *Palaeogeography*, *Palaeoclimatology*, *Palaeoecology*, *117* (1–2), 123–137.

Jonsson, S., and H. Valdimarsson (2004), A new path for the Denmark Strait overflow water from the Iceland Sea to Denmark Strait, *geophysical Research Letters*, *31*, L03305, doi:10.1029/2003GL019214.

Jouzel, J., N. I. Barkov, J. M. Barnola, M. Bender, J. Chappellaz, C. Genthon, V. M. Kotlyakov, V. Y. Lipenkov, C. Lorius, J. R. Petit, D. Raynaud, G. Raisbeck, C. Ritz, T. Sowers, M. Stievenard, F. Yiou, and P. Yiou (1993), Extending the Vostok ice-core record of palaeoclimate to the penultimate glacial period, *Nature*, *364*.

Julien, E., F. E. Grousset, S. R. Hemming, V. L. Peck, I. R. Hall, C. Jeantet, I. Billy (2006), Contrasting conditions preceding MIS3 and MIS2 Heinrich events, *Global and Planetary Change*, *54*, 225-238.

Kageyama, M., O. Peyron, S. Pinto, P. Tarasov, J. Guiot, J., Joussaume, and G. Ramstein, (2001), The Last Glacial Maximum climate over Europe and western Siberia: a PMIP comparison between models and data. *Climate Dynamics* , *17*, 23–43.

Kandiano, E. S., and H. A. Bauch (2002), Implications of planktic foraminiferal size fractions for the glacial-interglacial paleoceanography of the Polar North Atlantic, *Journal of Foraminiferal Research*, *32*, 245-251.

Kanfoush, S. L., D. A. Hodell, C. D. Charles, T. P. Guilderson, P. G. Mortyn, U. S. Ninnemann (2000), Millennial-Scale Instability of the Antarctic Ice Sheet During the Last Glaciation, *Science*, *288*, 1815 – 1819.

Keigwin, L. D., and S. J. Lehman (1994), Deep circulation change linked to HEINRICH event 1 and Younger Dryas in a mid-depth North Atlantic core, *Paleoceanography*, *9*, 185-194.

Keigwin, L. D., and E. A. Boyle (2008), Did the North Atlantic overturning halt 17,000 years ago?, *Paleoceanography*, *23*, PA1101, doi:10.1029/2007PA001500.

Keigwin, L. D., G. A. Jones, S. J. Lehman, and E. A. Boyle (1991), Deglacial meltwater discharge, North Atlantic deep circulation and abrupt climate change, *J. Geophys. Res*., *96*, 16,811 –16,826.

Kent, D. V., S. R. Hemming, and B. D. Turrin (2002), Laschamp Excursion at Mono Lake?, *Earth and Planetary Science Letters, 197, 3-4,* 151-164.

Kenyon, N. H., M. K. Ivanov, A. M. Akhmetzhanov, E. V. Kozlova, and A. Mazzini (2004), Interdisciplinary studies of North Atlantic and Labrador Sea Margin Architecture and Sedimentary Processes, *Rep. 68*, UNESCO.

Kido, Y., T. Koshikawa, R. Tada (2006), Rapid and quantitative major element analysis method for wet fine-grianed sediments using an XRF microscanner, *Marine Geology*, *229*, 209-225.

Kiefer, T., M. Sarnthein, H. Erlenkeusser, P. M. Grootes, and A. P. Roberts (2001), North Pacific response to millennial-scale changes in ocean circulation over the last 60 kyr, *Paleoceanography*, *16*, 179-189.

Kiefer, T., and M. Kienast (2005), Patterns of deglacial warming in the Pacific Ocean: a review with emphasis on the time interval of Heinrich event 1, *Quaternary Science reviews*, *24*, 1063-1081.

Kienast, M., T. J. J. Hanebuth, C. Pelejero, and S. Steinke (2003), Synchroneity of meltwater pulse 1a and the Bølling warming: New evidence from the South China Sea, *Geology*, *31*, 67-70.

Kim, S.-T., and J. R. O'Neil (1997), Equilibrium and nonequilibrium oxygen isotope effects in synthetic carbonates, *Geochimica et Cosmochimica Acta*, *91*, 3461-3475.

Kim, J. H., R. R. Schneider, P. J. Muller, and G. Wefer (2002), Interhemispheric comparison of deglacial sea-surface temperature patterns in Atlantic eastern boundary currents, *Earth Planet. Sci. Lett.*, *203*, 779–780.

King, J. W., S. K. Banerjee, J. Marvin, and O. Ozdemir (1982), Comparison of different magnetic methods for determining the relative grain size of magnetite in natural materials: Some results from lake sediments, *Earth and Planetary Science Letters, 59,* 404-419.

Kissel, C., C. Laj, B. Lehman, L. Labyrie, and V. Bout-Roumazeilles (1997), Changes in the strength of the Iceland-Scotland Overflow Water in the last 200,000 years: Evidence from magnetic anisotropy analysis of core SU90-33, *Earth Planet. Sci. Lett.*, *152*, 25-36.

Kissel, C., C. Laj, L. Labeyrie, T. Dokken, A. Voelker, and D. Blamart (1999a), Magnetic signatures of rapid climatic variations in North Atlantic sediments. in *Reconstructing Ocean History: A Window into the Future*, edited by Mix, A., pp. 419-437, Kluwer Academic/Plenum Publishers, New York.

Kissel, C., C. Laj, L. Labeyrie, T. Dokken, A. Voelker, and D. Blamart (1999b), Rapid climatic variations during marine isotopic stage 3: Magnetic analysis of sediments from Nordic Seas and North Atlantic, *Earth Planet. Sci. Lett.*, *171*, 489-502.

Knorr, G., and Lohmann (2003), Southern ocean origin for the resumption of Atlantic thermohaline circulation during deglaciation, *Nature*, *424*, 532-536.

Knorr, G., and G. Lohmann (2007), Rapid transitions in the Atlantic thermohaline circulation triggered by global warming and meltwater during the last deglaciation, *Geochemistry, Geophysics, Geosystems*, *8*, 12, Q12006, doi: 10.1029/2007C001604.

Knutti, R., J. Flückiger, F. T. Stocker, and A Timmermann (2004), Strong hemispheric coupling of glacial climate through freshwater discharge and ocean circulation, *Nature*, *430*, 851-856.

Knutz, P. C., W. E. N. Austin, and E. J. W. Jones (2001), Millennial-scale depositional cycles related to British Ice Sheet variability and North Atlantic paleocirculation since 45 yr B. P., Barra Fan, U. K. margin, *Paleoceanography*, *16*, 53-64.

Knutz, P. C., E. J. W. Jones, W. E. N. Austin, and T. C. E. van Weering (2002), Glacimarine slope sedimentation , contourite drifts and bottom current pathways on the Barra Fan, UK North Atlantic margin, *Marine Geology*, *188*, 129-146.

Knutz, P. C., R. Zahn, and I. R. Hall (2007), Centennial-scale variability of the British Ice Sheet: Implications for climate forcing and Atlantic meridional overturning circulation during the last deglaciation, *Paleoceanography*, *22*, PA1207, doi:10.1029/2006PA001298, 2007.

Krajewski, K. P. (2002), Catagenic ankerite replacing biogenic calcite in the Marhøgda Bed (Jurassic), Sassenfjorden, Spitsbergen. *Polish Polar Research*, *23*, 85–99.

Krajewski, K. P (2004), Carbon and oxygen isotopic survey of diagenetic carbonate deposits in the Agardhfjellet Formation (Upper Jurassic), Spitsbergen: preliminary results, *Polish Polar Research*, *25*, 1, 27-43.

Krajewski K. P., B. Łącka, M. Kuźniarski , R. Orłowski,and A. Prejbisz (2001) Diagenetic origin of carbonate in the Marhøgda Bed (Jurassic) in Spitsbergen, Svalbard, *Polish Polar Research*, *22*, 89–128.

Kroon, D., and K. Darling (1995), Size and upwelling control of the stable isotope composition of *Neogloboquadrina dutertrei* (d'Orbigny), *Globigerinoides ruber* (d'Orbigny), *Globigerina bulloides* (d'Orbigny): examples from the Panama Basin and Arabian Sea. *Journal of Foraminiferal Research, 25, 1*, 39-52.

Kroon, D., W. E. N. Austin, M. R. Chapman, G. M. Ganssen (1997), Deglacial surface circulation changes in the northeastern Atlantic: Temperature and salinity records off NW Scotland on a century scale, *Paleoceanography*, *12*, 755-763.

Kukla G. J., F. Heller, X. M. Liu, T. C. Xu, T. S. Liu, Z. S. An (1988), Pleistocene climates in China: dating by magnetic susceptibility, *Geology, 16*, 811-814.

Kukla, G., Z. S. An, J. L. Melice, J. Gavin and J. L. Xiao (1990), Magnetic susceptibility record of the Loess Plateau of central China during the last 130,000 years, *Quaternary Research, 36,* 29-36.

Labeyrie, L., J. -C. Duplessy, and P. L. Blanc (1987), Variations in marine carbonate sediment as indicators of ocean deep waters over the past 125,000 yrs, *Nature*, *327*, 477-482.

Labeyrie, L., L. Vidal, E. Cortijo, M. Paterne, M. Arnold, J. -C. Duplessy, M. Vautravers, M. Labracherie, J. Duprat, J. L. Turon, F. Grousst, and T. van Weering (1995), Surface and deep hydrology of the northern Atlantic Ocean during the past 150,000 years, *Philosophical Transactions, Royal Society London B*, *348*, 255-264.

Lagerklint, I. M., and J. D. Wright (1999), Late glacial warming prior to Heinrich event 1: The influence of ice rafting and large ice sheets on the timing of initial warming, *Geology*, *27*, 1099–1102.

Laj, C., C. Kissel, A. Mazaud, J. E. T. Channell, and J. Beer (2000), North Atlantic palaeointensity stack since 75 ka (NAPIS-75) and the duration of the Laschamp event, *Philosophical Transactions of the Royal Society of London A*, *358*, 1009-1025.

Laj, C., C. Kissel, A. Mazaud, E. Michel, R. Muscheler, and J. Beer (2002), Geomagnetic field intensity, North Atlantic Deep Water circulation and atmospheric $\Delta^{14}C$ during the last 50 kyr, *Earth Planet. Sci. Lett.*, *200*, 177-190.

Laj, C., C. Kissel, and J. Beer (2004), High resolution global paleointensity stack since 75 kyr (GLOPIS-75) calibrated to absolute values. In: Channell, J. E. T., D.V. Kent, W. Lowrie and J.G. Meert, Editors, *Timescales of the Paleomagnetic Field*, *Geophysical Monograph*, *145*, American Geophysical Union, Washington, D.C., pp. 255–265.

Lambeck, K. Y. Yokoyama, and T. Purcell (2002), Into and out of the Last Glacial Maximum: sea-level change during Oxygen Isotope Stages 3 and 2, *Quaternary Science Reviews*, *21*, 343–360.

Lamy, F., J. Kaiser, U. Ninnemann, D. Hebbeln, H. W. Arz, and J. Stoner (2004), Antarctic timing of surface water changes off Chile and Patagonian ice sheet response, *Science*, *304*, 1959-1962.

Lea, D. W., D. K. Pak, L. C. Peterson, and K. A. Hughen (2003), Synchroneity of tropical and high-latitude Atlantic temperatures over the last glacial termination, *Science*, *301*, 1361-1364.

Ledbetter, M. T. (1984), Bottom-current speed in the Vema Channel recorded by particle-size of sediment fine-fraction, *Marine Geology*, *58*, 137–149.

Ledbetter, M. T. (1986), A late Pleistocene time-series of bottom-current speed in the Vema Channel, *Palaeogeography, Palaeoclimatology, Palaeoecology*, *53*, 97–105.

Lehman, S. J., and Keigwin, L. D. (1992), Sudden changes in North Atlantic circulation during the last deglacation, *Nature*, *356*, 757-762.

Lekens, W. A. H., H. P. Sejrup, H. Haflidason, G. Ø. Petersen, B. Hjelstuen, and G. Gnorr (2005), Laminated sediments preceding Heinrich event 1 in the Northern North Seas and Southern Norwegian Sea: Origin, processes and regional linage, *Marine Geology*, *216*, 27-50.

Lekens, W. A. H., H. P. Sejrup, H. Haflidason, J. Knies, and T. Richter (2006), Meltwater and ice rafting in the southern Norwegian Sea between 20 and 40 calendar kyr B.P.: Implications for Fennoscandian Heinrich events, *Paleoceaongraphy*, 21, PA3013, doi:10.1029/2005PA001228.

Levi, S., and S. K. Banerjee (1976), On the possibility of obtaining relative paleointensities from lake sediments, *Earth and Planetary Science Letters, 29,* 219- 226.

Li, C., D. S. Battisti, D. P. Schrag, and E. Tziperman (2005), Abrupt climate shifts in Greenland due to displacements of the sea ice edge, *Geophys. Res. Lett., 32*, L19702, doi:10.1029/2005GL023492.

Licciardi, J. M., P. U. Clark, E. J. Brook, D. Elmore, and P. Sharma (2004), Variable responses of western U.S. glaciers during the last glaciation, *Geology*, *32*, 81-84.

Lindsay, R. W., and J. Zhang (2005), The thinning of Arctic sea ice, 1988–2003: Have we passed a tipping point?, *J. Clim.*, *18*, 4879-4894.

Liu, J. P., and J. Milliman (2004), Reconsidering Melt-water Pulses 1A and 1B: Global Impacts of Rapid Sea-level rise, *Journal of Ocean University of China*, *3*, 2, 183-190.

Lohmann, G., and M. Schulz (2000), Reconciling Bølling warmth with peak deglacial meltwater discharge, *Paleoceanography*, *15*, 5, 537-540.

Lowe, J. J. (2001), Climatic oscillations during the last glacial cycle-nature, causes and the case for synchronous effects, *Biology and Environment, Proceedings of the Royal Irish Academy*, *101B*, 1-2, 19-33.

Lowell, T.V., C. J. Heusser, B. G. Andersen, P. I. Moreno, A. Hauser, L. E. Heusser, C. Schlüchter, D. R. Marchant, and G. H. Denton (1995), Interhemisperic correlation of late Pleistocene glacial events, *Science*, *269*, 1541-1549.

Lowell, T. V., T. G. Fisher, G. C. Comer, I. Hajdas, N. Waterson, K. Glover, H. M. Loope, J. M. Schaefer, V. Rinterknecht, W. Broecker, G. Denton, and J. T. Teller (2005) Testing the Lake Agassiz meltwater trigger for the Younger Dryas, *Eos, Transactions, American Geophysical Union*, *86*, 40, 365-373.

Lundqvist, J., and B. Wohlfarth (2001), Timing and east-west correlation of south Swedish ice marginal lines during the Late Weichselian, *Quaternary Science Reviews*, *20*, 1127-1148.

Lynch-Stieglitz, J., and R. G. Fairbanks (1994), A conservative tracer for glacial ocean circulation form carbon isotope and paleo-nutrient measurements in benthic foraminifera, *Nature*, *369*, 308-310.

Lynch-Stieglitz,J., J. F. Adkins, W. B. Curry, T. Dokken, I. R. Hall, J. C. Herguera, J. J.-M. Hirschi, E. V. Ivanova, C. Kissel, O. Marchal, T. M. Marchitto, I. N. McCave, J. F. McManus, S. Mulitza, U. Ninnemann, F. Peeters, E.-F. Yu, R. Zahn (2007), Atlantic meriidional overturning circulation during the LGM, *Science*, *316*, 66-69.

MacAyeal, D. R. (1993), Binge/purge oscillations of the Laurentide ice sheet as a cause of the North Atlantic's Heinrich events, *Paleoceanography*, *8*, 775–784.

Manabe, S., and R. J. Stouffer (1997), Coupled ocean atmosphere model response to freshwater input: Comparison to Younger Dryas event, *Paleoceanography*, *12*, 321–336.

Manabe, S., and R. J. Stouffer (2000), Study of abrupt climate change by a coupled ocean-atmosphere model, *Quaternary Science Reviews*, *19*, 285-299.

Maqueda, M. A., and S. Rahmstorf (2002), Did Antarctic sea-ice expansion cause glacial CO_2 decline?, *Geophysical Research Letters*, *29*, 1, 1011, doi:10.1029/2001GL013240.

Marchitto, T. M., D. W. Oppo, and W. B. Curry (2002), Paired benthic foraminiferal Cd/Ca and Zn/Ca evidence for greatly increased presence of Southern Ocean Water in the glacial North Atlantic, *Paleoceanography*, *17*, 3, doi:10.1029/2000PA000598.

Marchitto, T. M., S. J. Lehman, J. D. Ortiz, J. Flückiger, and A. van Geen (2007), Marine Radiocarbon Evidence for the Mechanism of Deglacial Atmospheric CO_2 Rise, *Science, 316*, 1456-1459.

Marks, L. (2002), Last glacial maximum in Poland, *Quaternary Science Reviews*, *21*, 103-110.

Marshall, S. J., and M. R. Koutnik (2006), Ice sheet action versus reaction: Distinguishing between Heinrich events and Dansgaard-Oeschger cycles in the North Atlantic¸ *Paleoceanography*, *21*, PA2021, doi:10.1029/2005PA001247.

Martinson, D. G., N. G. Pisias, J. D. Hayes, J. Imbrie, T. C. Moore, and N. J. Shackleton (1987), Age dating and orbital theory of the ice-ages: development of high-resolution 0 to 300,000 year chronostratigraphy, *Quaternary Research*, *27*, 1-29.

Maslin, M., D. Seivdov, and J. Lowe (2001), Synthesis of the Nature and Causes of Rapid Climate Transitions During the Quaternary. in *The Oceans and rapid climate change: past, present and future*, edited by Seidov, D., Haupt, B.J. and Maslin, M., pp. 9-51, American Geohysical Union, 2001, Washington, D.C.

Mauritzen, C. (1996), Production of dense overflow waters feeding the north Atlantic across the Greenland-Scotland Rides. Part1. Evidence for a revised circulation scheme, *Deep Sea Research*, *43*, 6, 769-806.

Mayewski P. A., L. D. Meeker, S. Whitlow, M. S. Twickler, M. C. Morrison, R. B. Alley, P. Bloomfield, and K. Taylor (1993), The Atmosphere During the Younger Dryas, *Science*, *261*, 195-197.

Mayewski, P. A., L. D. Meeker, S. Whitlow, M. S. Twickler, M. C. Morrison, P. Bloomfield, G. C. Bond, R. B. Alley, A. J. Gow, P. M. Grootes, D. A. Meese, M. Ram, K. C. Taylor, and W. Wumkes (1994), Changes in Atmospheric Circulation and Ocean Ice Cover over the North Atlantic During the Last 41,000 Years, *Science*, *263*, 1747-1751.

Mayewski, P. A., L. D. Meeker, M. S. Twickler, S. Whitlow, Q. Yang, B. Lyons, and M. Prenice (1997), Major features and forcing of high-latitude northern hemisphere atmospheric circulation using a 110,000-year-long glaciochemical series, *Journal of Geophysical Research*, *102*, 26,345-326,366.

Mayewski, P. A., E. J. Rohling, J. C. Stager, W. Karlen, K. A. Maasch, D. L. Meeker, E. A. Meyerson, F. Gasse, S. van Kreveld, K. Holmgren, J. Lee-Thorp, G. Rosqvist, F. Rack, M. Staubwasser, R. R. Schneider, and E. J. Steig (2004), Holocene climate variability, *Quaternary Research*, *62*, 243-255.

McCabe, A. M. (1996), Dating and rhythmicity from the last deglacial cycle in the Britich Isles, *Journal of the Geological Society, London*, *153*, 499-502.

McCabe, A. M., and P. U. Clark (1998), Ice-sheet variability around the North Atlantic Ocean during the last degalciation, *Nature*, *392*, 373-376.

McCabe, A.M., P. U. Clark, and J. Clark (2005), AMS ^{14}C dating of deglacial events in the Irish Sea Basin and other sectors of the British–Irish Ice Sheet, *Quaternary Science Reviews*, *24*, 1673–1690.

McCabe, A. M., P. U. Clark, J. Clark, and P. Dunlop (2007), Radiocarbon constraints on readvances of the British–Irish Ice Sheet inthe northern Irish Sea Basin during the last deglaciation, *Quaternary Science Reviews*, *26*, 1204–1211.

McCartney, M. (1992), Recirculating components of the deep boundary current of the northern North Atlantic, *Progress in Oceanography*, *29*, 283-382.

McCartney, M. S., R. G. Curry, H. F. Bezdek (1996), North Atlantic's transformation pipeline chills and redistributes subtropical water, but its not a smooth process and it mightily effects climate, *Oceanus*, *Fall/Winter 2006*, 19-23.

McCave, I. N., and J. P. M. Syvitski (1991), Principles and methods of geological particle size analysis, in Principles, Methods and Application of Particle Size Analysis, edited by J. P. M. Syvitski, pp. 3–21, Cambridge Univ. Press, New York.

McCave, I. N., B. Manighetti, and N. A. S. Beverdige (1995a), Circulation in the glacial North Atlantic inferred form grain size measurements, *Nature*, *374*, 149-152.

McCave, I. N., B. Manighetti, and S. G. Robinson (1995b), Sortable silt and fine sediment size/composition slicing: Parameters for paleocurrent speed and paleoceanography, *Paleocanography* , *10*, 593-610.

McCave, I. N., I. R. Hall and G. G. Bianchi (2006), Laser vs. settling velocity differences in silt grainsize measurements: estimation of palaeocurrent vigour, *Sedimentology*, *53*, 919–928.

McCave, I. N. and I. R. Hall (2006), Size sorting in marine muds: Processes, pitfalls, and prospects for paleoflow-speed proxies, *Geochemistry, Geophysics, Geosystems*, *7*, Q10N05, doi:10.1029/2006GC001284.

McCrea, J. M. (1950), On the isotopic chemistry of carbonates and paleotemperature scale, *J. Chem. Phys.*, *18*, 849-857.

McElhinney, M. W., (1973). Palaeomagnetism and plate tectonics: Cambridge, Cambridge University Press.

McElhinney, M. W, and P. L. McFadden (1999), *Paleomagnetism: Continents and Oceans*, Academic Press, 1999, ISBN 0124833551, 9780124833555, pp.37-38.

McManus, J. F., R. Francois, J.-M. Gherardi, L. D. Keigwin, and S. Brown-Leger (2004), Collapse and rapid resumption of Atlantic meridional circulation linked to deglacial climate changes, *Nature*, *428*, 834-837.

Meese, D. A., A. J. Gow, R. B. Alley, G. A. Zielinski, P. M. Grootes, M. Ram, K. C. Taylor, P. Mayewski, and J. F. Bolzan (1997), The Greenland Ice Sheet Project 2 depth-age scale: Methods and results, *J. Geophys. Res.*, *102*, 26411-26423.

Meland, M. Y., E. Jansen, and H. Elderfield (2005), Constraints on SST estimates for the northern North Atlantic/Nordic Seas during the LGM, *Quaternary Science Reviews*, *24*, 835-852.

Meland, M. Y., T. M. Dokken, E. Jansen, and K. Hevrøy (2008), Water mass properties and exchange between the Nordic seas and the northern North Atlantic during the period 23–6 ka: Benthic oxygen isotopic evidence, *Paleoceanography*, *23*, PA1210, doi:10.1029/2007PA001416.

Menot, G., E. Bard, R. Rostek, W. H. Weijers, E. C. Hopmans, S. Scouten, and J. S. Sinninghe Damsté (2006), Early reactivation of European rivers during the last deglaciation, *Science,* , 313, 1623-1625.

Mignot, J., A. Ganopolski, and A. Levermann (2007), Atlantic Subsurface Temperatures: Response to a Shutdown of the Overturning Circulation and Consequences for Its Recovery, *Journal of Climate*, *20*, 4884–4898.

Mikutta, R., M. Kleber, K. Kaiser, and R. Jahn (2005), Review: Organic Matter Removal from Soils using Hydrogen Peroxide, Sodium Hypochlorite, and Disodium Peroxodisulfate, *Soil Science Society of America Journal*, *69*, 120-135.

Milankovitch, M. M., 1949, Kanon der Erdbestrahlung und seine Anwendung auf das Eiszeitenproblem. *Royal Serbian Sciences, Special Publication 132*, *section of Mathematical and Natural Sciences*, *33*, Belgrade, p. 633 (Canon of Insolation and the Ice Age Problem, English translation by Israel Program for Scientific Translation and published for the US Department of Commerce and the National Science Foundation, Washington D. C. (1969).

Millo, C., M. Sarnthein, A. Voelker, and H. Erlenkeuser (2006), Variability of the Denmark Overflow during the Last Glacial Maximum, *Boreas*, *35*, 50-60.

Mix, A. E., E. Bard and R. Schneider (2001), Environmental processes of the ice age: land, ocean, glaciers (EPILOG), *Quaternary Science Reviews*, *20*, 627–657.

Moore, T. C., Jr. (2005), The Younger Dryas: From whence the fresh water?, Paleoceanography, *20*, PA4021, doi:10.1029/2005PA001170.

Moreno, E., N. Thouveny, D. Delanghe, I. N. McCave, and N. J. Shackleton (2002), Climatic and oceanographic changes in the Northeast Atlantic reflected by magnetic properties of sediments deposited on the Portugese Margin during the last 340 Ma, *Earth and Planetary Science Letters*, *202*, 465-480.

Moros, M., R. Endler, K. S. Lackschewitz, H.-J. Wallrabe-Adams, J. Mienert, and W. Lamke (1997), Physical properties of Reykjanes Ridge sediments and their linkage to high-resolution Greenland Ice Sheet Project 2 ice core data, *Paleoceanography*, *12*, 687-695.

Mulder, T., and J. P. M. Syvitski (1995), Turbidity currents generated at river mouths during exceptional discharges to the world oceans, *Journal of Geology*, *103*, 285-299.

Mulder, T., P. M. J. P.M. Syvitski, S. Migeon, J.-C. Faugéres, B. Savoye (2003), Marine hyperpycnal flows: initiation, behavior and related deposits. A review, *Marine and Petroleum Geology*, *20*, 861–882

Mullarney, J. C., R. W. Griffiths, G. O. Hughes (2007), The role of freshwater fluxes in the thermohaline circulation: Insights from laboratory analogue, *Deep-Sea Research I*, *54*, 1-21.

Muscheler, R., J. Beer, G. Wagner, and R. C. Finkel (2000), Changes in deep-water formation during the Younger Dryas event inferred from ^{10}Be and ^{14}C records, *Nature*, *408*, 567-570.

Muscheler, R, B. Kromer, s. Björck, A. Svensson, M. Friedrich, K. F. Kaiser, and J. Southon (2008), Tree rings and ice cores reveal ^{14}C calibration uncertainties during the Younger Dryas, *Nature Geoscience*, *1*, 263-267.

Muxworthy, A. R., and D. J. Dunlop (2002), First-order reversal curve (FORC) diagrams for pseudo-single-domain magnetites at high temperature, *Earth Planetary Science Letters*, *203*, 369-382.

National Institute of Standards and Technology (1992), Report of Investigation, Reference Materials, 8543-8546.

Nørgaard-Pederson, N., R. F. Spielhagen, J. Theide, and H. Kassens (1998), Central Arctic surface ocean environment during the past 80,000 years, *Paleoceanography*, *13*, 193-204.

Nørgaard-Pederson, N., R. F. Spielhagen, H. Erlenkeuser, P. M. Grootes, J. Heinemeiner, and J. Knies (2003) Arctic Ocean during the Last Glacial Maximum: Atlantic and polar domains of surface water mass distribution and ice cover, *Paleoceanography*, *18*, doi: 10.1029/2002PA000781.

Nygård, A., H. P. Sejrup, H. Haflidason, W. A. H. Lekens, C. D. Clark, and G. R. Bigg (2007), Extreme sediment and ice discharge from marine-based ice streams: New evidence from the North Sea, *Geology*, *35*, 5, 395-398.

O' Brien, S. R., P. A. Mayewski, L. D. Meeker, D. A. Meese, M. S. Twickler, and S. Whitlow (1995), Complexity of Holocene Climate as Reconstructed from Greenland Ice Core, *Science*, *270*, 1962-1964.

O' Neil, J. R., R. N. Clayton, and T. K. Mayeda (1969), Oxygen isotope fractionation on divalent metal carbonates, *Journal of Chemical Physics, 51,* 5547-5558.

Opdyke, N. D., D. V. Kent, and W. Lowrie (1973), *Details of magnetic polarity transitions recorded in high deposition rate deep-sea core, Earth and Planetary Science Letters, 20*, 315-324.

Oppo, D. W., J. F. McManus, and J. L. Cullen (1998), Abrupt climate events 500,000 to 340,000 years ago: Evidence from subpolar North Atlantic sediments, *Science*, *279*, 1335–1338.

Paul, A. and M. Schulz (2002), Holocene climate variability on centennial-to-millennial time scales: 2. Internal and forced oscillations as possible causes, in Climate Development and History of the North Atlantic Realm, edited by G. Wefer, W. Berger, and E. Jansen, pp. 55–73, Springer, Berlin.

Peck, V. L., I. R. Hall, R. Zahn, H. Elderfield, F. Grousset, S. R. Hemming, and J. D. Scourse (2006), High resolution evidence for linkages between NW European ice sheet instability and Atlantic Meridional Overturning Circulation, *Earth and Planetary Science Letters*, *243*, 476–488.

Peck, V. L., I. R. Hall, R. Zahn, F. Grousset, S. R. Hemming, and J. D. Scourse (2007a), The relationship of Heinrich events and their European precursors over the past 60 ka BP: a multi-proxy ice-rafted debris provenance study in the North East Atlantic, *Quaternary Science Reviews*, *26*, 862–875

Peck, V. L., I. R. Hall, R. Zahn, and J. D. Scourse (2007b), Progressive reduction in NE Atlantic ventilation prior to Heinrich events: Response to NW European ice sheet instabilities?, *Geochemistry, Geophysics, Geosystems*, *8*, 1, doi: 10.1029/2006GC001321.

Peck, V. L., I. R. Hall, R. Zahn, and H. Elderfield (2008), Millennial-scale surface and subsurface paleothermometry from the northeast Atlantic, 55–8 ka BP, *Paleoceanography*, *23*, PA3221, doi:10.1029/2008PA001631.

Peeters, F. J. C., R. Acheson, G. J. A. Brummer, W. de Ruijter, R. R. Schneider, G. Ganssen, E. Ufkes, and D. Kroon (2004), Vigorous exchange between the Indian and Atlantic oceans at the end of the past five glacial periods, *Nature*, *430*, 661–665.

Peltier, W. R., and R. G. Fairbanks (2006), Global ice volume and Last Glacial Maximum duration from an extended Barbados sea-level record, *Quat. Sci. Rev.*, *25*, 3322–3337.

Petit, J. R., J. Jouzel, D. Raynaud, N. I. Barkov, J.-M. Barnola, I. Basile,M. Bender, J. Chappellaz, M. Davisk, G. Delaygue, M. Delmotte, V. M. Kotlyakov, M. Legrand, V. Y. Lipenkov, C. Lorius, L. Pépin, C. Ritz, E. Saltzmank, and M. Stievenard (1999), Climate and atmospheric history of the past 420,000 years from the Vostok ice core, Antarctica, *Nature*, *399*, 429-436.

Pflaumann, U., M. Sarhtein, M. Chapman, L. d'Abreu, B. Funnell, M. Huels, T. Kiefer, M. Maslin, H. Schulz, J. Swallow, S. van Krveled, M. Vautravers, E. Vogelsang, and M. Weinelt (2003), Glacial North Atlantic: Sea-surface conditions reconstructed by GLAMAP 2000, *Paleoceanography*, *18*, 3, 1065, doi:10.1029/2002PA000774, 2003.

Pickart, R. S., F. Straneo, and G. W. K. Moore (2003), Is Labrador Sea Water formed in the Irminger Basin?, *Deep Sea Research I*, *50*, 23-52.

Pierrehumbert, R. T. (1999), Huascaran $\delta^{18}O$ as an indicator of tropical climate during the last glacial maximum. *Geophysical Research Letters*, *26*, 1345–1348.

Pike, C. R., A. P. Roberts, and K. L. Verosub (1999), Characterizing interactions in fine magnetic particle systemsusing first order reversal curves, *Journal of Applied Physics*, *85*, 9, 6660-6667.

Pike, C. R., A. P. Roberts, M. J. Dekkers, and K. L. Verosub (2001), An investigation of multi-domain hysteresis mechanisms using FORC diagrams, *Physics of the Earth and Planetary Interiors*, *126*, 11–25.

Piotrowski, A. M., S. L. Goldstein, S. R. Hemming, and R. G. Fairbanks (2004), Intensification and variability of ocean thermohaline circulation through the last deglaciation, *Earth and Planetary Science Letters*, *225*, 205-220.

Rahmstorf, S. (1994), Rapid climate transitions in a coupled ocean-atmopshere model, *Nature*, *372*, 81-85.

Rahmstorf, S. (1995), Bifurcations of the Atlantic thermohaline circulation in response to changes in the hydrological cycle, *Nature*, *378*, 145-149.

Rahmstorf, S., and A. Ganopolski (1999), Long-term global warming scenarios computed with an efficient coupled climate model, *Climate Change*, *43*, 353–367.

Rahmstorf, S. (2000), The thermohaline circulation: a system with dangerous thresholds, *Climate Change*, *46*, 247-256.

Rahmstorf, S. (2002), Ocean circulation and climate over the past 120, 000 years, *Nature*, *419*, 207–214.

Rahmstorf, S. (2003), The current climate, *Nature*, *421*, 699.

Rahmstorf, S., M. Crucifix, A. Ganapolski, H. Goose, I. Kamenkovich, R. Knutti, G. Lohmann, R. Marsh, L. A. Mysak, Z. Wang, and A. J. Weaver, (2005), Thermohaline circulation hysteresis: A model intercomparison, *Geophysical Research Letters*, *32*, L23605, doi:10.1029/2005GL023655.

Rashid, H., R. Hesse, and D. J. W. Piper (2003), Distribution, thickness and origin of Heinrich layer 3 in the Labrador Sea. *Earth Planet. Sci. Lett*., *205*, 281– 293.

Rashid, H., and E. A. Boyle (2007), Mixed-Layer Deepening during Heinrich Events: A Multi-Planktonic Foraminiferal δ^{18}O Approach, *Science*, *318*, 439-441.

Rasmussen, T. L., D. Bäckström, J. Heinemeier, D. Klitgaard-Kristensen, P. C. Knutz, A. Kuijpers,, S. Lassen, E. Thomsen, S. R. Troelstra, and T. C. E. van Weering, (2002a), The Faeroe–Shetland Gateway: Late Quaternary water mass exchange between the Nordic seas and the northeastern Atlantic. *Marine Geol*ogy, *188*, 165– 192.

Rasmussen, T. L., E. Thomsen, S. R. Troelstra, A. Kuijpers, and M. A. Prins, (2002b), Millennial-scale glacial variability versus Holocene stability: changes in planktic and benthic foraminifera faunas and ocean circulation in the North Atlantic during the last 60 000 years, *Marine Micropaleontology*, *47*, 143-176.

Rasmussen, T. L., D. W. Oppo, E. Thomsen, and J. Lehman (2003), Deep sea records from the southeast Labrador Sea: Ocean circulation changes and ice-rafting events during the last 160,000 years, *Paleoceanography*, *18*, 1018 (doi: 1029/2001PA000736)

Rasmussen, T. L., and E. Thomsen (2004), The role of the North Atlantic Drift in the millenial timescale glacial climate fluctuations, *Paleoceanography, Paleoecology, Paleoclimatology*, *210*, 101-116.

Rasmussen, T. L., and E. Thomsen (2008), Warm Atlantic water inflow to the Nordic seas 34-10 calibrated ka B.P., *Paleoceanography*, *23*, doi:10.1029/2007PA001453.

Rasmussen, S .O., K. K. Andersen, A. M. Svensson, J. P. Steffensen, B. M. Vinther, H. B. Clausen, M.-L. Siggaard-Andersen, S. J. Johnsen, L. B. Larsen, D. Dahl-Jensen, M. Bigler, R. Röthlisberger, H. Fischer, K. Goto-Azuma, M. E. Hansson, M. E., and U. Ruth (2006), A new Greenland ice core chronology for the last glacial termination, *J. Geophys Res.*, *111*, D06102, doi:10.1029/2005JD006079.

Rasmussen, S.O., I. K. Seierstad, K. K. Andersen, M. Bigler, D. Dahl-Jensen, and S. J. Johnsen (2007), Synchronization of the NGRIP, GRIP, and GISP2 ice cores across MIS 2 and palaeoclimatic implications, *Quaternary Science Reviews*, INTIMATE special issue.

Raymo, M. E., D. W. Oppo, B. P. Flower, D. A. Hodell, J. F. McManus, K. A. Venz, K. F. Kelvin, and K McIntyre (2004), Stability of North Atlantic water masses in face of pronounced climate variability during the Pleistocene, *Paleoceanography*, *19*, PA2008, doi:10.1029/2003PA000921.

Reeh, N., H. Oerter, H. H. Thomsen (2002), Comparison between Greenland ice-margin and ice-core oxygen-18 records, *Annals of Glaciology, 35, 1,* 136-144.

Reimer, P. J., M. G. L. Baillie, E. Bard, A. Bayliss, J. W. Beck, C. J. H. Bertrand, P. G. Blackwell, C. E. Buck, G. S. Burr, K. B. Cutler, P. E. Damon, R. L. Edwards, R. G. Fairbanks, M. Friedrich, T. P. Guilderson, A. G. Hogg, K. A. Hughen, B. Kromer, G. McCormac, S. Manning, C. B. Ramsey, W. R. Reimer, S. Remmele, J. R. Southon, M. Stuiver, S. Talamo, F. W. Taylor, J. van de Plicht, and C. E. Weyhenmeyer (2004), IntCal04 terrestrial radiocarbon age calibration, 0-26 cal kyr BP, *Radiocarbon*, *46*, 1029-1058.

Reimer, P. J., and K. A. Hughen (2008), Tree rings floating on ice cores, *Nature Geoscience*, *1*, 218-219.

Rignot, E., and P. Kanagaratnam (2006), Changes in the Velocity Structure of the Greenland Ice Sheet, *Science*, *311*, 986-990.

Rinterknecht, V. R., P. U. Clark, M. Raisbeck, F. Yiou, A. Bitnas, E. J. Brook, L. Marks, V. Zelčs, J.-P. Lunkka, I. E. Pavlovskaya, J. A. Piotrowski, and A. Raukas (2006), The last deglaciation of the southeastern sector of the Scandinavian ice sheet, *Science*, *311*, 1449-1452.

Risebrobakken, B., E. Jansen, C. Andersson, E. Mjelde, and K. Hevrøy (2003), A high resolution study of Holocene paleoclimatic and paleoceanographic changes in the Nordic seas, *Paleoceanography*, *18*(1), 1017, doi:10.1029/2002PA000764.

Risebrobakken, B., E. Balbon, T. Dokken, E. Jansen, C. Kissle, L. Labeyrie, T. Richter, and L. Senneset (2006), The penultimate deglaciation: high-resolution paleoceanographic evidence from a north-south transect along the eastern Nordic Seas, *Earth and Planetary Science Letters*, *241*, 505-516.

Roberts, A. P., Y. Cui, and K. L. Verosub (1995), Wasp-waisted hysteresis loops: Mineral magnetic characteristics and discrimination of components in mixed magnetic systems, *J. Geophys. Res.*, *100*, 17,909– 17,924.

Roberts, A. P., Pike, C. R., and K. L. Verosub (2000), First Order Reversal Curve diagrams: A new tool for charactersing magnetic properties of natural samples, *Journal of Geophyscial Research*, *105*, B12, 28,461-28,475.

Roberts, A. P. (2006), high-resolution magnetic analysis of sediment cores: Strength, limitations and strategies for maximizing the value of long-core magnetic data, *Physics of the Earth and Planetary Interiors*, *156*, 162-178.

Robinson, S. G., M. A. Maslin, and I. N. McCave (1995), Magnetic susceptibility variations in Upper Pleistocene deep-sea sediments of the NE Atlantic: Implications for ice rafting and paleocirculation at the last glacial maximum, *Paleoceanography*, 2.

Robinson, L. F., J. F. Adkins, L. D. Keigwin, J. Southon, D. P. Fernandez, S.-L. Wang, and D. S. Scheirer (2005), Radiocarbon variability in the Western North Atlantic during the last deglaciation, *Science*, *310*, 1469-1473.

Roche, D., D. Paillard, A. Ganopolski, and G. Hoffmann (2004a), Oceanic oxygen-18 at the present day and LGM: equilibrium simulations with a coupled climate model of intermediate complexity, *Earth and Planetary Science Letters*, *218*, 317-330.

Roche, D., D. Paillard, and E. Cortijo (2004b), Constraints on the duration and freshwater release of Heinrich event 4 through isotope modeling, *Nature*, *432*, 379-382.

Rogerson, M., E. J. Rohling, P. P. E. Weaver, and J. W. Murray (2004), The Azores Front since the Last Glacial Maximum, *Earth and Planetary Science Letters*, *222*, 779-789.

Rohling, E. J., M. Fenton, F. J. Jorissen, P. Bertrand, G. Gansen, and J. P. Caulet (1998), Magnitudes of sea-level lowstands of the past 500,000 years, *Nature*, *394*, 162-165.

Rohling, E. J., and G. R. Bigg (1998), Paleosalinity and $\delta^{18}O$: a critical assessment, *Journal of Geophysical Research, 103, C1,* 1307-1318.

Rohling, E. J., and S. Cooke (1999), Stable Isotopes in Foraminiferal Carbonate. In Sen Gupta (ed.) *Modern Foraminifera*, Kluwer Academic, Dordrecht, The Netherlands, pp.239-258

Rohling, E. J., P. A. Mayewski, and P. Challenor (2003), On the timing and mechanism of millenial-scale climate variability during the last glacial cycle, *Climate Dynamics*, *20*, 257-267.

Rohling, E. J., R. Marsh, N. Wells, M. Siddall, and N. R. Edwards (2004), Similar meltwater contribution to glacial sea level changes from Antarctic and northern ice sheets, *Nature*, *430*, 1016-1021.

Rooth, C. (1982), Hydrology and ocean circulation, *Oceanography*, *11*, 131-149.

Ruddiman, W. F. (1977), Late Quaternary deposition of ice-rafted sand in the subpolar North Atlantic (lat 40° to 65°N), *Geol. Soc. Am. Bull.*, *88*, 1813–1827.

Ruddiman, W. F., and A. McIntyre (1973), Time-Transgressive Deglacial Retreat of Polar Waters from the North Atlantic, *Quaternary Research*, *3*, 117-130.

Rudels, B., D. Quadfasel, and H. Friedrich (1998), The Arctic Ocean deep water component in the Greenland-Scotland overflow. *In* Hansen, B., and S. Østerhus (Eds), *North Atlantic-Norwegian Sea Exchanges: The ICES NANSEN Project*, ICES Cooperative Research Report, 225, pp.172-194.

Rudels, B., E. Fahrbach, J. Meinke, G. Budeus, and P. Eriksson (2002), The East Greenland Current and its contribution to the Denmark Strait Overflow, *ICES Journal of Marine Science*, *59*, 1133-1154.

Rühlemann, C., S. Mulitza, P. M. Müller, G. Wefer, and R. Zahn (1999), Warming of the tropical Atlantic Ocean and slowdown of thermohaline circulation during the last deglaciation, *Nature*, *402*, 511–514.

Rühlemann, C., S. Mulitza, G. Lohmann, A. Paul, M. Prange, and G. Wefer (2004), Intermediate depth warming in the tropical Atlantic related to weakened thermohaline circulation: Combining paleoclimate data and modeling results for the last deglaciation, *Paleoceanography*, *19*, PA1025, doi:10.1029/2003PA000948.

Sachs, J. P., R. F. Anderson, and S. J. Lehman (2001), Glacial surface temperatures of the southeast Atlantic Ocean, *Science*, *293*, 2077–2079.

Santosa, A., and M. H. England (2004), Antarctic Intermediate Water Circulation and Variability in a Coupled Climate Model, *Journal of Physical Oceanography*, *34*, 2160-2179.

Sarnthein, M., K. Winn, S. Jung, J.-C. Duplessy, L. Labeyrie, H. Erlenkeuser, and G. Ganssen (1994), Changes in east Atlantic deepwater circulation over the last 30,000 years: Eight time slice reconstructions, *Paleoceanography*, *9*, 209-267.

Sarnthein, M., E. Jansen, M. Weinelt, M. Arnold, J.-C. Duplessy, H. Erlenkeuser, A. Flatroy, G. Johannessen, T. Johannessen, S. Jung, N. Koc, L. Labeyrie, M. Maslin, U. Pflaumann, and H. Schulz (1995), Variations in Atlantic surface ocean paleoceanography, 50-80^0 N: A time-slice record of the last 30,000 years, *Paleoceanography*, *10*, 1063-1094.

Sarnthein M., J. P. Kennett, J. Chappell, T. Crowley, W. Curry, P. Grootes, I. Hendy, C. Laj, J. Negendank, M. Schulz, N. J. Shackleton, A. Voelker, and B. Zolitschka (2000), Exploring Late Pleistocene climate variations, *EOS Trans. Am. Geophys. Union 81*, *625*, 629–630.

Schaefer, J. M., G. H. Denton, D. J. A. Barrell, S. Ivy-Ochs, P. W. Kubik, B. G. Andersen, F. M. Phillips, T. V. Lowell, C. Schlüchter (2006), Near synchronous interhemispheric termination of the Last Glacial Maximum in Mid-Latitudes, *Science*, *312*, 1510-1513.

Schiebel, R. (2002), Planktic foraminiferal sedimentation and the marine calcite budget. - *Global Biogeochemical Cycles, 16, 4,* 1065, doi: 10.1029/2001GB001459

Schiebel, R., and C. Hemleben (2005), Modern Planktonic foraminifera, *Palaeontologiische Zeitschrift*, *79/1*, 135-148.

Schiebel, R., J. Bijma and C. Hemleben (1997), Population dynamics of the planktic foraminifer Globigerina bulloides from the eastern North Atlantic, *Deep Sea Res*., *Part I*, *44*, 1701 – 1713, doi:10.1016/S0967-0637(97)00036-8.

Schiebel, R., S. Barker, R. Lendt, H. Thomas, and J. Bollmann (2007), Planktonic foraminiferal dissolution in the twilight zone, *Deep-Sea Research II, 54,* 676–686

Schiller, A., U. Mikolajewicz, and R. Voss (1997), The stability if the North Atlantic thermohaline circulation in a coupled ocean-atmosphere general circulation model, *Climate Dynamics*, *13*, 325-347.

Schmidt, G. A. (1999), Error analysis of paleosalinity claclulations, *Paleoceanography*, *14*, 3, 422-429.

Schmidt, M. W., H. J. Spero, and D. W. Lea (2004), Links between salinity variation in the Caribbean and North Atlantic thermohaline circulation, *Nature*, *428*, 160-163.

Schmitz, W. J., Jr., and M. S. McCartney (1993), On the North Atlantic circulation, *Rev. Geophys., 31*, 29-49.

Schmitz, W. J., Jr. (1996), On the World Ocean Circulation: Volume 1, Some global features/North Atlantic circulation, Woods Hole Oceanographic Institution Technical Report, WHOI-96-03.

Schmittner, A., O. A. Saenko, and A. J. Weaver (2003), Coupling of the hemispheres in observations and simulations of glacial climate change, *Quaternary Science. Reviews.*, *22*, 659-671.doi:10.1016/S0277-3791(02)00184-1.

Scourse, J. D., I. R. Hall, I. N. McCave, J. R. Young, and C. Sugdon (2000), The origin of Heinrich layers: Evidence fromH2 for European precursor events, *Earth and Planetary Science Letters, 182*, 87–195.

Seager, R., D.S. Battisti, J. Yin, N. Naik, N. Gordon, A.C. Clement, and M. Cane (2002), Is the Gulf Stream responsible for Europe's mild winters? *Quarterly Journal of the Royal Meteorological Society*, *128*, 2563-2586

Seager, R. and D. S. Battisti (2006), Challenges to our understanding of the general circulation: abrupt climate change, In: Scheider and Sobel (Eds) Global Circulation of the Atmosphere, Princeton University Press, pp. 331-71.

Seivdov, D., and M. Maslin (2001), Atlantic heat piracy and the bipolar climate see saw during Heinrich and Dansgaard-Oeschger events, *Journal of Quaternary Science*, *16*, *4*, 321-328.

Seivdov, D, R. J. Stouffer, and B. J. Haupt (2005), Is there a simple bi-polar seesaw?, *Global and Planetary Change*, *49*, 19-27.

Sejrup, H. P., H. Haflidason, B. O., Hjelstuen, A. Nygård, P. Bryn, and R. Lien (2004) Pleistocene development of the SE Nordic Seas margin, *Marine Geology*, *213*, 169-200.

Severinghaus, J. P., and E. Brook (1999), Abrupt climate change at the end of the last glacial period inferred from trapped air in polar ice, *Science*, *286*, 930-934.

Severinghaus J. P., T. Sowers, E. J. Brook, R. B. Alley, and M. L. Bender (1998), Timing of abrupt climate change at the end of the Younger Dryas period from thermally fractionated gases in polar ice, *Nature*, *391*, 141–146.

Shackleton, N. J. (1974), Attainment of isotopic equilibrium between ocean water and the benthonic foraminifera genus *Uvigerina*: isotopic changes in the ocean during the last glacial, CNRS, *Colloques Internationals, 219,* 203-209.

Shackleton, N. J. (2000), The 100,000-Year Ice-Age Cycle Identified and Found to Lag Temperature, Carbon Dioxide, and Orbital Eccentricity, *Science*, *289*, 1897-1902.

Shackleton, N. J., J. D. H. Wiseman, and H. A. Buckley (1973), Non-equilibrium Isotopic Fractionation between Seawater and Planktonic Foraminiferal Tests, *Nature*, *242*, 177-179.

Shackleton, N. J., M. A. Hall, and E. Vincent (2000), Phase relationships between millennial-scale events 64,000-24,000 years ago, *Paleoceanography*, *15*, 565-569.

Shaffer, G., S. M. Olsen, and C. J. Bjerrum (2004), Ocean subsurface warming as a mechanism for coupling Dansgaard-Oeschger climate cycles and ice-rafting events, *Geophysical Research Letters*, *31*, L24202, doi:10.1029/2004GL020968.

Siddall, M., E. J. Rohling, A. Almogi-Labin, C. Hemleben, D. Meischner, I. Schmelzer, and D. A. Smeed (2003), Sea-level fluctuations during the last glacial cycle, *Nature*, *423*, 853-858.

Simstich, J., M. Sarnthein, and H. Erlenkeuser (2003), Paired $\delta^{18}O$ signals *of Neogloboquadrina pachyderma* (s) and *Turborotalita quinqueloba* show thermal stratification structure in Nordic Seas, *Marine Micropaleontology*, *48*, 107-125.

Snowball, I., and M. Moros (2003), Saw-tooth pattern of North Atlantic current speed during Dansgaard-Oeschger cycles revealed by the magnetic grain size of Reykjanes Ridge sediments at 59ºN, *Paleoceanography*, *18*, 1026, doi:10.1029/2001PA000732.

Soulsby, R. (1997), Dynamics of marine sands, published by Thomas Telford, pp.129-155.

Spero, H. J., and D. F. Williams (1988), Extracting environmental information from planktonic foraminiferal $\delta^{13}C$ data, *Nature*, *335*, 717-719.

Spero, H. J., I. Lerche, and D. F. Williams (1991), Opening the carbon isotope 'vital effect' black box, 2, quantitative model for interpreting foraminiferal carbon isotope data, *Paleoceanography, 6, 6,* 639-655.

Spero, H. J., and D. W. Lea (1993), Intraspecific stable isotope variability in the planktic foraminifera *Globigerinoides sacculifer*: Results from laboratory experiments, *Marine Micropaleontology*, *22*, 221-234.

Spero, H. J., J. Bijma, D. W. Lea, and B. E. Bemis (1997), Effect of seawater carbonate concentration on foraminiferal carbon and oxygen isotopes, *Nature*, *390*, 497-500.

Spindler, M. (1996), On the salinity tolerance of the planktonic foraminifer *Neogloboquadrina pachyderma* from Antarctic sea ice, *Proc. NIPR Symp. Polar Biology*, *9*, 85-91.

Spofforth, D. J. A., H. Pälike and D. R. H. Green (2008), Paleogene record of elemental concentrations in sediments from the Arctic Ocean obtained by XRF analyses. *Paleoceanography, 23, PA1S09*, doi:10.1029/2007PA001489

Stanford, J. D., E. J. Rohling, S. E. Hunter, A. P. Roberts, S. O. Rasmussen, E. Bard, J. McManus, and R. G. Fairbanks (2006), Timing of mwp-1a and climate responses to metlwater injections, *Paleoceanography*, *21*, PA4103, doi:10.1029/2006PA001340, 2006.

Steig, E. J., E. J. Brook, J. W. C. White, C. M. Sucher, M. L. Bender, S. J. Lehman, D. L. Morse, E. D. Waddington, and G. D. Clow (1998), Synchronous Climate Changes in Antarctica and the North Atlantic, *Science*, *282*, 92-95.

Stocker, T. F. (1998), The seesaw effect, *Science*, *282*, 61–62.

Stocker, T. F. (1999), Abrupt climate changes: from the past to the future - a review, *International Journal of Earth Sciences*, *88*, 365-374.

Stocker, T. F. (2003), South dials north, *Nature*, *424*, 496-499.

Stocker, T. F., and D. G. Wright (1991), Rapid transitions of the ocean's deep circulation induced by changes in surface water fluxes, *Nature*, *351*, 729–732.

Stocker, T. F., and S. J. Johnsen (2003), A minimum thermodynamic model for the bipolar seesaw, *Paleoceanography*, *18*, 4, 1087, doi:10.1029/2003PA000920.

Stocker, T. F. , D. G. Wright, and W. S. Broecker (1992), The influence of high-latitude surface forcing on the global thermohaline circulation, *Paleoceanography*, *7*, 529– 541.

Stokes, C. R., C. D. Clark, D. A. Darby, D. A. Hodgson (2005), Late Pleistocene ice export events into the Arctic Ocean form the M'Clure Strait Ice Stream, Canadian Arctic Archipelago, *Global and Planetary change*, *49*, 139-162.

Stommel, H. (1961), Thermohaline convection with two stable regimes of flow, *Tellus*, *13*, 224-230.

Stoner, J. S., J. E. T. Channell, and C. Hillaire-Marcel (1995), Magnetic properties of deep-sea sediments off southwest Greenland: Evidence for major differences between the last two glaciations, *Geology*, *23*, 241-244.

Stoner, J. S., J. E. T. Channell, and C. Hillaire-Marcel (1996), The magnetic signature of rapidly deposited detrital layers form the Labrador Sea: Relationship to North Atlantic Heinrich layers, *Paleoceanography*, *11*, 3, 309-325.

Stoner, J. S., J. E. T. Channell, C. Hillaire-Marcel, and C. Kissel (2000), Geomagnetic paleointensity and environmental record from Labrador Sea core MD95-2024: global marine sediment and ice core chronostratigraphy for the last 100 kyr, *Earth and Planetary Science Letters*, *183*, 161-177.

Stouffer, R. J. (2004), Time Scales of Climate Response, *Journal of Climate*, *17*, 209-217.

Strass, V. H., E. Fahrbach, U. Schauer, and L. Sellman (1993), Formation fo Denmark Strait Overflow water by mixing in the East Greenland Current, *Journal of Geophysical Research*, *98*, C4, 6907-6919.

Stuiver, M., and P. M. Grootes (2000), GISP2 oxygen isotope ratios, *Quaternary Research*, *53*, 277-284.

Sundborg, A. (1956), The River Klaralven, a study of fluvial processes, *Geogr. Ann.*, *38*, 125–316.

Sutherland, D. A., R. S. Pickart (2008), The East Greenland Coastal Current: Structure, variability, and forcing, *Progress In Oceanography*, *78, 1*, 58-77.

Svensson, A., K. K. Andersen, M. Bigler, H. B. Clausen, D. Dahl-Jensen, S. M. Davies, S. J. Johnsen, R. Muscheler, S. O. Rasmussen, R. Röthlisberger, J. P. Steffensen, and B. M. Vinther (2006), The Greenland Ice Core Chronology 2005, 15-42 ka. Part 2: Comparison to other records, *Quaternary Science Reviews*, *25*, Shackleton special issue 24.

Swart, P. K. (1983), Carbon and oxygen isotope fractionation in scleractinian corals: a review, *Earth-Science Reviews, 19,* 51-80.

Swift, J. H. (1986), The Arctic Waters *In:* Hurdle, B. G, (Ed) *The Nordic Seas*, Springer-Verlag, New York, pp.129-154.

Syvitski, J. P. M. D. Morehead, D. B. Bahr, and T. Mulder (2000), Estimating fluvial sediment transport: The rating parameters**,** *Water Resources Research*, *36*, 9, 2747–2760.

Tan, F. C., and P. M. Strain (1980), The distribution of sea ice meltwater in the eastern Canadian Arctic, *Journal of Geophysical Research, 85, C4,* 1925-1932.

Tarasov, L., and W. R. Peltier (2005), Arctic freshwater forcing of the Younger Dryas cold reversal, *Nature*, *435*, 662-665.

Tauxe, L. (1993), Sedimentary records of relative paleointensity of the geomagnetic field: Theory and practice, *Reviews of Geophysics*, *31*, 319-354.

Taylor, K. C., G. W. Lamorey, G. A. Doyle, R. B. Alley, P. M. Grootes, P. A. Mayewsi, J. W. C. White, and L. K. Barlow (1993), The 'flickering switch' of late Pleistocene climate change, *Nature*, *361*, 432-436.

Teller, J. T., D. W. Leverington, and J. D. Mann (2002), Freshwater outbursts to the oceans from glacial Lake Agassiz and their role in climate change during the last deglaciation, *Quaternary Science Reviews*, *21*, 879–887

Timmerman, A., and H. Goosse (2004), Is the wind stress forcing essential for the meridional overturning circulation?, *Geophysical Research Letters*, *31*, L04303, doi:10.1029/2003GL018777, 2004.

Tjallingii, R., U. Röhl, M. Kölling, and T. Bickert (2007), Influence of the water content on X-ray fluorescence core- scanning measurements in soft marine sediments, *Geochemistry, Geophysics, Geosystems, Technical Brief*, *8*, 2, Q02004, doi:10.1029/2006GC001393.

Toscano, M. A., and I. G. Macintyre (2003), Corrected western Atlantic sea-level curve for the last 11,000 years based on calibrated ^{14}C dates from *Acropora palmate* framework and intertidal mangrove peat, *Coral Reefs*, *22*, 257-270.

Tucker, P. (1981), Paleointensities from sediments: Normalization by laboratory redeposition, *Earth and Planetary Science. Letters*, 56, 398-404.

Urey, H. C. (1947), The thermodynamic properties of isotopic substances. *Journal of the Chemical Society, 1,* 562-581.

Usdowski, E., and J. Hoefs (1993), Oxygen isotope exchanges between carbonic acid, bicarbonate, carbonate and water: A re-examination of the data of McCrea (1950) and an expression for the overall partitioning of oxygen isotopes between carbonate species and water, *Geochmica Cosmochemica Acta*, *57*, 3815-3818.

van Kreveld, S., M. Sarnthein, H. Erlenkeuser, P. Grootes, S. Jung, M. J. Nadeau, U. Pflaumann, and A. Voelker (2000), Potential links between surging ice sheets, circulation changes, and the Dansgaard-Oeschger cycles in the Irminger Sea, 60-18 kyr, *Paleoceanography*, *15*, 425-442.

Vellinger, M., and Wood, R. (2002), Global climate impacts of a collapse of the Atlantic thermohaline circulation, *Climate Change*, *54*, 3, 251–267.

Verosub, K. L., and A. P. Roberts (1995), Environmental magnetism: Past, present, and future, *J. Geophys. Res.*, *100*, 2175-2192.

Vidal, L., L. Labeyrie, and T. C. E. van Weering (1998), Benthic $\delta^{18}O$ records in the North Atlantic over the last glacial period (60–10 kyr): Evidence for brine formation, *Paleoceanography*, *13*, 245–251.

Vidal, L., R. R. Schneider, O. Marchal, T. Bickert, T. F. Stocker, and G. Wefer (1999), Link between the North and South Atlantic during the Heinrich events of the last glacial period, *Climate Dynamics*, *15*, 909-919.

Vinot-Bertouille, A.-C., and J.-C. Duplessy (1973), Individual isotopic fractionation of carbon and oxygen in benthic foraminifera, *Earth and Planetary Science Letters*, *18*, 247-252.

Vinther, B. M., H. B. Clausen, S. J. Johnsen, S. O. Rasmussen, K. K. Andersen, S. L. Buchardt, I. K. Seierstad, M.-L. Siggaard-Andersen, J. P. Steffensen, and A. M. Svensson (2006), A synchronized dating of three Greenland ice cores throughout the Holocene, *J. Geophys. Res.*, *111*, D13102, doi:10.1029/2005JD006921.

Voelker, A., M. Sarnthein, P. M. Grootes, H. Erlenkeuser, C. Laj, A. Mazaud, M. J. Nadeau, and M. Schleicher (1998), Correlation of marine ^{14}C-ages from the Nordic Seas with the GISP2 isotope record: Implications for radiocarbon calibration beyond 25 ka BP, *Radiocarbon, 40(1),* 517-534

Voelker, A. H. L., P. M. Grootes, M. J. Nadeau, and M. Sarntheim (2000), Radiocarbon levels in the Iceland Sea from 25–53 kyr and their link to the Earth's magnetic field intensity, *Radiocarbon, 42(3),* 437–52.

Volkmann, R. (2000), Planktic Foraminifers in the Outer Laptev Sea and the Fram Strait - modern distribution and ecology, *Journal of Foraminiferal Research*, *30*, 157-176.

von Grafenstein, U., H. Erlenkeuser, A. Brauer, J. Jouzel, S. J. Johnsen (1999), A Mid-European Decadal Isotope-Climate Record from 15,500 to 5000 Years B.P., *Science*, *284*, 1654-1657.

Waelbroeck, C., J.-C. Duplessy, E. Michel, L. Labeyrie, D. Pallard, and J. Duprat (2001), The timing of the last deglaciation in North Atlantic climate records, *Nature*, *412*, 724-727.

Waelbroeck, C., L. Labeyrie , E. Michel, J.-C. Duplessy, J. F. McManus, K. Lambeck, E. Balbon, and M. Labracherie (2002), Sea-level and deep water temperature changes derived from benthic foraminifera isotopic records, *Quaternary Science Reviews*, *21*, 295-305.

Walden, J., E. Wadsworth, W. E. N. Austin, C. Peters, J. D. Scourse, and I. R. Hall (2007), Compositional variability of ice-rafted debris in Heinrich layers 1 and 2 on the northwest European continental slope identified by environmental magnetic analyses, *Journal of Quaternary Science*, *22*, 2, 163–172.

Wang L., M. Sarnthein, H. Erlenkeuser, J. Grimalt, P. Grootes, S. Heilig, E. Ivanova, M. Kienast, C. Pelejero, U. Pflaumann (1999), East Asian monsoon climate during the late Pleistocene: High-resolution sediment records from the South China Sea, *Marine Geology*, *156*, 245–284.

Wang, Y. J., H. Cheng, R. L. Edwards, Z. S. An, J. Y. Wu, C.-C. Shen, and J. A. Dorale (2001), A High-Resolution Absolute-Dated Late Pleistocene Monsoon Record from Hulu Cave, China, *Science*, *294*, 2345-2348.

Weaver, A. J., J. Marotzke, P. F. Cummins, and E. S. Sarachik (1993), Stability and variability of the thermohaline circulation, *J. Phys. Oceanogr.*, *23*, 39–60.

Weaver, A.J., O. A. Saenko, P. U. Clark, and J. X. Mitrovica (2003), Meltwater pulse 1A from Antarctica as a trigger of the Bølling-Allerød warm interval, *Science*, *299*, 1709-1713.

Weeks, R., C. Laj, L. Endignoux, M. Fuller, A. P. Roberts, R. Manganne, E. Blanchard, and W. Goree (1993), Improvements in long-core measurment techniques: applications in palaeomagnetism and palaeoceanography, *Geophys. J. Int.*, 114, 651-662.

Weeks R. J., C. Laj, L. Endignoux, A. Mazaud, L. Labeyrie, A. P. Roberts, C. Kissel, and E. Blanchard (1995), Normalised NRM intensity during the last 240,000 years in piston cores from the central North Atlantic Ocean: Geomagnetic field intensity or environmental signal?, *Physics of the Earth and Planetary Interiors, 87, 3-4,* 213-229.

Wefer, G., and W. H. Berger (1991), Isotope paleontology: growth and composition of extant calcareous species, *Marine Geology*, *100*, 207-248.

Weinelt, M., M. Sarnthein, U. Pflaumann, H. Schulz, S. Jung, and H. Erlenkeuser (1996), Ice-free Nordic Seas during the Last Glacial Maximum? Potential sites of deepwater formation, *Paleoclimates*, *1*, 283-309.

Weinelt, M. E. Vogelsang, M. Kucera, U. Pflaumann, M. Sarnthein, A. Voelker, H. Erlenkeuser, and B. A. Malmgren (2003), Variability of North Atlantic heat transfer during MIS 2 *Paleoceanography*, *18*, 3, 1071, doi:10.1029/2002PA000772.

Weldeab, S., D. W. Lea, R. R. Schneider, and N. Andersen (2007), 155,000 Years of West African Monsoon and Ocean Thermal Evolution, *Science*, *316*, 1303-1307.

Wilkinson, D. and S. Bacon (2005), The spatial and temporal variability of the East Greenland Current from historic data, *Geophysical Research Letters*, *104*, 18059-18072.

Williams, P. W., D. N. T. King, J.-X. Zhao, and K. D. Collerson (2005), Late Pleistocene to Holocene composite speleotherm ^{18}O and ^{13}C chronologies from South Island, New Zealand – did a global Younger Dryas really exist?, *Earth and Planetary Science Letters*, *230*, 301-317.

Winton, M. (1997), The effect of cold climate upon North Atlantic Deep Water formation in a simple ocean-atmosphere model, *J. Clim.*, *39*, 37– 51.

Wolf-Gladrow, D. A., J. Buma, and R. E. Zeebe (1999), Model simulation of the carbonate chemistry in the microenvironment of symbiont bearing foraminifera, *Marine Chemistry, 64, 3,* 181-198.

Worthington, L. V. (1976), On the North Atlantic Circulation, *John Hopkins Oceanographic Studies*, *6*, 1-110.

Wunsch, C. (2000), On sharp spectral lines in the climate record and the millennial peak, *Paleoceanography*, *15*, 417-424.

Wunsch, C. (2002), What is the Thermohaline Circulation?, *Science*, *298*, 1179-1180.

Wunsch, C. (2003), Greenland-Antarctic phase relations and millennial time-scale climate fluctuations in the Greenland ice-cores, *Quaternary Science reviews*, *22*, 1631-1646.

Wunsch, C. (2006), Abrupt climate change: An alternative view, *Quat. Res., 65*, 191-203.

Wust, G. (1935), The stratosphere of the Atlantic Ocean, *Wiss. Ergebn. Dtsch. Atlant. Exped. 'Meteor', 6*, 1, 109-288.

Yaroshevsky, A. A. (2006), Abundances of Chemical Elements in the Earth's Crust, *Geochemistry International*, *44*, 48-55.

Yokoyama, Y., K. Lambeck, P. D. Deckker, P. Johnston, and L. K. Fifield (2000), Timing of Last Glacial Maximum from observed sea level minima, *Nature*, *406*, 713-716.

Yu, Z., and H. E. Wright, Jr., (2001) Response of interior North America to abrupt climate oscillations in the North Atlantic region during the last deglaciation, *Earth- Science Reviews*, *52*, 333-369.

Yuan, D., H. Cheng, R. L. Edwards, C. A. Dykoski, M. J. Kelly, M. Zhang, J. Qing, Y. Lin, Y. Wang, J. Wu, J.A. Dorale, Z. An, and Y. Cai (2004), Timing, duration, and transitions of the last interglacial Asian monsoon, *Science*, *304*, 575–578.

Zachos, J. C., L. D. Scott, and K. C. Lohmann (1994), Evolution of early Cenozoic marine temperatures, *Paleoceanography, 9, 2,* 353-387.

Zaragosi, S., F. Eynaud, C, Pujol, G. A. Auffret, J.-L. Turon, and T. Garlan, (2001), Initiation of the European deglaciation as recorded in the northwestern Bay of Biscay slope environments (Meriadzek Terrace and Trevelyan Escarpment): a multi-proxy approach. *Earth and Planetary Science Letters*, *188*, 493–507.

Zimmerman, S. H., S. R. Hemming, D. V. Kent, and S. Y. Searle (2006), Revised chronology for late Pleistocene Mono Lake sediments based on paleointensity correlation to the global reference curve, *Earth and Planetary Science Letters*, *252*, 94-106.

Zhou, H., J. Zhao, Y. Feng, M. K. Gagan, G. Zhou, and J. Yan (2008), Distinct climate change synchronous with Heinrich event one, recorded by stable oxygen and carbon isotopic compositions in stalagmites from China, *Quaternary Research*, *69*, 306–315.

APPENDICES

Appendix 1. Radiocarbon (AMS^{14}C) age versus calendar age plots for the Sunda Shelf and Vietnamese Shelf datings.

Appendix 1 presents the calibration plots for the radiocarbon (AMS^{14}C) ages that make up the Sunda Shelf sea level record (Hanebuth *et al.*, 2000). The data were obtained from the Supplementary information with Hanebuth *et al.* (2000). The plots were generated using Calib 5. 0. 1 (Reimer *et al.*, 2004).

Appendix 2. Digital copy of the thesis and data used within

APPENDIX 1

Radiocarbon (AMS^{14}C) age versus calendar age plots for the Sunda Shelf and Vietnamese Shelf datings.

Sunda Shelf Datings

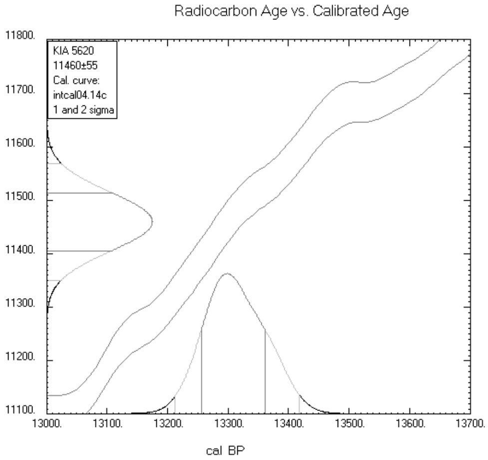

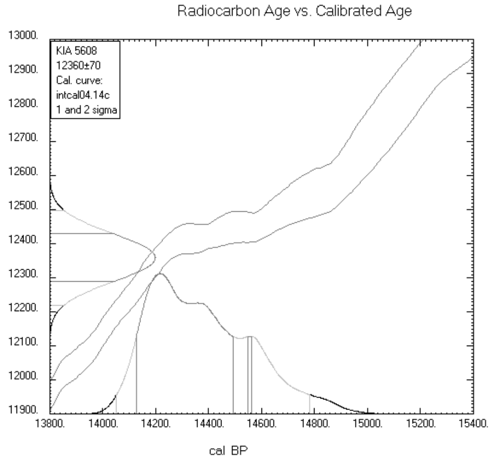

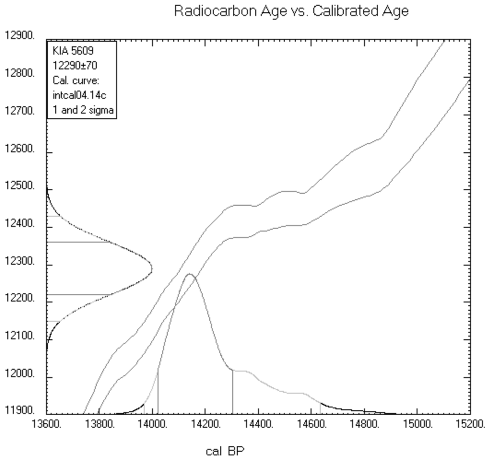

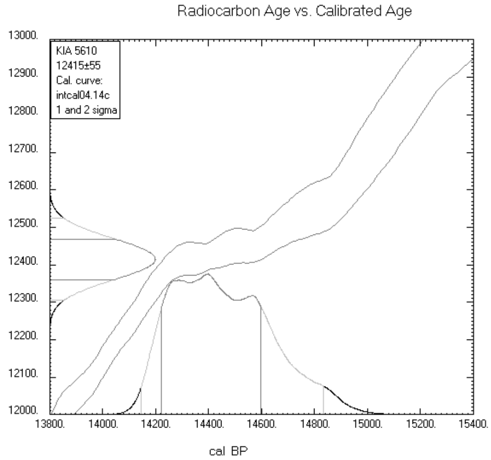

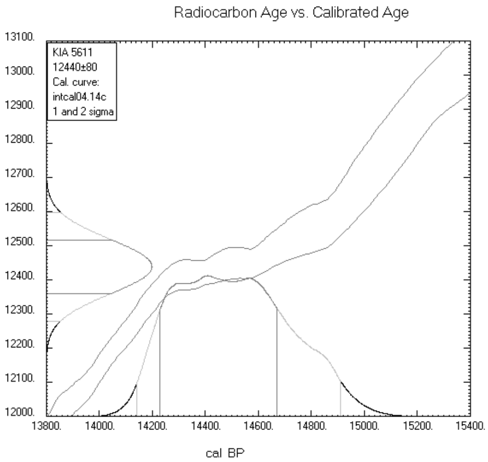

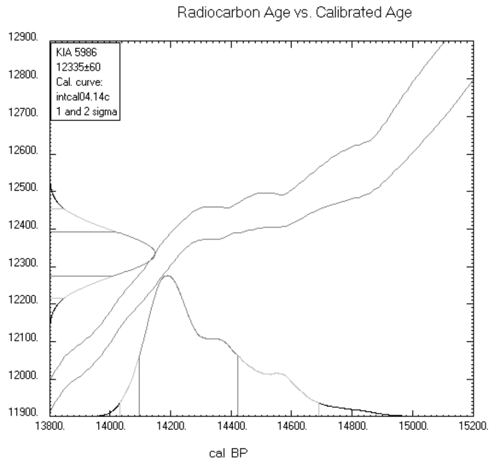

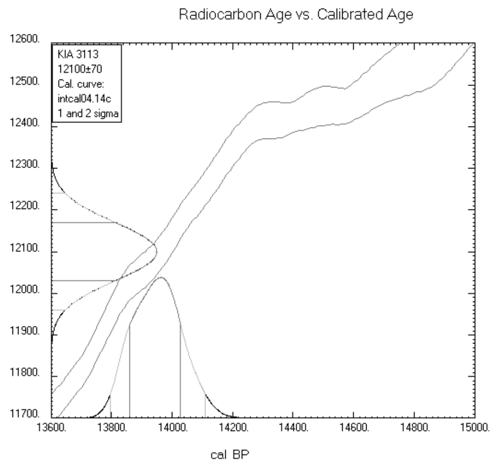
Radiocarbon Age vs. Calibrated Age
KIA 3113
12100±70
Cal. curve:
intcal04.14c
1 and 2 sigma
cal BP

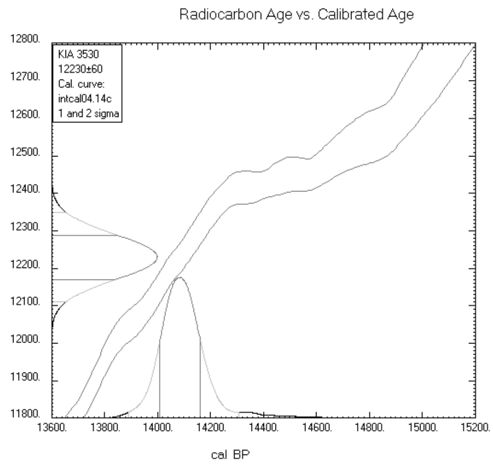
Radiocarbon Age vs. Calibrated Age
KIA 3530
12230±60
Cal. curve:
intcal04.14c
1 and 2 sigma
cal BP

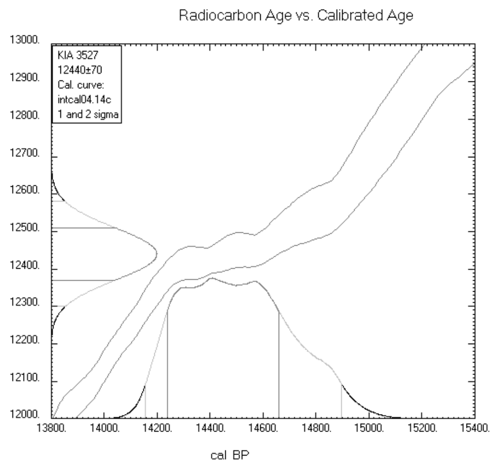
Radiocarbon Age vs. Calibrated Age
KIA 3527
12440±70
Cal. curve:
intcal04.14c
1 and 2 sigma
cal BP

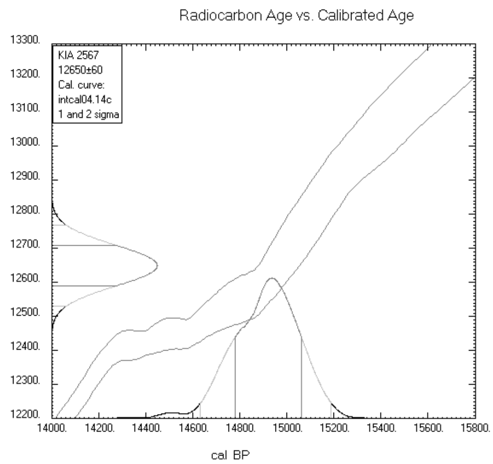
Radiocarbon Age vs. Calibrated Age
KIA 2567
12650±60
Cal. curve:
intcal04.14c
1 and 2 sigma
cal BP

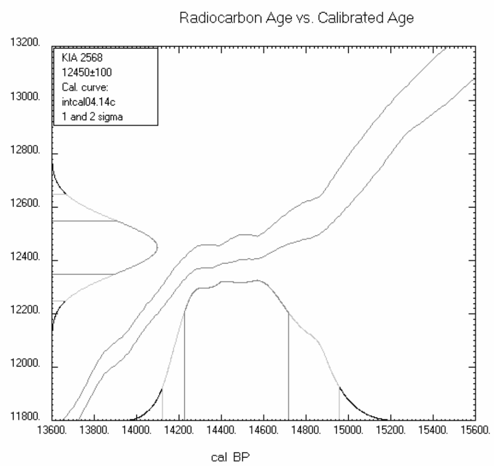
Radiocarbon Age vs. Calibrated Age
KIA 2568
12450±100
Cal. curve:
intcal04.14c
1 and 2 sigma
cal BP

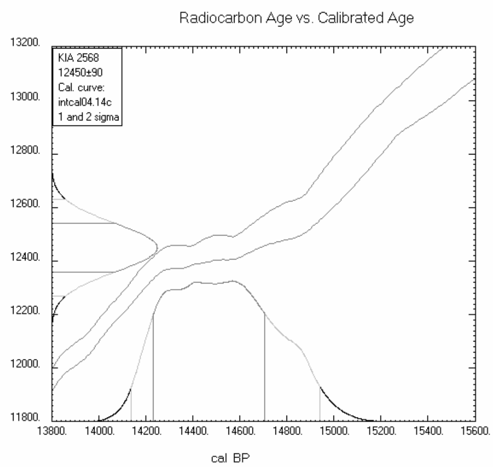
Radiocarbon Age vs. Calibrated Age
KIA 2568
12450±90
Cal. curve:
intcal04.14c
1 and 2 sigma
cal BP

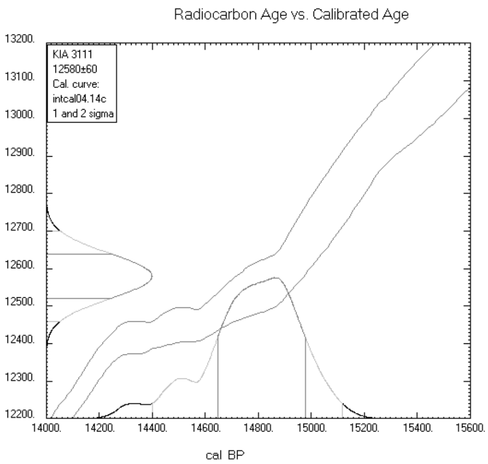
Radiocarbon Age vs. Calibrated Age
KIA 3111
12580±60
Cal. curve:
intcal04.14c
1 and 2 sigma
cal BP

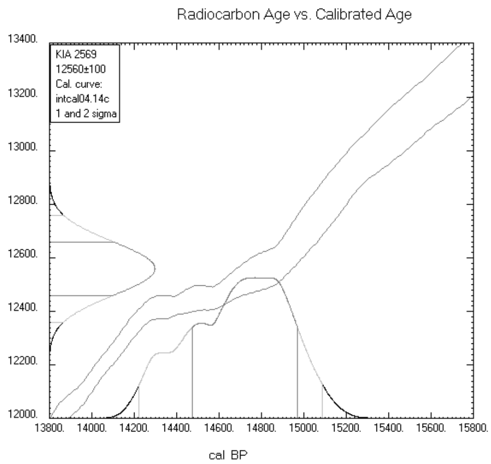
Radiocarbon Age vs. Calibrated Age
KIA 2569
12560±100
Cal. curve:
intcal04.14c
1 and 2 sigma
cal BP

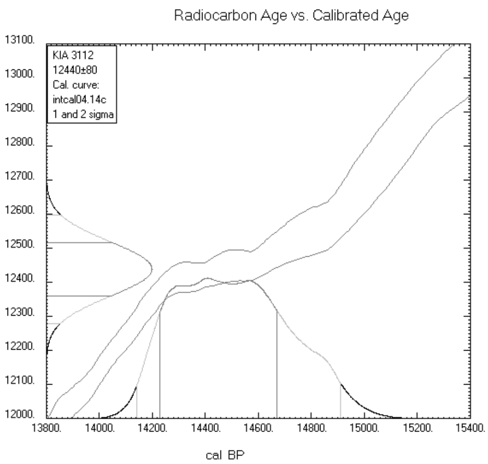
Radiocarbon Age vs. Calibrated Age
KIA 3112
12440±80
Cal. curve:
intcal04.14c
1 and 2 sigma
cal BP

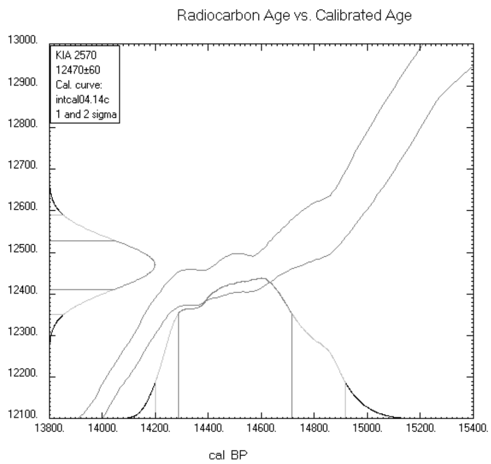
Radiocarbon Age vs. Calibrated Age
KIA 2570
12470±60
Cal. curve:
intcal04.14c
1 and 2 sigma
cal BP

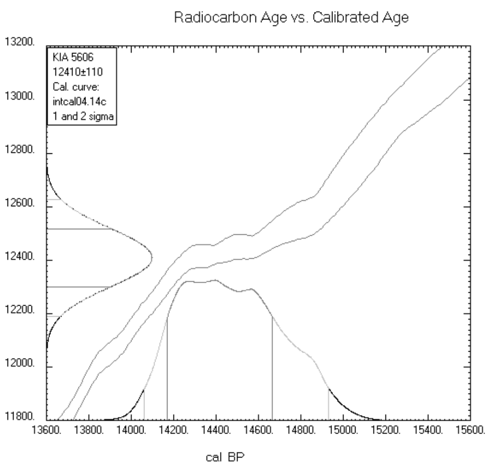
Radiocarbon Age vs. Calibrated Age
KIA 5606
12410±110
Cal. curve:
intcal04.14c
1 and 2 sigma
cal BP

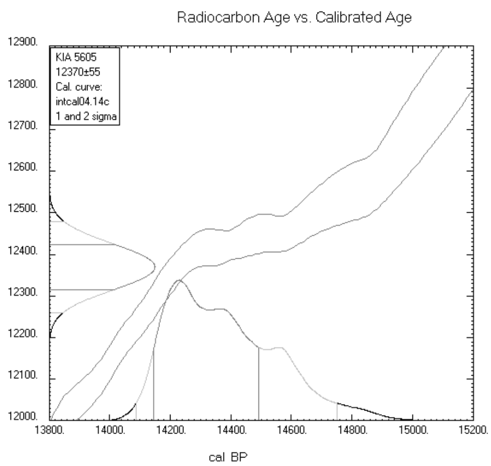
Radiocarbon Age vs. Calibrated Age
KIA 5605
12370±55
Cal. curve:
intcal04.14c
1 and 2 sigma
cal BP

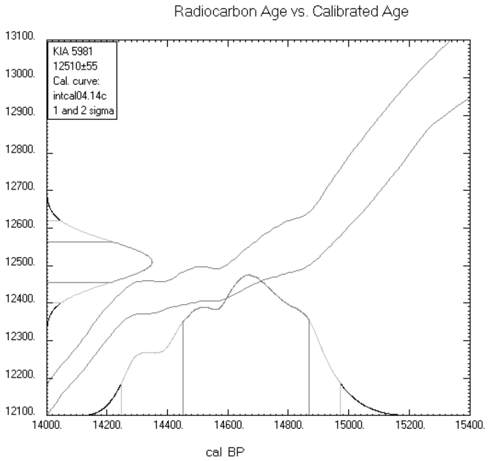
Radiocarbon Age vs. Calibrated Age
KIA 5981
12510±55
Cal. curve:
intcal04.14c
1 and 2 sigma
cal BP

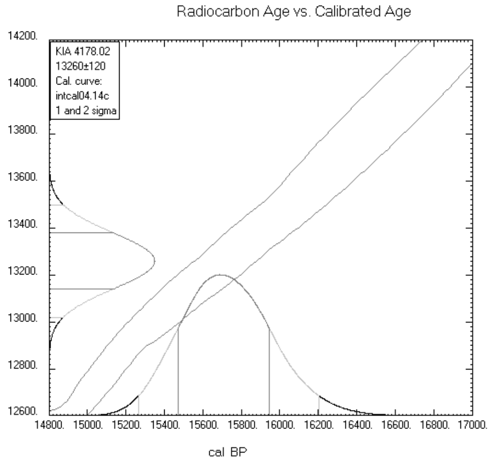
Radiocarbon Age vs. Calibrated Age
KIA 4178.02
13260±120
Cal. curve:
intcal04.14c
1 and 2 sigma
cal BP

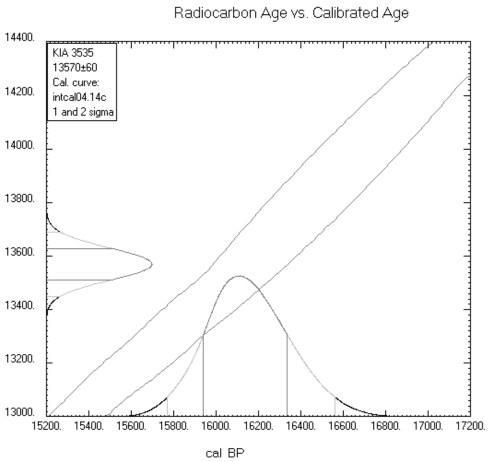
Radiocarbon Age vs. Calibrated Age
KIA 3535
13570±60
Cal. curve:
intcal04.14c
1 and 2 sigma
cal BP

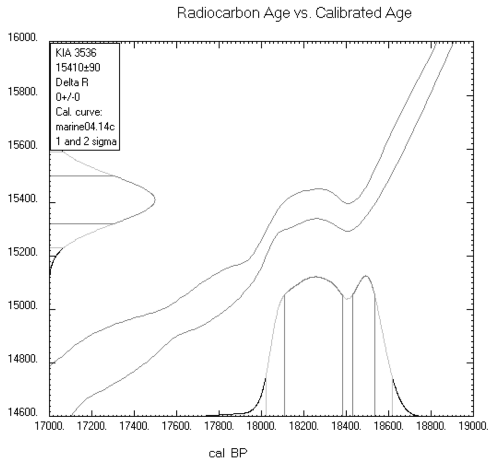
Radiocarbon Age vs. Calibrated Age
KIA 3536
15410±90
Delta R
0+/-0
Cal. curve:
marine04.14c
1 and 2 sigma
cal BP

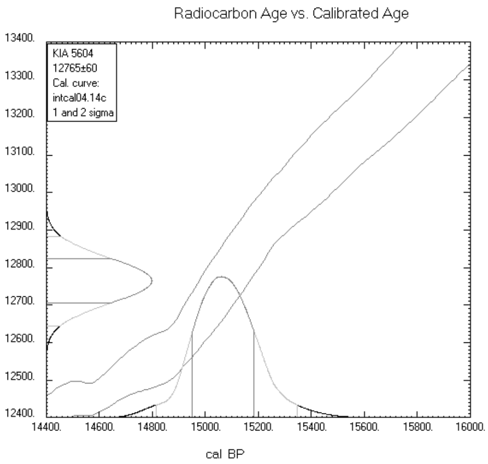
Radiocarbon Age vs. Calibrated Age
KIA 5604
12765±60
Cal. curve:
intcal04.14c
1 and 2 sigma
cal BP

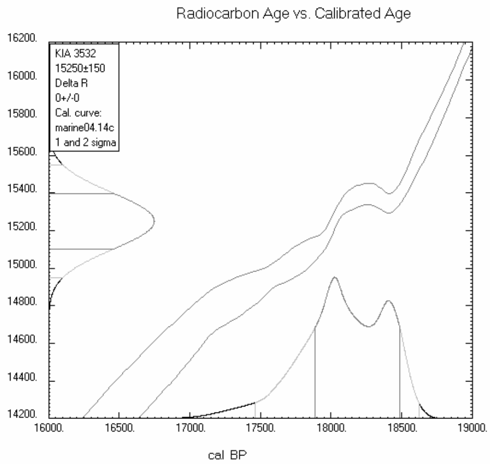
Radiocarbon Age vs. Calibrated Age
KIA 3532
15250±150
Delta R
0+/-0
Cal. curve:
marine04.14c
1 and 2 sigma
cal BP

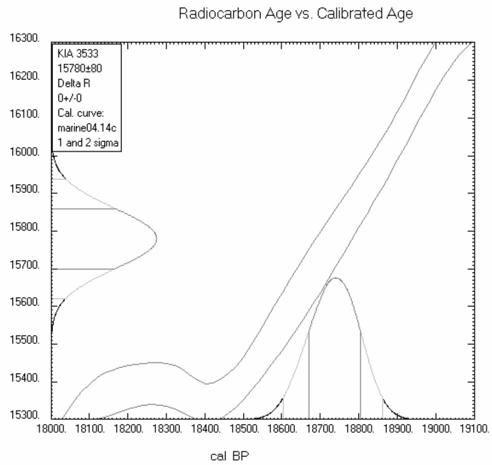
Radiocarbon Age vs. Calibrated Age
KIA 3533
15780±80
Delta R
0+/-0
Cal. curve:
marine04.14c
1 and 2 sigma
cal BP

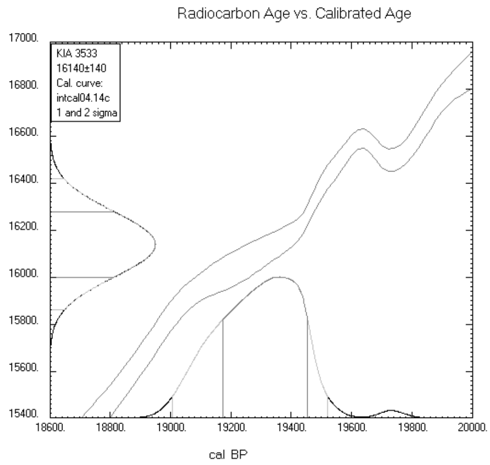
Radiocarbon Age vs. Calibrated Age
KIA 3533
16140±140
Cal. curve:
intcal04.14c
1 and 2 sigma
cal BP

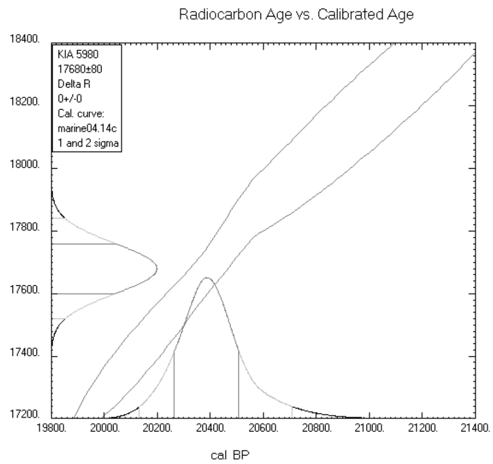
Radiocarbon Age vs. Calibrated Age
KIA 5980
17680±80
Delta R
0+/-0
Cal. curve:
marine04.14c
1 and 2 sigma
cal BP

Vietnamese Shelf Datings